

School of Chemical, Environmental and Mining Engineering



**DESIGN AND OPTIMISATION OF
SWIRL PIPES AND TRANSITION
GEOMETRIES FOR SLURRY
TRANSPORT**

Chanchala Ariyaratne, BEng (Hons), IndDip

Thesis submitted to the University of Nottingham

for the degree of Doctor of Philosophy

August 2005

ABSTRACT

This thesis is primarily concerned with the design and optimisation of transition ducts for lobed swirl-inducing pipes. Single-phase swirl-inducing pipe flows were modelled and optimised using Computational Fluid Dynamics (CFD). Optimised pipes were manufactured using rapid prototyping and an experimental investigation examines their effect on settling slurries of different densities.

The CFD model was successfully validated by experimental measurements of pressure loss and tangential velocity. An optimum transition geometry was determined for use as an entry and an exit duct with optimised swirl inducing pipe. Transition pipes either before or after the swirl inducing pipe reduced entry and exit pressure losses by providing a gradual transition from circular to lobed cross-section. They also increased induced swirl and reduced swirl decay.

CFD simulations with carboxymethyl cellulose (CMC) instead of water as the flow medium indicated that as the viscosity increased, a smaller pitch, thereby a tighter twist, is required in the swirl-inducing pipe to achieve effective swirl induction.

Settling slurry experiments showed that swirl induction resulted in better particle distribution and prevented solids dragging along the bottom of the pipe. This suggests reduction in localised erosion and provides an opportunity to operate at lower flow velocities without blockage. Lower velocities mean lower energy costs and further erosion reduction. When transitions were incorporated pressure losses across the swirl inducing pipe were reduced and the length of particle suspension increased.

It was proven, by CFD and experimentation, that entry and exit transition should be an integral part of the swirl inducing pipe. This results in an efficient swirl induction which reduces energy costs from high pressure losses that otherwise occur due to sudden changes in flow geometry.

ACKNOWLEDGEMENTS

I would like to thank Universities UK and the International Office of The University of Nottingham for the scholarships awarded to make this PhD possible.

Special thanks to my supervisors Prof. Nick Miles and Dr Trevor Jones for their support, advice, guidance, inspiration and invaluable input to this research.

I extend my gratitude to:

Tony Gospel for his assistance and advice regarding laboratory work throughout the research

Dr Ben Raylor, Dr Jeya Ganeshalingam, Dr Ruth Tonkin and Dr Dave Hargreaves for their suggestions and advice regarding CFD and experimental work

Dan Edge at IMC UK for help with Pro Engineer and Stereo lithography

Prof. Barry Azzopardi and Dr Warren Jones for looking out for me throughout the time I have been at the University

Dr Ian Lowndes for allowing the use of the CFD Lab

The School of Mechanical, Materials and Manufacturing Engineering and Phil Rogers for the loan of the PIV equipment

My friends at Nottingham (Jen Nee, Ravi, Yi Xiang, Smeeta, Chris, Shaman, Aled, Arun, and many others) for encouragement and entertainment at trying times; Rob for being the general punch bag, for his help and advice with just about everything and his imperfect cups of tea.

Finally, my parents and my brother for their love, support and understanding, particularly with regards to the many cancelled visits home...

TABLE OF CONTENTS

ABSTRACT	i
ACKNOWLEDGEMENTS	ii
TABLE OF CONTENTS.....	iii
LISTS OF FIGURES	ix
LIST OF TABLES	xiv
NOMENCLATURE	xv
CHAPTER 1: INTRODUCTION.....	1
1.1 General Introduction	1
1.2 Aims and Objectives	2
1.3 Thesis Outline	3
CHAPTER 2: LITERATURE REVIEW	
2.1 Introduction	6
2.2 Slurry Transport Characteristics- Issues and Problems	7
2.2.1 Types of Slurry Flow.....	7
2.2.2 Correlations for Settling Slurry and Definition of Terms	10
2.2.2.1 Pressure Drop.....	10
2.2.2.2 Critical Velocity	12
2.2.2.3 Particle Settling Velocity	13
2.2.2.4 Deposit Velocity	14
2.2.2.5 Economical Velocity	15
2.2.2.6 Slip Velocity	15
2.2.3 Minimising Frictional Pressure Loss in Settling Slurry	16
2.2.4 Wear in Pipeline.....	18
2.2.5 Measurements in Slurry Pipeline Technology	20
2.2.5.1 Invasive Flow Measurement Techniques	22

2.2.5.2 Non-invasive Flow Visualisation and Measurement Techniques.....	23
2.3 Swirling Flow	25
2.3.1 Advantages of Swirling Flow	25
2.3.2 Different Swirl Inducing Methods and Non-Circular Pipe Geometries	26
2.3.3 Previous Research on <i>Swirly-Flo</i> Pipe	30
2.3.4 Definition of Terms and Equations for Swirling Flow	34
2.4 Modelling Flow	36
2.4.1 Multiphase Modelling	38
2.4.1.1 Euler-Lagrange Model (Discrete Phase Model)	40
2.4.1.2 Euler-Euler Model	42
2.5 Conclusions	44

CHAPTER 3: SWIRL AND TRANSITION PIPE DESIGN.....45

3.1 Introduction	45
3.2 Methodology	45
3.3 Geometry Definition.....	46
3.3.1 Summary of Swirl Pipe Calculations	46
3.3.2 Summary of Transition Pipe Calculations	47
3.3.3 Different Types of Transition.....	49
3.3.3.1 Alpha Transition	49
3.3.3.2 Beta Transition	50
3.3.3.3 Transition Multiplier	51
3.3.3.4 Variable Helix	53
3.4 Geometry Creation	54
3.5 Producing Pipes for Experimentation	58
3.5.1 Lost Wax Process.....	58
3.5.2 Stereo Lithography	60
3.6 Conclusions	62

CHAPTER 4: COMPUTATIONAL FLUID DYNAMICS METHODOLOGY...63

4.1 Introduction	63
4.2 Modelling Turbulence	64
4.2.1 RANS Approach	66
4.2.1.1 Standard k- ϵ Model.....	67

4.2.1.2 Re-Normalisation Group (RNG) and Realizable k- ϵ Model	68
4.2.1.3 Reynolds Stress Model (RSM).....	69
4.2.2 Choice of Turbulence Model	69
4.2.3 Near Wall Treatment for Turbulent Flows.....	71
4.2.3.1 Standard Wall Functions.....	73
4.2.3.2 Non-Equilibrium Wall Functions	74
4.2.3.3 Grid Adaption at the Wall	75
4.3 Model Description	75
4.3.1 Enabling Assumptions.....	76
4.3.2 Solver Parameters	76
4.3.3 Numerical Discretisation Techniques	78
4.3.3.1 Finite Difference Method.....	79
4.3.3.2 Finite Element Method	79
4.3.3.3 Finite Volume Method	80
4.3.4 Upwinding Scheme.....	81
4.3.4.1 First-Order Upwind Scheme	82
4.3.4.2 Second-Order Upwind Scheme	82
4.3.5 Solver	82
4.3.6 Under Relaxation	83
4.3.7 Judging Convergence	83
4.3.7.1 Residual Convergence.....	84
4.3.7.2 Mass Imbalance	85
4.3.7.3 Inlet Pressure Convergence	86
4.4 Meshing	87
4.4.1 Swirl Pipe Mesh	89
4.4.2 Transition Pipe Mesh	90
4.4.3 Circular Pipe Mesh	92
4.4.4 Examining Mesh Quality.....	94
4.4.4.1 Aspect Ratio	94
4.4.4.2 Equi-Angle Skew	95
4.4.4.3 Volume	95
4.4.5 Grid Independence Tests	96
4.5 The Importance of Velocity Profile.....	100
4.6 Conclusions	101

CHAPTER 5: OPTIMISATION OF TRANSITION PIPES USING COMPUTATIONAL FLUID DYNAMICS	102
---	------------

5.1 Introduction	102
5.2 Comparison of 3-Lobed Transition to 4-Lobed	102
5.3 Comparison of Alpha and Beta Transition Pipe and Swirl Pipe	103
5.4 Transition Multiplier Optimisation	105
5.4.1 Entry Transition Optimisation by Transition Multiplier	105
5.4.2 Exit Transition Optimisation by Transition Multiplier	107
5.5 Variable Helix Optimisation	109
5.6 Advantage of Using Entry Transition	111
5.7 Advantage of Using Exit Transition	114
5.8 Conclusions	116

CHAPTER 6: EXPERIMENTAL FLOW LOOP..... 117

6.1 Introduction	117
6.2 Perspex Rig Layout	118
6.3 Particle Analysis	121
6.4 General Operational Procedure	123

CHAPTER 7: VALIDATION OF COMPUTATIONAL FLUID DYNAMICS RESULTS 126

7.1 Introduction	126
7.2 Background to CFD Verification and Validation	126
7.3 Pressure Drop Validation	128
7.3.1 Cylindrical Pipe	128
7.3.2 4-Lobed Swirling Flow Pipe	130
7.3.3 Optimum Entry Transition Pipe	133
7.4 Tangential Velocity Validation	135
7.4.1 PIV Setup and Methodology	136
7.4.2 Procedure for Calculating Tangential Velocity	139
7.4.2.1 With Cross-sectional Viewer as used by Tonkin	139
7.4.2.2 With Laser and Camera at an Angle (Oblique Laser Sheet)	140
7.4.3 Swirl Pipe Results Validation	142
7.4.3.1 Qualitative Comparison and Type of Swirl	146
7.4.4 Swirl Decay	148
7.5 Conclusions	153

**CHAPTER 8: ADVANTAGE OF TRANSITIONS IN SWIRL INDUCTION
ON SETTLING SLURRY 155**

8.1 Introduction	155
8.2 Background	155
8.3 Pressure Drop	159
8.3.1 Effect of Velocity on Pressure Drop	159
8.3.2 Effect of Solids Density on Pressure Drop	162
8.3.3 Effect of Solids Concentration on Pressure Drop	163
8.3.4 Pressure Advantage of Transition	164
8.4 Settling Length	166
8.4.1 Effect of Velocity on Settling	166
8.4.2 Effect of Solids Density on Settling	169
8.4.3 Effect of Solids Concentration on Settling	170
8.4.4 Advantage of Transition in Delaying Settling	171
8.5 Flow Patterns.....	173
8.6 Conclusions	178

**CHAPTER 9: OPTIMISING SWIRL PIPE FOR NON-NEWTONIAN
FLUIDS..... 180**

9.1 Introduction and Background	180
9.2 Non-Newtonian Fluids	181
9.3 CFD Methodology	182
9.3.1 Defining a Non-Newtonian Fluid in Fluent CFD Software.....	182
9.3.2 Swirl Pipe Geometry	184
9.3.3 Parameters used in the Solver	185
9.3.4 Grid Independence Tests	186
9.4 Optimisation Results	187
9.4.1 Optimisation Results for $k = 0.6$	187
9.4.2 Optimisation Results for $k = 1.2$	191
9.5 Conclusions	193

CHAPTER 10: CONCLUSIONS AND FUTURE WORK 195

10.1 Conclusions	195
10.1.1 CFD Optimisation and Validation for Single Phase Flow	195

10.1.2 Swirling Flow and Transitions in Settling Slurry.....	196
10.1.3 Contributions to Knowledge	197
10.2 Future Work.....	198
10.2.1 CFD Modelling	198
10.2.2 Changes to Swirl Pipe Geometry.....	198
10.2.3 Experimental Methodology	199
BIBLIOGRAPHY	201

APPENDICES

LIST OF FIGURES

Figure 2.1: Flow Patterns in Settling Slurry	9
Figure 2.2: Boiler Tube <i>Swirly-Flo</i> Pipe used by Raylor and Ganeshalingam	31
Figure 2.3: Results Comparing Circular Pipe Flow to Swirl Pipe Flow of Particles in Fluent DPM	41
Figure 3.1: Illustration of Calculation of x_{offset} and y_{offset} for 3-Lobed Pipe...	46
Figure 3.2: Transition Pipe at Intermediate Stage	48
Figure 3.3: Calculation of Lobe Co-ordinates at Intermediate Stage.....	49
Figure 3.4: Tangential Velocity Contours at Exit of Swirl Pipe	50
Figure 3.5: Entry transition; Comparison of Lobe Area development with Length for Alpha, Beta and Linear Law	51
Figure 3.6: Entry Transition: Effect of Transition Multiplier	52
Figure 3.7: Effect of Variable Helix	54
Figure 3.8: Graph of Twist versus Length (geodesic helix shown).....	56
Figure 3.9: Example of 13 Sections used to Sweep and Blend to form Solid Transition Pipe	57
Figure 3.10: Bend Produced using the Lost Wax Process (After Jones (Jones 2004))	60
Figure 3.11: Pipes Produced using Stereo Lithography before Removal from Build Tank	62
Figure 4.1: Variation of Pressure Drop	70
Figure 4.2: Variation of Tangential Velocity.....	71
Figure 4.3: Near-Wall Region in Turbulent Flows	71
Figure 4.4: Scaled Residuals Reduced by Five Orders of Magnitude ($<1 \times 10^{-05}$)	85
Figure 4.5: Histogram of Mass Imbalance	86
Figure 4.6: Variation of Mass Imbalance (Inlet-Outlet) with Iteration number (Last 100 iterations were closely inspected in addition)	86
Figure 4.7a: Variation of Static Pressure at Inlet with Residuals	87
Figure 4.7b: Variation of Static Pressure at Inlet with Residuals (Last 100 iterations).....	87
Figure 4.8: Swirl Pipe Meshes Generated in Gambit	90
Figure 4.9: Typical 4-Lobed Transition Pipe Hybrid Mesh Generated in Gambit (interval size (is) 3.3mm)	91

Figure 4.10: Mesh generated using GridGen Software (Raylor 2003) for Exit Transition	92
Figure 4.11: Highly Skewed Cells at Pipe Intersection	93
Figure 4.12: Structured Hex Mesh Attempted for Circular Pipe.....	94
Figure 4.13: Development of Velocity Profile (CMC, $v=1.5\text{m/s}$) (Figure on the right is with an inlet velocity profile applied).....	101
Figure 5.1: Swirl Effectiveness versus Length for 4- and 3-Lobed Alpha Transitions (Type $n=1$)	103
Figure 5.2: Entry Transition Optimisation; Tangential Velocity versus Length for Different Transition Geometries.....	105
Figure 5.3: Entry Transition Optimisation; Tangential Velocity versus Transition Multiplier n	106
Figure 5.4: Entry Transition Optimisation; Pressure Drop versus Transition Multiplier n	106
Figure 5.5: Entry Transition Optimisation; Swirl Effectiveness versus Transition Multiplier n	107
Figure 5.6: Exit Transition Optimisation; Tangential Velocity versus Transition Multiplier n	108
Figure 5.7: Exit Transition Optimisation; Pressure Drop versus Transition Multiplier n	108
Figure 5.8: Exit Transition Optimisation; Swirl Effectiveness versus Transition Multiplier n	109
Figure 5.9: Entry Transition Optimisation; Tangential Velocity versus t Value	110
Figure 5.10: Entry Transition Optimisation; Pressure Drop versus t Value	110
Figure 5.11: Entry Transition Helix Optimisation; Swirl Effectiveness versus t Value	111
Figure 5.12: Simulation Geometry for Advantage from use of Entry Transition as opposed to Cylindrical Inlet Pipe.....	112
Figure 5.13a: Comparison of use of Entry Transition to use of Cylindrical Pipe; Pressure Drop versus Length	112
Figure 5.13b: Comparison of use of Entry Transition to use of Cylindrical Pipe; Tangential Velocity versus Length	113
Figure 5.13c: Comparison of use of Entry Transition to use of Cylindrical Pipe; Swirl Effectiveness versus Length.....	114
Figure 5.14: Simulation Geometry for Advantage from use of Exit Transition as opposed to Cylindrical Exit Pipe.....	114

Figure 5.15a: Comparison of use of Exit Transition to use of Cylindrical Pipe; Tangential Velocity versus Length	115
Figure 5.15b: Comparison of use of Exit Transition to use of Cylindrical Pipe; Pressure Drop versus Length	116
Figure 6.1: Schematic Diagram of Perspex Rig (After Ganeshalingam (Ganeshalingam 2002))	119
Figure 6.2: Pressure Transducer Calibration- Transducer P7	120
Figure 6.3: Pressure Transducer Calibration- Transducer P8	120
Figure 6.4: Manometer used on the Rig	121
Figure 6.5: Density Tracers used in Slurry Tests; Red, RD 1.4, Blue, RD 2.7 and Yellow, RD 4.5	122
Figure 6.6: Set-up of Three Digital Cameras for Photographing Solids Distribution	124
Figure 7.1: Pressure Loss Validation for a Cylindrical Pipe	130
Figure 7.2: Geometry for the CFD Analysis of Swirl Pipe Pressure Loss ...	131
Figure 7.3: Pressure Loss Validation for a 4-Lobed Swirl Pipe	133
Figure 7.4: Geometry for CFD Analysis of Entry and Swirl Pipe Pressure Loss	134
Figure 7.5: Pressure Loss Validation for a 4-Lobed Entry Transition Pipe in Conjunction with Swirl Pipe	135
Figure 7.6: PIV Setup and Camera Angle for the Cross-sectional Velocity Measurement (After Tonkin (Tonkin 2004))	137
Figure 7.7: Schematic Diagram of PIV Setup and Camera Angle with the Laser at an Angle	138
Figure 7.8: Vector Diagram Post Cross-Correlation	139
Figure 7.9: Calculation of Circumferential (Tangential) Velocity Component	140
Figure 7.10: Vector Diagram with the Laser at an Angle (Camera optical axis is perpendicular to the laser plane (PIV image)	141
Figure 7.11: Comparison of Experimentally Measured Tangential Velocity to CFD Prediction at Different Axial Velocities	143-145
Figure 7.12: Classification of Swirl Types (After Steenbergen and Voskamp, 1998)	146
Figure 7.13: Tangential Velocity Development through Length of the Swirl Pipe (L=0 Swirl Pipe Entrance, L=0.4 Swirl Pipe Exit)	148
Figure 7.14: Decay of Swirl Intensity with Length (at a Reynolds number of 100,000)	150

Figure 7.15: Exponential Decay of Swirl Intensity with Length (at a Reynolds number of 100, 000)	151
Figure 7.16: Ganeshalingam's (Ganeshalingam 2002) Comparison of CFD Predicted and Calculated (Steenbergen and Voskamp, 1998) Swirl Decay at a Reynolds Number of 100,000	152
Figure 7.17: Exit Transition Reduces Decay Rate	153
Figure 8.1: Comparison of Pressure Loss across Marine <i>Swirly-Flo</i> Pipe and Optimised Swirl Pipe and Transitions	157
Figure 8.2: Pressure Loss Curve for 'Water only'	160
Figure 8.3: Pressure Loss Curve for R.D. 1.4; 2kg of solids added, 1.8% w/w and 1.35% v/v	160
Figure 8.4: Pressure Loss Curve for R.D. 2.7; 2kg of solids added, 2.0% w/w, 0.77% v/v	161
Figure 8.5: Pressure Loss Curve for R.D. 4.5; 2kg of solids added, 1.38% w/w and 0.31% v/v	161
Figure 8.6: Pressure Loss Curve for 'Swirl + Entry + Exit transition' case; 2kg of each density added (R.D. 1.4 1.9% w/w, R.D. 2.7 1.9% w/w, R.D. 4.5 1% w/w)	163
Figure 8.7: Effect of Solids Concentration for 'Swirl +Entry + Exit transition' Case with R.D. 1.4 Solids	164
Figure 8.8: Pressure Saving from use of Entry and Exit Transition Pipes (over a total pipe length of approximately 3.325m); 2kg of solids added in each test	165
Figure 8.9: Settling Length for R.D. 1.4 Solids; Length Downstream when Settling Begins; 2kg of solids added in each test	167
Figure 8.10: Settling Length for R.D. 2.7 Solids; Length Downstream when Settling Begins; 2kg of solids added in each test	168
Figure 8.11a: Settling Length for R.D. 2.7 Solids; Length Downstream when Settling Begins; 2kg of solids added in each test	168
Figure 8.11b: Settling Length for R.D. 4.5 Solids; Length Downstream when Settling is 'Clearly Visible'; 2kg of solids added in each test	169
Figure 8.12: Effect of Solids Density on Settling for 'Swirl + Entry + Exit Transition' Case; 2kg of solids added in each test	170
Figure 8.13: Effect of Solids Concentration on Settling for 'Swirl + Entry + Exit Transition' Case; R.D. 1.4 solids	171
Figure 8.14: Swirl Advantage from use of Entry and Exit Transition Pipes; 2kg of solids added in each test	172

Figure 8.15: Illustration of Particle Tracks in the Cylindrical Pipe following Helical Paths defined by Lobe Surfaces of the Swirl Pipe	173
Figure 8.16: Photographs of Flow Velocities 1 to 1.75m/s; 'Swirl + Entry + Exit Transition' Case, RD 1.4 Solids, 4% w/w	174
Figure 8.17: Photographs of Flow Velocities 1 to 1.75m/s; 'Swirl + Entry + Exit Transition' Case, Mixed Densities RD 1.4 (Red), 2.7 (Blue) and 4.5 (Yellow).....	177
Figure 9.1: Velocity Distribution of Fluid between Two Planes	181
Figure 9.2: Variation of Viscosity with Shear Rate according to the Non-Newtonian Power Law (Fluent Inc. Lebanon 2001)	183
Figure 9.3: Rheograms and Rheological Parameters (Pseudoplastic Model) of the CMC Before and After Testing, (up and down curves shown, each is mean of 3 trials, after Tonkin).	184
Figure 9.4: Swirl Pipes of Different P:D Ratios.....	185
Figure 9.5: Viscosity Variation through the Pipe.....	187
Figure 9.6: Viscosity Patterns in Pipe Cross-sections (P:D = 4).....	188
Figure 9.7: Pressure Drop versus Length Characteristic for Pipes of Different P:D with CMC (Result for Water is shown for comparison).....	189
Figure 9.8: Tangential Velocity versus Length Characteristic for Pipes of Different P:D with CMC (Result for water is shown for comparison)	190
Figure 9.9: Optimising Swirl Pipe for P:D Ratio with respect to Swirl Effectiveness Parameter (evaluated at a length of 0.5m)	191
Figure 9.10: Optimising Swirl Pipe for P:D Ratio with respect to Swirl Effectiveness Parameter (evaluated at a length of 0.5m)	192
Figure 9.11: Comparison of k=0.6 and k=1.2 Results	192-193

LIST OF TABLES

Table 3.1: Deviations from Theoretical for 3-Lobed Beta Transition	58
Table 4.1: Comparison of Turbulence Models for Entry Transition.....	70
Table 4.2: Flow Parameters for the CFD Simulations	78
Table 4.3: Mesh Quality Analysis for a Selection of Geometries.....	96
Table 4.4: Grid-Independence Test for Swirl Pipe	98
Table 4.5: Grid-Independence Test for Entry Transition Pipe	98
Table 4.6: Grid-Independence Test for Exit Transition Pipe	99
Table 4.7: Grid-Independence Test for Circular pipe.....	99
Table 4.8: Effect of Inlet Velocity Profile on Circular Pipe Pressure loss ...	100
Table 5.1: Comparison of α and β Transition Pipes ($n=1$) and an Optimised Swirl Pipe (all 4-lobed)	104
Table 7.1 Pressure Drop Results for Cylindrical Pipe	129
Table 7.2: Pressure Drop Results for Swirl Pipe	132
Table 7.3: Pressure Loss Results from Inclusion of Entry Transition Pipe .	134
Table 7.4: Maximum Tangential Velocities	146
Table 8.1: Solids Concentration	158
Table 8.2: Mixed Density Run	176
Table 9.1: Flow Parameters for the CFD Simulations	186

NOMENCLATURE

A	Area	m ²
C _μ	Constant	
C _D	Drag coefficient for free-falling sphere	
C _o	Delivered vol. concentration of solid particles	%
C _M	Concentration by mass	%
C _V	Concentration by volume	%
C _w	Concentration by weight	%
d	Particle diameter	m
D	Pipe diameter	m
d _h	Hydraulic pipe diameter	m
e	roughness	m
E	Empirical constant (a function of the wall roughness) (=9.81 for smooth walls)	
f	Fanning or Darcy friction factor	
f'	Moody friction factor ($f' = 8\Phi$, $f' = 4f$)	
Fr	Froude no.	
g	Gravitational acceleration	m/s ²
H	Holdup ratio	
I	Turbulence intensity	%
is	Interval size in mesh (distance between nodes in a mesh)	mm
k	2.5 and varies with particle properties (Einstein's equation for laminar suspensions)	
k	Consistency coefficient in the power law equation for non-Newtonian fluids	
k	Turbulent kinetic energy	m ² /s ²
K _s	Wall roughness height	m
L	Distance when settling begins	m
L ₁	Distance when settling is clearly visible	m
n	Flow behaviour or power law index in the power law equation for non-Newtonian fluids	
P	Static pressure of slurry flow	Pa
P	Wetted perimeter	m
P _w	Static pressure of pure water only	Pa
Q _{AR}	Aspect ratio of a mesh element	

Q_{EAS}	Equi-angle skewness of a mesh element	
R	Pipe radius	m
r	Radius at point where tangential velocity is calculated	m
Ra	Shear stress on surface	N/m ²
Re	Reynolds number	
s	Relative density (ρ_s/ρ_w)	
S	Swirl intensity	
St	Stokes number	
S_0	Initial swirl intensity	
T	Temperature	K
T_0	Reference temperature	K
t	power law variable for twist	
t_s	System response time	s
u	Axial velocity	m/s
U^+	Dimensionless mean velocity = u/u_τ	
u_s	Slip velocity	m/s
u_τ	friction velocity = $\frac{\tau_w}{\rho}$	
V	mean velocity of slurry flow	m/s
V_{DC}	deposition critical velocity	m/s
V_{IL}	In-situ liquid velocity	m/s
V_{IS}	In-situ solids phase velocity	m/s
V_r	Radial velocity	m/s
V_s	Settling velocity in still water	m/s
V_θ	Circumferential (or tangential) velocity	m/s
w	tangential velocity	m/s
x	Distance along pipe	m
y	Normal distance to the wall	m
y^+	Non-dimensional distance of a point from the wall $= \frac{\rho y u_\tau}{\mu}$	
α	Empirical coefficient	
β	Swirl decay rate parameter = $\alpha * f'$	
γ	Shear rate	s ⁻¹
δ	Under-relaxation	
ΔP	Pressure difference	Pa
$\Delta \phi$	Computed change in a variable ϕ	
ε	Turbulence dissipation rate	m ² /s ³

η	Non-Newtonian viscosity	kg/ms
κ	von Karman constant (=0.42)	
μ_t	Turbulent viscosity	kg/ms
ρ	Fluid density	kg/m ³
ρ_M	Mixture density	kg/m ³
ρ_s	Solids density	kg/m ³
ρ_w	Water density	kg/m ³
τ	Shear stress	Pa
τ_w	Shear stress at the wall	Pa
τ_d	Particle response time	s
Φ	Friction factor (= $R/\rho u^2$)	
ϕ_{NEW}	New value of variable	
ϕ_{OLD}	Old value of variable	

Notation used in Swirl and Transition Design

r_f	Lobe radius of fully developed swirl pipe	mm
(x_{offset}, y_{offset})	Co-ordinates used in transition geometry	
ϕ	Angle used in transition geometry	deg
R_1	Circular pipe radius	mm
R_{CS}	Minimum core radius of circular pipe	mm
γ	Angle used in transition geometry	deg
N_{inc}	Number of increments	
f, f_1	Calculated terms used in transition calculation	
y	Length variable in transition calculation	mm
R	Intermediate core radius in transition	mm
r	Intermediate lobe radius in transition	mm
LA_i	Intermediate lobe area in transition	mm ²
LA_{FD}	Fully developed lobe area in swirling flow pipe	mm ²
α	Variable in transition design	
β	Variable in transition design	
x	Intermediate pipe length	mm
L	Total pipe length	mm
(x_{lobe1}, y_{lobe1})	Co-ordinates used in transition geometry	
$(x_{lobe1twisted}, y_{lobe1twisted})$	Co-ordinates used in transition geometry	
z	distance of lobe centre from origin	mm
n	Lobe number	

θ	Angle in swirl pipe design calculation	deg
d_e	Equivalent diameter of swirl pipe	mm
R_c	Radius of curvature (in bends)	m

Abbreviations

CFD	Computational Fluid Dynamics
PIV	Particle Image Velocimetry
CMC	Carboxymethyl Cellulose
DPM	Discrete Phase Model
PDE	Partial Differential Equation
DNS	Direct Numerical Simulation
LES	Large Eddy Simulation
RANS	Reynolds Averaged Navier Stokes
RSM	Reynolds Stress Transport Models
LDV	Laser Doppler Velocimetry
PDA	Phase Doppler Anemometry
PET	Positron Emission Tomography
MRI	Magnetic Resonance Imaging
ECT	Electrical Capacitance Tomography
ERT	Electrical Resistance Tomography
RD	Relative Density

Terminology

Swirl pipe	General term for lobed helical pipes
<i>Swirly-Flo</i> pipe	Trade name for lobed helical pipes found in boiler tubes and based on Spanner (Spanner 1940; Spanner 1945) patent
Swirling flow pipes	Optimised swirl pipe geometry (4-lobed, 400mm length, 50mm diameter, P:D ratio 8)
P:D ratio	Pitch-to-diameter ratio (where pitch is the axial length for the lobed cross-section to rotate through 360°)

CHAPTER 1: INTRODUCTION

1.1 General Introduction

It is well documented that swirling flow increases particle distribution and reduces localised wear in hydrotransport (Wolfe 1967a; Schriek 1974; Raylor 1998; Raylor 1999; Wood 2001; Ganeshalingam 2002; Heywood 2003). The tangential velocity component imparted upon the flow in swirl induction effectively sweeps and lifts deposited particles in the lower part of the pipe into the upper part creating a more homogeneous flow pattern (Wolfe 1967a, Schriek 1974, Heywood 2003). Additionally, swirling flow within bends causes particles to rotate about the pipe axis thereby spreading particle impingements over the entire surface of the bend thus reducing the potential for wear hotspots (Raylor 1998, Raylor 1999, Wood 2001, Ganeshalingam 2002).

Since swirling flow returns settled particles to the main stream, deposition velocities are reduced providing the opportunity to operate at lower flow velocities. Thereby the energy costs to keep particles in suspension and avoid pipeline blockage are reduced with swirling flows (Charles 1971; Schriek 1974; Singh 1976). The lower velocities imply further reduction of pipeline wear.

In 1993, Jones suggested the design of a helical pipe with a lobed cross-section for swirling the flow in slurry transport (Jones 1997). Research was begun by Raylor (Raylor 1998) into its feasibility. He showed experimentally that the use of such a pipe before a vertical bend reduced the pressure loss across the bend and provided better particle distribution, thus potentially reducing localised wear.

A considerable body of work involving numerical modelling, flow visualisation and experimentation on settling slurries has been undertaken at the University of Nottingham on the influence of swirl on hydrotransport. Ganeshalingam (Ganeshalingam 2002) continued Raylor's work on swirling flow pipes and optimised its geometry using Computational Fluid Dynamics

(CFD) software. He showed that a higher concentration of solids can be carried using swirling flow pipes without the danger of blockage.

Both Raylor and Ganeshalingam carried out their experimental investigations using a swirl pipe found in marine boilers which is used to improve heat exchanger efficiency. This pipe was used due to its immediate availability. However, it was not the optimum geometry of pipe for use in slurry transport as shown by Ganeshalingam through CFD optimisation (Ganeshalingam 2002; Jones 2002). Furthermore, its flow area was smaller than the pipes on the experimental flow rig and its surface roughness much greater. Therefore one of the tasks for the current research was the manufacture of an optimised swirl pipe, as suggested by Ganeshalingam, for testing.

In addition, both these researchers found that there were high entry and exit pressure losses across the swirl pipe due to the sudden change in cross-section from lobed to circular and vice versa. Transition geometries prior to and after the swirl pipe were suggested to eliminate these pressure losses. This should further improve the applicability of the swirling flow pipes.

The current thesis is mainly concerned with the design and optimisation using CFD of such transition geometries and assessing their viability for use in hydraulic transport. The possibility of modifications to the CFD model was also considered so that more complex pipe flow scenarios could be investigated.

1.2 Aims and Objectives

The main aim was to optimise and prove the viability of swirl and transition pipes for hydraulic transport.

The intentions of the research were to:

- Complete a comprehensive literature survey on slurry transport, swirling flow and modelling techniques used by current and previous researchers to enable the establishment of a sound numerical model

for investigating swirling flows and gain knowledge of methodology and practises in slurry transport.

- Design efficient swirl and transition pipes and produce prototypes for experimental assessment
- Establish a CFD model for investigating swirling pipe flow and perform grid independence and convergence tests for swirl and transition pipe geometries
- Optimise transitions, and swirl pipes where necessary, using the CFD model
- Validate CFD results using experimentally measured pressure loss and tangential velocity across swirl and transition pipes
- Test the viability of swirl and transition pipes for hydraulic transport via testing the transport of different density solids
- Analyse the possibility of modifying the established CFD model for more complex situations involving non-Newtonian transport media and solid particles

1.3 Thesis Outline

The following is a brief description of each chapter contained within this thesis.

The current chapter, Chapter 1, introduces the research and outlines the aims and objectives of the work carried out.

Chapter 2 is a general literature review considering current issues in slurry transport with particular emphasis on swirl inducing methods and modelling slurry flow. The important terms and equations for swirling flow are defined and explained. Multiphase modelling is briefly considered and the problems encountered are presented with interesting aspects for future investigations.

Chapter 3 details the calculations in the design of transitions and describes the different transition geometries that are later optimised using CFD in Chapter 5. Geometry creation of swirl pipes, swirl bends and transitions for use in CFD simulations, and for making prototypes to be used on the flow rig, are discussed.

Problems encountered with modelling turbulent flow are considered in [Chapter 4](#) and the CFD model used in optimisation simulations is described in depth. The model description includes considerations given to meshing of the various pipe geometries and detailed grid independence tests for each main type of pipe geometry.

[Chapter 5](#) presents the key results of this thesis and contains CFD optimisation results for various entry and exit transition geometries. The advantages from use of entry and exit transitions in terms of increased swirl generation and reduced pressure loss are also investigated.

The next three Chapters are mainly concerned with the experimental flow rig. [Chapter 6](#) contains preliminary results of particle size and density analyses which helped in establishing particles for use in slurry tests. It also introduces the experimental rig and the procedure employed in Chapters 7 and 8.

In [Chapter 7](#) CFD predictions are compared to pressure and tangential velocity results measured on the flow rig. Problems with Particle Image Velocimetry (PIV) measurements are detailed and the best method of tangential velocity measurement using PIV is presented. A qualitative comparison of the observed type of swirl is given and the swirl decay from CFD is critically analysed and compared to theoretical and empirical findings of other researchers.

Experimental findings from settling slurry runs, with and without entry and exit transitions, in swirling pipe flow are presented in [Chapter 8](#). The effect of transitions on pressure and settling length of particles is evaluated. In addition, the effect of slurry density and concentration on swirling pipe flow, and on the advantage provided by transitions is examined. The differences in flow regime before and after the swirling flow pipe are discussed. This analysis was important since all optimisation simulations described in Chapter 5, and validated in Chapter 7, are for single phase flow and the effect of particles on the flow was not taken into account.

[Chapter 9](#) explores the optimisation of the swirl pipe geometry for a non-Newtonian fluid with carboxymethyl cellulose (CMC) as an example. This is following on from findings of previous researchers that the optimised swirl

pipe was not as effective on a non-Newtonian fluid as on water. It demonstrates how the existing CFD model can be used to model more complex situations with few modifications.

Finally, Chapter 10 draws together all the conclusions from the research that is presented in the thesis. Possible future work to follow on from the current findings are also presented and discussed.

CHAPTER 2: LITERATURE REVIEW

2.1 Introduction

Slurries may be defined as liquid-solid suspensions which facilitate the transport of solid raw materials by ensuring all voids between particles are filled with liquid (Grossel 1998; Heywood 1999).

The transportation decision is normally between rail, truck, conveyor and slurry pipeline. Slurry pipelines can have strong advantages over these (Aude 1971; Charles 1971; Doron 1995; Doron 1996) such as:

- Friendliness to the environment
- Needing relatively little infrastructure
- Possibility of low operation and maintenance costs
- Continuous operation
- Immunity to adverse weather conditions

The major applications of slurry transport are coal-water slurry pipeline, iron ore transportation, mineral concentrate pipelines, sand removal and tailings disposal (Doron 1995).

The efficient transport of slurry is difficult due to its tendency to settle, cause erosive wear, and consume pumping power. The application of swirl was aimed at ameliorating these problems and therefore it was necessary to predicate the literature review of swirl pipes with a review of the published literature for relevant slurry transport characteristics and issues.

Additionally, modelling of flow in pipes with Computational Fluid Dynamics (CFD) had to be studied before CFD could be applied to the special problem of swirl pipes. CFD provides information that is difficult and time consuming to obtain experimentally. As long as CFD models are rigorously validated, they provide a means of investigating swirl pipes in a practicable time scale. The main findings with regards to modelling turbulent swirling pipe flow are

located in Chapter 4 (CFD Methodology). A review of CFD multiphase modelling forms the latter part of this review.

2.2 Slurry Transport Characteristics- Issues and Problems

The interplay of three fundamental areas of fluid mechanics are encountered in slurry flow; rheology, hydraulics and particle dynamics (Hanks 1986). Thus its characterisation is not simple.

2.2.1 Types of Slurry Flow

Slurry flow can be divided into two main types:

1. Homogeneous flow
2. Heterogeneous flow

In homogeneous slurry, solid particles are homogeneously distributed in the liquid media and the slurries are characterised by high solids concentrations and fine particle sizes (Aude 1971). The solid particles do not settle under gravity in the carrier fluid, or settle relatively slowly, and there is uniform concentration of the solid in the pipeline. Homogeneous slurries are often non-Newtonian. Examples are sewage sludge and clay slurries.

They are also termed non-settling slurries and are sufficiently stable. The particles often serve to increase the mixture's density and viscosity, but otherwise, the slurry behaves as a liquid. This greatly simplifies the handling of this type of system.

In heterogeneous slurries, concentration gradients exist along the vertical axis of a horizontal pipe even at high flow rates (Aude 1971). The fluid and solid phases retain their separate identities. Heterogeneous slurries tend to be of lower solids concentration and have larger particle sizes.

The turbulence present at a reasonable average velocity is insufficient to completely counteract the settling tendency of the particles (Charles 1971).

Heterogeneous slurries are characterised by a much greater concentration of solid particles at the bottom of the pipe than at the top. This non-uniform distribution of solids across the pipe causes higher frictional losses.

The critical velocity in these two cases is different (Aude 1971; Hanks 1986):

- For heterogeneous slurry, a deposition critical velocity is defined which identifies the transition from bed building to full movement.
- For homogeneous slurry, a viscous transition critical velocity is defined which identifies the transition from laminar flow to turbulent flow.

Many types of slurry encountered commercially are of a mixed nature; finer particles join with the liquid media to form a homogeneous vehicle, while the coarse sizes act heterogeneously. An example of this is pipeline coal slurry (Aude 1971).

As the slurry flow velocity is increased a transition through flow patterns is observed as illustrated in Figure 2.1.

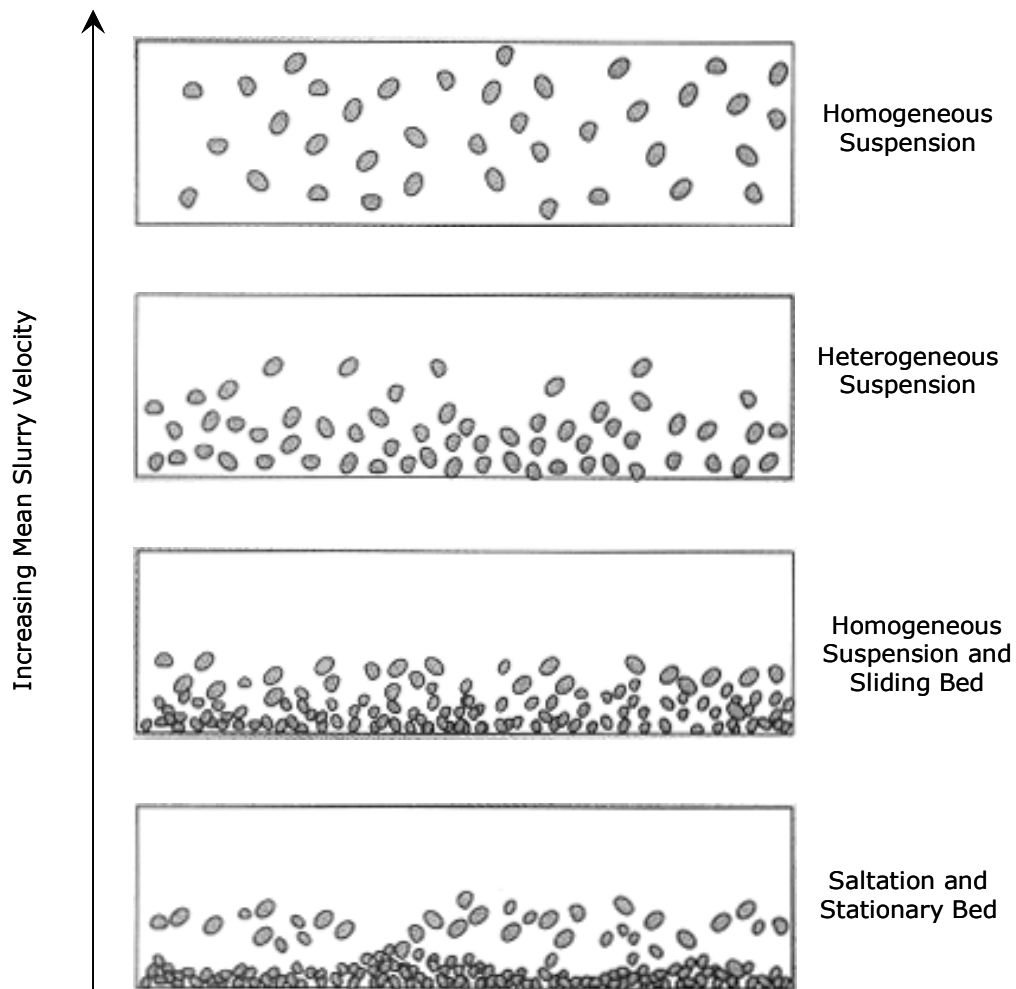


Figure 2.1: Flow Patterns in Settling Slurry (After Heywood (Heywood 1999))

The carrier fluid may be either Newtonian or non-Newtonian. Most common industrial slurries show a decrease in viscosity with increasing shear rate and are therefore non-Newtonian in nature (Heywood 1999).

Non-Newtonian fluids are of widespread importance in industry. Sometimes non-Newtonian fluids are used to carry coarse particles. Bain and Bonnington (Bain 1970) state that non-Newtonian carriers can lead to reduced pressure drop and Heywood et al (Heywood 2004) agree that shear-thinning media are highly suitable for transporting coarse particles. Use of swirl inducing pipes with non-Newtonian liquid as the carrier fluid was investigated by Tonkin and Jones (Geldard 2002; Jones 2004; Tonkin 2004) and is discussed in Chapter 9.

2.2.2 Correlations for Settling Slurry and Definition of Terms

Correlations for pressure loss, limit deposit velocity and critical velocity have been presented by previous researchers studying *Swirly-Flo* pipes (found in boiler tubes) (Raylor 1998; Ganeshalingam 2002). Therefore only the most important correlations are given below.

Researchers have in the past defined many different types of velocities to denote the transition in slurry flow and to facilitate description of some of the various flow patterns encountered. Some of these main velocities are also considered.

2.2.2.1 Pressure Drop

Of the equations to predict pressure drop, those of Durand (by far the most generally used) and Newitt have gained widespread recognition and use (Marumaya 1979; Marumaya 1980).

Durand equation:

$$\phi = 81.0 \left(Fr \sqrt{C_D} \right)^{-1.5} \quad (2.1)$$

Newitt equation:

$$\phi = 63.9 \left(Fr \sqrt{C_D} \right)^{-1.0} \quad (2.2)$$

Where:

$$\phi = \frac{\Delta P - \Delta P_w}{C_0 \Delta P_w}$$

The Froude no. and drag coefficient (from Newton's law of turbulent settling) are defined as:

$$Fr = \frac{V^2}{gD(s-1)} \quad (2.3)$$

$$C_D = \frac{4}{3} \frac{dg(s-1)}{V_s^2} \quad (2.4)$$

g = gravitational acceleration, m/s^2

P = static pressure of slurry flow, Pa

P_w = static pressure of pure water only, Pa

C_o = delivered volume concentration of solid particles, %

C_D = drag coefficient for free-falling sphere

V = mean velocity of slurry flow, m/s

s = relative density (ρ_s/ρ_w)

d = particle diameter, m

D = pipe diameter, m

V_s = settling velocity in still water, m/s

ρ_s = solids density, kg/m^3

ρ_w = water density, kg/m^3

Fr = Froude no.

The above equations are for spherical particles and therefore cannot be directly used for irregularly shaped particles.

Modified forms of the Durand equation have been used by researchers to check experimental validity of pressure loss measurements with theory for sand slurries (Charles 1971; Singh 1976). Reasonably good agreement was obtained for fine sand.

Wang (Wang 1973) investigated the head loss in non-circular pipes with and without solids. Non-circular pipes were treated in the same way as circular and pressure losses were calculated using the hydraulic radius and using Darcy-Weisbach equation for clear water and Durand and Condolios equation for solids (spherical glass beads). However, the pressure loss due to the artificial roughness of the non-circular walls is then disregarded and, with the swirl pipe geometry in particular, this is an important factor.

The fluid only pressure drop can be calculated using the Darcy-Weisbach equation and either the Colebrook equation or the Blasius equation for the friction factor.

Darcy Weisbach equation:

$$\Delta P = \frac{l}{D} \frac{f'}{2} \rho V^2 \quad (2.5)$$

Colebrook equation:

$$\frac{1}{\sqrt{f'}} = -2 \log \left(\frac{e/D}{3.7} + \frac{2.51}{\text{Re} \sqrt{f'}} \right) \quad (2.6)$$

Blasius equation (for smooth pipes):

$$f' = 0.03168 \text{Re}^{-0.25} \quad (2.7)$$

- ΔP = pressure difference, Pa
- ρ = fluid density, kg/m³
- f' = Moody friction factor ($f' = 8\Phi$, $f' = 4f$)
- Φ = friction factor ($= \text{Ra}/\rho u^2$)
- f = Fanning or Darcy friction factor
- e = roughness (m)
- Re = Reynolds number

The above equations (2.5-2.7) have been used to theoretically validate experimental and Computational Fluid Dynamics (CFD) data for liquid only flow in circular pipes in the latter part of this thesis (Chapter 7).

2.2.2.2 Critical Velocity

The critical velocity is the velocity corresponding to minimum pressure drop at a constant concentration of solids (Marumaya 1979; Marumaya 1980). It may be used for a rough estimation of the 'deposit velocity'. Graphical

representation of critical velocity on a plot of pressure drop versus velocity is the best way of identification.

It is the minimum velocity that assures the positive movement of the solid particles or the minimum fluid velocity required to prevent the particles from depositing in a horizontal pipe. Chien (Chien 1994), in his studies of critical velocity in sand slurries, considered it to be the velocity at the starting of a moving bed flow or at the starting of a complete suspension.

Several correlations of critical velocity exist (Chien 1994):

- Durand (1953) for coal, sands and gravel
- Spells (1955) for particle sizes from 50-500 μm
- Newitt et al (1955) for particles <30 μm
- Shook (1969)
- Bain and Bonnington (1970) (Bain 1970)

The critical velocity generally reduces for viscous fluids.

2.2.2.3 Particle Settling Velocity

Particle settling velocity is a balance of the viscous drag against the gravitational force in still fluid (not flowing). It is the settling velocity of a single particle in the fluid medium and is a function of the particle diameter and density as well as the viscosity and density of the fluid medium.

It has only a minimal role in the flow pattern of solids in horizontal flow since the axial flow velocity is expected to be much greater than the settling velocity of a given particle. Newitt et al (1955) (as quoted by Chien (Chien 1994)) stated that the critical velocity should be 17 times the settling velocity.

For irregularly shaped particles (Chien 1994):

$$V_s = 12.0034 \left(\frac{\mu}{d\rho} \right) \left[\sqrt{1 + 0.2386 \left(\frac{\rho_{sand}}{\rho} - 1 \right) \left(\frac{d\rho}{\mu} \right)^2} - 1 \right] \quad (2.8)$$

V_s = settling velocity of a particle, ft/s

μ = viscosity of fluid, lbm/sec

d = particle diameter, ft

ρ = fluid density, lbm/ft³

ρ_{sand} = density of sand, lbm/ft³

2.2.2.4 Deposit Velocity

This is the velocity at which particles start to settle out as the flow rate is lowered (Schriek 1974). It can also be defined as the boundary between asymmetric, but fully suspended flow and saltating, but non-stationary or 'sliding-bed' flow (Hanks 1986). Furthermore, Heywood (Heywood 1999) described it as the lowest mean slurry velocity in a horizontal pipe at which no particles settle out onto the pipe bottom for more than 1 to 2 seconds. Also Doron (Doron 1995) described it as the mixture velocity at the transition from flow with a stationary bed to flow with a moving bed. It is thus a difficult term to exactly define. However its importance is noted because it signifies the safe flow velocity for a pipeline to operate at without blockage.

Durand calculated the deposition critical velocity using the following formula:

$$V_{DC} = F' [2gD(s-1)]^{1/2} \quad (2.9)$$

where F' is an empirical function of particle diameter and concentration (Hanks 1986).

This original correlation has been modified later by various researchers. A much more complex but very accurate model of the deposition velocity is that of Hanks and Sloan (Hanks 1986). It requires a sophisticated computer programme for solution.

Doron (Doron 1995) created a three-layer model to predict limit deposit velocity and pressure drop for solid-liquid flow in pipes. He best denotes the difference between the deposition velocity and the critical velocity graphically. On a plot of pressure drop versus flow rate, he defines the limit

deposit velocity as the point where the slope undergoes an abrupt change, and the critical velocity as the point of minimal pressure gradient.

Schriek (Schriek 1974) observed the deposit velocity experimentally at various P:D (pitch to diameter) ratios in helically ribbed swirl inducing pipe. The method used involved initially getting all the solids in complete suspension, then lowering the mean velocity until the first sediment is observed sliding along the bottom of the conduit. Schriek concluded that deposit velocity decreased with decreasing P:D ratio (smooth pipe should be considered as having a P:D ratio of infinity rather than zero). However, all estimates of deposit velocity were approximate because interpolation was involved and visual determination of velocities was dependent on the interpretation of the observer.

2.2.2.5 Economical Velocity

The economical velocity for any slurry transportation (Howard 1938) can be defined as the one at which any given volume of solids per hour can be transported through a given length of pipe with the least expenditure of power per volume of solids transported. The economical velocity is determined by:

- pipeline characteristics
- energy required to produce the desired flow
- characteristics of solid particles to be transported
- solids concentration that will cause a minimum head loss at the desired velocity

Of these factors the characteristics of the solid particles, in particular the particle size and density, are most pertinent. Therefore each class of material will probably have an inherent economical velocity for the same size of pipe.

2.2.2.6 Slip Velocity

Slip velocity is defined specifically in saltation (Hanks 1986; Heywood 1999) where the solids are being held up with respect to the liquid phase and the

average solids velocity is less than that of the liquid. It occurs because the average velocity of the diluted slurry above the bed is much larger than that of the deposited solids in the bed. The difference between the two is called the 'slip' velocity.

$$u_s = v_{IS} - v_{IL} \quad (2.10)$$

$$H = \frac{v_{IL}}{v_{IS}} \quad (2.11)$$

v_{IS} = in-situ solids phase velocity, m/s

v_{IL} = in-situ liquid velocity, m/s

H = holdup ratio

u_s = slip velocity, m/s

2.2.3 Minimising Frictional Pressure Loss in Settling Slurry

Some methods of minimising the frictional pressure loss for settling slurries are (Sauermann 1978; Heywood 1999):

- adding soap or a high molecular weight polymer
- oscillating the slurry flow rate or pressure gradient to give pulsating flow
- vibrating or oscillating the pipeline about its axis while maintaining a constant slurry flow rate
- inserts such as spiral ribs and vanes or segmented pipe to reduce the limit deposit velocity and hence power consumption
- use of non-circular pipes

Adding polymers could alter a slurry formulation irreversibly or could incur significant costs to return the slurry to its original state. However, if the slurry is a waste material this technique may be considered.

All non-circular cross-sections suffer from the disadvantage of points of stress intensification, thereby making thicker walled pipes necessary. Wang and Seman (Wang 1973) studied the head losses within pipes of different cross-sections and showed that a pipe with a wider base, i.e. a rectangular

pipe, resulted in lower head loss than circular for a given minimum carrying velocity. This was due to the fact that the wider base ensured a thinner layer of settled solids on the pipe bottom which could be lifted into suspension much easier. Sauermann (Sauermann 1978) then examined the use of a segment plate within circular pipes to take advantage of this effect. The pressure could also then be equalised above and below the segment plate by means of a few small holes for example thereby retaining the advantage of uniform stress distribution in a circular pipe. The segment plate could also act as a wear plate. However difficulties may be experienced at pipe connections where smooth connections of the segment plates are required to avoid excessive wear. Additionally, the flow area is reduced in comparison with a normal circular pipe.

The manufacturing cost for pipes with inserts or non-circular cross-sections is greater than regular circular pipes. Additionally the use of inserts within pipes will result in high wear rates of the inserts themselves and will present obstructions to the flow.

The use of swirl inducing pipes falls into the latter two categories of using inserts and non-circular cross-sections. Past researchers have found that the pressure loss across the lobed swirl pipe itself is greater than circular pipe due to the additional turbulence generated through artificial roughness of the non-circular pipe surfaces. However, the particle dispersion achieved through the turbulence may mean that lower velocities are required to keep the particles in suspension and thus the deposition velocity is lowered. In turbulent flow, pressure loss increases approximately with flow rate to a power of between 1.5 and 2. Thus halving the flow rate will often lead to pressure losses being reduced almost four-fold (Heywood 1999). Careful design of the pipe could also offer a gradual induction of swirl thereby eliminating sudden increases in turbulence which may otherwise result in high pressure losses.

Previous research has shown that when swirl inducing pipes are used prior to a bend, the pressure loss across the bend is reduced (Raylor 1998; Ganeshalingam 2002). This is further discussed in Section 2.3.3.

2.2.4 Wear in Pipeline

Slurries can cause wear in pipelines in one of many ways due to their abrasive nature. They can:

- 'sandblast' on impinging at high velocities
- act as a 'grinding compound' between moving mechanical parts
- act as a 'cutting tool' when throttled through a restriction
- have the effect of 'sandpaper' when dragged along the bottom of a pipe (Aude 1971).

The low internal surface roughness of circular pipes encourages the settling of low velocity slurries, thus causing erosive wear from particles being dragged along the bottom of the pipe. Non-circular pipes which encourage swirl can move particles into suspension at lower velocities thereby preventing this form of wear. The greater particle dispersion which results will also cause impact dispersion, thus preventing localised attack and elongating pipe life, particularly in the case of bends (Wood 2001). Bends can act like concave mirrors reflecting the flow to wear hot spots. In pneumatic systems erosion rate of bends is 50 times higher than that of straight pipe (Fan 2001).

Erosion is proportional to (particle velocity)ⁿ with n usually in the range $2 < n < 2.5$ for ductile materials, and much higher for brittle materials. Brittle materials are highly resistant to oblique impact and suffer most material loss at high angles of incidence. Ductile materials have maximum erosion rates at a relatively low angle of incidence (20-30°). Erosion in any equipment can thus be reduced by changing the pattern of particle movement, altering impingement angle and reducing impact velocity.

There are two main erosion mechanisms (Wood 2001):

1. Cutting
2. Deformation

Cutting wear is likely for low impact angles (0-40°) of relatively hard materials on ductile targets where the shear stress induced by the impact

exceeds the shear strength of the target. Deformation wear is applicable at high impact angles (30-90°). A stress field is generated within the contact inducing plastically deformed sub-layers where the stress exceeds the yield strength of the target material.

Wood (Wood 2001) developed simple erosive wear models to investigate the effect of *Swirly-Flo* pipe. Computer models using Fluent CFD software with an embedded multiphase model were used to define the impact sites on the internal surfaces of 90° bends. The velocity and angle of impact were used as input to a simple erosion model based on carbon-steel properties with sand as the erodent. From the angles of impact within the bends it was concluded that swirling flow is likely to decrease deformation type wear leaving cutting wear only. Additionally, the greater particle impact dispersion observed in swirling flow within bends would reduce localised attack and give greater bend life.

This is because upstream swirl induction increases impact angles but distributes impacts and velocities of impacts more uniformly. Generally, although the angles have increased, the impact velocities are relatively low. Erosion is less sensitive to a doubling of impact angle than a doubling of velocity. Thus, as the swirl flow generally reduces the velocity but increases the impact angle, the net effect on erosion should be beneficial.

Other than *Swirly-Flo* pipes, researchers have investigated the effects of other forms of swirl-induction such as ribbed pipes in reducing erosion. Various researchers (Song 1996; Yao 2000; Fan 2001; Yao 2002) carried out experimental and numerical investigations with gas-particle flows in ribbed bends and pipes.

For ribbed bends, impact velocities of a particle with the bend tend towards lower values (Yao 2002). The impingement angle of particle-bend tends to locate in the low angle range (<10°) by adding ribs. This plays an important role in decreasing erosion rate. Average erosion rates of ribbed bends are around 33% of that of smooth bends (Fan 2001). Ribs will prevent particles sliding and rolling along the wall surface.

Robust erosive wear models are necessary to fully explore the advantages of swirling flow and subsequent particle dispersion. A suitable criterion in

quantifying and measuring wear must also be sought to complement the models.

Researchers have used many different units and criteria for wear (Truscott 1975). Absolute units of wear rate are usually expressed as:

- weight or volume loss of material/unit time as expressed by Bitter (Bitter 1963)
- wear depth or thickness reduction/unit time as expressed by James and Broad (James 1983) and by Elkholy (Elkholy 1983; Gupta 1995)

It must be borne in mind that mass loss as a global value may not be sufficient to determine the erosion reduction capability of swirling pipe flow. Dispersion of particles obtained through swirl would prevent erosion being concentrated at a specific point. Therefore weighing pipes alone would be inadequate. Using an ultrasonic thickness gauge may be a better way of evaluating specific wear on the pipe walls. However, these are very user-dependent and the loss in thickness must be sufficient for the sensitivity of the gauge.

2.2.5 Measurements in Slurry Pipeline Technology

The main slurry variables of concern that are usually measured are:

- slurry density
- slurry viscosity
- settling rate of particles
- particle size distribution
- solids concentration
- slurry velocity

The slurry density can be estimated using the formulae below (Nesbitt 2000):

$$\rho_M = \rho_L + \frac{C_v(\rho_S - \rho_L)}{100} \quad (2.12)$$

$$\rho_M = \frac{1}{\left(\frac{C_M}{100\rho_S} + \frac{1}{\rho_L} - \frac{C_M}{100\rho_L} \right)} \quad (2.13)$$

ρ_M = mixture density

ρ_L = liquid density

C_v = concentration by volume, %

C_M = concentration by mass, %

If settling is significant, the concept of slurry viscosity becomes largely meaningless, and slurries have to be treated as a two-phase mixture (Heywood 1999). However, if this is not the case, the level of dispersion of a flocculated slurry, and therefore indirectly its viscosity, can now be assessed online through measurement of the particles' zeta potential (or electric charge) using an electro acoustic sensor (Heywood 2003).

Reological behaviour is largely defined by the extent to which particles in suspension interact with each other. One key factor dictating the level of interaction is the charge present at the particle surface. Zeta potential is a measure of this charge. An electroacoustic sensor can be used to apply high frequency alternating voltage pulses across a slurry causing slurry particles to move back and forth. This motion generates high frequency sound waves which depend on particle size and electric charge. An ultrasonic transducer detects the sound waves which can then be used to calculate the particle size and charge.

Where a clear interface forms during gravity settling, the settling rate can be found by monitoring the rate of fall of this interface visually when an initially well-mixed sample of slurry is placed in a graduated cylinder. Otherwise optical or radiation absorption methods can be used (Heywood 1999).

Particle size/size distribution can be found using laser diffraction equipment, the coulter counter, sedimentation balance or a series of sieves (Heywood 1999).

Online solids concentration, particle size distribution and velocities are studied to identify the conditions that induce particle settlement, particle re-suspension and particle size segregation. In particular some form of flow

visualisation and measurement is required to demonstrate the advantages of swirling flow and to examine its dynamics. The various techniques used are broadly divided into two main categories; invasive and non-invasive.

2.2.5.1 Invasive Flow Measurement Techniques

Invasive techniques use probes present within the flow for data capture. Local disturbances and changes in the solids concentration in the probe area may result in poor measurements. Some examples of researchers who used invasive techniques are:

- In 1939 Howard (Howard 1939) measured concentrations of sand and gravel in water over a cross-sectional area by inserting a bent tube into the end of the pipe. The tube was held in place by a plate that could be raised or lowered between two hinges in order to give vertical control.
- Li and Tomita (Li 1994) used a 3-holed spherical head probe to measure the radial velocity and pressure profiles at 15 different pipe sections in swirling pneumatic flow. At each section, measurements were carried out at 20 radial locations and the swirl intensity was calculated.
- Ito and Ogana (Ito 1980) used an electrolytic solution to measure swirling flow electrochemically. The kinematic viscosity of the solution used was nearly equal to that of water. To measure the 3D velocity components, a spherical multi-electrode probe was used.
- Senoo and Nagata (Senoo 1972) measured the direction and total pressure of swirling flow of air with a cobra probe and the static pressure with a sphere static probe.
- Kitoh (Kitoh 1991) measured the flow angle and the mean velocity using a hot wire in swirling water flow. Using the flow angle and the resultant velocity, the axial and tangential velocity components could be obtained.

2.2.5.2 Non-invasive Flow Visualisation and Measurement Techniques

Non-invasive techniques have no physical parts within the flow and therefore do not cause any flow disturbances. LDV (Laser Doppler Velocimetry), PDA (Phase Doppler Anemometry), PIV (Particle Image Velocimetry) and all tomography techniques are non-invasive.

LDV is a single point measurement whereby the Doppler shift in wavelength of laser light scattered by small particles moving with the fluid is used to calculate velocity. The technique offers good accuracy and allows measurement of all three velocity components. PDA is an extension of LDV where two receiving lenses and photodetectors are used to enable particle size to be measured in addition to particle velocity. PIV is a whole-flow-field technique providing instantaneous velocity vector measurements in a cross-section of a flow (see Chapter 7). LDV and PIV are both limited in their use to very low solids concentration distributions or very small particle sizes.

Tomography produces cross-sectional images of high temporal and spatial resolution of the distribution of flow components in a pipeline. However it does not allow direct measurement of velocity components of the flow. Currently available tomographic techniques are X-ray, gamma ray, PET (Positron Emission Tomography), MRI (Magnetic Resonance Imaging), ultrasonic, Electrical (Resistance, Capacitance and Impedance), optical and infra-red tomography (Fokeer 2004). The choice of technique is dictated by many factors including the physical properties of the flow, desired spatial and temporal resolution of imaging, cost of the equipment, its physical dimensions, human resources needed to operate it and potential hazards to the personnel involved (e.g. radiation).

In Electrical Resistance Tomography (ERT), the continuous phase is a conductive fluid, e.g. water, and the second phase may be either non-conductive or highly conductive particles, e.g. silica sands or metallic mineral particles. Boundary voltage measurements are obtained from a number of electrodes that are fixed around the inner pipe wall by applying current to one or more pairs of the electrodes and measuring voltages from these electrodes using tomographic sensing strategies. The conductivity distribution is then reconstructed using specific algorithms to reflect the

second phase distribution in the flow. It is a popular technique because it is relatively fast, simple to operate, has a rugged construction and is sufficiently robust to cope with most industrial environments.

Many researchers have previously used LDV, PIV and tomography techniques specifically for measurements of solids concentration/distribution and velocity components in swirling flows:

- Steenbergen and Voskamp (Steenbergen 1998) measured velocities using LDV. The complete LDV system could be rotated about the axis of the pipe. By combining results of two measurements taken in the same point, under different orientations of the system's optical axis, the three velocity components can be measured.
- Jones and Tonkin (Jones 2004b): carried out PIV (Particle Image Velocimetry) measurements to determine tangential velocities of swirling pipe flow of water and carboxymethyl cellulose (CMC) solutions. Some of their results have been used for the purpose of validating the CFD model used in this work. The PIV technique and its use in validation are discussed in detail in Chapter 7.
- Wang (Wang 2003) used Electrical Resistance Tomography (ERT) to understand the effect of particle suspension and effect on the wear of pipes by solid particle impingement due to application of a swirl-inducing pipe.
- Ganeshalingam (Ganeshalingam 2002) used ERT to gain understanding of the solids distribution downstream of swirl-inducing pipe and to characterise the settling process of solid particles due to swirl decay.

Additionally, Jones and Tonkin (Jones 2004b) also estimated tangential velocity using photographs. By using an appropriate shutter speed, the track of particles could be captured and the photographs subsequently analysed to mathematically describe the path of particles. Tangential velocities were calculated assuming that the particle paths captured were at the extreme edge of the pipe. However, this technique used the outermost particles which would have been affected the most by the helical wall pattern.

Therefore the tangential velocity measured was expected to be higher than the average. This technique enabled valuable comparisons of the effect of the swirling flow pipe on different slurries.

2.3 Swirling Flow

Swirl flow can be defined as a fluid flow with a tangential velocity component (Jones 2004).

2.3.1 Advantages of Swirling Flow

Swirling flow has been applied in pneumatic conveying technology to reduce pressure drop and power requirements and to prevent particle deposition and pipeline blockage (Li 1994; Li 2000).

Potential advantages in hydraulic transport are as follows:

- Settling particles in the carrier liquid can be kept in suspension at lower velocities (Wood 2001).
- Pumping power (approximately proportional to V^3) and cumulated erosion at a critical location (approximately proportional to $V^{3.5}$) can, in theory, be reduced by a program of strategically placed swirl induction with lowered pipe velocity (Heywood 2003)
- Pressure losses in bends and fittings can be reduced by the application of swirl upstream
- Particle distributions at strategic locations can often be improved by upstream swirl induction
- Wear could be reduced by better particle distribution (Jones 2002)

The cost is in maintaining the pressures required to induce swirl.

2.3.2 Different Swirl Inducing Methods and Non-Circular Pipe Geometries

Many forms of pipe have been investigated over the years for their potential to induce swirl. A chronological discussion of these is given below. It must be borne in mind that all non-circular cross-sections suffer from the disadvantage that points of stress intensification occur in the pipe wall and thicker walls become necessary. Moreover, ribs and fins will be subject to direct impacts from particles resulting in damage and wear.

1899 (Gordon 1899): Gordon patented a ribbed pipe for conducting liquids in such a manner as to leave the pipe free from any deposit of sediment.

The object of his invention was to direct the flowing liquid nearest the bottom and the sides of the pipe from a straight course into a transverse course, constantly sweeping the subsiding and deposited sediment up into the higher flowing body of liquid to be carried forward through the pipe. This was done by locating ribs within the pipe, inclined towards the inlet end. A series of such ribs were alternately disposed at any angle to each other to produce alternately opposing currents of the liquid.

1921 (Robinson 1921): Robinson patented a rifling rib. The particles were continuously brought from their lower sections to the upper sections, and in their attempt to fall under gravity, were inevitably maintained in a condition of practically homogeneous mixture. The ribs were arranged spiralling running longitudinally of the pipe and radially from its interior surface inwardly. The ribs caused the current of water to follow a violent spiral or whirling course through the pipe.

1927 (Yuille 1927): Yuille suggested alternate finned sections in pipeline. On alternate sections of pipe, a pipe of larger outside diameter than the regular sections with a spiral fin within, was used. Yuille believed that this may be more economical than a continuous series of spiral fins.

1938/1939 (Howard 1938; Howard 1939): Rifles or vanes were installed on the inside of pipeline to improve the capacity of pipelines used for transporting sand and gravel. The effect was a reduction in concentration of

solids at the bottom of the pipe and in plugging that may occur at low pipeline velocities. The distribution of solids was more uniform in the rifled pipe than in plain pipe.

Howard continued tests on rifled pipe with silt, clay and pea gravel. He found a superior efficiency for rifled pipe upto the velocity at which material begins to move freely in the pipe. He concluded that rifling increases the efficiency where settling occurs in appreciable quantities.

1940 (Spanner 1940): Spanner suggested a tube with spiral grooves as an improvement in tubular heat exchangers. The spiral grooves could be formed by pressing the wall of the tube inwards towards the axis of the tube. These inwardly pressed grooves force the gas to take a partially spiral path in passing from one end of the tube to the other and also to come into more intimate contact with the wall of the tube.

The pipes were produced by a patented process in which treated circular pipes are drawn through a rotating die to give them an internal 3-start spiral profile. A pipe of this design was used by Raylor and Ganeshalingam (Raylor 1999; Ganeshalingam 2002) in their experimental work (see Section 2.3.3). This was thus the basic design for the original *Swirly-Flo* pipe.

Spanner suggested that additional beneficial effect may be obtained when grooves are deepened in a stepped or tapered manner or modified in angle and direction of pitch towards the exit of the end of the tube (as investigated by Raylor and in Chapter 5 of this thesis for swirl transitions).

1967 (Wolfe 1967a; Wolfe 1967b): Wolfe investigated helically ribbed pipes and concluded that a much lower velocity was required to transport particles thereby resulting in power savings and reduced pipe wear.

The helical motion imparted to the flowing mixture effectively returned settled solid particles to the main stream. The flow could be stopped and started without difficulty because on starting, the rotation of the fluid impinged on any settled particles and they were quickly lifted up again into the main stream.

Wolfe also observed that for transport of fluid only, the ribs were a distinct disadvantage because they provided a built-in resistance to flow. Where thorough mixing is desired, or any solids were involved however, they provided many desirable qualities. He concluded that a P:D (pitch to diameter, see Section 2.3.4) ratio of PI ($\pi = 3.14$) was optimum.

He suggested forming the rib by inserting the helix within the pipe to obtain the desired position and using the resiliency of the helix to expand into engaging with the inner pipe wall. The rib could be rigidly secured to the inner pipe wall by spot welding or forming the rib integral with the pipe. Otherwise the pipe could also be fabricated by extruding a metal such as aluminium or a plastic material in the required rib shape, pitch and spacing.

1971 (Charles 1971): Charles carried out tests in ribbed pipe with sand/water slurries (5-18%). Ribs were found to be a disadvantage at relatively high velocities but an advantage at velocities less than the critical deposit velocity for flows in the smooth pipe.

He concluded that it was impossible to determine the optimum P:D ratio as a function of the several variables involved, but it was likely that a P:D ratio of approximately 5 would prove to be optimum. However only pipes of P:D ratios from 1 to 5 were investigated.

1973 (Wang 1973): Wang tested several different non-circular cross-sectional geometries of pipe (square, triangle, rectangle) for hydraulic transport of solids. Only the rectangular geometry (with wide base) had a lower solids head loss than circular. The base area of the pipe was found to be the most important geometric characteristic for slurry transport. When the gravitational forces are larger than the forces produced because of turbulence, particles settle on the bottom of the conduit and form a sliding bed. If the base area is wide, this layer of solids is very thin and therefore can be moved with less energy. This explained the superiority of the rectangular geometry with wide base.

1974 (Schriek 1974): Schriek investigated helically ribbed pipe with P:D ratio 1.8 to 11 in 6 and 2 inch diameter pipes with sand. The P:D ratio requiring the minimum specific energy consumption for the particular type of sand tested was found to be approximately 8.

He noted that although deposit velocity decreased with decreasing P:D ratio, reductions below 3.3 did not reduce the deposit velocity further. Although a greater amount of pressure energy is converted to kinetic energy by the helical ribs in the low P:D ratio pipes, this energy will not support additional solids and is largely dissipated into heat. Presumably a portion of the energy is dissipated by direct sliding contact between the wall and the solids, which experience large centrifugal forces in pipes with low P:D ratios.

The suspension process also appeared to function inefficiently at low solids concentrations (in terms of energy requirement). This behaviour also occurred in smooth pipes.

The best P:D ratio was a rather weak function of solids concentration. Concentrations of 18% or greater would be carried most economically with P:D ratio 8. Schriek noted that there was a range of P:D ratios from 5-11 over which energy requirements did not change significantly.

1976 (Singh 1976): Singh concluded that the smallest value of pressure gradient occurred at P:D ratio greater than 5 and probably at 8 from tests with ribbed pipes.

1978 (Sauermann 1978): Sauermann investigated a pipe with a horizontal plate welded to the inner perimeter in the lower part of the pipe. This formed a wide flat base for the solids to flow over and functioned as a wear plate.

Power requirement of same solids throughput was reduced by 16% in segmented pipe of the same cross-sectional area and minimum transport velocity was also reduced. This may be explained by the conclusions of Wang (Wang 1973) with regards to a wider base of pipe (see above).

1998 (Steenbergen 1998): A swirl generator was created for water that can generate different types of swirl. It consisted of a contraction with a streamlined inner body that contains a central channel. The part of the fluid which is guided around this body was set into rotation by flowing through an array of 18 vanes, whose angle can be adjusted. The rate of swirl decay of

different types of swirl was investigated and compared to other researchers' findings (see Chapter 7).

2000 (Li 2000): Li used a vaned type swirler to measure particle velocities and concentration profiles using photographing image techniques in pneumatic conveying. The particle concentrations in the swirling flow pneumatic conveying exhibited symmetric distributions with respect to the pipe axis and the higher particle concentrations appeared near the wall in the acceleration region. The particle concentrations of the swirling flow pneumatic conveying at the bottom of the pipe were lower than that of axial flow pneumatic conveying.

In addition Statiflo (Statiflo International Ltd. Cheshire, UK) produce motionless mixers using various elements inside channels and pipes to provide online mixing.

2.3.3 Previous Research on *Swirly-Flo* Pipes

In 1993 Jones proposed a new approach to the problem of settling particles in which a pipe section could be given a helical profile to promote suspension of particles at relatively low velocities (Jones 1997).

At the University of Nottingham research was begun by Raylor (Raylor 1998) into *Swirly-Flo* pipes, and then continued by Ganeshalingam (Ganeshalingam 2002) and Tonkin (Tonkin 2004). Raylor and Ganeshalingam carried out all their experimental investigations based upon a swirl pipe found in marine boilers which is used to improve heat exchanger efficiency. The pipe is illustrated in Figure 2.2 and has the trade name '*Swirly-Flo* pipe'.

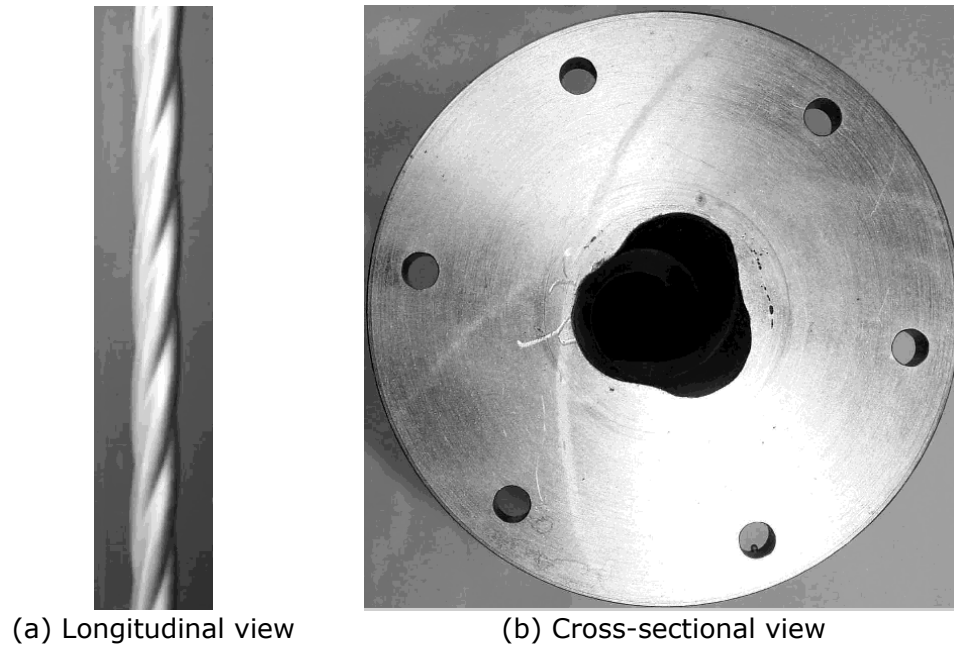


Figure 2.2: Boiler Tube *Swirly-Flo* Pipe used by Raylor and Ganeshalingam (After Ganeshalingam)

Raylor's (Raylor 1998) main aim was to reduce wear and produce better particle distribution throughout a bend. The methodology undertaken was both experimental and numerical using CFD.

Swirling flow before a bend produced less pressure drop across the bend than non-swirling flow for water and water/particle (plastic beads) mixtures. *Swirly-Flo* pipe produced a greater pressure drop across its length than standard pipe. This was always larger than the gain in pressure across the bend. However, this may be partly explained by the greater surface roughness of the electroplated steel *Swirly-Flo* pipe compared to the Transpalite standard pipes used. High pressure losses also resulted at the entry and exit of the pipe due to sudden change in cross-section and sudden constriction and enlargement. Raylor recommended the design of entry and exit ducts to minimise these effects.

Swirling particles before the bend ensured more even distribution of particles throughout the bend which has the potential to remove characteristic wear zones.

Raylor used Fluent commercial CFD software which allowed him to examine various shapes for pipes and flow fields in a swirl inducing pipe. He indicated

that as the P:D ratio in a geodesic pipe decreased, the swirl produced increased with increasing pressure loss.

Raylor suggested that the regular (geodesic) helix of the *Swirly-Flo* pipe may be subjecting the flow to deceleration. This may be improved by a 'brachistochrone' helix. This can be explained by the two criteria for the curve inside the cylinder. When examined by simplifying the case to that of a single particle:

- Geodesic: the locus with the shortest distance between two points constituting a full cycle
- Brachistochrone: the locus taking the shortest time between two points constituting a full cycle. A fixed time locus is mathematically identical to a constant angular acceleration locus. The brachistochrone gives the largest angular acceleration.

When extrapolated for a greater pipe length (greater than 1m), the brachistochrone gave Raylor more tangential velocity for less pressure drop than standard *Swirly-Flo* pipe. However, for shorter lengths of pipe, the geodesic was better than the brachistochrone in terms of tangential velocity produced for a given pressure cost.

Raylor described his experimental rig assembly in detail. The same rig was used for the experimentation described in this thesis with very few modifications. The few improvements suggested by Raylor were carried out by Ganeshalingam. These were the addition of more pressure transducers and a new data logger.

Raylor used plastic beads (also used by Ganeshalingam and Tonkin) which he measured to be of specific gravity 1.46. The original plan was to use the same beads for the experimental research of this thesis. However, on carrying out density tests on an identical set of the beads that were not previously used, it was discovered that the density had altered. This may be due to effects of long term storage. It was also found that the beads used by Raylor were damaged by the pump and the density varied in this case too (see Chapter 6). Therefore it was necessary to identify a different source of solids for use in the experimental tests.

Raylor also concluded that the inlet and exit orientation of the *Swirly-Flo* pipe was important and showed that alignment with a lobe at entry at the bottom of the pipe was most favourable. This was the orientation used in all CFD simulations and experimentation in this research.

No experimental measurements of the cross-sectional velocity were taken. Therefore no direct validation of CFD through internal flow measurement was achieved by Raylor.

Ganeshalingam (Ganeshalingam 2002) continued Raylor's work of CFD modelling of swirl inducing pipe flow. He validated the CFD code used with results from PIV, ERT and pressure measurements. He also carried out further optimisation of the swirl-inducing pipe using CFD and continued experimental work on solid-liquid mixture flows.

Validation of CFD pressure loss across the circular and swirl pipes gave agreement to within 15%. PIV results of axial velocity were in good agreement with CFD predictions. Tangential velocity measurement using PIV was unsuccessful (see Chapter 7).

Ganeshalingam's radial distribution of the tangential velocities downstream of the *Swirly-Flo* pipe (determined by CFD) fitted with the 'Wall Jet' classification of Steenbergen and Voskamp (Steenbergen 1998). An exponential decay of the swirl downstream of a swirl pipe was implied from CFD and the decay was reported to be faster at higher Reynolds number. A further discussion and a comparison of the current results of swirl type and decay to those of Ganeshalingam are given in Chapter 7.

Ganeshalingam also tested various cross-sections of pipe (triangular, square, pentagon, hexagon, 2, 3, 4 and 5 lobed) and concluded that the 4-lobed cross-section was most effective at swirl generation. He recommended a P:D ratio of 8 and 400mm of length as optimal for the 4-lobed pipe.

Ganeshalingam also extended Raylor's tests with swirl pipe prior to bends. He used bends of various radii of curvature. Pressure loss across bends (horizontal to vertical) showed significant reductions when swirl induction was used at low flow velocities (0.75-1.5 m/s). Also the amount of pressure loss reduction became less for a large bend as compared to a small bend,

and it became less dependent on flow velocity and solids concentration for the large radius bends.

All solids used were of the same density and size. Thus the testing of a range of densities of solids and particle sizes was not attempted.

As mentioned earlier, and as with Raylor, all experimental work by Ganeshalingam was carried out using a 3-lobed *Swirly-Flo* pipe. The flow area of this pipe was less than the circular standard pipe in the experimental rig. The 4-lobed optimum design was never tested experimentally and the aim with the present research was thus to custom-make swirl and transition pipes for use on the rig.

Tonkin's (Tonkin 2004) main aim was the experimental investigation of application of swirling flow pipe to non-Newtonian (shear thinning) carrier liquids. She used custom-made (as described in Chapter 3), optimised swirling flow pipes. A time independent fluid, CMC (carboxymethyl cellulose) was chosen to avoid changes in rheology as pumping time increased.

Tests were carried out with sand and magnetite. PIV was used to measure tangential velocity downstream of an optimised 4-lobed swirling flow pipe (optimised for water) with water and CMC. Some of her results have been used for the CFD validation given in Chapter 7. No swirl pattern was detected with CMC. She concluded that further testing to optimise the swirl pipe for viscous non-Newtonian fluids should be performed (see Chapter 9).

2.3.4 Definition of Terms and Equations for Swirling Flow

The hydraulic diameter of a pipe is defined as (Nesbitt 2000):

$$d_h = \frac{4A}{P} \quad (2.14)$$

d_h = hydraulic diameter, m

P = wetted perimeter, m

A = area, m²

All swirl and transition pipes used in the experimental work of this thesis had an equivalent cross-sectional area to the circular pipe delivering fluid to the swirl/transition pipes. Thus the swirl/transition pipes had an 'equivalent' diameter of 50mm. However, the hydraulic diameter of a 4-lobed swirl pipe with equivalent diameter to that of a circular pipe of 50mm is 45.2mm.

Singh (Singh 1976) defined the pitch as the axial distance travelled by the rib as it rotates (for helically ribbed pipe) through 360 degrees. This was the basis used for definition of the pitch of the swirling flow pipe. Thus a pitch to diameter (P:D) ratio of 8 indicates that the lobed cross-section rotates by 360 degrees in a length equivalent to 8 diameters.

Swirl number., S , also termed the Swirl Intensity is defined by (Senoo 1972; Li 1994; Steenbergen 1998):

$$S = \frac{\int_0^R uwr^2 .dr}{R \int_0^R u^2 r.dr} \quad (2.15)$$

w = tangential velocity, m/s

r = radius at point where tangential velocity is calculated, m

R = pipe radius, m

u = axial velocity, m/s

S = swirl intensity

It is the ratio of the angular momentum flux to the product of the pipe radius and the axial momentum flux.

The effectiveness of swirl induction was deemed to be the swirl intensity that could be induced for a given pressure drop. Ganeshalingam (Ganeshalingam 2002) defined a Swirl Effectiveness parameter, based on the ratio of the swirl intensity produced to the pressure loss, and used it in all optimisation calculations. This is the parameter used in this research for the optimisation of transition and swirl pipes.

$$Swirl\ Effectiveness = \frac{Swirl\ Intensity}{\frac{\Delta P}{\frac{\rho \times u^2}{2}}} \quad (2.16)$$

In the research of swirling flow pipes, the prevailment of swirl is an important aim and thus a parameter for measuring swirl decay would be useful. There is no unanimous agreement on the decay rates in swirling pipe flows (Halsey 1987).

To determine the length over which swirl will prevail several researchers (Senoo 1972; Halsey 1987; Li 1994; Reader-Harris 1994; Steenbergen 1998) suggest an exponential decay function:

$$S = S_0 e^{\beta \frac{x}{D}} \quad (2.17)$$

where:

S = swirl intensity (in some cases replaced by the angular momentum flux)

S_0 = initial swirl intensity

β = swirl decay rate parameter = $\alpha * f'$

x = distance along pipe, m

D = pipe diameter, m

f' = Moody friction factor

α = empirical coefficient

The swirl decay observed from CFD analysis of swirling pipe flow is discussed in Chapter 7.

2.4 Modelling Flow

There are several advantages in modelling the flow through pipelines:

- Experimentation can be costly
- It is a means of non-intrusive testing

- Data can be obtained for a variety of variables; velocity, pressure, etc.
- An insight is gained into the flow field which is difficult to measure experimentally
- Can be used as a 'what if' tool
- Scale-up issues are eliminated

It is now possible to make numerical predictions using CFD for many single phase flows that are more precise than the most accurate experimental local measurements (Grace 2004). For a complete analysis and explanation of the CFD technique refer to Chapter 4 (CFD Methodology).

While CFD also holds great promise for multiphase flows, obtaining accurate solutions is much more challenging, not just because each of the phases must be treated separately, but, in addition, a number of new and difficult factors come into play as discussed in Section 2.4.1.

Due to the problems with multiphase modelling in the Fluent CFD software Ganeshalingam (Ganeshalingam 2002) simulated the presence of solids in *Swirly-Flo* pipes by approximate changes to density and viscosity, so that a single liquid could be used as a simulant for dense particulate slurry. He calculated the average density of the solid-liquid mixture using Equation 2.12.

The viscosity was calculated by Einstein's proposed equation for laminar suspensions (Hanks 1986).

$$\frac{\mu_{mixture}}{\mu_{pureliquid}} = 1 + kC_v \quad (2.18)$$

$k = 2.5$ and varies with particle properties

C_v = concentration by volume, %

$\mu_{mixture}$ = viscosity of the disperse system, kg/ms

$\mu_{pureliquid}$ = viscosity of the continuous phase, kg/ms

Einstein considered the laminar flow of a dilute suspension of small spheres in a Newtonian fluid with 'no-slip' between the spheres and the fluid. He showed by considering detailed particle dynamics and hydraulics of this

system that the gross response of the suspension could be analysed as if the mixture were in reality a fictitious homogeneous Newtonian fluid whose 'viscosity' was related to that of the suspending liquid by a given equation. However, as soon as the particles become large hydraulically and dynamically so that the 'slip' effects begin to be manifest, this model fails.

Ganeshalingam found that the effect of dense particulate slurry on average tangential velocity was insignificant using this method though the pressure loss increased with increasing solids concentration. He concluded that a multiphase approach on CFD is required to model particulate slurry, particularly if one is to obtain details such as particle distributions, impact angles and velocities.

2.4.1 Multiphase Modelling

Although a single phase model was used in the current work, multiphase modelling was investigated briefly to establish the ease with which the current model could be modified for a more complex situation. The following is an overview of the findings.

Some of the factors that come into play when particles are introduced into the flow of a fluid are (Triesch 2001; Grace 2004):

- drag, Magnus and Saffman lift forces and 'slip'
 Magnus force: After impact on the wall, because of their angular velocity, particles are diverted perpendicular to their axis of rotation and their flow direction relative to the flow. The resulting force is known as the Magnus force and strengthens the movement of particles towards the centre of the pipe after wall collision.
 Saffman lift force: Besides particle-wall collision, the velocity gradient is a further source of particle spin. The resulting force acts in the same direction as the Magnus force.
- electrostatic or electrophoretic forces
- particles are a range of shapes, sizes and densities
- inter-particle forces
- inter-particle collisions and collisions/interactions of particles with the wall of the containing vessel

- influence of the surface roughness on the particle-wall collision
- laws of impact distinguishing between sliding and adhesive friction
- angular velocity of the particles that is initiated by wall collisions

Therefore modelling slurry flow, i.e., flow of particles in fluid, presents many more challenges than single phase flow.

There are two approaches for the numerical calculation of multiphase flows:

1. The Euler-Lagrange approach
2. The Euler-Euler approach

The Euler-Lagrange approach is followed by the discrete phase model (DPM) in Fluent. The fluid is treated as a continuum by solving the time-averaged Navier Stokes equations, while the dispersed phase is solved by tracking a large number of particles through the calculated field. The dispersed phase can exchange momentum, mass and energy with the fluid phase. The particle trajectories are computed individually at specified intervals during the fluid phase calculation. The coupling can be added to the Eulerian fluid momentum equations as a source term.

Euler-Euler approach views both the continuous and dispersed phases as continua. The continuity and dynamic equations of two-phase are solved. This approach cannot give the motion information of single particles.

The Stokes number and the particle loading can be used to determine the most appropriate multiphase model that should be used. The Stokes number can be defined as the relation between the particle response time and the system response time.

$$St = \frac{\tau_d}{t_s} \quad (2.19)$$

where

$$\tau_d = \frac{\rho_d d_d^2}{18\mu_c}$$

$$t_s = \frac{L_s}{V_s}$$

St = Stokes number

τ_d = particle response time, s

t_s = system response time, s

ρ_d = discrete phase density, kg/m³

μ_c = continuous phase viscosity, kg/ms

d_d = discrete phase diameter, m

L_s = characteristic length of the system under investigation, m

V_s = characteristic velocity of the system under investigation, m/s

Calculating Stokes no. (for example in the case of sand, $\rho_d = 2674\text{kg/m}^3$ $d_d = 0.001\text{m}$) for our system gives a value greater than 3 at the velocities typically employed (1 - 1.5m/s). Fluent recommends using either the DPM or the Eulerian method (see Section 2.4.1.2) where $St > 1$. In this situation, the particle moves independently of the flow.

2.4.1.1 Euler-Lagrange Model (Discrete Phase Model)

Fluent allows the user to include a discrete phase in the model by defining the initial position, velocity and size of individual particles. It can predict particle trajectories in the fluid phase as a result of forces acting on the particle and can compute wall wastage. Lagrangian trajectory calculations are performed by means of an equation which expresses equilibrium per unit particle mass between inertia, drag and gravity. The coupling between the phases and its impact on both the discrete phase trajectories and the continuous phase flow can be included. The predicted trajectories of the particles can be viewed graphically and alphanumerically.

The main limitation with the DPM is the assumption that the second phase is sufficiently dilute (10-12%), and particle-particle interactions and the effect of the particle volume fraction on the fluid phase are negligible. This means that DPM may be used to analyse the particle tracks in the flow, however it does not provide a basis for modelling slurry flow where the effect of particle-particle interactions affects settling.

This form of multiphase modelling can be relatively easily applied to the existing single phase model. Some initial investigations were carried out with appropriate modifications to the model. A coupled approach was used whereby the continuous phase flow pattern was impacted by the discrete phase and vice versa. The procedure was to solve the continuous-phase flow, create the discrete-phase injections, then solve the coupled flow and track the injections. Stochastic tracking was turned on which will include the effect of turbulent velocity fluctuations on the particle trajectories. It includes the effect of instantaneous turbulent velocity fluctuations on the particle trajectories through the use of stochastic methods. However, the particles have no direct impact on the generation or dispersion of turbulence in the continuous phase. Inputs were such that the particles had the properties of sand and were initially stationary at the bottom of the pipes. The fluid flow was at 1.5m/s.

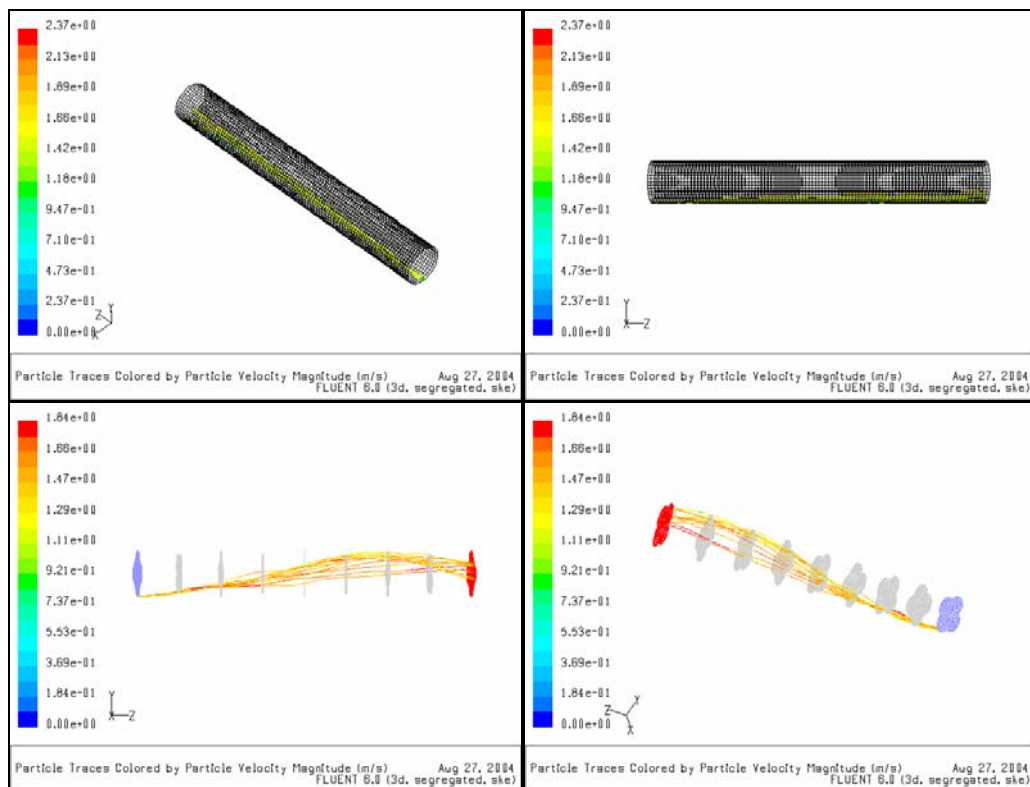


Figure 2.3: Results Comparing Circular Pipe Flow to Swirl Pipe Flow of Particles in Fluent DPM
(Swirl pipe inlet is coloured blue and exit is coloured red)

It was clear from the particle tracks (Figure 2.3) that the particles were travelling at the bottom of the pipe in the case of the circular pipe. With the swirl pipe, the particles were following the fluid streamlines and a better

distribution was observed. As predicted and observed by many previous researchers (Wolfe 1967a; Wolfe 1967b; Raylor 1998) with regards to effect of a swirling pipe flow, the particles were being swept into the flow from the bottom of the pipe.

There is also an erosion/accretion model included with the DPM that calculates the rates at wall boundary faces when particle tracks are updated. It may be interesting for future work to investigate the effect of particle size and density in how the particles follow the flow path through swirl and transition pipes.

User defined functions (UDF) can be used to customize the DPM to include additional forces and terms and make it more applicable for modelling slurry transport. This procedure was used by (Triesch 2001). Triesch used Fluent to simulate upstream gas-solids flow in pipes using a Lagrangian approach for calculating the dispersed phase. Calculated data was compared to data obtained from PDA (Phase Doppler Anemometry). He found that good agreement between PDA and the model was obtained only if some further important aspects of particle movement were considered. These models were included via programmed subroutines and concerned particle-wall interaction, particle-particle collision and particle angular velocity.

2.4.1.2 Euler-Euler Model

In the Euler-Euler approach, the different phases are treated as interpenetrating continua. Since the volume of a phase cannot be occupied by other phases, the concept of phasic volume fraction is introduced. These volume functions are assumed to be continuous functions of space and time and their sum is equal to one. Conservation equations for each phase are derived to obtain a set of equations, which have similar structure for all phases.

There are three different Euler-Euler models available:

1. volume of fluid
2. mixture model
3. Eulerian model

Of these only either the mixture model or Eulerian model are applicable to slurry flow. The mixture model may be used where the loading is low or where the slurries are homogeneous. However, due to the moderate to high solids loading and high Stokes number in the current applications for swirling flow, the Eulerian model is the most applicable. With high loading, one must take into account two-way coupling plus pressure and viscous stresses due to particles (4-way coupling). Only the Euler model will handle this correctly.

Defining a granular secondary phase requires the following information: particle diameter, granular viscosity, granular bulk viscosity, frictional viscosity, angle of internal friction, packing limit (maximum volume fraction for the granular phase). Defining the interaction between the phases requires the following: drag function, restitution coefficients for collisions between particles.

Eulerian multiphase modelling of slurry flow will require much time and effort and in the initial process of optimising the pipes it was not required. In addition, such a model is difficult to validate experimentally.

Other research has been carried out in the past to model two-phase flow to determine pressure drop, flow patterns, limit deposit velocity and erosion.

Fan (Fan 2001) carried out numerical investigation into ribbed bends erosion in gas particle flows. Particles were spherical and assumed to flow as a dilute phase free from particle-particle collisions. Particle rotation and electrostatic forces were neglected. He used $k-\epsilon$ model of turbulence (see Chapter 4) with a Lagrangian formulation for the particles.

In addition, Yao, Fan and Song (Song 1996; Fan 2001; Yao 2002) carried out numerical investigation of erosion of ribbed pipes in gas-particle flows (see Section 2.2.4). Both Eulerian and Lagrangian approaches have been used.

2.5 Conclusions

- Several correlations have been considered for calculating pressure loss and velocities denoting flow regime transitions in settling slurry.
- Swirling flow pipes may be a means of reducing frictional pressure loss through the requirement of lower slurry velocities.
- Pipes which encourage swirl and move particles into suspension prevent wear from particles dragging along the bottom of the pipe.
- Global mass loss is not sufficient in determining the erosion reduction capacity of swirl inducing pipes.
- On-line measurement techniques have been considered with particular attention to measurement of velocity components in swirling flow.
- Previous research on swirl inducing pipes has been studied carefully to aid continuity of the work.
- Important terms and equations in swirling flow have been identified.
- Multiphase modelling presents many challenges and requires accurate representation of the flow of particles in fluid. A simplified Lagrangian approach may be possible with few modifications to the existing model in Fluent. However, particle-particle interactions and additional forces must be included using user defined functions.

CHAPTER 3: SWIRL AND TRANSITION PIPE DESIGN

3.1 Introduction

Previous researchers (Raylor 1998; Ganeshalingam 2002) established the importance of equal cross-sectional area of swirl pipe to circular pipe in avoiding sudden constriction and divergence. Therefore 3-lobed and 4-lobed swirl-inducing pipes were designed and constructed to explore this condition.

A transition geometry prior to the swirl pipe, and perhaps also after it, was considered to be beneficial. This may reduce the pressure drop resulting from the sudden entry to swirl pipe from circular pipe, and vice versa, since the circular pipe will gradually change into the lobed geometry. This may also result in greater swirl intensity at the exit of the swirl pipe. This chapter details the design of several types of transition.

3.2 Methodology

Spreadsheet models were developed for optimised 3 and 4-lobed swirl pipe geometries. Models were also developed for transition pipe geometries to fit these optimised swirl pipes.

Using the geometries thus defined, solid 3 dimensional pipes were designed using a combination of Gambit (Fluent Inc. Lebanon 2000) and Pro Engineer (PTC Needham, MA, USA) software. These pipes were then built using rapid prototyping technology for use in experimental work. The process of geometry creation and prototyping are described in Sections 3.4 and 3.5 respectively.

3.3 Geometry Definition

Spreadsheets were created to define the geometry of the 3-lobed and 4-lobed swirl and transition pipes. These spreadsheets provide the co-ordinates of the pipe cross-sections in x and y direction at any given length (along z co-ordinate axis). A summary of the calculations involved is given below. The detailed calculations for 3-lobed and 4-lobed pipe, along with some of the results can be found in Appendices A3.1 and A3.2.

3.3.1 Summary of Swirl Pipe Calculations

1. Calculate r_f (lobe radius) by equating swirl pipe cross-sectional area to circular pipe area of radius R_1 (to give equal flow area)
2. Calculate x and y offsets (x_{offset} , y_{offset}) for each lobe using known value of z (see Figure 3.1)
3. Calculate x and y co-ordinates of lobe points (from $\phi=0$ to $\phi=180^\circ$), for each lobe, using r_f and x_{offset} , y_{offset}

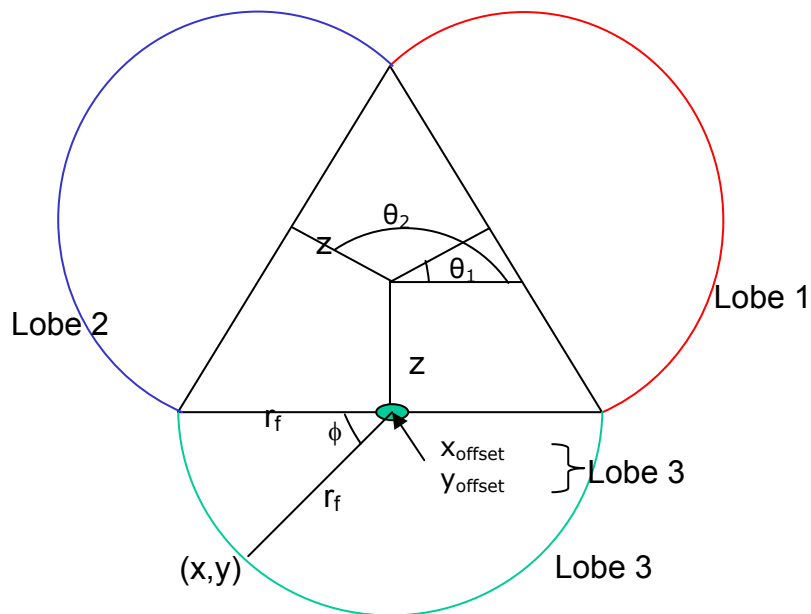


Figure 3.1: Illustration of Calculation of x_{offset} and y_{offset} for 3-Lobed Pipe

3.3.2 Summary of Transition Pipe Calculations

1. Calculate r_f (lobe radius for fully developed swirl pipe) by equating swirl pipe cross-sectional area to circular pipe area of radius R_1 (to give equal flow area)
2. Calculate the pipe length based on one lobe twisted 120° for 3-lobed pipe and 90° for 4-lobed pipe using P:D ratio such that the lobe pattern repeats in the length of the transition
3. Calculate R_{cs} (minimum core radius: radius of circular section of fully developed swirl pipe) using r_f
4. Introduce γ (increases from 60 to 90° in given no. of increments (N_{inc}) as lobes develop (see Figure 3.2) for 3-lobed pipe and increases from 45 to 90° for 4-lobed pipe)
5. For each increment of γ follow steps 6-12
6. Introduce variables f and f_1 to facilitate calculation of area of segments and y (Figure 3.2)).
7. At each increment of γ calculate R (intermediate core radius), y and r (intermediate lobe radius) keeping the cross-sectional area equal for all stages
8. Calculate lobe area for each intermediate stage (LA_i) as a function of f , R and r
9. Calculate lobe area for fully developed lobes as a function of R_{cs} and r_f
10. Introduce

$$\alpha = \frac{LA_i}{LA_{FD}} \quad (3.1)$$

LA_i = intermediate lobe area, mm^2

LA_{FD} = total lobe area for fully developed lobes, mm^2

LA is the sum of the area of the pipe minus the area of the circular core.

11. Calculate x/L (length ratio) as a cosine function of α (see Equation 3.2 below) to avoid discontinuity in the case of a linear relationship (see Figure 3.5). Function α can now be defined as desired to determine lobe development in transition.
12. Calculate the twist at each stage as a function of length

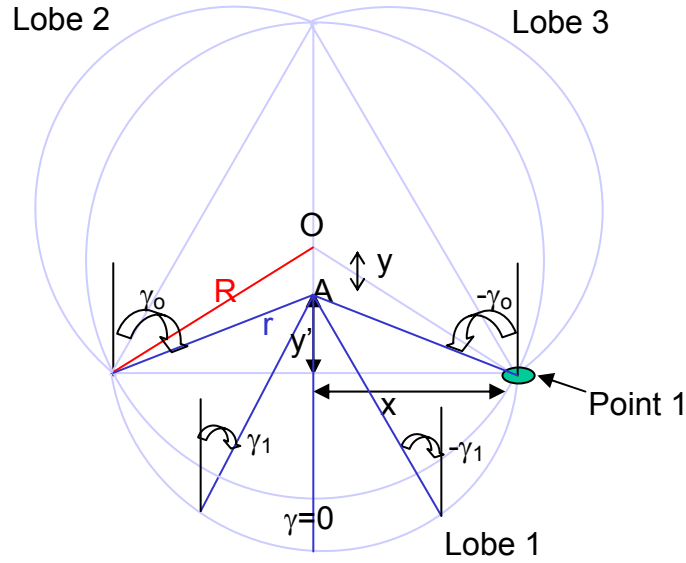


Figure 3.3: Calculation of Lobe Co-ordinates at Intermediate Stage

3.3.3 Different Types of Transition

The transition consists of a gradual change from circular cross-section to lobed cross-section. Two main types of transition, α and β transition, were defined based on the relationship of lobe area growth with length.

3.3.3.1 Alpha transition

As detailed in Section 3.1 (Bullet 10.), a variable α was defined which is a ratio of intermediate lobe area at any one stage to total lobe area for fully developed lobes. α is also equated to a cosine function of length as in Equation 3.2 below. Therefore the lobe area development will have a cosine relationship with length along the transition pipe. The utilization of a cosine function avoids the discontinuity that would result from the use of a linear relationship, as illustrated by the linear law in Figure 3.4, giving a smooth transition.

$$\alpha = \frac{LA_i}{LA_{FD}} \quad (3.1)$$

$$\alpha = \left[\frac{1 - \cos\left[\pi \frac{x}{L}\right]}{2} \right] \quad (3.2)$$

LA_i = intermediate lobe area, mm^2

LA_{FD} = total lobe area for fully developed lobes, mm^2

x = intermediate pipe length, mm

L = total pipe length, mm

3.3.3.2 Beta transition

CFD modelling results of previous researchers (Ganeshalingam 2002) indicated that with the 4-lobed swirl pipe there were two distinctive types of flow, namely the core flow and the lobe flow. This was not as obvious in the 3-lobed swirl pipe. It was observed that, with the 4-lobed pipe, the core flow consisted mainly of axial velocity, whereas the lobe flow consisted mainly of tangential velocity as shown in Figure 3.4. 4-lobed pipe showed less instability than the 3-lobed and had more distinct “core” and “lobe” flow of axial and tangential velocities.

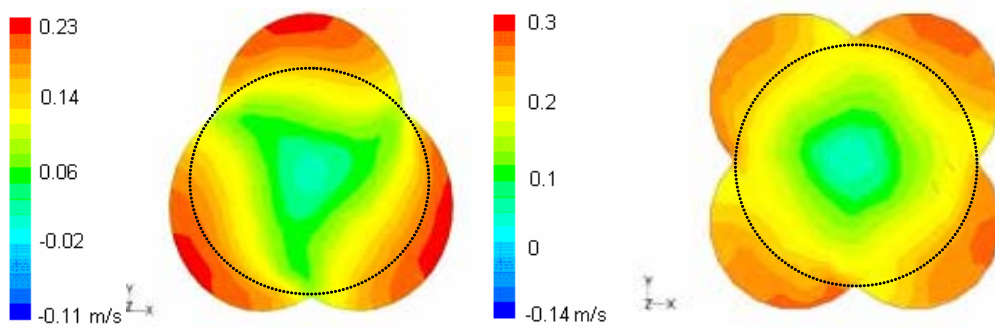


Figure 3.4: Tangential Velocity Contours at Exit of Swirl Pipe (After Ganeshalingam (Ganeshalingam 2002))

(Dotted circle indicates the “core”)

Therefore it was envisioned that defining the transition in terms of lobe area growth to core area (circular area only) would provide better results for 4-lobed transition. This was achieved by defining a variable β , which is effectively a ratio of lobe area to core area. Variable β then replaces α in Equation 3.2 (and in Equation A13 of Appendix A3.1).

$$\beta = \frac{\frac{LA_i}{\pi R^2 - LA_i}}{\frac{LA_{FD}}{\pi R^2 - LA_{FD}}} \quad (3.3)$$

Figure 3.5 shows the comparison of Alpha and Beta transition and how the lobe area develops in each of these cases. Note that for β transition the lobe development is faster than for α transition. It is expected that this will result in greater swirl induction in the β transition since the lobes prevail for a longer length and tangential velocity is generally concentrated in the lobe areas of the pipes.

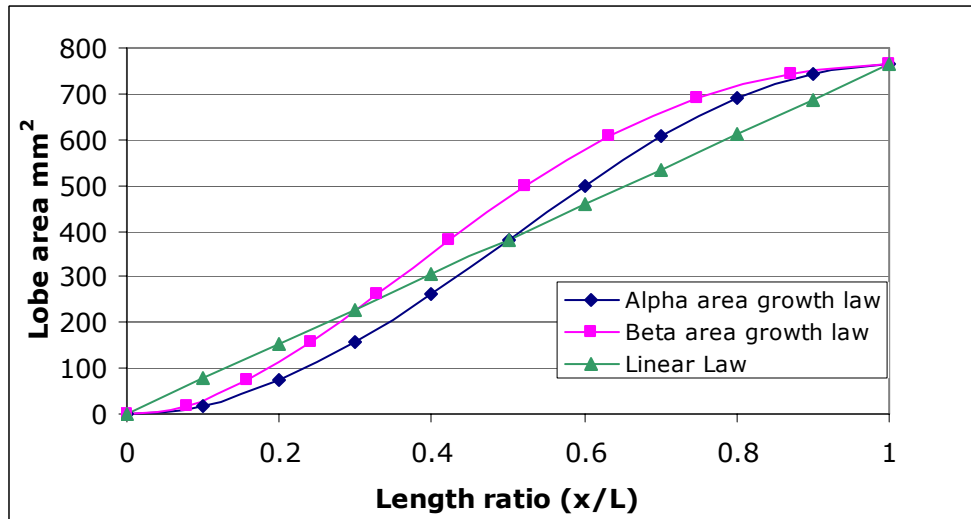


Figure 3.5: Entry transition; Comparison of Lobe Area development with Length for Alpha, Beta and Linear Law

3.3.3.3 Transition Multiplier

Further, the application of a transition multiplier, n , created a set of transition curves by the variation of its value as shown in Figure 3.6.

Equation 3.2 is then changed to:

$$\alpha = \left[\frac{1 - \cos \left[\pi \frac{x}{L} \right]}{2} \right]^n \quad (3.4)$$

Thus in the first instance the transition multiplier n was 1.

As illustrated in Figure 3.6, for α transition when

$n < 1$: the 50% point of lobe development is brought nearer the start

$n = 1$: the 50% lobe development point is at exactly mid-length

$n > 1$: sends 50% point away from the 50% length point

Figure 3.6 shows that for β transition the 50% point of lobe development is nearer the start than for α transition for each case of transition multiplier n . This implies greater lobe area growth at the front of the transition, and therefore a quicker lobe development for β transition.

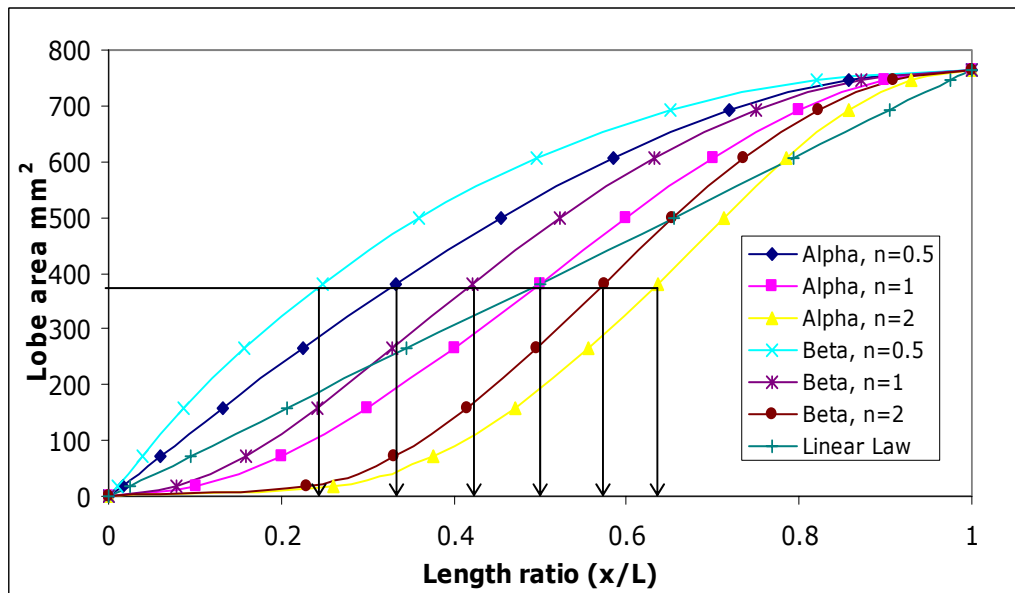


Figure 3.6: Entry Transition: Effect of Transition Multiplier
(Arrows point to 50% lobe development point)

3.3.3.4 Variable Helix

The pipes described above all have a constant change in twist with respect to length (geodesic helices). Another interesting factor for investigation was a variable helix within the transition. Raylor (Raylor 1998) investigated a brachistochrone helix for swirl pipes. The brachistochrone helix is the theoretical “path of shortest time” for a particle constrained to the inside surface of a cylinder. The variable helix was shown to give a marginal improvement, but investigations into families of loci were needed to assess its effectiveness.

In the family of cases investigated in the current work, the twist has a power law relationship with respect to length ratio.

$$Twist = \left(\frac{x}{L} \right)^t \times TwistAngle \quad (3.5)$$

t = power law variable for twist which can be changed to apply an increasing or decreasing helix as desired

So for the original geodesic case t was unity.

As illustrated in Figure 3.7 when

t<1: the helix is faster nearer the start of the transition

t=1: constant or geodesic helix where twist is linear with length

t>1: the helix is faster nearer the end of the transition

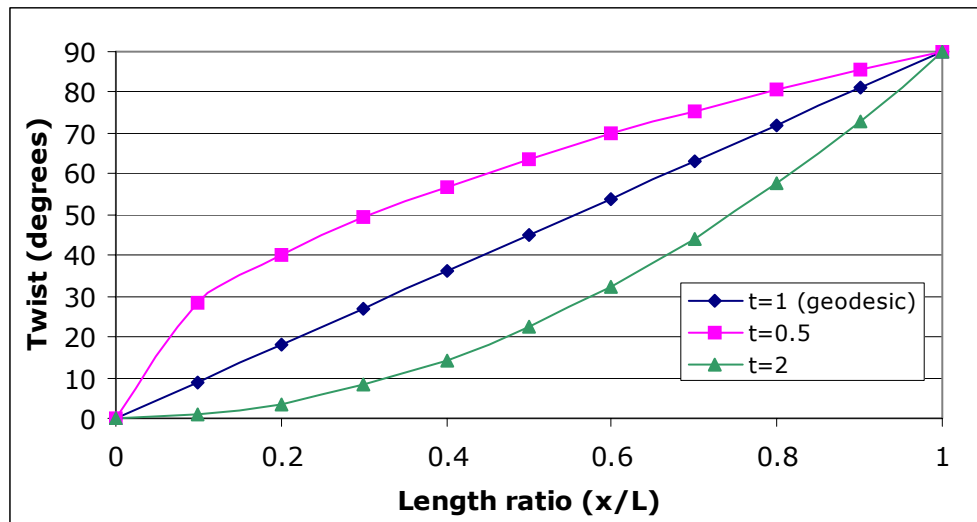


Figure 3.7: Effect of Variable Helix

3.4 Geometry Creation

Swirl pipes and swirl bends (see Appendix A3.5) were drawn in Gambit (Fluent Inc. Lebanon 2000) software. Gambit is the pre-processor and mesh generation software for Fluent CFD software (see Chapter 4).

Co-ordinate systems were used with a function which allows the user to sweep a given cross-section along any direction (or along a given curve) while twisting the cross-section in the swept direction. Flanges were also designed to specification. The designed pipe geometries were then exported in IGES (Initial Graphics Exchange Specification) (National Computer Graphics Association, Fairfax, USA) format to Pro Engineer software. These files, once in IGES format, were used to produce pipes using rapid prototyping.

The transition pipe geometry however was not as easily drawn since twist and lobe area both vary along the length of the pipe. Various software packages were considered for its design including Gambit, Matlab, AutoCAD (ACAD) and Fortran programming language.

It was first thought that the geometry could not be drawn as a continuously changing (and therefore mathematically accurate) solid. Therefore an attempt was made to draw many cross-sections along the length of the pipe and sweep one cross-section onto the next and so on to form the solid pipe.

A programme was found which reads x , y , z cross-sectional data and plots the sections in ACAD. These cross-sections could then be swept using Gambit or Pro/E software. Provided a large number of cross-sections are used, the mathematical inaccuracy from connecting many separate volumes to form the solid pipe could be reduced.

Ultimately however, it was discovered that the transition geometry could be created in Pro/E software using as little as 11 cross-sections. This was achieved through a feature in Pro/E that allows the user to sweep and blend a given cross-section. This feature, whilst sweeping the cross-section along the length (z axis) transforms it into the shape of the cross-section it is being swept onto. It projects one 2D shape at the beginning along a user-defined trajectory and transitions into another 2D shape at the end (Graham 2002).

An attempt was made to make this process more accurate. Originally the spreadsheet was created such that the transition was defined at constant " γ " intervals (see Section 3.3.1, Bullet 4.). It was later modified to give constant length intervals. However γ signifies the lobe area change directly. The use of constant γ interval cross-sections along the length of the pipe for sweeping and blending in Pro/E results in constant lobe area changes. This provides better accuracy in sweeping one face onto the next.

The use of constant γ intervals results in more twist between the 1st and 2nd, and penultimate and final faces if using 11 faces. Therefore intermediate sections were added here to give less change in twist between these faces as shown in Figure 3.8. This would not matter in the case of geodesic transitions but where the relationship of twist with length is non-linear this was crucial to gain accurate representation of the pipe geometry.

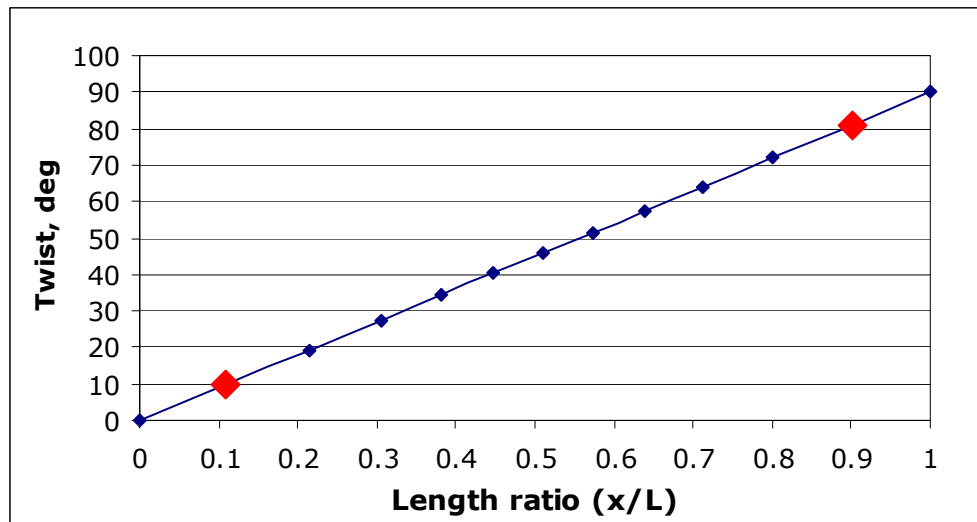


Figure 3.8: Graph of Twist versus Length (geodesic helix shown)
(Red points illustrate where additional surfaces were inserted)

An example of the resulting 13 cross-sections generated (for alpha transition $n=1$ case) to be used in sweeping and blending to form a three-dimensional transition pipe geometry is shown in Figure 3.9. This procedure of using 13 sections and constant γ intervals was used for designing all the transition pipes.

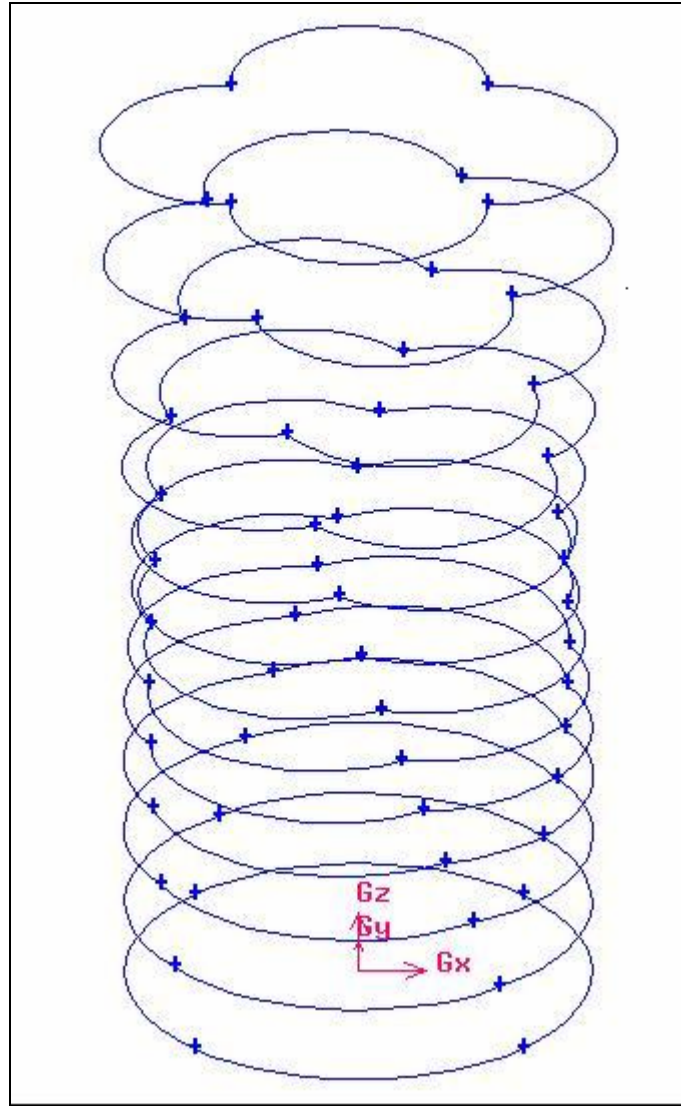


Figure 3.9: Example of 13 Sections used to Sweep and Blend to form Solid Transition Pipe

To quantify the error in design, 10 random cross-sections (or faces) were generated and superimposed onto the solid pipe in Pro/E. The pipe was next divided into 3 (in the case of 3-lobed pipe) or 4 surfaces (in the case of 4-lobed pipe) and the deviations between the faces and the solid body were evaluated. The results for a 3-lobed transition pipe are given in Table 3.1.

Table 3.1: Deviations from Theoretical for 3-Lobed Beta Transition

Drawn using Gambit/Pro E and 13 sections

L = 100mm

D = 50mm

Pitch/Diameter = 6

	Minimum Deviation, mm	Maximum Deviation, mm
Surface A	0.0002	0.0006
Surface B	0.0002	0.0009
Surface C	1×10^{-5}	0.0005
Joint between A+B	0.0002	0.0009
Joint between B+C	0.0002	0.0009
Joint between C+A	0.0001	0.0008

The maximum deviation obtained was much smaller than the accuracy that could be guaranteed in the machine-built parts (+/- 0.1mm at best).

3.5 Producing Pipes for Experimentation

3.5.1 Lost Wax Process

Strictly the 'lost wax process' is used to duplicate sculptures in bronze. A mould is made from the original in order to obtain a wax "positive" of the sculpture. The moulds are then used to form wax figures; a series of layers of molten wax are poured into the mould. When the wax is cooled, the mould is pulled away from the wax. The wax duplicate is removed from the mould.

The wax is then coated with a ceramic shell (investment) to withstand the heat of the molten bronze. The ceramic shell is one of the few materials that can stand the heat of molten bronze. Several layers are applied creating a stable mould, which is allowed to cure for several days. When the shell is cured, it is fired in a kiln. This bakes the shell and eliminates the wax, leaving a cavity in its place and thus the term "lost wax".

After being heated in a kiln, molten bronze is poured into the form. After cooling, the ceramic shell is carefully broken away, revealing a rough casting.

This technique was adapted for cold casting the pipe forms (Jones 2004) so that the ceramic investment stage could be eliminated. The curing of casting resin also causes a rise in temperature, but damage can be eliminated by incorporating a small quantity of stearic acid into the candle wax.

In the case of the swirl pipes, a mould of the pipe core was made using the pipe geometry drawn as discussed in Section 3.4. Hot wax was poured into the mould and allowed to cool. Once the wax was solidified the wax core was removed. This wax core was then inserted into a pipe and cement poured into the pipe to fill the gap between the wax core and the pipe wall. Once the cement set, the pipe was inserted into a hot oven. The wax melted away thus providing a pipe where the internal wall had the impression left by the wax core.

Bends and other structures can be created by painstakingly slicing original wax cores and reassembling the slices to form the required shape. Figure 3.10 gives an example of a swirl bend prepared by this method.

However this approach is time-consuming and the inner surface of the pipe produced was not smooth enough for initial experimental work. Therefore stereo lithography was examined for building the pipes (see below).



Figure 3.10: Bend Produced using the Lost Wax Process (After Jones (Jones 2004))

3.5.2 Stereo Lithography

Stereo lithography is a form of rapid prototyping which uses liquid photopolymer and a laser 'paints' the solid object layer by layer by exposing the photopolymer and hardening it. Other types of rapid prototyping are (Harrison 2003):

- Laminated object manufacturing; layers of adhesive sheet material are bounded together to form a prototype. Part has a wood-like structure and needs sealing and finishing to prevent water damage.
- Selective laser sintering; a laser beam fuses powdered material into prototype
- Fused deposition modelling; filaments of heated thermoplastics are extruded from a moving tip
- 3D ink-jet printing; an inkjet printing head selectively deposits or 'prints' a binder fluid to fuse powder material together

Of these different techniques stereo lithography was the best based on accuracy and surface finish. The stereo lithography procedure was carried out by IMC U.K. Ltd.

The stereo lithography machine has four fundamental parts:

1. A tank filled with liquid photopolymer
2. A perforated platform immersed in the tank
3. An ultraviolet laser
4. A computer that drives the laser and the platform.

The basic process involves the following (Jacobs 1992; Jacobs 1996):

- Creating a 3 dimensional computer-aided design (CAD) model of the object (as discussed in section 3.4)
- A piece of software that slices the CAD model into thin layers (10 layers/millimetre). The object is mathematically sectioned by the computer into a series of parallel horizontal planes.
- The 3-D printer's laser "paints" one of the layers, exposing the liquid plastic in the tank and hardening it
- The platform drops down into the tank a fraction of a millimetre and the laser paints the next layer
- This process repeats layer by layer until the model is complete

Figure 3.11 shows some of the built pipes in the tank. The following pipes were built for experimental use:

- 3 x 3-lobed straight pipes (each 200mm in length)
- 2 x 4-lobed straight pipes (each 200mm in length)
- 3 x 4-lobed bends of different radii of curvature
- 1 x 4-lobed Alpha transition $n=1$ (100mm length)
- 1 x 4-lobed Beta transition $n=1$ (100mm length)
- 1 x 4-lobed Beta transition $n=2$ (100mm length)
- 1 x 4-lobed Beta transition $n=0.5$ (100mm length)



Figure 3.11: Pipes Produced using Stereo Lithography before Removal from Build Tank

3.6 Conclusions

- Spreadsheet models of 3-lobed and 4-lobed swirl and transition geometries were developed.
- Different types of transition were defined based on lobe area growth and variable helix.
- 3D models of the swirl and transition pipes were next drawn and subsequently used in making the pipes using stereo lithography.

CHAPTER 4: COMPUTATIONAL FLUID DYNAMICS METHODOLOGY

4.1 Introduction

CFD can be described as the use of computers to produce information about the ways in which fluids flow in given situations. It is the analysis of systems involving fluid flow, heat transfer and associated phenomena such as chemical reactions by means of computer-based simulation (Versteeg 1995). It is used in a variety of industrial sectors, such as aerospace, defence, power, process, automotive, electrical and civil engineering.

The equations which govern fluid flow are termed the 'Navier–Stokes Equations';

1. Continuity (Conservation of Mass)
2. Conservation of Momentum
3. Conservation of Energy

For a complete analysis of these equations refer to Appendix A4.1.

These are a series of partial differential equations (PDEs). They can be discretised to produce a numerical analogue of the equations. When boundary conditions and initial conditions that are specific to the flow problem being simulated have been applied, they can be solved using a variety of direct or iterative solution techniques producing a numerical simulation of the given flow problem (Shaw 1992).

Broadly, the strategy of CFD is to replace the continuous problem domain with a discrete domain using a grid. In the continuous domain, each flow variable is defined at every point in the domain. In the discrete domain, each flow variable is defined only at the grid points (Bhaskaran 2003). The values at other locations are determined by interpolating the values at the grid points. Setting up the discrete system and solving it involves a very large number of repetitive calculations, thus the need for computer solution.

In the research of swirl pipes, analysis was needed for a wide range of flow geometries. Therefore experimental testing would be costly and time-consuming. Computer modelling eliminates the difficulty and cost of making the pipes and gives an insight into the flow field which is difficult to measure experimentally. Fluent CFD software was used with its pre-processor Gambit (Fluent Inc. Lebanon, NH, USA).

4.2 Modelling Turbulence

The Reynolds number of a flow gives a measure of the relative importance of inertia forces and viscous forces. At values below a critical Reynolds number the flow is smooth and adjacent layers of fluid slide past each other in an orderly fashion. This regime is called laminar flow (Versteeg 1995).

At Reynolds number above a critical value the flow behaviour is random and chaotic. This regime is called turbulent flow. Turbulent flows are characterized by fluctuations in velocity and pressure in both space and time (Bhaskaran 2003). These fluctuations mix transport quantities such as momentum, energy and species concentration, and cause the transported quantities to fluctuate as well. In modelling slurry flow, and in particular swirling flow, turbulence is an important factor.

It is theoretically possible to directly resolve the Navier-Stokes equations for the whole spectrum of turbulent scales using Direct Numerical Simulation (DNS). DNS is not, however, feasible for practical engineering problems. The mesh sizes required for DNS are prohibitive since these turbulent fluctuations can be of small scale and high frequency.

Two alternative methods can be employed to transform the Navier-Stokes equations in such a way that the small-scale turbulent fluctuations do not have to be directly simulated:

1. Filtering: Large Eddy Simulation (LES)
2. Reynolds averaging: Reynolds Averaged Navier Stokes Equations (RANS)

Filtering using LES provides an alternative approach in which the large eddies are computed in a time-dependent simulation that uses a set of 'filtered' equations. It is essentially a manipulation of the exact Navier-Stokes equations to remove only the eddies that are smaller than the size of the filter, which is usually taken as the mesh size. Basically large eddies are resolved directly in LES, while small eddies are modelled. Conceptually, LES is situated somewhere between DNS and Reynolds averaging.

Solving only the large eddies and modelling the smaller scales results in mesh resolution requirements that are much less restrictive than with DNS. Modelling less of the turbulence and solving more reduces errors. In practical terms, however, extremely fine meshes and large computer resources are still required and its use in industrial flows is in its infancy and is not well documented.

In Reynolds averaging, the RANS equations represent transport equations for the mean flow quantities only, with all the scales of the turbulence being modelled (see Section 4.2.1).

Both methods result in a modified set of Navier-Stokes equations that are computationally less expensive to solve. However, the modified equations contain additional unknown variables and there are an insufficient number of equations to solve for all the unknowns. Turbulence models are needed to determine these variables in terms of known quantities.

Versteeg (Versteeg 1995) defined a turbulence model as a computational procedure to close the system of mean flow equations so that a more or less wide variety of flow problems can be calculated. No turbulence model is currently available that is valid for all types of flows and so it is necessary to choose and fine-tune a model for particular classes of flows. The following sections detail the choice of turbulence models available for the Reynolds averaging (RANS) approach.

4.2.1 RANS Approach

In Reynolds averaging, the solution variables in the instantaneous (exact) Navier-Stokes equations are decomposed into the mean (ensemble-average or time averaged) and fluctuating components. For the velocity components:

$$u_i = \bar{u}_i + u_i' \quad (4.1)$$

where \bar{u}_i and u_i' are the mean and fluctuating velocity components

Likewise, the same is applied for pressure and other scalar quantities. Substituting expressions of this form for the flow variables into the instantaneous continuity and momentum equations and taking a time (or ensemble) average (and dropping the overbar on the mean velocity) yields the Reynolds averaged Navier-Stokes equations (RANS).

The RANS equations thus have the same form as the instantaneous Navier-Stokes equations (Appendix A4.1) with the velocities and other solution variables now representing ensemble-averaged or time averaged values. This greatly reduces computational effort. Additional terms now appear that represent the effects of turbulence. These are the Reynolds stresses, $[-\rho \overline{u_i' u_j'}]$, and must be modelled in order to close the equations.

The Reynolds stresses can be modelled using:

- Boussinesq approach; as used by Spallart-Allmaras, k- ϵ and its variants, k- ω turbulence models
- Reynolds stress transport models (RSM)

The Boussinesq hypothesis simplifies the additional terms and treats them as additional viscous stresses produced by the turbulence in the flow (Shaw 1992). The additional viscosity, μ_t , can then be calculated from other flow variables. In the Spalart-Allmaras model, only one additional transport equation (representing turbulent viscosity) is solved to calculate μ_t . In the case of k- ϵ and k- ω models, two additional transport equations (for the turbulent kinetic energy k and either the turbulence dissipation rate, ϵ or the

specific dissipation rate ω) are solved, and μ_t is computed as a function of k and either ε or ω . For example, in the k - ε model,

$$\mu_t = C_\mu \rho \frac{k^2}{\varepsilon} \quad (4.2)$$

where C_μ is a constant.

The advantage of the Boussinesq approach is the relatively low computational cost associated with the computation of the turbulent viscosity, μ_t . The disadvantage is that it assumes μ_t is an isotropic scalar quantity, which is not strictly true. Isotropy implies that the ratio between Reynolds stress and mean rate of deformation is the same in all directions. This assumption fails in many categories of flow and can lead to inaccurate flow predictions. In these situations it is necessary to derive and solve transport equations for the Reynolds stresses themselves using Reynolds stress transport models (RSM).

In RSM, transport equations for each of the Reynolds stresses are solved. This means that seven additional transport equations are required in 3D flows; six transport equations, one for each Reynolds stress and the transport equation for the rate of dissipation of kinetic energy, ε . Solving the 7 extra PDEs gives rise to a substantial increase in the cost of CFD simulations when compared to models based on the Boussinesq approach.

In many cases, models based on the Boussinesq hypothesis perform very well, and the additional computational expense of the RSM is not justified (Fluent Inc. Lebanon 2001). However, the RSM is clearly superior for situations in which the anisotropy of turbulence has a dominant effect on the mean flow. Such cases include highly swirling flows and stress-driven secondary flows. The following section discusses models based on the Boussinesq hypothesis (k - ε and its variants) and the RSM in more detail.

4.2.1.1 Standard k - ε Model

Two transport equations, one for the turbulent kinetic energy k , and one for the rate of its dissipation ε , are solved. These are then used to calculate the

turbulent viscosity, μ_t , to close the RANS equations. The shortcomings of the standard k- ϵ model are as follows:

- It is valid when all Reynolds stresses are of the same order (isotropic eddy viscosity). If the eddy viscosity is not isotropic, the standard k- ϵ model is inadequate
- Applicability is limited to high Reynolds number flows
- The model is semi-empirical; transport equations for k and ϵ involve constants that are taken from measurements
- Near wall treatment is accomplished via a wall function

Robustness, economy and reasonable accuracy for a wide range of turbulent flows explain its popularity in industrial flow simulations.

Launder (Launder 1974) carried out a test to determine whether the k- ϵ model was sufficient for simulating swirling flow along a twisted tape. Twisted tape inserts were used to impart a swirling motion to the fluid thereby increasing the surface heat transfer coefficient. Variation of friction factor with Reynolds number was checked (for a P:D ratio of 3.14) with experimental results. The agreement was not very good. The main source of discrepancy may stem from the turbulent viscosity becoming strongly non-isotropic in the complicated strain field of this flow.

4.2.1.2 Re-Normalization Group (RNG) and Realizable k- ϵ Models

The effect of swirl on turbulence is included in the RNG model, enhancing its accuracy for swirling flows. It is more accurate and reliable for a wider class of flows than the standard k- ϵ model.

Both the Realizable and RNG k- ϵ models have shown substantial improvements over the standard k- ϵ model where the flow features include strong streamline curvature, vortices and rotation (Fluent Inc. Lebanon 2001). Since realizable k- ϵ is still relatively new, it is not clear in exactly which instances it consistently outperforms the RNG model.

4.2.1.3 Reynolds Stress Model (RSM)

Abandoning the Boussinesq hypothesis of isotropic eddy viscosity, the RSM closes the RANS equations by solving transport equations for the Reynolds stresses, together with an equation for the dissipation rate as explained earlier.

The RSM accounts for the effects of streamline curvature, swirl, rotation and rapid changes in strain rate in a more rigorous manner than models based on the Boussinesq approach. It has a greater potential to give accurate predictions for complex flows. However, the RSM in Fluent CFD software requires 50-60% more CPU time per iteration on average compared to the k - ϵ models and needs 15-20% more memory (Fluent Inc. Lebanon 2001).

4.2.2 Choice of Turbulence Model

In his work on *Swirly-Flo* pipes, Ganeshalingam (Ganeshalingam 2002) chose to use the standard k - ϵ model of turbulence for being the simplest and most widely used, and because swirl inducing pipe flow represented a weakly swirling flow. Although RNG, Realizable k - ϵ models and RSM should show substantial improvements in results compared to standard k - ϵ where the flow features include streamline curvature and rotation, Ganeshalingam indicated that the accuracy gained is not considerable when the extra time consumed is taken into account. He concluded that the standard k - ϵ model was useful for repeated case studies and time-consuming investigative trials, while the RSM should be used to refine the designs.

A quick turbulence model sensitivity study was carried out for an entry transition pipe alone and the results are shown in Table 4.1, Figure 4.1 (pressure loss variation) and Figure 4.2 (tangential velocity variation). The RNG k - ϵ model gave results much closer to the RSM than the standard k - ϵ model. The time taken for an RSM simulation was more than double the time for standard k - ϵ . In addition, the k - ϵ results closely followed RSM trends as illustrated in figures 4.1 and 4.2. Due to the large number of cases to be studied in the case of optimisation simulations, the k - ϵ model would therefore be sufficient.

The Fluent help manual (Fluent Inc. Lebanon 2001) recommends that RSM should be used in cases where swirl intensity (Ω) is greater than 0.5. Transition pipes alone provide a swirl intensity of approximately 0.07 and swirl pipes of 0.14 (for the longest length of optimised swirl pipe used). Therefore it was decided that the standard k- ϵ model should be sufficient for initial work.

Table 4.1: Comparison of Turbulence Models for Entry Transition

Pipe: 4-lobed, β type, $n=0.5$, length 100mm

Model parameters: Water only simulation, uniform axial velocity inlet of 1.5m/s

Turbulence Model	Pressure Drop, Pa	Exit Tangential Velocity, m/s	Time for Simulation (approx.), mins
Standard k- ϵ	138.44 (+2.6%)	0.137 (+6.1%)	22
RNG k- ϵ	134.54 (-0.3%)	0.133 (+3%)	18**
Realizable k- ϵ	136.48 (+1.2%)	0.135 (+4.8%)	20**
RSM	134.88	0.129	50**

*Percentages show the variation from the RSM result

** For RNG, realizable k- ϵ and RSM simulations, simulation using standard k- ϵ model was carried out before and used as initial condition (as recommended in Fluent help manual (Fluent Inc. Lebanon 2001)). The times shown do not include the additional time for the standard k- ϵ simulation.

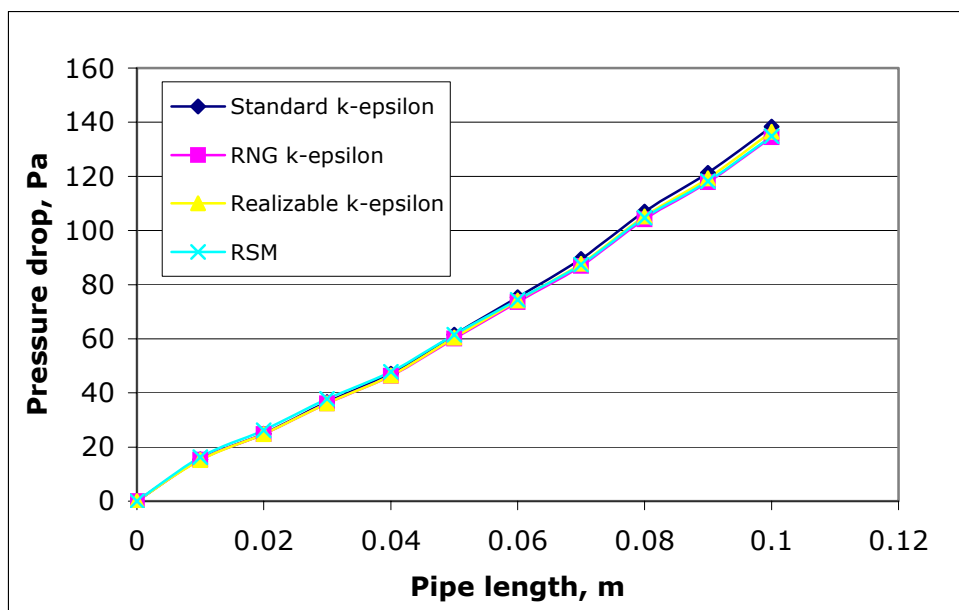


Figure 4.1: Variation of Pressure Drop

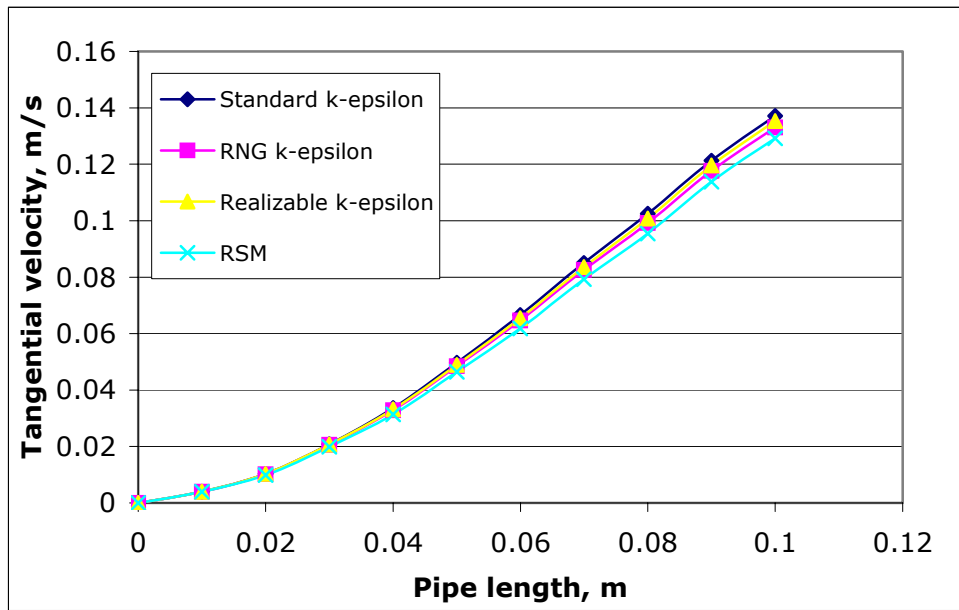


Figure 4.2: Variation of Tangential Velocity

4.2.3 Near Wall Treatment for Turbulent Flows

In laminar flow, the velocity components near a wall can be set to equal the velocity of the wall. When the flow is turbulent, the situation is more complex because the velocity of the flow varies extremely rapidly near a wall. Many grid points are required near the wall to capture this variation.

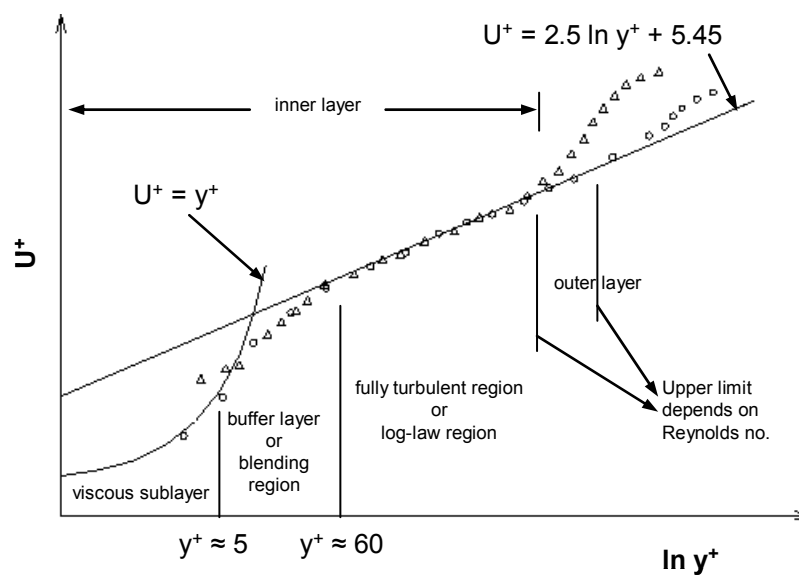


Figure 4.3: Near-Wall Region in Turbulent Flows

In a turbulent flow, the near wall region can be subdivided into three layers as illustrated in Figure 4.3:

1. Viscous sublayer: This is the innermost layer where the flow is almost laminar because the effects of turbulence are damped out by the wall itself. Viscosity plays a dominant role in momentum and heat or mass transfer.
2. Buffer layer: The interim region where effects of molecular viscosity and turbulence are equally important
3. Fully turbulent layer (log-law region): This is the outer layer where the boundary layer and the external flow merge. Turbulence plays a major role.

The turbulence models previously discussed are primarily valid for fully turbulent flows. Close to the solid walls, there are inevitably regions where the local Reynolds number of turbulence is so small that viscous effects predominate over turbulent ones. Consideration must be given to make the models suitable for wall-bounded flows. Thus the overall success of all modern turbulence models is determined in large by the treatment of the boundary conditions (BC) at solid walls (Chen 1988). Two approaches are taken in modelling the near wall region:

1. Enhanced wall approach

The turbulence models are modified to enable the viscosity affected region to be resolved with a mesh all the way to the wall. It is used if there are significant phenomena occurring inside the boundary layer region. A very fine mesh is required and simulation will be slow.

2. Wall function approach

Viscous sub-layer and buffer layer are not resolved. Instead 'wall functions' are used to bridge this viscosity affected region between the wall and the fully-turbulent region. The use of wall functions obviates the need to modify the turbulence models to account for the presence of the wall. There are two methods of wall functions:

- 2.1. Standard wall functions
- 2.2. Non-equilibrium wall functions

In most high-Reynolds-number flows, the wall function approach substantially saves computational resources, because the viscosity-affected near-wall region, in which the solution variables change most rapidly, does not need to be resolved. In addition it is popular because it is economical, robust, and reasonably accurate. The standard wall function approach was used in the current work. The following sections detail the differences between the two kinds of wall functions.

4.2.3.1 Standard Wall Functions

This approach uses the 'log law' whereby the mean velocity is taken as a logarithmic function of the distance from the wall in the fully turbulent region. Therefore if the mesh is built so that the first point where the velocity is calculated is in the log-law region, then the very rapid variation near the wall need not be modelled.

$$U^+ = \frac{1}{\kappa} \ln(Ey^+) \quad 30 < y^+ < 60 \quad (4.3)$$

The log-law is known to be valid for y^+ between 30 and 60, where y^+ is the non-dimensional distance of a point from the wall. When y^+ at the wall adjacent cells are low ($y^+ < 11.225$) the laminar stress-strain relationship is applied.

$$U^+ = y^+ \quad y^+ < 11.225 \quad (4.4)$$

U^+ = dimensionless mean velocity = u/u_τ

$$u_\tau = \text{friction velocity} = \frac{\tau_w}{\rho}$$

u = velocity tangent to the wall at a distance y from the wall

τ_w = wall shear stress

κ = von Karman constant (=0.42)

E = empirical constant (a function of the wall roughness) (=9.81 for smooth walls)

$$y^+ = \text{non-dimensional distance of a point from the wall} = \frac{\rho y u_\tau}{\mu}$$

y = normal distance to the wall

ρ = density of fluid

μ = dynamic viscosity of fluid

The production of k and its dissipation rate ε , are assumed to be equal in the wall-adjacent control volume. The wall boundary conditions for the solution variables, including mean velocity, temperature, species concentration, k and ε are all taken care of by the wall functions.

The wall function approach becomes less reliable when the flow conditions depart too much from the ideal conditions underlying the wall functions. For example when there are severe pressure gradients leading to boundary layer separations, strong body forces or high three-dimensionality in the near-wall region.

For a further discussion of standard wall functions refer to Ganeshalingam (Ganeshalingam 2002).

4.2.3.2 Non-Equilibrium Wall Functions

When near wall flows and turbulence are subjected to severe pressure gradients, and change rapidly, and when the flows are in strong non-equilibrium, the non-equilibrium wall functions can improve results.

In the non-equilibrium wall functions the log-law for mean velocity is sensitized to pressure-gradient effects. In addition a two-layer-based concept is adopted to compute the budget of turbulent kinetic energy in the wall-neighbouring cells. The wall-neighbouring cells are thus assumed to consist of a viscous sublayer and a fully turbulent layer. The turbulence is effectively sensitised to the proportions of the viscous sublayer and the fully turbulent layer, which varies widely in non-equilibrium flows. It effectively relaxes the local equilibrium assumption (production=dissipation) that is adopted by the standard wall functions in computing the turbulence. This, in effect, partly accounts for non-equilibrium effects neglected in the standard wall functions.

In the current investigations, the standard wall functions approach was used. A comparison to use of non-equilibrium wall functions approach was

carried out for the case of [Swirl pipe (400mm) + Exit transition (100mm, $n=1$)]. The results are in Appendix A4.2. It was observed that trends were closely followed in both cases and the difference in final result was 3% greater pressure drop and 0.3% lower tangential velocity when standard wall functions were used.

4.2.3.3 Grid Adaption at the Wall

When using wall functions, the distance from the wall of the wall-adjacent cells must be determined considering the distance over which the log-law is valid ($30 < y^+ < 60$).

Therefore using an excessively fine mesh near the walls was avoided because the wall functions cease to be valid in the viscous sublayer ($y^+ < 30$). Where necessary in the simulations, the grid was refined to ensure that the condition of $y^+ < 60$ was satisfied at the walls and the y^+ values were checked to be reasonably within the log-law region.

4.3 Model Description

The CFD predictions were single phase consisting pure fluid only. A fully multiphase Eulerian approach is necessary to model the particles in settling slurry flow. As explained in Chapter 2 this poses many challenges and potential problems. Further reasons for initial single phase CFD simulations were:

- A starting solution or 'baseline' was needed to make prototypes for physically testing more complex mixtures and rheologies.
- Whatever the proposed duty of the pipe, at some stage or other it will almost certainly be carrying only liquid.
- Solutions are fairly easily adaptable to more viscous liquids and should be adaptable for particle and liquid models in future. The general applicability of the solutions may be lost if complex situations were attempted to start with and pure fluid was not simulated initially.

4.3.1 Enabling Assumptions

A set of assumptions were made to simplify the problem of flow within swirl pipes as follows:

- The flow was assumed to be steady and isothermal
- Fully developed turbulent flow was assumed at the inlet of the pipe.
- Simulations were carried out with single-phase flow (water or other fluid only).
- The "no-slip" boundary condition was employed at the wall. This specifies that the fluid sticks to the wall and is stationary where the wall is stationary.
- The pressure drop was estimated by considering hydraulically smooth pipes unless otherwise stated.
- Effects of molecular viscosity were assumed to be negligible

4.3.2 Solver Parameters

Solver parameters used are summarised below. They are discussed in further detail in following sections.

- Fluent v6.0.2 with pre-processor Gambit v2.0 was used for simulations. The following were considered in deciding the type of CFD software used; interfacing to Computer Aided Design (CAD), speed of solution, availability of turbulence models, mesh type (structured or unstructured), user friendliness, user support and users with similar flow problems.
- Tetrahedral/T Grid mesh was used which is an unstructured mesh in which cells are positioned in an irregular manner (see Section 4.4). It gives greater flexibility for complex geometries such as swirl inducing pipes.
- Equi-angle skewness specification was used for a measure of the skewness of the 3 dimensional elements. A skewness of less than 0.8 for tetrahedral cells was specified. Where hexahedral cells were used a skewness of less than 0.65 was specified (see Section 4.4.4).
- Smoothing and face swapping of the grid were carried out to complement grid adaption. This generally increases the quality of the

final numerical mesh. Smoothing repositions the nodes and face swapping modifies the cell connectivity. The skewness-based smoothing method was used. The minimum skewness for which node smoothing was attempted was set to 0.8.

- Inlet boundary condition of uniform mean flow velocity (except where velocity profiles were loaded at the inlet) was specified.
- Outlet boundary condition of zero uniform static pressure was specified.
- The turbulence was specified in terms of intensity and hydraulic diameter at the inlet and the outlet. It is the recommended method for fully developed internal flows. The turbulence intensity is defined as the ratio of the root-mean-square of the velocity fluctuations to the mean velocity. It was calculated from:

$$I = \frac{u'}{u_{avg}} = 0.16(\text{Re})^{-\frac{1}{8}} \quad (4.5)$$

Therefore, for a Reynolds number of approximately 50,000 to 100,000, I is approximately 4%. Earlier investigators (Raylor 1998; Ganeshalingam 2002) used a value of 10%. For a comparison of the result of using a lower value refer to Appendix A4.3.

- k- ϵ model of turbulence was used in all cases unless otherwise specified.
- Standard wall functions were used and y^+ was checked to be between 30 and 60 (see Section 4.2.3).
- The segregated solver was used as recommended for incompressible flows (Section 4.3.3).
- Second order accuracy was obtained in all cases (Section 4.3.4). However an initial 1st order solution was used as a starting solution for the 2nd order simulations.
- The 'SIMPLE' discretization technique was used for the pressure-velocity coupling (generally used for steady state calculations).
- Gravitational body forces were included in the simulation.
- Operating density was not specified, thereby allowing the solver to calculate it by averaging over all cells.
- Unless specified explicitly, zero wall roughness was used corresponding to hydraulically smooth walls. Wall roughness, where specified, was modelled by specifying the roughness height, K_s .

- Grid independence tests were carried out in all cases (Section 4.4.5).

The flow parameters which were assumed for the simulations are summarised in Table 4.2.

Table 4.2: Flow Parameters for the CFD Simulations

Length of pipe (transition/swirl/combination)	0.1m – 0.6m
Axial velocity (u) at inlet*	1.5ms ⁻¹
Radial velocity (v) at inlet*	0 ms ⁻¹
Tangential velocity (w) at inlet*	0 ms ⁻¹
Reynolds number	75,000
Pressure at outlet	0 Pa
Turbulence intensity at inlet	4%
Hydraulic diameter	0.05 m
Density of water	998.2kgm ⁻³
Viscosity of water	0.001kgm ⁻¹ s ⁻¹

*Except where a velocity profile was loaded for the inlet

4.3.3 Numerical Discretization Techniques

Numerical discretization is the process of transforming a continuous system of partial differential equations into a numerical analogue of discrete equations which a computer can solve (Shaw 1992).

In CFD, the discrete equations are applied to the grid points (or cells in the finite-volume method) in the interior of the domain. For grid points (or cells) at or near the boundary, a combination of the discrete equations and boundary conditions are applied. In the end, a system of simultaneous algebraic equations is obtained with the number of equations being equal to the number of independent discrete variables (Bhaskaran 2003). This system of equations is written in matrix form for convenience. An iterative procedure is then used to invert the matrix.

The momentum conservation equation for a fluid is nonlinear due to the convection term. Phenomena such as turbulence and chemical reaction

introduce additional non-linearities. The strategy adopted to deal with nonlinearity is to linearize the equations about a guess value of the solution and to iterate until the guess agrees with the solution to a specified tolerance level.

There are three major discretization techniques as discussed below.

4.3.3.1 The Finite Difference Method

This is based upon the use of Taylor series to build a library or toolkit of equations that describe the derivatives of the variable at various points in space or time (Shaw 1992). When dealing with flow problems the dependent variables are the velocity components and fluid pressure, etc. and the independent variables are the spatial coordinates and time. Imagine that the value of some dependent variable, and all of its derivatives with respect to one independent variable is known, at some given value of this independent variable, a reference value. Taylor series expansions can then be used to determine the value of the dependent variable at a value of the independent variable a small distance from the reference value (Shaw 1992).

Expressions known as difference formulae are generated. They involve calculating derivatives using the simple differences between the values of the variable taken at various points.

Points are placed within the domain under consideration. At each of these points, the derivatives can be replaced by the appropriate difference formula, giving an equation that consists solely of the values of variables at the given point and its neighbours. If this process is repeated at all points, a set of equations for the variables at all the points is formed and these are solved to give the numerical solution.

4.3.3.2 The Finite Element Method

In this method the domain over which the PDE applies is split into a finite number of sub-domains known as elements.

4.3.3.3 The Finite Volume Method

Fluent uses the finite volume technique of discretization. It is probably the most popular method. It is similar in some ways to the finite difference method, but some implementations of it also draw on features taken from the finite element method.

Essentially, the governing PDEs are converted into a numerical form by a physically based transformation of the equations. For example, the momentum equations can be considered as a series of fluxes into a volume of fluid, together with a source term which is the pressure gradient. It is therefore a numerical method for solving PDEs by calculating the values of the conserved variables averaged across the volume. A solution is found such that mass, momentum, energy and other relevant quantities are conserved for each cell or volume.

The integral form of the conservation equations are applied to the control volume defined by a cell to get the discrete equations for the cell. Usually the values at the cell centres are stored. The face values are obtained by suitably interpolating the cell-centre values for adjacent cells (Bhaskaran 2003) (see Section 4.3.4 on Upwinding).

One advantage of the finite volume method over finite difference method is that it does not require a structured mesh. Furthermore, it is preferable to other methods because boundary conditions can be applied non-invasively. This is true because the values of the conserved variables are located within the volume element, and not at nodes or surfaces.

The three discretization techniques have several common features.

Each method:

- Produces equations for the values of the variable at a finite number of points in the domain under consideration
- Requires a set of initial conditions to start the calculation
- Requires the boundary conditions of the problem to be known so that the values of the variables at the boundaries can be found.
- Can produce explicit or implicit schemes

The differences are:

- The finite difference method and the finite volume method both produce the numerical equations at a given point based on the values at neighbouring points, whereas the finite element method produces equations for each element independently of all the other elements.
- The finite difference method requires that the grid is topologically regular. This means that the grid must look cuboid in a topological sense (see Section 4.4 on Meshing).

The finite element method produces the numerical equations for each element from data at known points on the element and nowhere else. Consequently, there is no restriction on how the elements are connected. This flexibility of element placement allows modelling of very complex geometries.

Algorithms have been developed with the finite volume method that can use irregular, finite element-like meshes to enable calculations to be carried out in complex geometries.

4.3.4 Upwinding Scheme

As stated, Fluent uses the finite volume technique. This consists of integrating the governing equations about each control volume, yielding discrete equations that conserve each quantity on a control-volume basis.

Fluent stores discrete values of the scalar quantity at the cell centres. However, face values are required for the convection terms and must be interpolated from the cell centre values. This is accomplished using an upwinding scheme.

Upwinding means that the face value is derived from quantities in the cell upstream, or 'upwind', relative to the direction of the normal velocity.

4.3.4.1 First Order Upwind Scheme

When 1st order accuracy is desired, quantities at cell faces are determined by assuming that the cell-centre values of any variable represent a cell-average value and hold throughout the entire cell; the face quantities are identical to the cell quantities. Thus when 1st order upwinding is selected, the face value is set to equal the cell centre value in the upstream cell.

4.3.4.2 Second Order Upwind Scheme

When 2nd order accuracy is utilized, quantities at cell faces are computed through a Taylor series expansion of the cell-centered solution about the cell centroid.

When the flow is aligned with the grid, 1st order upwinding may be acceptable. For triangular and tetrahedral grids, as used in meshing swirl pipes, the flow is never aligned with the grid. More accurate results may be obtained by using 2nd order upwinding. Therefore while 1st order discretization generally yields better convergence than the 2nd order scheme, it generally yields less accurate results, especially on tetrahedral grids.

In this work, a 2nd order discretization scheme was utilised in all simulations carried out. However, a 1st order solution was used as the initial condition for the 2nd order simulation.

4.3.5 Solver

Fluent provides a choice of segregated, coupled implicit or coupled explicit solvers.

The segregated and coupled approaches differ in the way that the continuity, momentum, energy and species equations are solved. In the segregated solver, these equations are solved sequentially (segregated from one another), while in the coupled solver they are solved simultaneously.

The coupled solver is recommended for high speed compressible flows with strong body forces or flows being solved on very fine meshes. However it requires more memory (1.5 to 2 times) than the segregated solver. Therefore the segregated solver was considered sufficient for swirl pipe flows.

4.3.6 Under Relaxation

Because of the non-linearity of the RANS equations, it is necessary to control the change of a calculated variable ϕ during the iterative solution process. This is achieved by under-relaxation, which reduces the change of a variable ϕ during each iteration:

$$\phi_{NEW} = \phi_{OLD} + \delta \Delta \phi \quad (4.6)$$

ϕ_{NEW} = New value of variable

ϕ_{OLD} = Old value of variable

δ = Under-relaxation

$\Delta \phi$ = Computed change in Φ

So lowering the under-relaxation value δ would mean a smaller change in the variable ϕ from old calculated value to new value. This will result in better accuracy but the solution will be slower.

Reducing the under-relaxation factors facilitates convergence. In the current work, the default under-relaxation parameters in Fluent were used at the start of the simulation since they are near optimal for many problems. They were then reduced in a step-by-step process where necessary to facilitate convergence.

4.3.7 Judging Convergence

A solution is converged when all conservation equations are obeyed at all points to a specified tolerance (Fluent Inc. Lebanon 2001).

The convergence criterion used for simulations was that the scaled residuals of x , y , z velocities and k and ϵ have decreased by five orders of magnitude and their residuals are no longer changing with more iterations. It was also ensured that mass imbalance and inlet pressure no longer changed dramatically with more iterations. Once the solution had converged, the mass imbalance was checked.

These criteria are illustrated and explained in the following sections.

4.3.7.1 Residual Convergence

The residual is the imbalance of the conservation equation for a general variable ϕ summed over all the computational cells. They are a measure of error in the discretised equations, summed over all control volumes and are a guide to convergence.

At the end of each solver iteration, the residual sum for each of the conserved variables is computed and stored in Fluent, thus recording the convergence history. On a computer with infinite precision, the residuals would go to zero as the solution converges. On an actual computer, the residuals decay to some small value and then stop changing (level out).

Figure 4.4 shows the scaled residuals for an example case of 4-lobed swirling flow pipe.

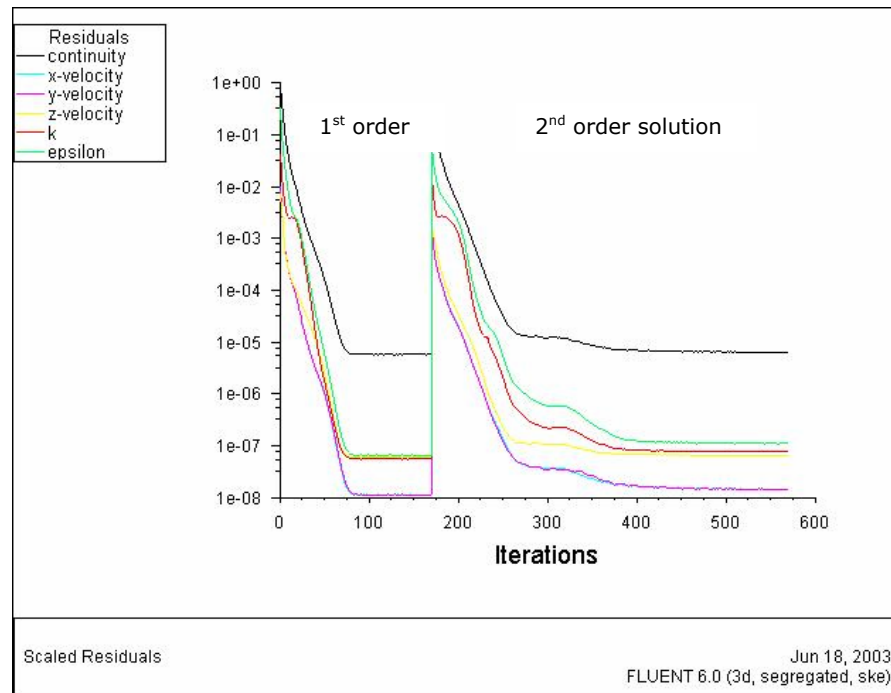


Figure 4.4: Scaled Residuals Reduced by Five Orders of Magnitude ($<1 \times 10^{-5}$)

4.3.7.2 Mass Imbalance

The mass imbalance for all cells was generally in the range of 10^{-8} (Figure 4.5). In addition the mass imbalance between inlet and outlet was also checked and monitored as the solution proceeded (Figure 4.6).

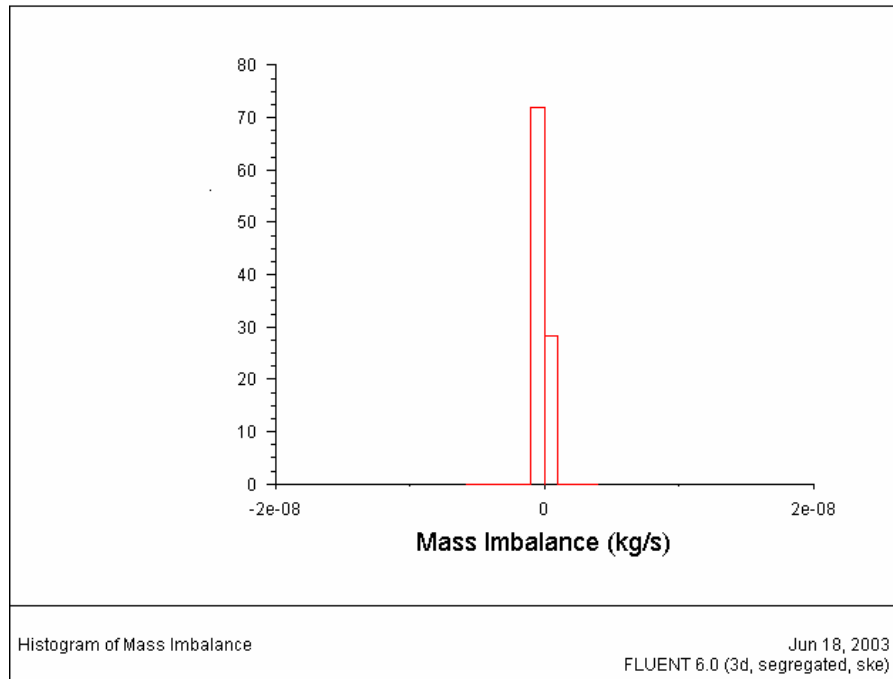


Figure 4.5: Histogram of Mass Imbalance

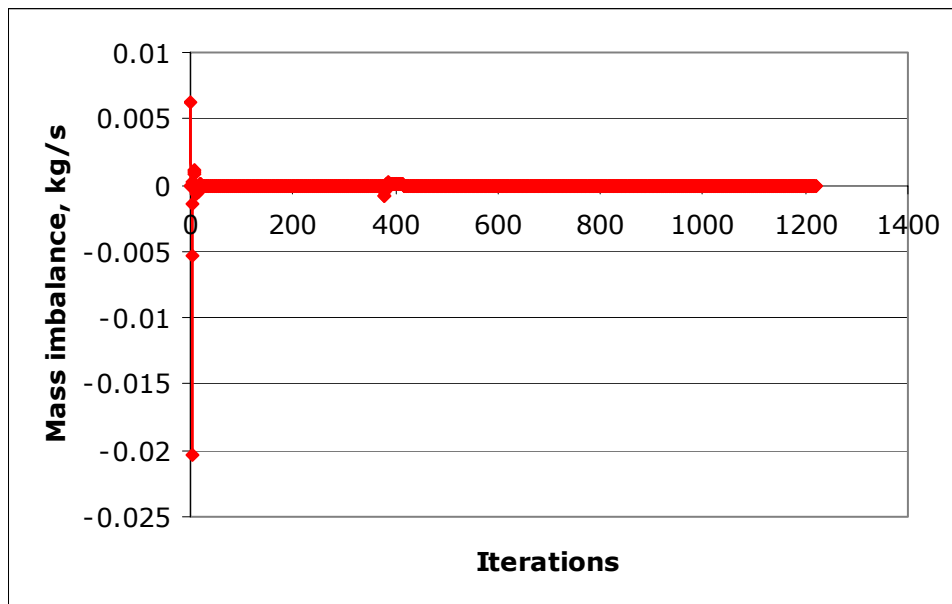


Figure 4.6: Variation of Mass Imbalance (Inlet-Outlet) with Iteration Number (Last 100 iterations were closely inspected in addition)

4.3.7.3 Inlet Pressure Convergence

The inlet pressure convergence was checked as the solution proceeded as shown in Figure 4.7. The last 100 iterations were closely inspected (Figure 4.7b) to ensure that the pressure was effectively constant.

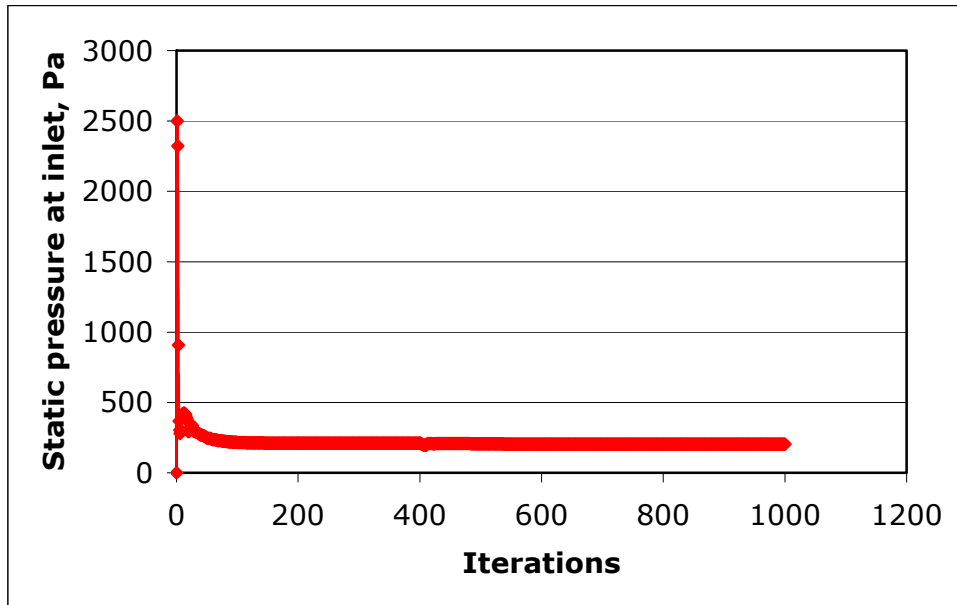


Figure 4.7a: Variation of Static Pressure at Inlet with Iteration Number

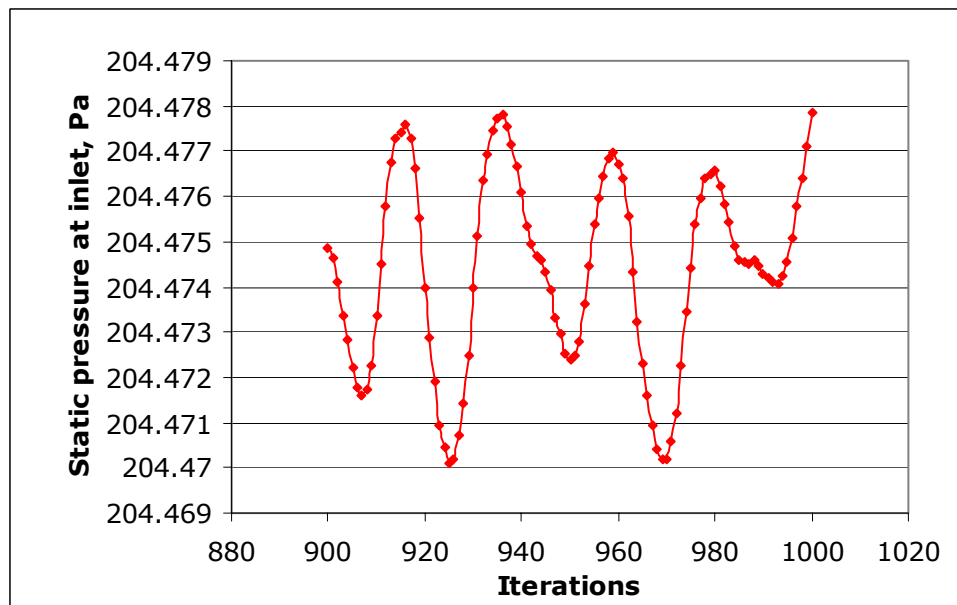


Figure 4.7b: Variation of Static Pressure at Inlet with Iteration Number (Last 100 iterations)

4.4 Meshing

A mesh of points has to be produced within the volume of the fluid to provide discretization of the space in which the flow takes place (Shaw 1992).

When the finite volume method is used, as with Fluent, the points are arranged so that they can be grouped into a set of volumes and the PDEs can be solved by equating various flux terms through the faces of the volumes.

There are two ways in which the mesh structure can be arranged:

1. A regular structure or topology (structured)

The points of the mesh can be imagined as a grid of points placed in a regular way throughout a cuboid. These points can then be stretched to fit a given geometry. The stretching takes place as if the mesh is made of rubber, and the so-called topology, or form, of the mesh remains the same. Consequently, if we consider any point in the mesh it will be connected to the same neighbouring points both before and after the stretching process. These meshes are called 'structured' meshes as they have a well defined structure, or 'mapped' meshes as they can be seen as a cuboid mesh that has been mapped onto some other geometry.

2. An irregular structure (unstructured)

The points fill the space to be considered but are not connected with a regular topology. The fact that any particular node is attached to an element cannot be known from the form of the mesh, and so a numerical table must exist that describes the arrangement of the mesh by listing which nodes are attached to each element. This contrasts with the regularly structured mesh where knowledge of the location of a cell within the mesh enables the labels of the points at its corners to be found implicitly. A mesh with an irregular structure is often referred to as an unstructured mesh.

When a structured mesh is used there is an advantage in that the solver program should run faster than if an unstructured mesh was used. This is due to the implicit relationship that exists between the number of a cell or a point and the numbers of its neighbours in a structured mesh, which enables data to be found easily. However, unstructured meshing reduces the amount

of time spent generating meshes and can handle more complex geometries (Fluent Inc. Lebanon 2001).

Fluent uses grids comprising tetrahedral, hexahedral, pyramid and wedge cells in 3D. The choice of which mesh type to use depends on the application.

When complex geometries are involved (such as swirl or transition pipe geometries) the creation of structured or block-structured grids consisting of hexahedral elements can be extremely time-consuming. A triangular or tetrahedral mesh can often be created for complex geometries with far fewer cells than the equivalent mesh consisting of hexahedral elements. However, a large aspect ratio in a tetrahedral cell will affect the skewness of the cell, which can impede the accuracy and convergence. In addition, when tetrahedral mesh is used, the flow can never be aligned with the grid. Numerical diffusion is minimised when the flow is aligned with the mesh. Therefore, if it is a relatively simple geometry in which the flow conforms well to the shape of the geometry, a mesh of quadrilateral or hexahedral cells should be used.

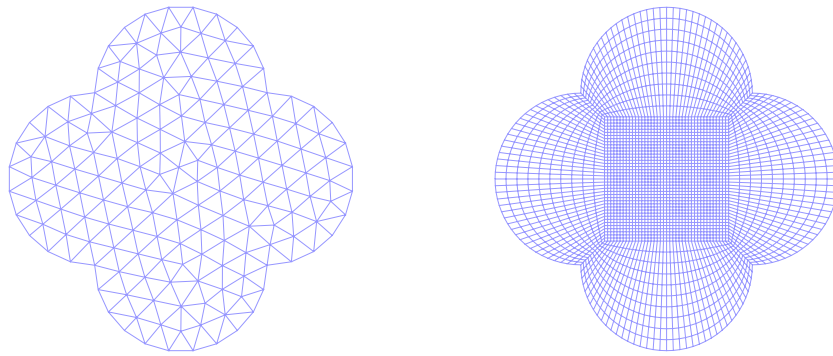
All meshes used in the current work, for all geometries of swirl, transition and circular pipes, comprised of unstructured tetrahedral elements. Although other potentially better meshes using structured hexahedral elements were investigated, an alternative was not found. The problems encountered during the investigations are discussed in the following sections.

4.4.1 Swirl Pipe Mesh

The geometry of the swirl-inducing pipes can involve sharp angles, for example at the intersection of lobes. For this reason a three-dimensional unstructured tetrahedral mesh was used by previous researchers (Ganeshalingam 2002; Jones 2002) as illustrated in Figure 4.8a.

An unstructured hexahedral mesh could not be generated for the swirling flow pipe owing to its high P:D ratio. An attempt was made to create a structured hexahedral mesh (Figure 4.8b). This required the creation of 5 separate volumes for the swirl pipe. However, the swirl pipe mesh thus

created could not be connected to cylindrical pipe mesh, which is an essential step in simulations. The generation of a structured hexahedral mesh using non-conformal meshing in Fluent is currently being investigated by Fokeer (Fokeer 2004a). Non-conformal meshing allows the combination of two different meshes in two separate files into one mesh.

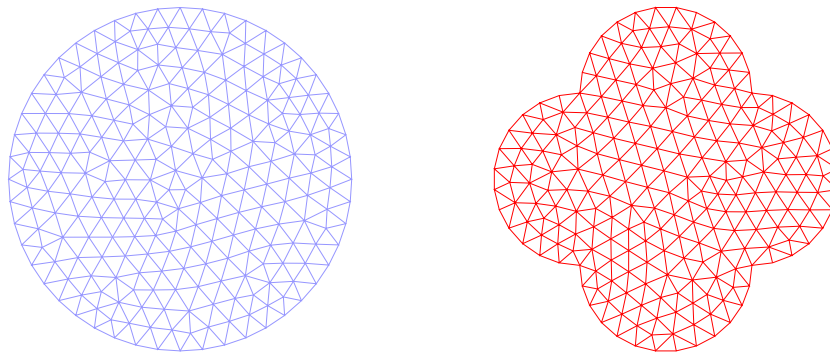


(a) Unstructured Tet Mesh Used (b) Structured Hex Mesh Attempted

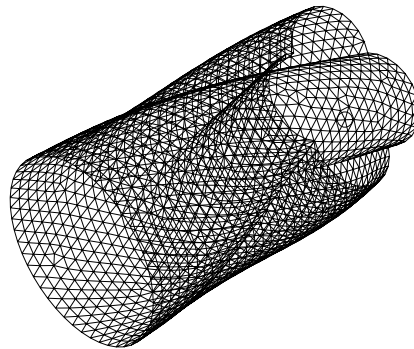
Figure 4.8: Swirl Pipe Meshes Generated in Gambit

4.4.2 Transition Pipe Mesh

The mesh used for a typical entry transition pipe design is shown in Figure 4.9.



(a) Cross-sectional View: Entry (left) and Exit (right)



(b) Isometric View

Figure 4.9: Typical 4-Lobed Transition Pipe Hybrid Mesh Generated in Gambit (interval size (is) 3.3mm)

With the entry transition pipe, grid independence was reached relatively easily with just over 50,000 tetrahedral cells. When the same geometry was used as an exit transition, a much larger number of cells was required to attain grid independence, particularly since the pressure drop result did not stabilize (see Section 4.4.5 on Grid Independence Tests).

To check that this problem was not due to the unstructured mesh used, a structured hexahedral mesh was generated for the transition case using GridGen software (Pointwise Inc., Texas, USA) by Raylor (Raylor 2003). GridGen is a specialist mesh generation software and was not readily available for use in the current research. This mesh was used as a comparison against the unstructured tetrahedral mesh used for the exit transition.

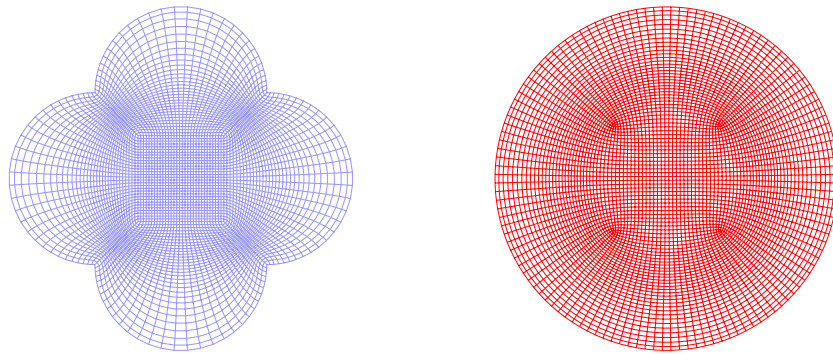


Figure 4.10: Mesh generated using GridGen Software (Raylor 2003) for Exit Transition

The structured mesh had approximately 300,000 hexahedral cells. A grid independence test was not carried out. The tetrahedral mesh used for comparison was a grid-independent case with approximately 200,000 cells.

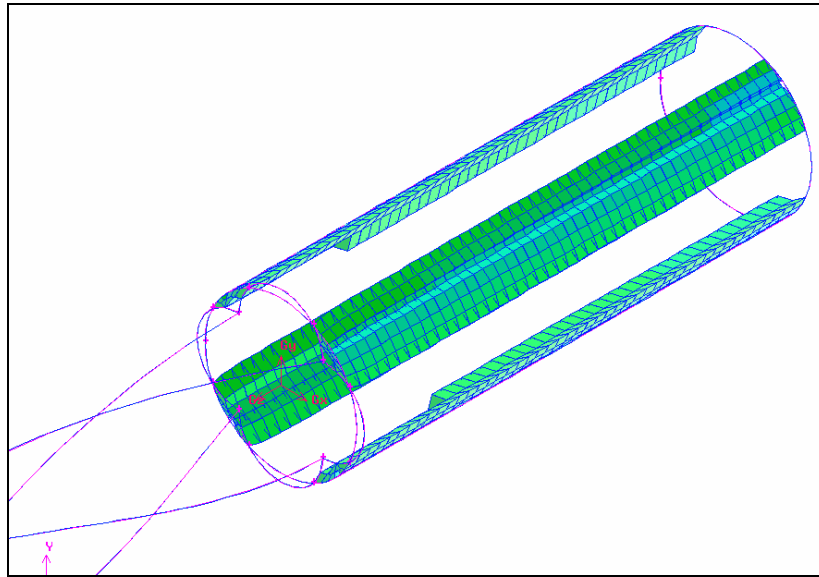
The structured hexahedral mesh gave values of pressure drop and tangential velocity that were 5% and 1% less respectively than the tetrahedral mesh. The difference in the swirl effectiveness was only 0.45% greater in the case of the tetrahedral mesh. The detailed results are given in Appendix A4.4.

4.4.3 Circular Pipe Mesh

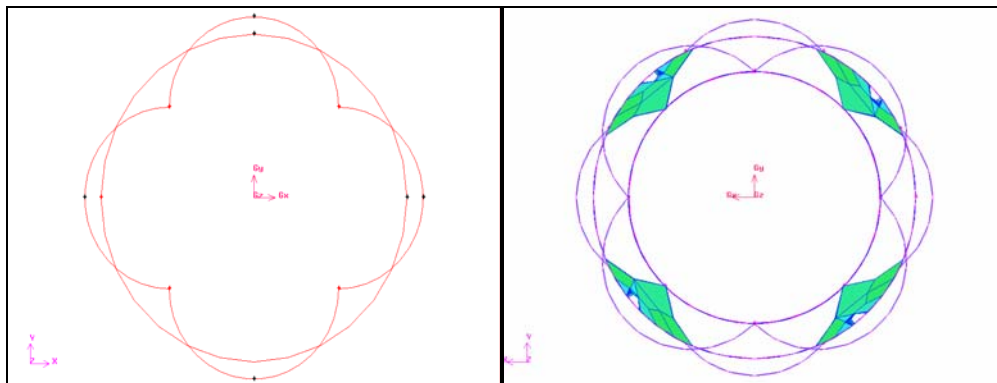
When an unstructured hexahedral mesh was used for the circular pipe, highly skewed cells were obtained at the intersection of the swirl pipe and the circular pipe due to the sharp corners that are introduced by the swirl

pipe (Figure 4.11). Highly skewed cells can decrease accuracy and destabilise the solution.

A structured hexahedral mesh (Figure 4.12) was not successful due to problems with connections to other pipes, as with the structured swirl pipe mesh. Therefore it was necessary to use an unstructured tetrahedral mesh for the simple geometry of the circular pipe as well.



(a) Isometric View



(b) Cross-sectional View

Figure 4.11: Highly Skewed Cells at Pipe Intersection

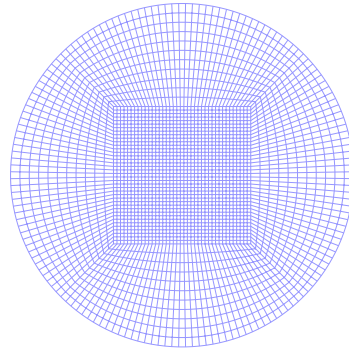


Figure 4.12: Structured Hex Mesh Attempted for Circular Pipe

4.4.4 Examining Mesh Quality

Checking the quality of the mesh is important because properties such as skewness can greatly affect the accuracy and robustness of the CFD solution (Fluent Inc. Lebanon 2001). The following mesh quality-type specifications were checked for all grids generated and the results for the basic geometries are given in Table 4.3.

4.4.4.1 Aspect Ratio

For tetrahedral elements:

$$Q_{AR} = \frac{1}{3} \left(\frac{R}{r} \right) \quad (4.7)$$

Where r and R represent the radii of the spheres that inscribe and circumscribe, respectively, the mesh element

Therefore $Q_{AR} = 1$ describes an equilateral element and the closer the value is to 1 the better.

4.4.4.2 Equi-Angle Skew

A normalised measure of skewness defined as:

$$Q_{EAS} = \max\left(\frac{\theta_{\max} - \theta_{eq}}{180 - \theta_{eq}}, \frac{\theta_{eq} - \theta_{\min}}{\theta_{eq}}\right) \quad (4.8)$$

θ_{\max} = largest angle in the cell

θ_{\min} = smallest angle in the cell

θ_{eq} = angle for an equiangular cell

$Q_{EAS} = 0$ perfect (equilateral)

Q_{EAS} should be ≤ 0.8 for tetrahedral cells for swirl pipe

Q_{EAS} should be ≤ 0.65 for hexahedral cells

4.4.4.3 Volume

This represents mesh quality in terms of mesh element volumes. Rapid changes in cell volume between adjacent cells should be avoided because they translate into larger truncation errors. Truncation error is the difference between the partial derivatives in the governing equations and their approximations.

Table 4.3: Mesh Quality Analysis for a Selection of Geometries

Mesh Analysis Type	4-Lobed Swirl Pipe L = 400mm	4-Lobed β Transition n=0.5, L = 100mm	Circular Pipe L = 200mm	Circular Pipe L = 200mm
Type of elements	Tet, T Grid	Tet, T Grid	Tet, T Grid	Hex, Cooper
Interval size (is), mm	4	3.3	2.4	2.1
No. of elements	93809	41597	220326	52477
Equi-angle skewness: cells within 0-0.65 range	99.5%	99.4%	99.4%	100%
Equi-angle skewness: maximum	0.79	0.79	0.8	0.65
Maximum aspect ratio	3.23	3.25	3.3	2
Volume, mm ³	1.5-21	0.8-13	0.2-6	2.2-11

4.4.5 Grid-Independence Tests

It was important to establish that the results of the simulations were largely independent of the size of the grid. Earlier studies (Ganeshalingam 2002) have indicated that an interval size (is) of 4mm between the cells may be sufficient for the swirl pipe. It would be extremely time-consuming to carry out grid independence tests for each case (or combinations of pipe) studied. Therefore grid-independence tests were carried out on swirl, transition, and circular pipes individually. The tests were carried out based on an interval size of 4mm.

An observation made in all cases of initial grid independence tests was an unexpectedly large change in tangential velocity result within 10mm of the outlet. In addition, negative pressures were reached prior to the outlet

inspite of the 'zero uniform pressure' condition specified. The value of pressure then returned to zero at the outlet.

A possible explanation may have been the specification of "uniform" pressure at the outlet. Outlet conditions where the pressure had been fixed as a constant may be unsuitable for flow if it swirled out through the outlet (as would be the case for swirl and transition pipes).

An attempt was made to rectify this problem using an 'outflow' condition instead of "pressure outlet", whereby Fluent calculated both inlet and outlet pressure (thus not specifying zero outlet pressure). However a similar problem was encountered. It is stated in the Fluent help manuals (Fluent Inc. Lebanon 2001) that the use of pressure outlet condition instead of an outflow condition results in a better rate of convergence when backflow occurs during iteration. Also, previous workers (Ganeshalingam 2002) used pressure outlet, therefore it was decided to continue using pressure outlet boundary condition in all simulations.

Since the problem occurred within 10mm of the outlet, the pipes were extended by 50mm beyond the required length in all simulations so that the discrepancy and the constant pressure specification were further from the area of concern.

In the grid independence tests, the initial grid was refined by approximately doubling the number of elements. The values for pressure, average tangential (w) velocity and swirl intensity were checked. This procedure was carried out until the same trends were observed on examining graphical results. In addition it was ensured that the results between the final grids were converging to a reasonable degree.

The following tables present a summary of the results. In all cases presented, refined grid 1 was chosen as sufficiently grid independent. The percentages shown are a comparison of the value to that obtained from refined grid-2. For detailed results including graphical comparisons, refer to Appendix A4.5.

Table 4.4: Grid-Independence Test for Swirl Pipe

Pipe: 4-lobed, 400mm length

Model parameters: Water only simulation, uniform axial velocity inlet of 1.5m/s

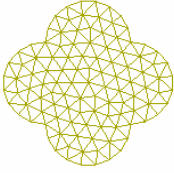
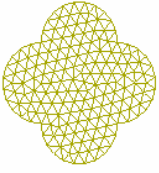
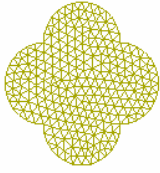
			
	Initial grid	Refined grid-1	Refined grid-2
Total no. of cells	56079	98914	205412
Pressure drop (Pa)	437.86 (+1.74)	426.52 (-0.89%)	430.37
w (tangential) velocity at exit (m/s)	0.2809 (-1.61%)	0.28353 (-0.69%)	0.28549
S, swirl intensity at exit	0.13457 (-2.1%)	0.13673 (-0.5%)	0.13744
Swirl effectiveness	0.34514 (-3.8%)	0.35999 (+0.4%)	0.35863

Table 4.5: Grid-Independence Test for Entry Transition Pipe

Pipe: 4-lobed, beta n = 1 type, 100mm length

Model parameters: Water only simulation, uniform axial velocity inlet of 1.5m/s

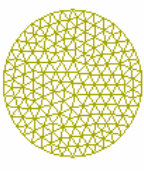


			
	Initial grid	Refined grid-1	Refined grid-2
Total no. of cells	27434	52360	122831
Pressure drop (Pa)	132.8 (+5.72%)	125.05 (-0.45%)	125.61
w (tangential) velocity at exit (m/s)	0.12037 (+0.87%)	0.1202 (+0.73%)	0.11933
S, swirl intensity at exit	0.06751 (+0.8%)	0.0675 (+0.8%)	0.06696
Swirl effectiveness	0.7133 (+19%)	0.60616 (+1.3%)	0.59863

Table 4.6: Grid-Independence Test for Exit Transition Pipe

Pipe: 4-lobed, beta $n = 1$ type, 100mm length

Model parameters: Water only simulation, uniform axial velocity inlet of 1.5m/s, $y+$ (30-60) adaption after 1st order solution and before 2nd order solution

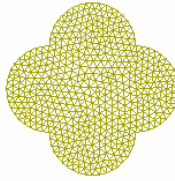
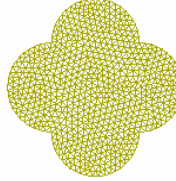
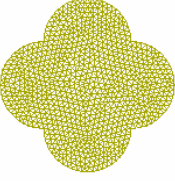
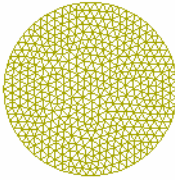
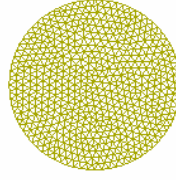
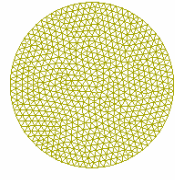
			
	Initial grid	Refined grid-1	Refined grid-2
Total no. of cells	202157	312300	404500
Pressure drop (Pa)	131.08(-3.13%)	132.99 (-1.71%)	135.31
w (tangential) velocity at exit (m/s)	0.09876 (-0.31%)	0.09873 (+0.34%)	0.09907

Table 4.7: Grid-Independence Test for Circular pipe

Pipe: 100mm length

Model parameters: Water only simulation, uniform axial velocity inlet of 1.5m/s, $y+$ (30-60) adaption after 1st order solution, before 2nd order solution

			
	Initial grid	Refined grid-1	Refined grid-2
Total no. of cells	163407	216894	329192
Pressure drop (Pa)	59.02(-4.19%)	60.77 (-1.35%)	61.6

For the entry transition pipe, for example, an initial grid of some 27400 cells (is 4mm) was refined twice by approximately doubling the number of elements. The results in Table 4.5 show the pressure drop, average w velocity, swirl intensity and swirl effectiveness. While the initial grid was in need of further refinement, refined grids 1 and 2 followed the same trends

on examining graphical trends of tangential velocity and pressure. In addition, the differences in values of tangential velocity and pressure between these two grids were less than 1%. Refined grid 1 with an interval size of 3.3 mm was therefore concluded to be sufficient for our investigations on entry transitions.

The need for a much finer mesh for the exit transition than for entry transition (300,000 cells as opposed to 50,000) was interesting. This may be expected because the tangential flows were decelerating and transferring their angular momentum in the exit transition. Perhaps standard wall functions (Section 4.2.3) were not sufficient for such a complex situation.

4.5 The Importance of Velocity Profile

Initial CFD results of pressure drop in circular pipes indicated a significant difference from experimental and theoretically determined values. The reason was that the viscous boundary layer was not fully developed in the CFD simulation. This was rectified by running a simulation over 0.5m of pipe, then using the 'outlet' velocity profile thus obtained as the inlet profile in all cases, thus applying a 'velocity profile'.

Table 4.8: Effect of Velocity Profile on Circular Pipe Pressure Loss

Pipe: 500mm length

Model parameters: Water only simulation, axial velocity of 1.5m/s

Method	Pressure Drop Result, Pa/m
CFD tet cells (no profile)	519.97
CFD tet cells + inlet velocity profile	475.17
Blasius equation	430.73
Colebrook equation	440.83
Experimental result	450.92

It is important to establish a fully developed viscous boundary layer. When this has been achieved, the flow is fully-developed and there is no variation of the velocity profile in the axial direction. This is best explained by an

illustration of the flow with and without the application of a velocity profile (Figure 4.12).

In initial optimisation simulations for transition pipes, an inlet profile was not used. It was not considered necessary since the overall optimisation result would not be affected, though the end values (in pressure and tangential velocity) may vary. Previously, Ganeshalingam did not apply a velocity profile in his optimisation of the swirl pipe geometry either.

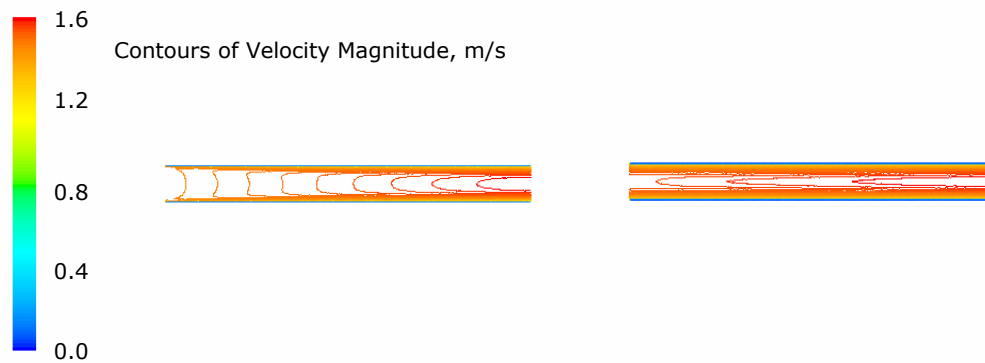


Figure 4.13: Development of Velocity Profile (CMC, $v=1.5\text{m/s}$)
(Figure on the right is with an inlet velocity profile applied)

4.6 Conclusions

- The CFD technique has been described in detail.
- Turbulence is an important aspect of modelling swirling flow. The choice of turbulence model and treatment of near wall flows were important in obtaining accurate CFD solutions.
- The CFD model used has been described including assumptions made and model parameters, and methods used in judging convergence.
- An unstructured tetrahedral mesh was used for all geometries in simulations. However, alternatives were investigated.
- Grid independence tests and mesh quality analyses were carried out for all main geometries.
- The importance of a 'velocity profile' has been highlighted.

CHAPTER 5: OPTIMISATION OF TRANSITION PIPES USING COMPUTATIONAL FLUID DYNAMICS

5.1 Introduction

The parameter used for optimisation of the transition and swirl pipe geometries was 'Swirl Effectiveness'. This parameter is defined and discussed in Chapter 2 (Section 2.3.4). Fluent 6.0.2 was used in all optimisation simulations. The simulations were carried out as detailed in Chapter 4.

It was concluded by previous researchers (Ganeshalingam 2002) that the 4-lobed swirl pipe was more effective at swirl generation than the 3-lobed swirl pipe. Therefore the first task was testing that the superiority of the 4-lobed geometry held for the basic transition design. Once this was proven, all other optimisations (based on transition multiplier and helix) were carried out on a 4-lobed design.

Different transition geometries generated as detailed in Chapter 3 were optimised for use as an entry and an exit to optimised swirl pipe geometry. The entry and exit transition optimisations were carried out separately.

The concept of 'optimisation' was based on indivisible increments of twist. One increment of twist represents the axial displacement undergone before the lobe pattern repeats. Thus a 4-lobed transition pipe will have twisted $\frac{1}{4}$ turn, an angle $\pi/2$ (90°), in one increment of twist (100mm of length for a pipe of pitch:diameter ratio 8:1).

5.2 Comparison of 3-Lobed Transition to 4-Lobed

The first task was comparison and contrast of the 4-lobed transition design to the 3-lobed. Since the 4-lobed swirl pipe produced swirl more effectively

than the 3-lobed, it was expected that the same would hold in the case of transition.

The swirl effectiveness parameter (see Chapter 2, Section 2.3.4 for definition) across the length of an α transition pipe ($n=1$, the very basic design) was calculated from a CFD simulation in both cases. Figure 5.1 illustrates the result obtained. It is clear that, except at a length less than 20mm, the 4-lobed transition design produces more tangential velocity at a lower cost of pressure than the 3-lobed transition.

Therefore further optimisation was carried out on the 4-lobed transition design.

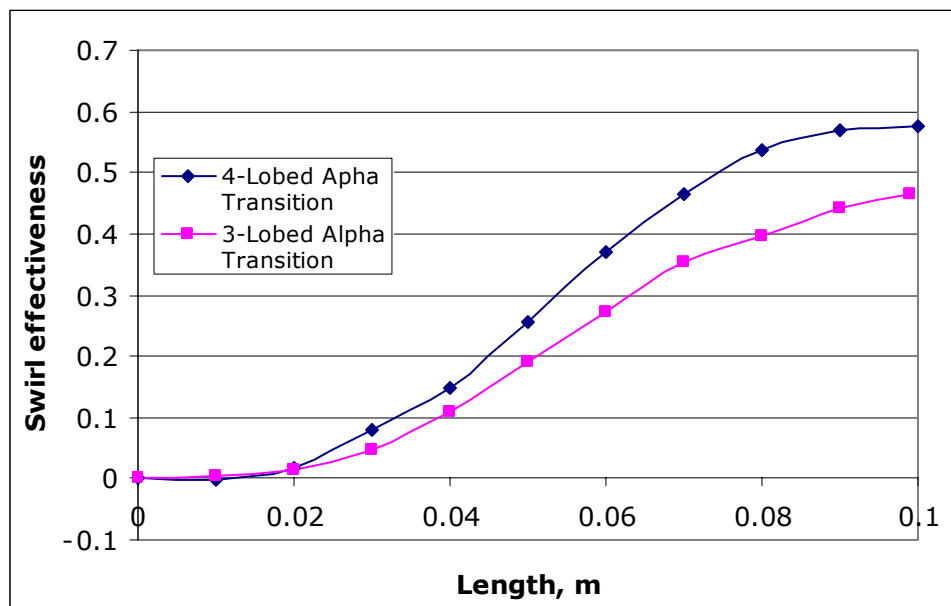


Figure 5.1: Swirl Effectiveness versus Length for 4- and 3-Lobed Alpha Transitions (type $n=1$)

5.3 Comparison of Alpha and Beta Transition Pipe and Swirl Pipe

The next task was determining whether, as predicted, the Beta (β) transition design was an improvement on the basic Alpha (α) transition design (Chapter 3), and how transition pipes compared to the optimised swirl pipe. Table 5.1 summarises a comparison of simulation results for 4-lobed α and β

entry transition ($n=1$) and optimum swirl pipe. The results given are from the exit of each pipe.

As expected, β transition was more effective at swirl induction than α . Its value of swirl effectiveness was 5% greater than that of α . Therefore further optimisation from here onwards was carried out only on the 4-lobed β type transition.

In addition the transition pipes were more effective at swirl induction than the optimised swirl pipe since their swirl effectiveness value was greater. This was because the gradual transition from circular cross-sectional geometry to lobed geometry reduced frictional losses from the pipe walls thereby producing a more efficient swirl induction.

However, the overall tangential velocity produced by the transition pipes was not as high as swirl pipe. As shown from the contours and vector plots of tangential velocity (see Appendix A5.1), swirl was much more developed at the exit of the optimised swirl pipe (0.4m in length) than at the exit of transition pipe (0.1m in length). Therefore its benefits were from use in conjunction with swirl pipe. Transition should be considered as a modification to the swirl pipe.

Table 5.1: Comparison of α and β Transition Pipes ($n=1$) and an Optimised Swirl Pipe (all 4-lobed)

	Swirl pipe	Alpha (α) transition pipe	Beta (β) transition pipe
Length, m	0.4	0.1	0.1
Tangential velocity, m/s	0.284	0.11	0.12
Pressure drop, Pa	426.52	119.42	125.05
Swirl intensity	0.137	0.061	0.068
Swirl effectiveness	0.36	0.58	0.61

5.4 Transition Multiplier Optimisation

5.4.1 Entry Transition Optimisation by Transition Multiplier

Several β transition geometries were produced for different values of transition multiplier, n , as described in Chapter 3. These geometries were then meshed in accordance with grid independence results (Chapter 4) and CFD simulations carried out. A uniform axial velocity of 1.5 m/s was used. The tangential velocity, pressure drop and swirl effectiveness values were calculated for pipes with a range of values of transition multiplier n . The results at the exit are plotted against the n value of the relevant pipe in Figures 5.3 to 5.5.

Figure 5.2 shows the development of tangential velocity along the pipe length for pipes with different n values. As transition multiplier n reduces the rate of tangential velocity generation is greater resulting in a greater final value of tangential velocity at the pipe exit.

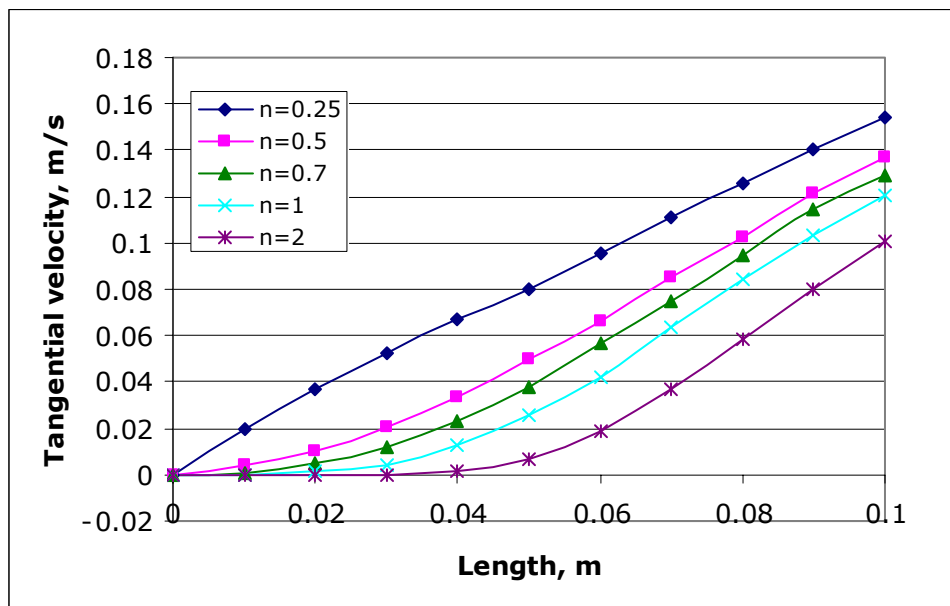


Figure 5.2: Entry Transition Optimisation; Tangential Velocity versus Length for Different Transition Geometries

As shown in figures 5.3 and 5.4, the smaller the value of the transition multiplier n , the greater the tangential velocity generated, however the greater is the pressure loss. The swirl effectiveness parameter is a balance of these two values.

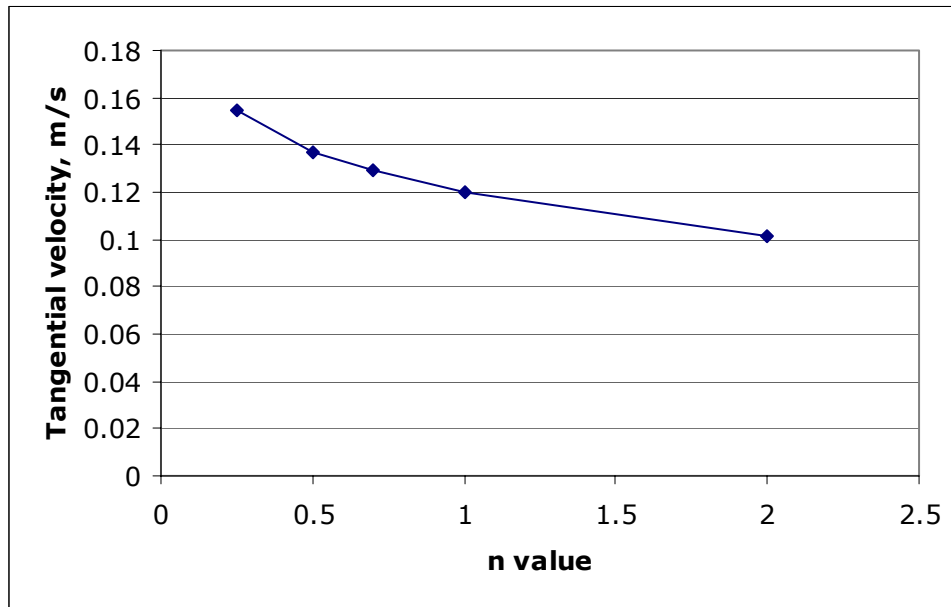


Figure 5.3: Entry Transition Optimisation; Tangential Velocity versus Transition Multiplier n

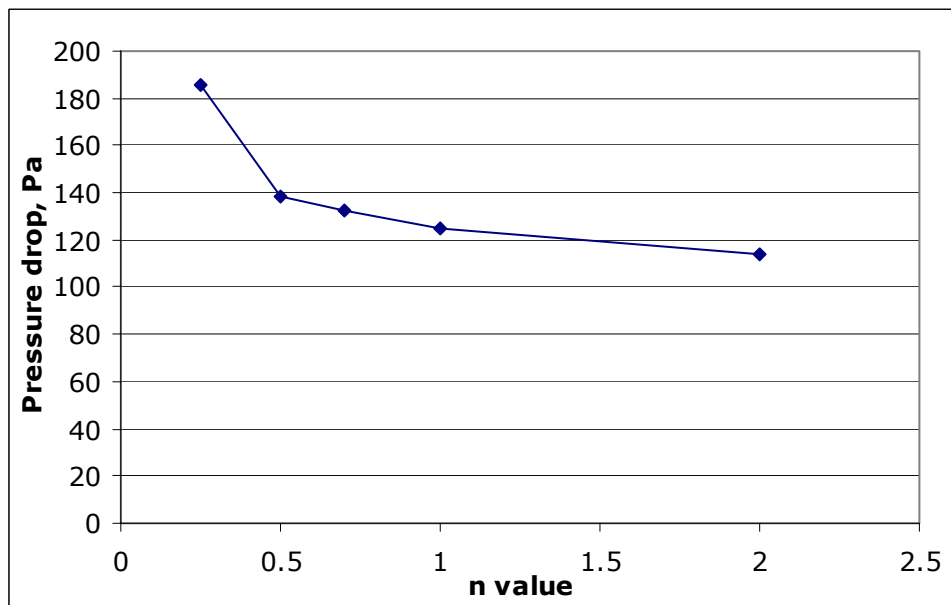


Figure 5.4: Entry Transition Optimisation; Pressure Drop versus Transition Multiplier n

The swirl effectiveness was found to be optimum at a value of $n=0.5$ (Figure 5.5). This is the case where the lobes developed faster in the transition than with the original β transition case of $n=1$ (see Chapter 3).

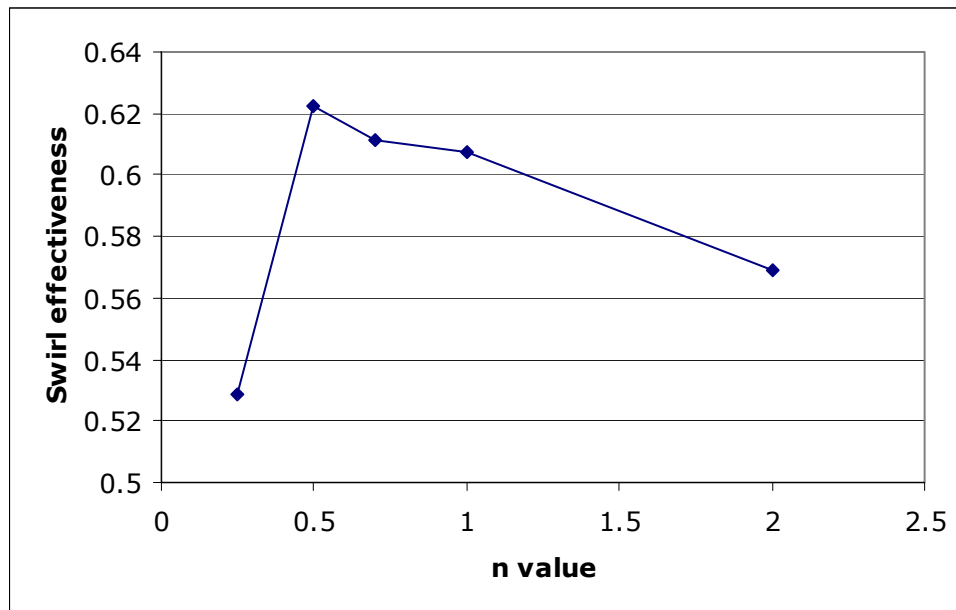


Figure 5.5: Entry Transition Optimisation; Swirl Effectiveness versus Transition Multiplier n

5.4.2 Exit Transition Optimisation by Transition Multiplier

Initially, velocity profiles from a separate simulation of optimised swirl pipe were used at the inlet to the exit transition pipe. However, this resulted in different initial values of velocity for the different cases of exit transition as the simulation progressed, making direct comparison of the different geometries difficult. Therefore combined cases of swirl pipe and exit transition geometry for several different values of transition multiplier were simulated. A uniform inlet velocity of 1.5m/s was used at the entry to the swirl pipe.

Pressure loss, tangential velocity and swirl effectiveness at the exit of the transition have been plotted in Figures 5.6 to 5.8. The same geometry as for entry transition, with multiplier $n=0.5$, was optimum for the exit transition since it gave the maximum swirl effectiveness (Figure 5.8).

Overall trends of pressure drop (Figure 5.6) and tangential velocity (Figure 5.7) with respect to transition multiplier were similar to trends from entry transition.

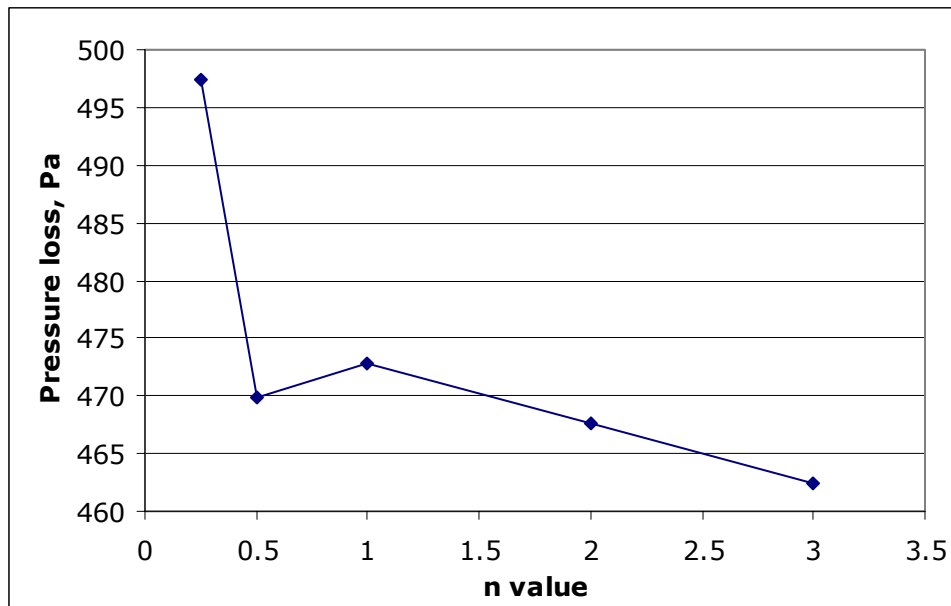


Figure 5.6: Exit Transition Optimisation; Tangential Velocity versus Transition Multiplier n

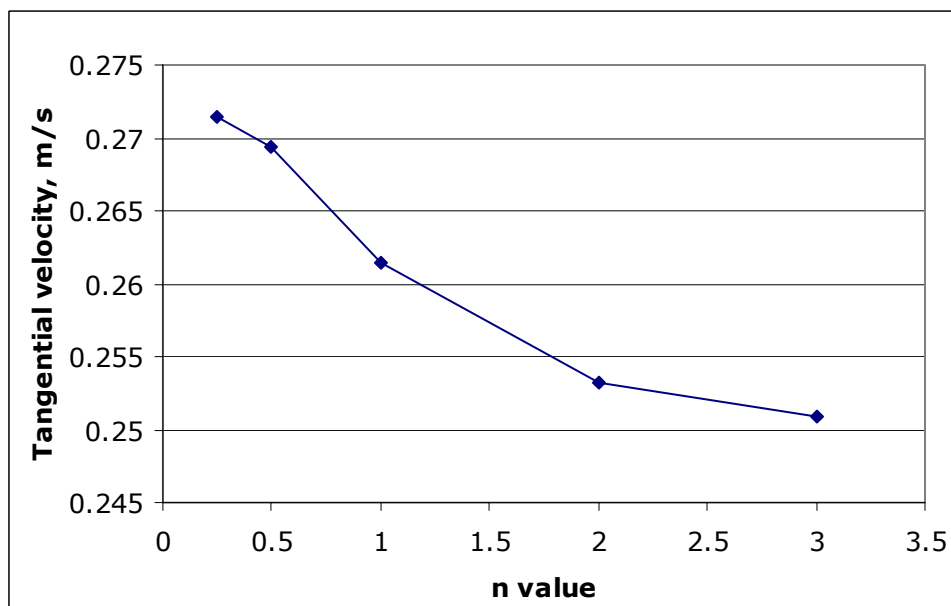


Figure 5.7: Exit Transition Optimisation; Pressure Drop versus Transition Multiplier n

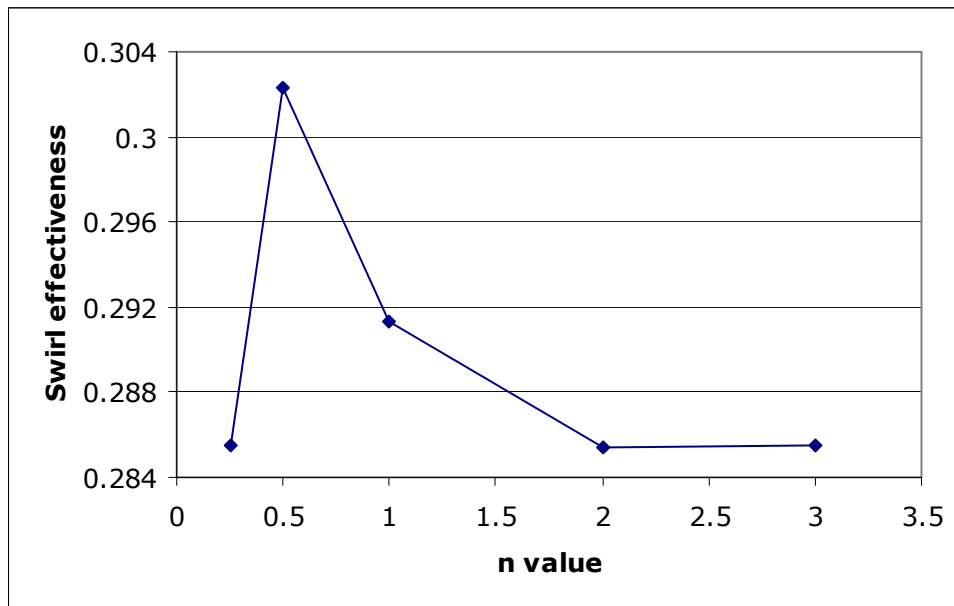


Figure 5.8: Exit Transition Optimisation; Swirl Effectiveness versus Transition Multiplier n

5.5 Variable Helix Optimisation

The optimum entry transition case (4-lobed β , $n=0.5$) was then used for optimisation with regards to the helix. The variable helix applied is described in Chapter 3.

As the t value, and thereby the helix increased, the tangential velocity generated (Figure 5.9) increased together with the pressure drop (Figure 5.10)..

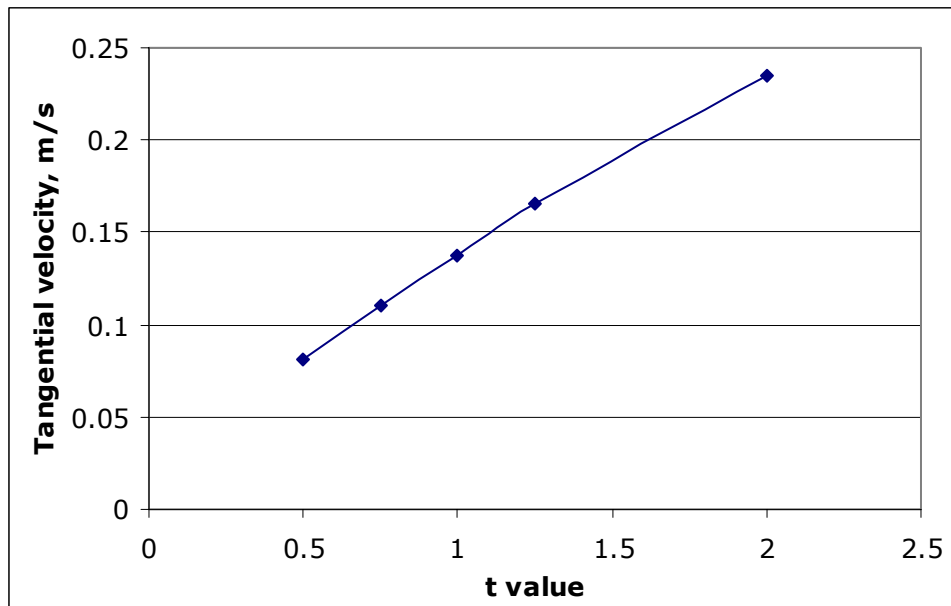


Figure 5.9: Entry Transition Optimisation; Tangential Velocity versus t Value

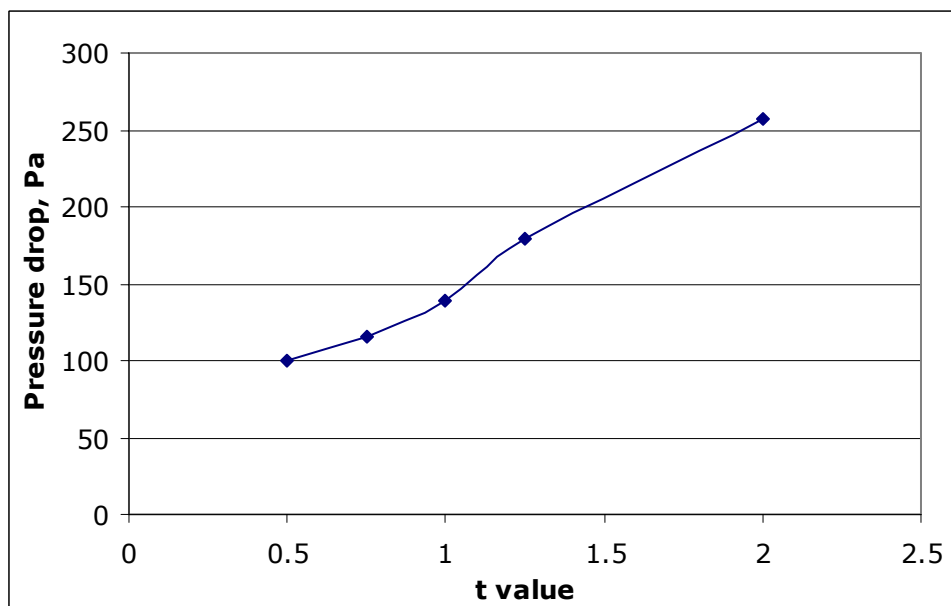


Figure 5.10: Entry Transition Optimisation; Pressure Drop versus t Value

The graph of swirl effectiveness, Figure 5.11, shows that the geodesic helix (regular helix with t equal to unity) was optimal as opposed to a variable helix for the cases studied. It must however be borne in mind that this is the optimum based on the criterion of 'swirl effectiveness'. It may be that swirl effectiveness, as defined in Equation 2.16 in Chapter 2, may be putting too much emphasis on reducing pressure loss. For some applications, a higher cost in terms of pressure loss across the swirl-inducing pipe may be acceptable to gain greater swirl intensity

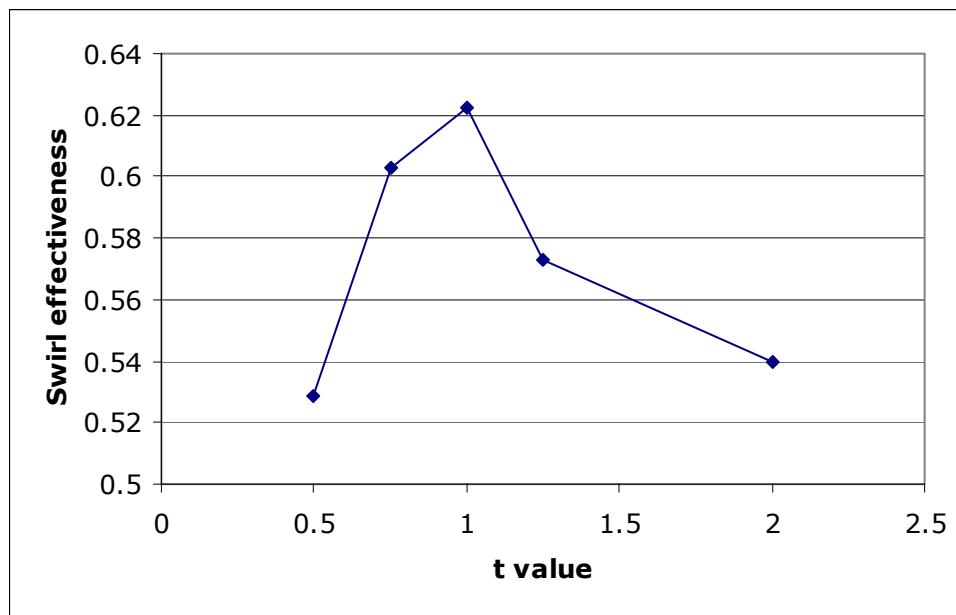


Figure 5.11: Entry Transition Helix Optimisation; Swirl Effectiveness versus t Value

5.6 Advantage of using Entry Transition

Standard wall functions with grid adaption at the walls for turbulence were used. The cylindrical pipe was specified a roughness of $1.89 \times 10^{-08} \text{m}$ and the transition pipe of $2.09 \times 10^{-06} \text{m}$. These were roughness values experimentally measured using a Taylor Hobson Talysurf machine (procedure was carried out by the School of Mechanical, Materials and Manufacturing Engineering). This is a contact method using a stylus whereby the vertical deviations when traversing the surface are measured and a mean deviation from the average line over a surface is reported. The geometry used in the simulation was as illustrated in Figure 5.12. The results given are for a near-optimum transition case (β transition $n=1$, geodesic).

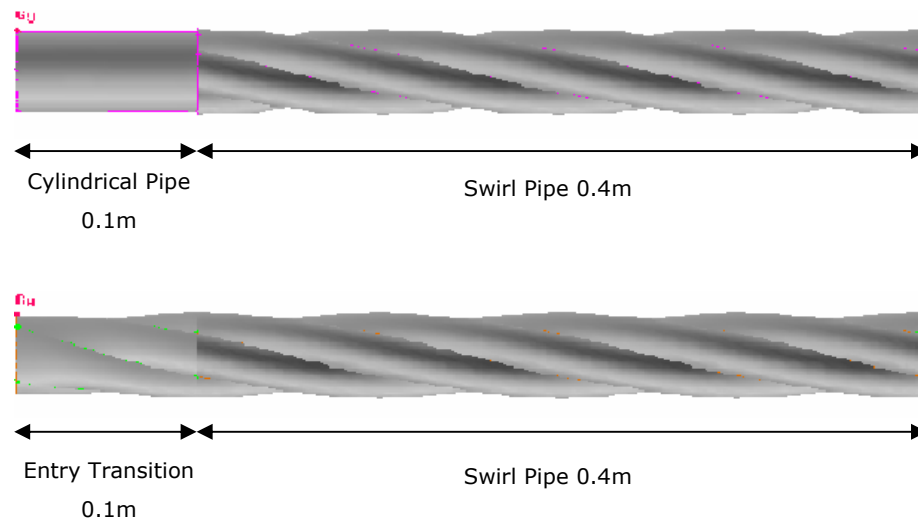


Figure 5.12: Simulation Geometry for Effect of using Entry Transition in place of Cylindrical Inlet Pipe

Figure 5.13a shows that, with entry transition, initial pressure loss was greater due to the lobed geometry of the transition as opposed to the smooth walls of the cylindrical pipe. However at the joint to the swirl pipe there was a smooth transition of flow from one pipe to the next and the sudden loss that results due to sudden change in cross-section was avoided. Therefore post-transition pressure loss remained substantially lower than with cylindrical pipe.

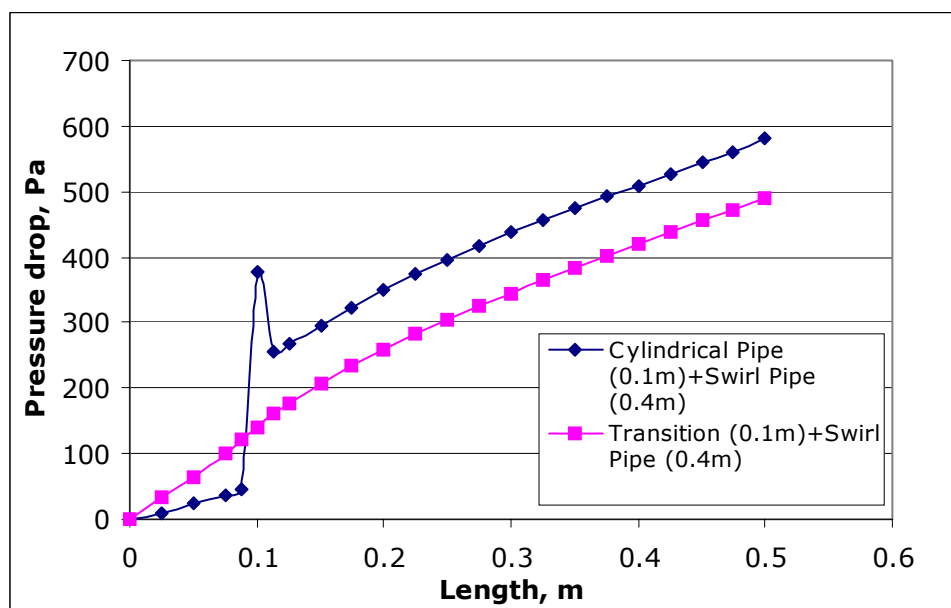


Figure 5.13a: Effect of using Entry Transition in place of Cylindrical Pipe; Pressure Drop versus Length

In addition, Figure 5.13b shows that the transition generated an initial high tangential velocity which continued inside the swirl pipe. With cylindrical pipe inlet the tangential velocity is negligible until the entry point of the swirl pipe (0.1m length) where there is a high rate of tangential velocity generation. However, the tangential velocity with cylindrical pipe inlet remains lower than that with entry transition.

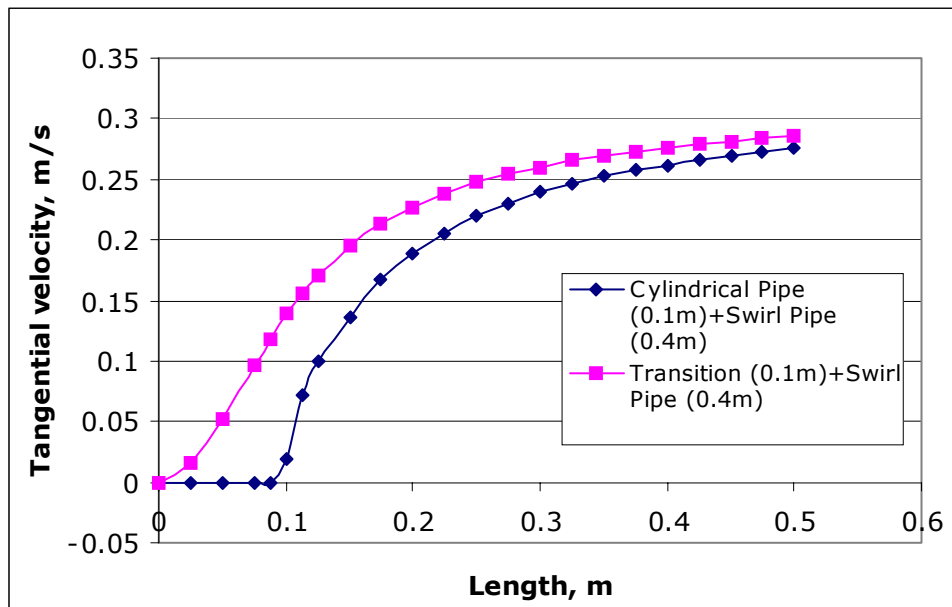


Figure 5.13b: Effect of using Entry Transition in place of Cylindrical Pipe; Tangential Velocity versus Length

Inclusion of transition increased the tangential velocity at the exit of the swirl pipe and reduced the pressure drop from entry losses. The overall effect was greater swirl effectiveness as illustrated in Figure 5.13c. Also the length of swirl pipe required to achieve a certain tangential velocity was less when the transition was incorporated at the start.

It is also evident that the swirl pipe was restricting the tangential velocity generated by the transition pipe from the negative slope in Figure 5.13c. It may be worth investigating changing the pitch of the swirl pipe along its length to sustain the additional swirl generated by the entry transition.

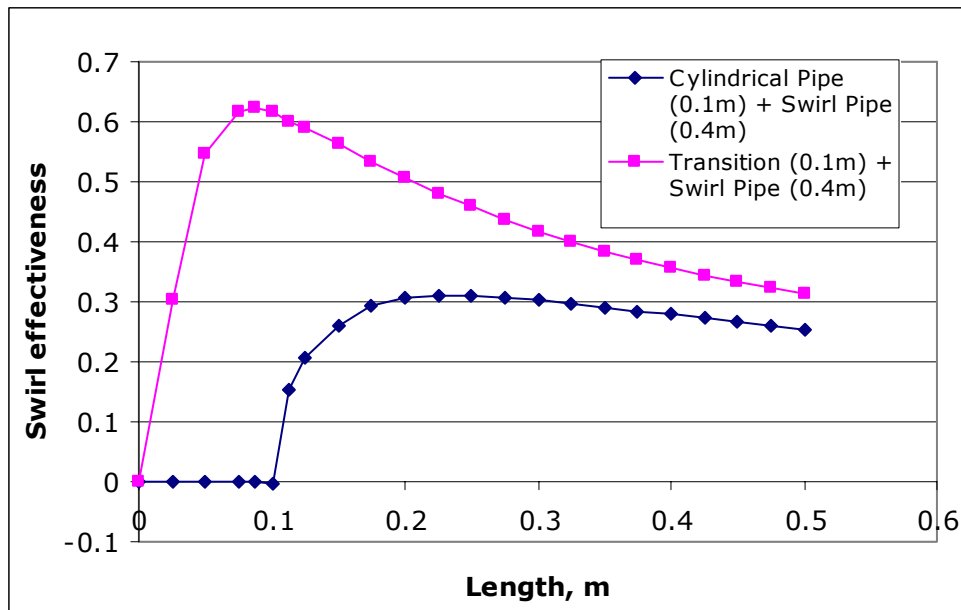


Figure 5.13c: Effect of using Entry Transition in place of Cylindrical Pipe; Swirl Effectiveness versus Length

5.7 Advantage of using Exit Transition

The flow parameters used were as detailed in Section 5.6. The results given are for a near-optimum case of exit transition pipe. The simulation geometry is illustrated in Figure 5.14.

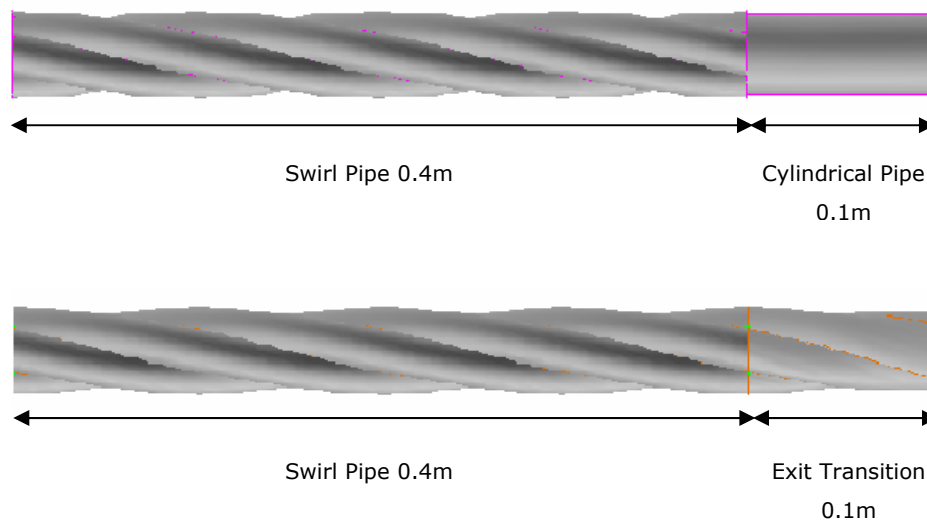


Figure 5.14: Simulation Geometry for Effect of using Exit Transition in place of Cylindrical Exit Pipe

The tangential velocity was almost equivalent with cylindrical exit pipe and exit transition as shown in Figure 5.15a. There is a sudden decrease and

increase of tangential velocity at the joint of the swirl pipe to exit cylindrical pipe. This was due to disturbance of the flow caused by the sudden cross-sectional change in transferring from swirl pipe to cylindrical. The tangential velocity dissipates quicker within the cylindrical pipe than in the exit transition thus resulting in a slightly greater tangential velocity at the exit of the transition.

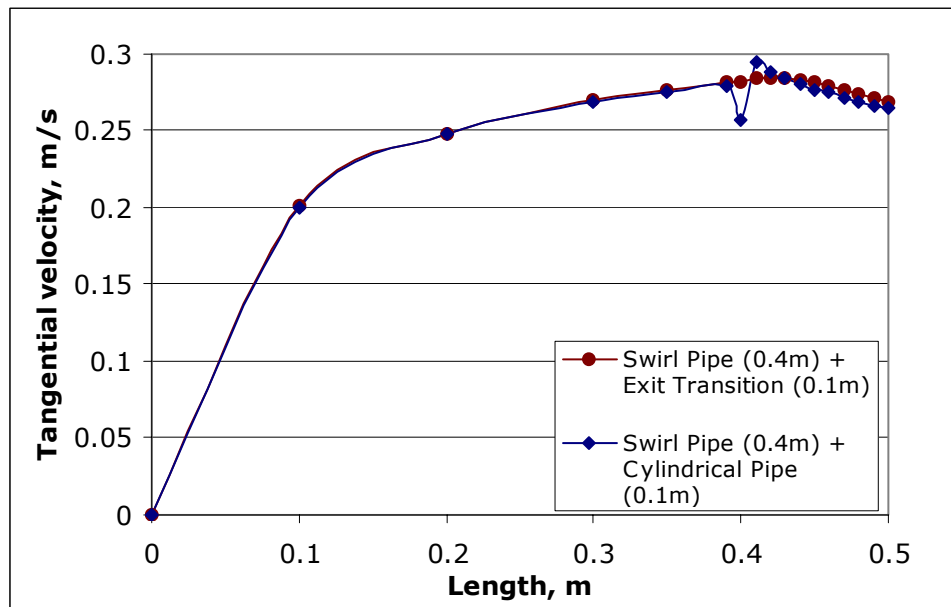


Figure 5.15a: Effect of using Exit Transition in place of Cylindrical Pipe; Tangential Velocity versus Length

The main advantage gained was through a reduction in pressure loss as shown in Figure 5.15b. Once again, exit losses from sudden cross-sectional change were reduced when exit transition was used.

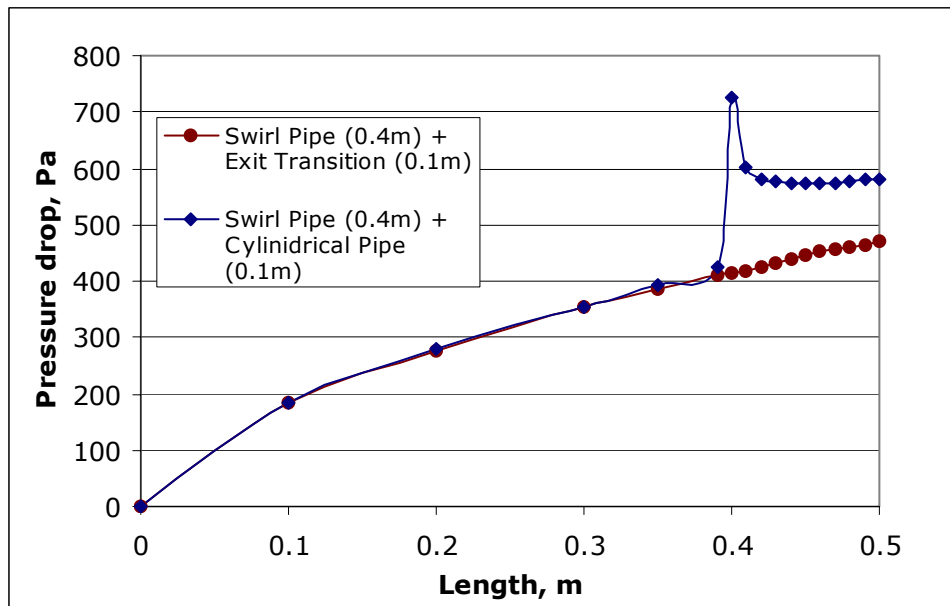


Figure 5.15b: Effect of using Exit Transition in place of Cylindrical Pipe; Pressure Drop versus Length

5.8 Conclusions

- The 4-lobed transition geometry was found to be more effective at swirl generation than the 3-lobed in agreement with results from swirl pipe optimisation carried out by Ganeshalingam.
- Entry transition geometries were more effective at swirl generation than the swirl pipe itself and should be considered as a modification to the optimised swirl pipe.
- 4-lobed β transition with transition multiplier $n=0.5$ was optimum in both cases of entry and exit transition from several geometries tested.
- The variable helix studied was not as effective as the geodesic when tested for an entry transition.
- Entry transition increased swirl generated at the exit of the swirl pipe and reduced pressure losses.
- Exit transition reduced exit pressure losses and showed a very small increase in swirl generated. It may also reduce initial swirl decay (see Chapter 7).

CHAPTER 6: EXPERIMENTAL FLOW LOOP

6.1 Introduction

The existing Perspex flow loop used by both Raylor (Raylor 1998) and Ganeshalingam (Ganeshalingam 2002) was used with very few modifications. This flow loop was used because it allows for easy flow visualisation and also for direct comparison of results that have been previously obtained by the above authors. Experimental work was carried out with and without swirl and transition pipes on the top horizontal section of the rig. The variables measured were pressure losses and swirl decay length at varying flow rates and slurry concentrations. A range of different solid densities was used.

In all experimental work carried out by Ganeshalingam and Raylor (Raylor 1998; Ganeshalingam 2002) on *Swirly-Flo* pipes, the equivalent diameter of the swirl pipe used was slightly smaller than that of the test loop. The smaller cavity through the swirl pipe may have acted as a constriction and resulted in higher pressure drop and impact velocity. This may be eliminated by experimenting with swirl pipe of different diameters. In the first instance it is important to use a swirl pipe that has the same flow area as the test loop, thereby retaining continuity of the flow. In all the experiments in this thesis a swirl pipe of equivalent cross-sectional area to that of the test loop has been used.

It was also noted that it may be beneficial to have a transition geometry prior to, and following the swirl pipe. However the transition section would have to be short and effective. Otherwise it will increase overall pressure drop and, in the case of exit transition, may decrease swirl intensity. Such transition geometries were designed and produced as detailed in Chapter 3. The purpose of the experimental work was the validation of CFD results that have been the basis for the optimisation of these geometries and the examination of the effect of presence of solids that cannot yet be fully tested with CFD technology.

A flow velocity in the range of 1 to 2.25 m/s was used in the experimentation. The flow velocity generally in use in industry is 2 to 3m/s. However, at high velocities swirl may cause particles to be thrown outwards towards the walls. Swirl also has the effect of lowering the required velocity to transport a given slurry as detailed in Chapter 2. Therefore benefits from swirl are accrued at lower velocities.

6.2 Perspex Rig Layout

The layout of the rig is shown in Figure 6.1. It is described in detail by both Raylor and Ganeshalingam (Raylor 1998; Ganeshalingam 2002). The pipes were clear acrylic with an internal diameter of 50mm.

All measurements of pressure and flow visualisation were carried out on the top horizontal section of the rig of length 6.44m. The pressure tappings were moved from the configuration shown by Ganeshalingam in Figure 6.1. P7 was moved further away from the bend (2m away from the bend) to avoid bend effects (Azzi 2000; Azzi 2002) and P8 was moved further from the tank (1.2m away from tank) to avoid negative pressures that were observed at the vicinity of the tank. The current induced by the pressure transducers and electromagnetic flow meter were fed to a PC.

Some of the main concerns with regards to making online measurements within slurry pipeline have been discussed by Aude (Aude 1971):

- Wear may affect the measuring elements
- Plugging of the sensing element can occur
- Segregation of a slurry in the element

To avoid pressure taps from plugging, the use of a diaphragm close-mounted to the pipe has been recommended. This separates the slurry from the pressure sensor. The pressure transducers on the rig used for the experimental work in this thesis were mounted 'recessed' to the pipe. This prevented any direct wear or plugging from the solids. However, it should be noted that a 'flush' arrangement is perhaps better because that would ensure contact with the slurry flow. Aude also states that transmitters or gauges should not be mounted on the piping around positive displacement

pumps, because they will often fail from the vibration. This may explain the failing of the transmitter closest to the pump on the rig used in experimental work.

Heywood (Heywood 2003) states that some transducers are sensitive to swirl and care must be taken when positioning such transducers downstream of a bend or special swirl inducers. It was ensured that pressure transducers on the rig were not placed immediately before or after the swirl inducing pipes. All pressure tapings were therefore placed within cylindrical pipes and at a length of more than 1m away from swirl inducing pipes.

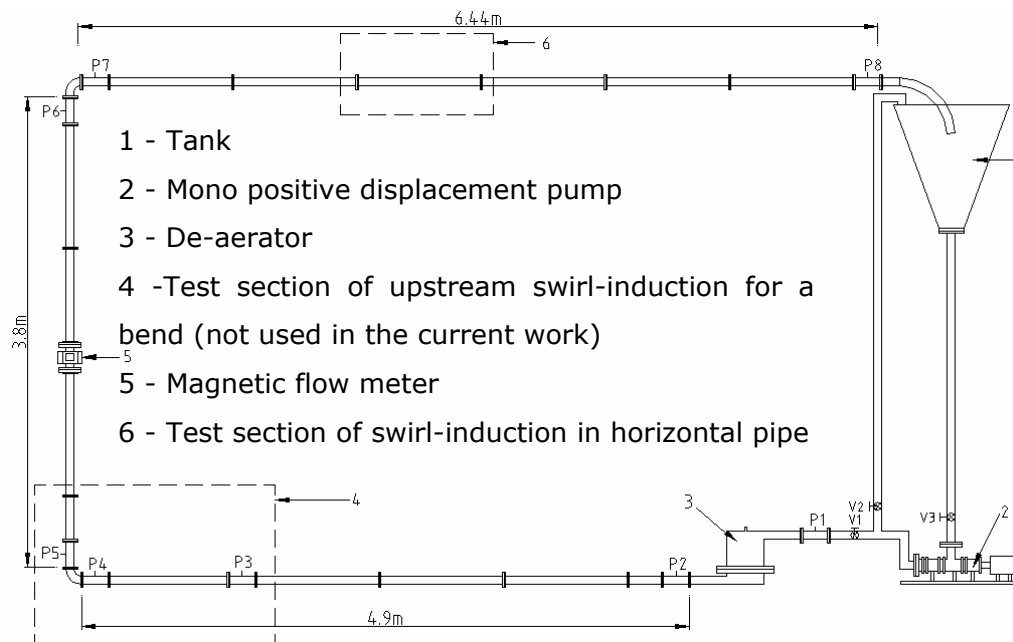


Figure 6.1: Schematic Diagram of Perspex Rig (After Ganeshalingam (Ganeshalingam 2002))

Calibration of the pressure transducers was carried out by measuring a constant head of water over the transducers and then calculating the theoretically expected pressure which was compared to the transducer value (figures 6.2 and 6.3). Next the parameter used for calculating the scaled value of pressure from the raw data in the PC was changed to display the theoretically expected pressure.

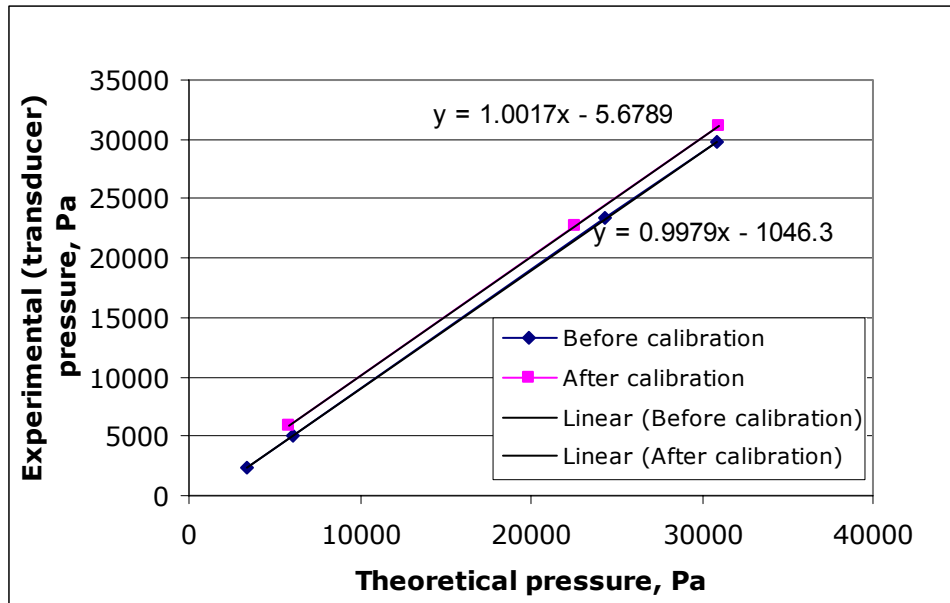


Figure 6.2: Pressure Transducer Calibration- Transducer P7

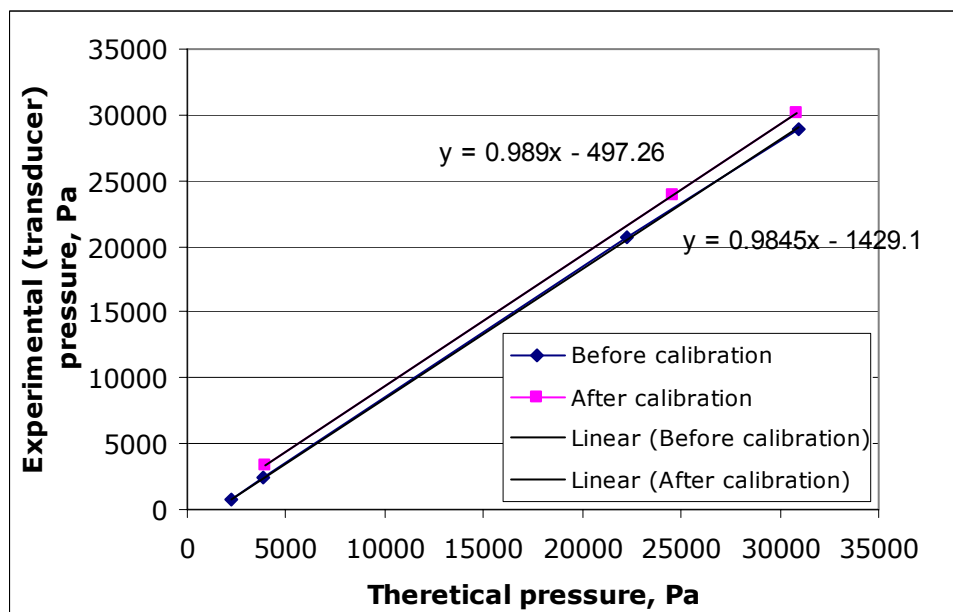


Figure 6.3: Pressure Transducer Calibration- Transducer P8

The pressure transducers required constant re-calibration. Therefore it was decided, in addition, to use an inverted manometer which was open to the atmosphere. Manometers are very simple and require no calibration. Flexible tubes from the manometer were attached to the existing pressure transducer tappings as shown in Figure 6.4. The pressure head on each manometer leg was read off a centimetre scale placed beside them. The eye

was kept in level with the bottom of the meniscus and the lowest point of the meniscus read to the nearest mm.

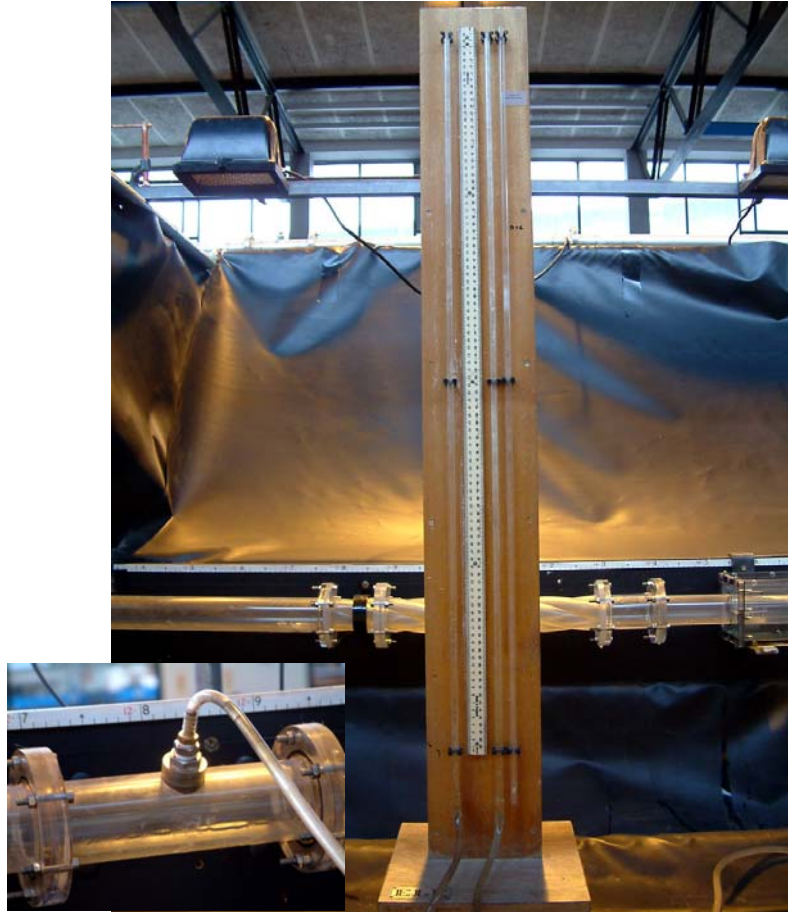


Figure 6.4: Manometer used on the Rig

There was also slight drift in the flow meter calibration. The flow meter was recalibrated by estimating the actual flow from water collected at the exit to the tank. The procedure is detailed in Appendix A6.1.

6.3 Particle Analysis

Previously, plastic cylindrical beads were used in swirl pipe tests by Ganeshalingam (Ganeshalingam 2002) and Raylor (Raylor 1998), and sand and magnetite were used by Tonkin (Tonkin 2004). The pump on the current rig could not support material as crude as sand, magnetite and coal. Therefore it was initially planned to use the plastic beads as used by Raylor and Ganeshalingam.

The plastic beads previously used had clearly been flattened in the rig and their effective density was changed from the original. Relative density was previously reported to be about 1.45 by Raylor (Raylor 1998) using a float and sink analysis with sodium polytungstate solution. However, using the same density analysis technique, it was measured to be about the same as water in new (unused) condition and about 1.3 in used condition. The density analysis is described in Appendix A6.2. In addition the flattening by the pump will cause changes in size, volume and shape. Therefore beads identical to previous researchers could not be used.

Density tracers provided by Partition Enterprises Ltd. were identified as an alternative. Particles of several densities representing common industrial slurries were selected. Relative densities (RD) of 1.4, 2.7 and 4.5 were chosen to represent coal, quartz and a metal ore.

All the tracers were within ± 0.05 of the nominal value of density and irregularly shaped. They were non-magnetic and non-fluorescing in the sieve size range 2.00 to 3.15 mm. They were coloured red, blue and yellow to indicate density. No leaching of the pigments and dyes was expected.

During the experimental trials breakage of the tracers from the mono pump was observed. This was to be expected with the use of any type of positive displacement pump. A centrifugal pump may have been a much better choice in this case but one was not immediately available.

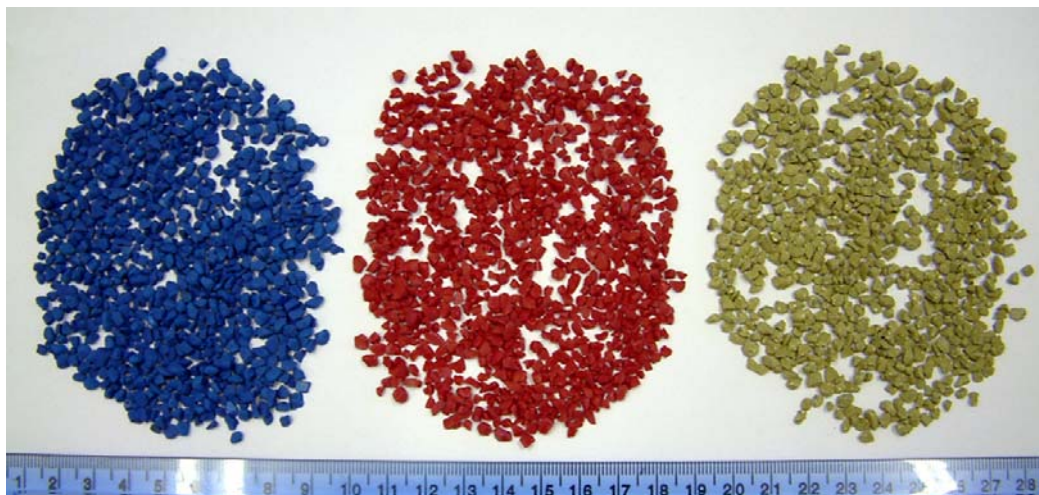


Figure 6.5: Density Tracers used in Slurry Tests; Red, RD 1.4, Blue, RD 2.7 and Yellow, RD 4.5

Low volume concentrations of solids (2-6% w/w) and low velocities (1-1.75m/s) were used in rig tests incorporating solids to reduce breakage. Particle size analysis was carried out on the solids prior to and after each test run (see Appendix A6.3) and the fines removed before the next series of tests.

6.4 General Operational Procedure

230l of water was used in all tests with an approximate tank fill level of 160l. Once the rig was filled with water, the pump was started and the velocity increased gradually using a pump inverter. The rig was then allowed to run at maximum velocity for five minutes to expel any air bubbles that may have formed, especially near the pressure tapplings. When manometers were in use, the flexible tubes of the manometers were examined for air bubbles and any remaining air bubbles were drawn out.

The flow velocity was then lowered and all readings taken on an up-curve of velocity (at increasing velocities- see Tonkin (Tonkin 2004)). Where solid particles were used, they were slowly added to the open tank. Although particles will be better distributed when added at high flow velocities, this results in a high level of breakage at the start of the test. An interval of about 3 minutes was allowed between adding the solids and taking readings. In addition, a short interval (about 2 minutes) was allowed before readings were taken whenever velocity was changed. Long intervals were avoided to prevent particle breakage. In tests involving water alone, the time lapses between readings were much longer (5-10 minutes) to allow the flow to settle and reach steady state.

Flow rate and pressure transducer data were collected using a Lab View-controlled data acquisition system. Following on from Tonkin (Tonkin 2004), over 1600 data points were collected for each test at a rate of 5 readings per second. The standard error in the flow meter reading was estimated to be less than 0.2% in all experiments. Where manometer readings of pressure were recorded, an average value was estimated over a period of about 1 minute. The standard error in manometer pressure measurement was in the range of 0.3 to 4% for water only tests (see Appendix A7.1), with

a value generally less than 1% at flow velocities greater than 1m/s. For solids tests the standard error in manometer reading was mostly in the range of about 0.6 to 8%. The high error with the incorporation of solids was due to high solids concentration variation in the rig.

Two types of swirl decay lengths were estimated visually as:

1. Distance when particles are just beginning to settle (L)
2. Distance when particles are visibly settled (L_1)

Solids distribution up to 20 pipe diameters downstream of the swirl and transition pipes was photographed using three digital cameras in series as shown in Figure 6.6. The cameras were operated simultaneously using a remote control system. The three resulting digital images were merged using Adobe Photoshop 7.0 (Adobe Systems Incorporated, San Jose, CA, USA) to produce one single montage of the pipe section.



Figure 6.6: Set-up of Three Digital Cameras for Photographing Solids Distribution

The delivered solids concentration was measured by collecting samples of the slurry at the exit to the tank. Approximately 20l of slurry were collected using buckets. The slurry weight, solids only weight (after draining the water

and drying at room temperature), and the weight of the buckets were measured to estimate the solids concentration by weight and volume.

At the end of each test, solids were removed with the use of a sieve at the exit to the tank. The pump speed was gradually lowered and drain valves from the pump and de-aerator were opened. The solids were allowed to air-dry at room temperature before re-use.

CHAPTER 7: VALIDATION OF COMPUTATIONAL FLUID DYNAMICS RESULTS

7.1 Introduction

The main variables of importance in CFD simulations were pressure drop and tangential velocity since these are the parameters that determine swirl effectiveness. Experiments were carried out on the pipe rig with several combinations of cylindrical, swirl and entry transition pipes in order to obtain pressure drop and tangential velocity results to validate CFD simulation results.

Pressure drop was initially measured using piezo-resistive pressure sensors. However, the calibration of these sensors changed rapidly and it became necessary to re-calibrate them regularly. Therefore the utilisation of an inverted manometer was necessary in subsequent tests. This provided more accurate pressure drop results.

Particle Image Velocimetry (PIV) was used in an attempt to measure tangential velocity at the exit of the swirl and transition pipes. However, a different set-up was used from previous researchers and the attempt was unsuccessful. Tangential velocity results from CFD simulations have been validated using PIV results obtained by Tonkin (Tonkin 2004; Jones 2004b).

7.2 Background to CFD Verification and Validation

The terms 'verification' and 'validation' have been defined by various authors (Oberkampf 1998; Roache 1998; Stern 2001; Grace 2004). In the simplest terms, verification is solving the equations right and validation is solving the right equations.

Thus verification deals with the accuracy of the solution of the assumed mathematical model while validation deals with the accuracy of the solution as it relates to the real world, i.e. experimental data.

Verification is a mathematical or computational issue addressing the correctness and functionality of the computations themselves. Validation involves a process of assessing simulation modelling uncertainty by using benchmark experimental data and, when conditions permit, estimating the sign and magnitude of the modelling error itself.

Minimum requirements for validating are as follows (Stern 2001):

- The model has been applied to a broad spectrum of conditions and variables.
- Predictions have been compared with an extensive array of experimental data.
- The model and experimental results used in the comparison are independent of each other, i.e. the experimental information has not been used for 'calibration' of the model. It is not the best fit amongst a pool of data.
- Differences between the model predictions and the experimental data have consistently satisfied pre-set tolerances or standards.

Experimental errors and uncertainties should be estimated and avoided where possible and may be either random or systematic. Random errors can be readily estimated by carrying out replicate tests, for example, the scatter in the measurement of pressure can be reduced by taking many readings. Bias or systematic errors are much more difficult to quantify. They arise from a number of different factors, for example, errors in calibration of instruments, damping of signals, etc.

Sources of numerical errors can be grouped into four broad categories (Oberkampf 1998):

1. Physical modelling errors- subdivided into three categories
 - a. Partial Differential Equations (PDE) describing the flow: turbulence modelling is the single most important limitation to obtaining

accurate simulations to many flows, the other is steady state assumption

- b. Auxiliary (closure) physical models: use of wall functions to remove the requirement of a fine grid near the walls
 - c. Boundary conditions for all of the PDEs: for example, inaccurate representation of the wall geometry where physical hardware has not been accurately fabricated
2. Discretization errors- those caused by the numerical replacement, or discrete mapping of the PDEs, the auxiliary physical models and the continuum boundary conditions, into algebraic equations
- a. Spatial and temporal resolution: also referred to as truncation error and is due to finite resolution in the spatial and temporal discretization
 - b. Over-specification of the boundary conditions which can cause divergence of the iterative or temporal solution
 - c. Under-specification of the boundary conditions which will cause the solution not to converge or to converge to different solutions depending on initial conditions, grid size, relaxation parameters, etc.
 - d. Discrete solution or iterative convergence error: the difference between the exact solution to the discrete equations and the approximate, i.e. computer, solution obtained
 - e. Programming errors
3. Computer round-off errors: due to the finite precision of the computer

Sharing the code with other users can test and increase confidence in the code (Grace 2004). This can be achieved by using commercially distributed and widely spread CFD software such as Fluent. This also gives repeatable and comparable results.

7.3 Pressure Drop Validation

7.3.1 Cylindrical Pipe

An initial comparison was made between experimental pressure drop for cylindrical pipe and CFD and theoretically calculated pressure drop. The pressure drop across 3.11m of cylindrical pipe was measured using piezo-

resistive pressure sensors. The measurements were later repeated with a manometer. The results have been compared to the expected pressure drop from the Colebrook equation, the Blasius equation and CFD simulation.

For the CFD simulation a tetrahedral mesh was used for cylindrical pipe of length 0.5m. Velocity profiles were applied at the inlet to simulate fully developed flow thereby ensuring that the viscous boundary layer is developed. $k-\epsilon$ model of turbulence was used. An experimentally measured pipe roughness of $1.89 \times 10^{-08} \text{m}$ (see Section 5.6, Chapter 5) was applied.

The pressure loss results in Table 7.1 and Figure 7.1 are presented per unit length. Therefore the total pressure loss measured in all cases was divided by the length of pipe employed to obtain units of Pa/m.

In CFD and theoretical pressure loss estimates exact values of flow velocities of 1.0, 1.25, 1.5, 1.75, 2.0, 2.25m/s were used. In experimentation it is difficult to attain these exact flow velocities. Therefore the experimental pressure losses at the above exact velocities were estimated by fitting a quadratic to the experimental data points. This procedure is detailed in Appendix A7.1. This also facilitated the estimation of experimental pressure losses from transition and/or swirl pipe only (where pressure loss was measured across a combination of swirl and cylindrical pipe) as explained in Sections 7.3.2 and 7.3.3. The raw data from manometer measurements and a complete error analysis of uncertainty in reading the manometers is given in Appendix A7.1.

Table 7.1 Pressure Drop Results for Cylindrical Pipe

Velocity m/s	Experimental		CFD ΔP , Pa/m	Darcy-Weisbach		Error CFD to Experimental (Manometer) %
	Transducers	Manometer		Colebrook equation for f'	Blasius equation for f'	
	ΔP , Pa/m	ΔP , Pa/m		ΔP , Pa/m	ΔP , Pa/m	
1.00	228.84	222.16	231.89	213.70	211.86	4.20
1.25	324.09	328.05	343.86	318.30	313.07	4.60
1.50	450.92	453.38	475.17	440.83	430.73	4.59
1.75	546.32	598.15	623.31	581.06	564.10	4.04
2.00	687.45	762.37	790.57	738.96	712.60	3.57
2.25	839.28	946.02	975.17	913.51	875.71	2.99

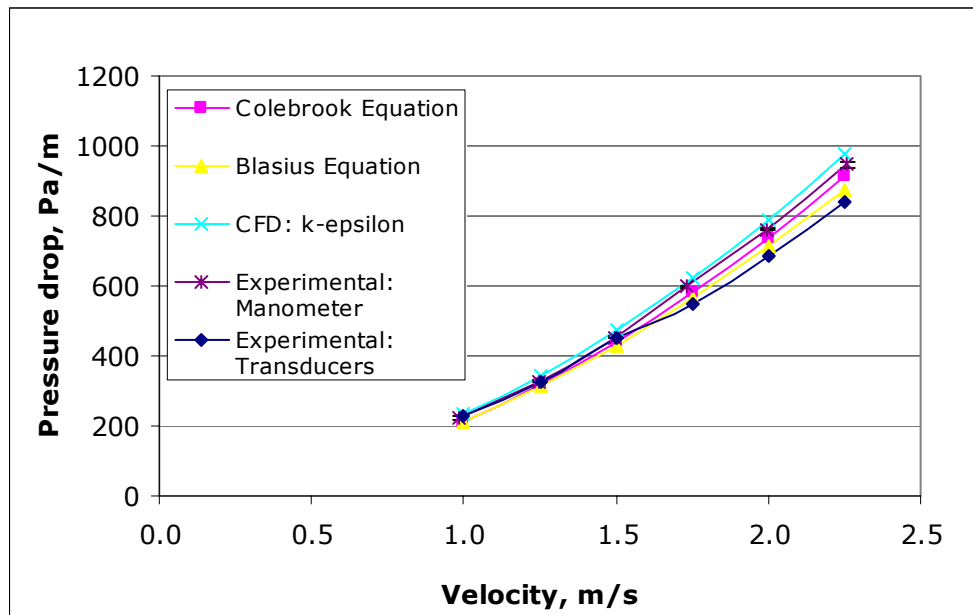


Figure 7.1: Pressure Loss Validation for a Cylindrical Pipe (Standard error in manometer reading indicated on graph)

The standard error in the reading of the manometers was estimated to be in the range of 0.4 to 3% (see Appendix A7.1 for the complete error analysis), with the greatest percentage error at the lowest velocity. The error between CFD predicted value and experimental value (manometer) was less than 5%. It may be possible to reduce these errors further with the use of a periodic boundary condition at the inlet in the CFD simulation. A periodic boundary condition is equivalent to having an infinite length of pipe.

7.3.2 4-Lobed Swirling Flow Pipe

A 400mm 4-lobed swirling flow pipe was next installed in the top-horizontal section of the flow loop and the pressure loss measured using transducers and a manometer.

The pressure loss was measured across a section of swirling flow pipe and 2.925m of cylindrical pipe. It was important to measure the pressure at a substantial distance from the swirl inducing pipe because the swirling flow may otherwise affect the result (see Chapter 6, Section 6.2). This was the reason for pressure measurement across a long section of cylindrical and swirling flow pipe.

To obtain the pressure loss across the swirl pipe only the pressure loss due to the cylindrical pipe was subtracted from the measured value. The cylindrical pipe pressure loss was approximated from previously determined experimental values given in Table 7.1. The procedure is detailed in Appendix A7.1. This introduces further error to the swirl pipe pressure loss. The standard error in the manometer measurement of pressure loss across the swirl pipe only, taking into account errors from subtracting cylindrical pipe pressure loss, was estimated to be between 1 and 7.3% (see Appendix A7.1 for the analysis). The error was less than 2% other than at the lowest flow velocity of 1m/s.

The geometry used in the CFD simulation is shown in Figure 7.2. The pressure loss at the intersection of the cylindrical pipe and the swirl pipe at entry to and exit from the swirl pipe is important for comparison with experiment. Therefore sections of cylindrical pipe of 200mm were added to the geometry at entry and exit.

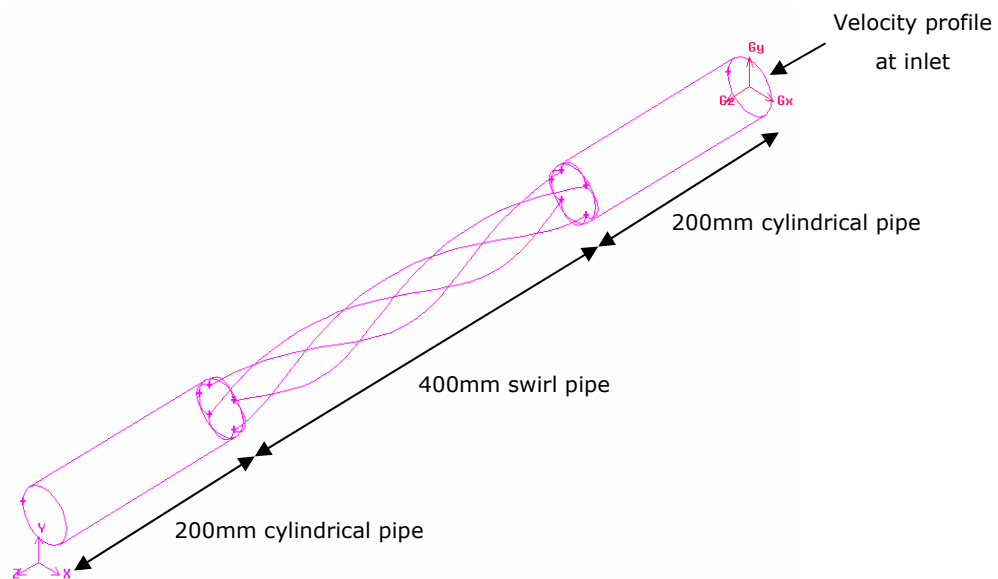


Figure 7.2: Geometry for the CFD Analysis of Swirl Pipe Pressure Loss

Experimentally measured roughness values of $1.89 \times 10^{-08} \text{m}$ and $2.09 \times 10^{-06} \text{m}$ (see Section 5.6, Chapter 5) were used for cylindrical and swirl pipe respectively. A Reynolds stress turbulence model (RSM) was used with an inlet velocity profile. A comparison to the result from the $k-\epsilon$ turbulence model is shown in addition. The CFD pressure loss across the swirl pipe geometry only, taking into account entry and exit losses, has been

compared to the experimental pressure loss across the swirl pipe only in Table 7.2 and Figure 7.3.

Table 7.2: Pressure Drop Results for Swirl Pipe

Velocity m/s	Experimental		CFD		Error CFD to Experimental
	Transducers ΔP , Pa	Manometer ΔP , Pa	k- ϵ ΔP , Pa	RSM ΔP , Pa	RSM to Manometer %
1.00	289.23	274.32	282.42	264.41	-3.75
1.24	482.55	386.68	435.46	408.96	5.45
1.50	602.51	527.67	617.43	584.09	9.66
1.75	896.98	697.29	831.70	787.89	11.50
2.00	1170.59	895.54	1077.21	1022.00	12.37
2.25	1485.07	1122.42	1358.14	1291.36	13.08

There was evident drift in the calibration of the pressure transducers and the results from the transducers varied on repetition of the measurements.

The error between CFD predicted pressure drop and manometer result was in the range of about -4 to +13%. The error increased with increasing velocity in this case with a general trend for the CFD software to over-predict the pressure drop as velocity increases. Grid independence tests (Chapter 4, Section 4.4.5) were carried out at a flow velocity of 1.5m/s. The grid may not be sufficiently fine to resolve the greater turbulence generated at the higher velocities. Additionally, use of turbulence models with greater turbulence at the higher velocities introduces larger errors to the CFD simulation. Other possible explanations are the steeper velocity gradient near the wall at higher flow velocities (introducing errors due to use of standard wall functions, Section 4.2.3, Chapter 4), the requirement of a longer cylindrical pipe length to establish a fully developed viscous boundary layer at the higher flow velocities, and the use of 'uniform pressure' outlet condition.

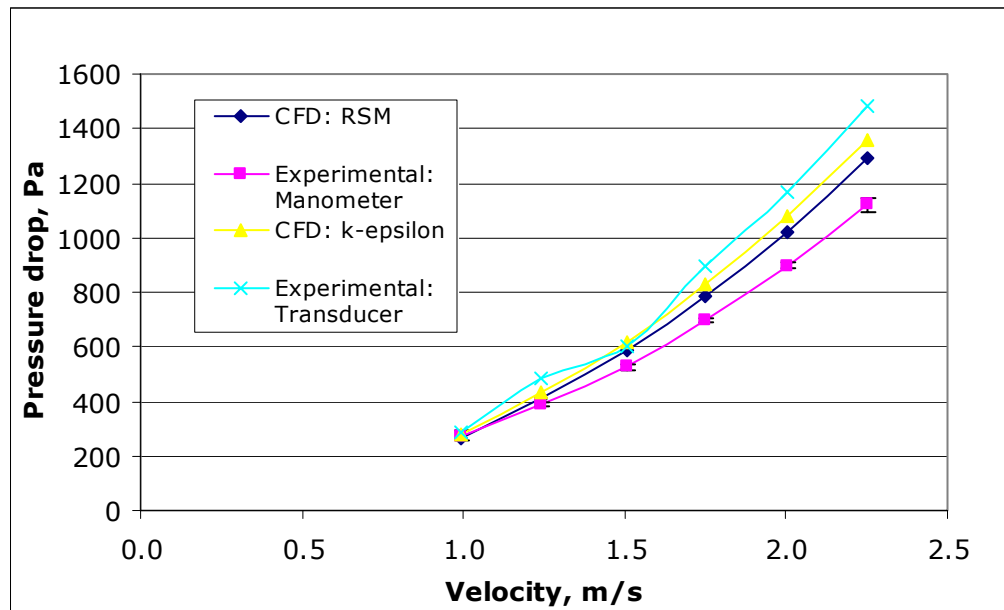


Figure 7.3: Pressure Loss Validation for a 4-Lobed Swirl Pipe (Standard error in manometer reading indicated on graph)

7.3.3 Optimum Entry Transition Pipe

A 100mm 4-lobed transition pipe (beta type $n=0.5$, P:D ratio = 8) was then added onto the rig as entry transition to the swirl pipe and the pressure drop measurements repeated. The experimental measurement was across a combination of entry transition pipe, swirling flow pipe and 2.83m of cylindrical pipe.

Once again pressure readings were repeated with a manometer due to problems with the piezo-resistive pressure transducers involving repeated calibration and the necessity to repeat measurements.

As with the swirl pipe test, pressure drop due to the cylindrical pipe was subtracted from experimentally measured values to obtain pressure loss across the transition and swirl pipe only (see Appendix A7.1). The standard error in the manometer reading of pressure loss, taking into account errors due to subtracting cylindrical pipe pressure loss, was 2 to 8.1% (see Appendix A7.1). The error was less than 2.2% other than at the lowest velocity of 1m/s.

The geometry used in the CFD simulation is illustrated in Figure 7.4. Roughness values of $2.09 \times 10^{-6} \text{m}$ for the swirl and transition pipes, and $1.89 \times 10^{-8} \text{m}$ for the cylindrical pipe were specified. A Reynolds stress model of turbulence was used with an inlet velocity profile. The CFD pressure loss across entry transition and swirl pipe only has been compared to experimental value across transition and swirl pipe in Table 7.3 and Figure 7.5.

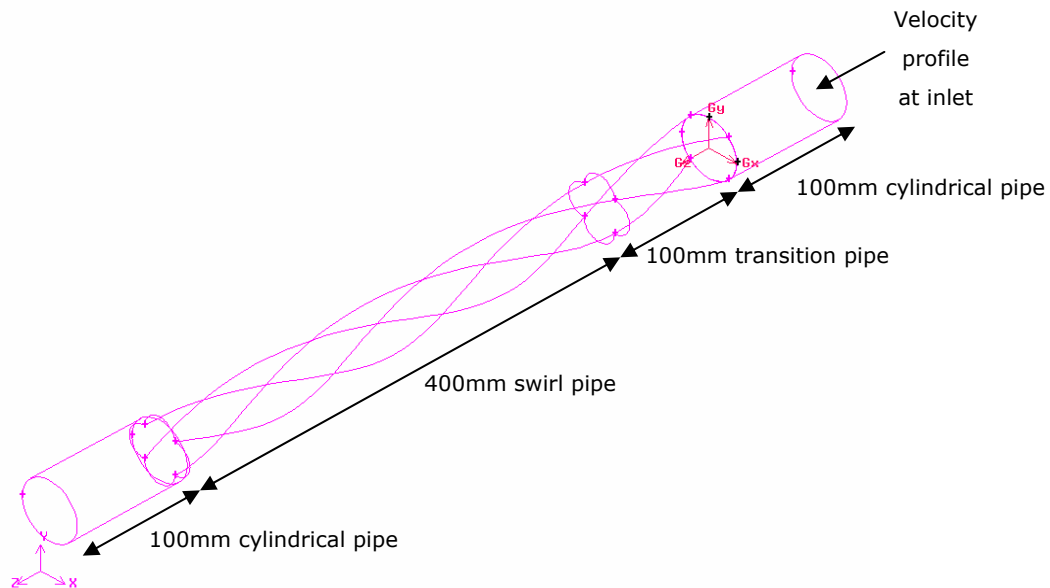


Figure 7.4: Geometry for CFD Analysis of Entry and Swirl Pipe Pressure Loss

Table 7.3: Pressure Loss Results from Inclusion of Entry Transition Pipe

Velocity m/s	Experimental		CFD		Error CFD to Experimental
	Transducers ΔP , Pa	Manometer ΔP , Pa	k- ϵ ΔP , Pa	RSM ΔP , Pa	RSM to Manometer %
0.998	284.24	274.73	272.92	259.95	-5.68
1.217	407.89	391.30	417.18	398.04	1.69
1.487	526.99	535.00	591.19	564.43	5.21
1.727	776.34	705.82	791.57	753.47	6.32
1.971	935.66	903.75	1024.08	979.79	7.76
2.271	1152.45	1128.81	1284.33	1229.56	8.19

The maximum error between CFD prediction and experimental result was 8%. Once again, CFD tended to over predict the pressure drop with increasing velocity.

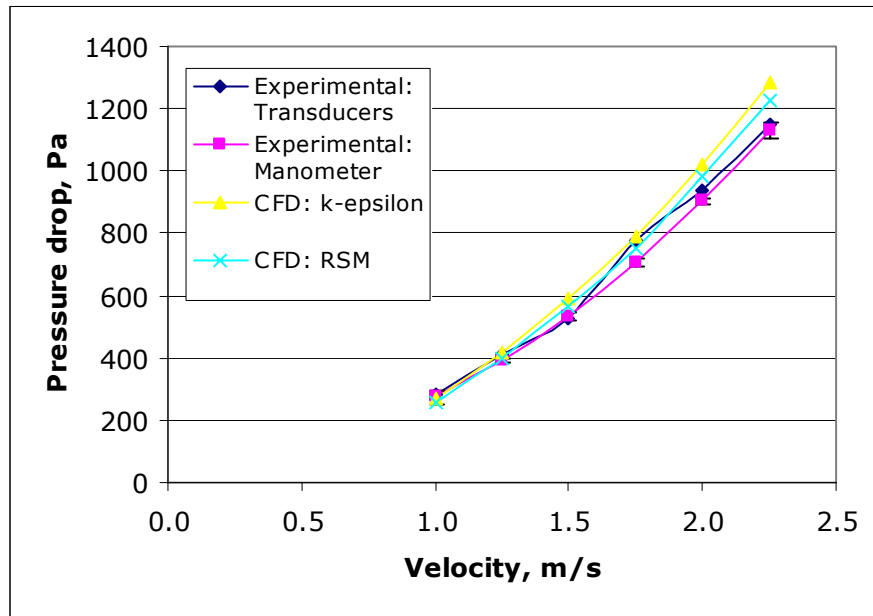


Figure 7.5: Pressure Loss Validation for a 4-Lobed Entry Transition Pipe in Conjunction with Swirl Pipe (Standard error in manometer reading indicated on graph)

7.4 Tangential Velocity Validation

Particle Image Velocimetry (PIV) was chosen as the best method for validating CFD tangential velocity results.

PIV is a whole field technique which allows the measurement of velocity of a fluid in a cross-section of the flow illuminated by a two dimensional light sheet. Thus it allows the measurement of large parts of the flow and is unique in this feature. Except for Doppler Global Velocimetry, which is a new technique for high speed air flows, all other techniques for velocity measurement of flow velocity are at a single point, though in most cases with a high temporal resolution. With PIV the spatial resolution is large, whereas the temporal resolution is limited (Raffel 1962).

PIV offers a unique opportunity for defining a common ground with CFD. For example, the velocity field information obtained through PIV can be used for the purpose of straight validation or checking on the flow dimensionality, geometric definition and velocity. Furthermore, other quantities such as

vorticity, deformation and forces can also be derived which provide a common ground with CFD.

7.4.1 PIV Setup and Methodology

Cross-sectional velocity measurements (of tangential velocity) were to be attempted using the PIV technique at various distances downstream of the swirl-inducing pipe at axial velocities of 1, 1.5 and 2m/s. In addition, the type of swirl detected from PIV was to be compared to the CFD predicted type based on classification of swirl types by Steenbergen and Voskamp (Steenbergen 1998).

In PIV, the flow is seeded with particles to act as markers that will follow the flow without affecting the fluid properties to be measured. The flow in the target area is then illuminated with a laser light sheet and the motion of the particles recorded using a CCD (Charge Coupled Device) camera. A sequence of two light pulses is recorded and the images are divided into subsections called interrogation areas. The interrogation areas are next correlated, pixel by pixel. The correlation produces a signal peak identifying the common particle displacement. This displacement can then be used to construct a 2D vector map (Smits 2000).

The same Dantec FlowMap (Dantec Measurement Technology Inc., Skovlunde, Denmark) PIV system as used by Ganeshalingam (Ganeshalingam 2002) and Tonkin (Tonkin 2004) was used.

Ganeshalingam (Ganeshalingam 2002) measured axial velocity of the flow downstream of a swirl-inducing pipe and showed that there was good agreement with CFD predicted values. His attempts at measuring tangential velocity, however, were unsuccessful.

Tonkin (Tonkin 2004; Jones 2004b) measured the tangential velocity of the flow downstream of a swirl pipe by diverting the flow as illustrated in Figure 7.6. She placed the camera perpendicular to the cross-section and focused through an optical window. Initially only a part of the cross-section was visible with the tangential viewer. It was adapted by adding a viewing box.

This was filled with water to prevent total internal reflection, so the whole pipe cross-section could be viewed.

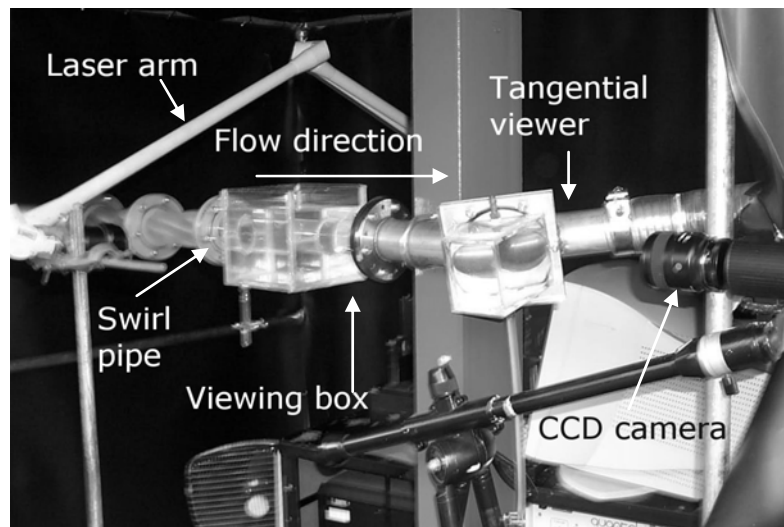
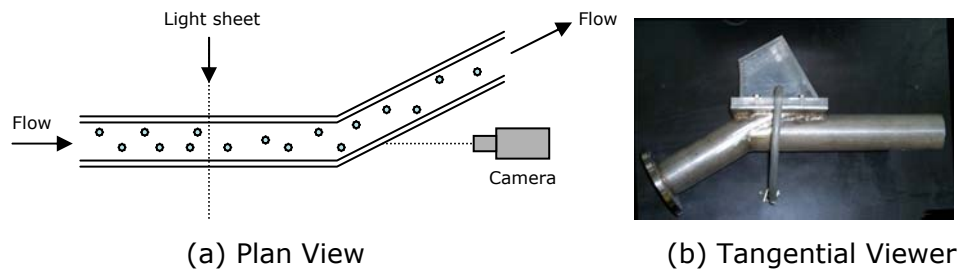


Figure 7.6: PIV Setup and Camera Angle for the Cross-sectional Velocity Measurement (after Tonkin (Tonkin 2004))

With a tangential viewer, measurements at distances further downstream than $L/D = 5$ (5 pipe diameters) may not be possible because the camera cannot focus that far through the viewer. This will prevent analysis of swirl decay downstream of the swirl pipe. Therefore it was decided to attempt PIV measurement of tangential velocity with the laser and the camera at an angle as shown in Figure 7.7 which had previously not been attempted.

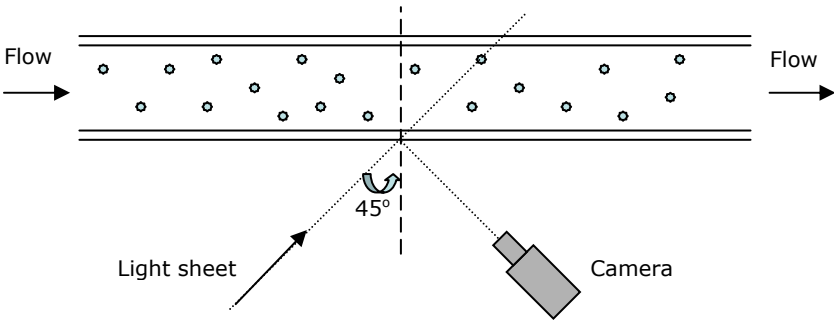


Figure 7.7: Schematic Diagram of PIV Setup and Camera Angle with the Laser at an Angle

The flow was seeded with small tracer particles of talc. A twin pulsed Nd:YAG laser was used as the light source to create two pulses of light at a wavelength of 532nm, and operated at a frame rate of 10Hz.

A Dantec CCD camera, model 700, was used to image the flow field. The CCD camera was mounted perpendicular to the light sheet and connected to a computer. The laser and the camera were synchronised via a Dantec PIV 2000 processor and software.

The following settings were used:

- Processing: Image Map 768 x 484 pixels
- Timing Exposure: Time between pulses 100μs
 Light pulses per recording 2
 Duration of each pulse 0.01μs
 Bursts: Time between recordings 266.67ms
 Time between bursts 1000ms
- Quantel twins 150mJ, 15Hz, low power

A photographic image of the pipe was obtained and a mask applied to the image to determine the pipe area on which cross-correlation was to be carried out.

Next, cross-correlation was carried out through the processor which generates a vector diagram. This vector diagram was then filtered to eliminate the vectors that are out of range. The data thus generated can

now be exported in the form of x , y position data of the vectors and the components of the velocity vectors in the laser plane U and V . This data can be manipulated to obtain axial and tangential velocities.

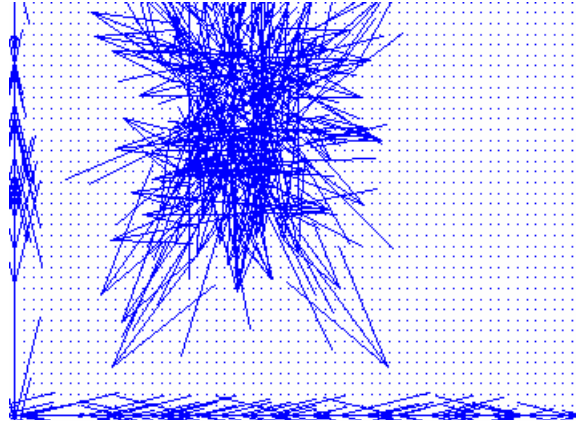


Figure 7.8: Vector Diagram Post Cross-Correlation

7.4.2 Procedure for Calculating Tangential Velocity

7.4.2.1 With Cross-sectional Viewer as used by Tonkin

Tonkin describes the procedure in detail (Tonkin 2004). A brief summary is provided below.

With the cross-sectional viewer, the velocities U_{across} and V (velocities in x and y directions respectively in the laser plane, see Figure 7.9) are calculated by the PIV processor in a cross-section of the pipe since the laser is perpendicular to the pipe surface and a cross-section is photographed.

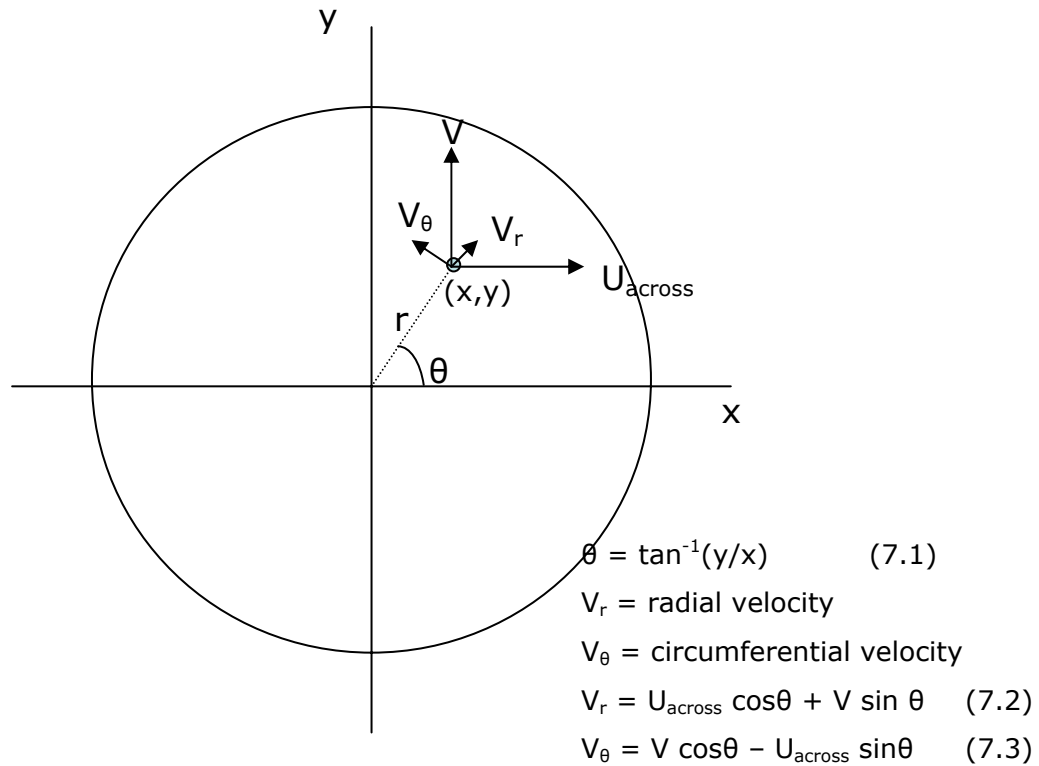


Figure 7.9: Calculation of Circumferential (Tangential) Velocity Component

Therefore the components of velocity calculated by the PIV processor can be used directly in the calculation of tangential velocity as shown in Figure 7.9 using Equation 7.3 without further manipulation.

7.4.2.2 With Laser and Camera at an Angle (Oblique Laser Sheet)

As stated previously an oblique laser angle was used such that velocities further downstream can be measured.

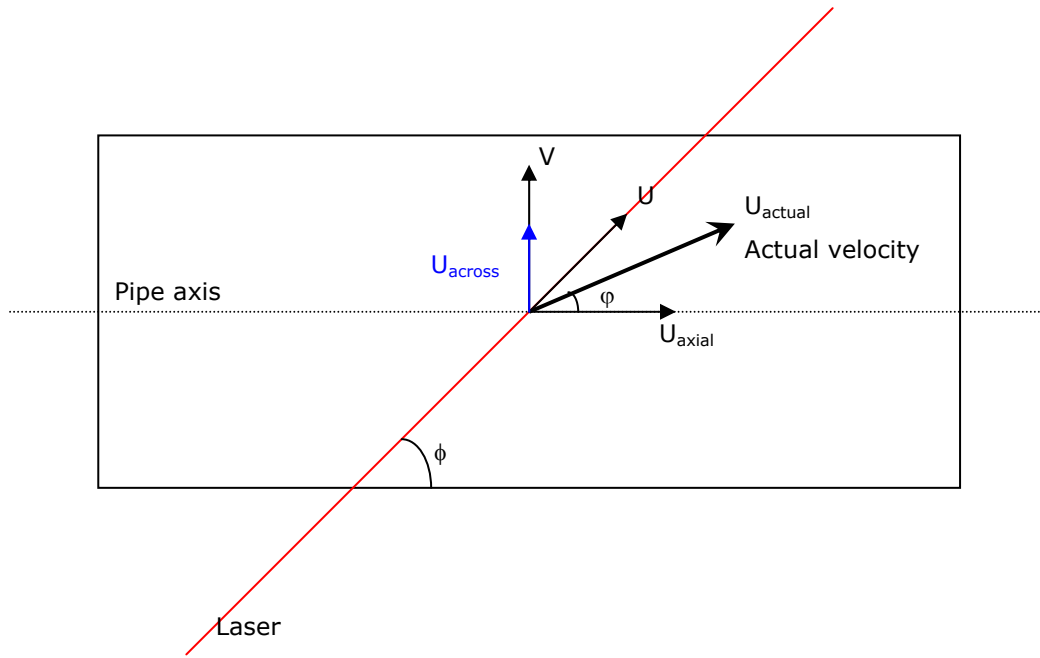


Figure 7.10: Vector Diagram with the Laser at an Angle (Camera optical axis is perpendicular to the laser plane (PIV image))

U_{axial} = velocity in axial pipe direction

V = velocity in vertical direction, unchanged where the laser sheet cuts the pipe vertically

U_{actual} = actual velocity of the particle in the direction of the vector

U_{across} = velocity perpendicular to pipe axis

U = velocity across PIV image plane (value given by processor); the component of the actual velocity vector in the PIV image plane

ϕ = angle between laser plane and pipe axis

ϕ = angle of actual velocity vector to pipe axis

In order that we may use Equation 7.3 above (see Figure 7.9) to calculate circumferential velocity, we must know U_{across} .

$$U_{across} = U_{actual} \sin \phi \quad (7.4)$$

The PIV processor calculates U for us. We can calculate U_{actual} from:

$$U = U_{actual} \cos(\phi - \phi) \quad (7.5)$$

$$U_{actual} = \frac{U}{\cos(\phi - \phi)}$$

$$U_{across} = \frac{U}{\cos(\phi - \varphi)} \times \sin \varphi$$

Now we need φ (angle of actual velocity vector to axial flow) to calculate U_{across}

$$U_{axial} = U_{actual} \cos \varphi$$

$$\cos \varphi = \frac{U_{axial}}{U_{actual}} = \frac{U_{axial}}{U} \times \cos(\phi - \varphi)$$

$$\frac{\cos \varphi}{\cos(\phi - \varphi)} = \frac{U_{axial}}{U}$$

Therefore we need U_{axial} , either from another PIV plane or from previous experiments, in order to calculate U_{across} .

Due to time constraints this was not attempted and the initial PIV results were not used to calculate tangential velocities. This confirmed that the cross-sectional viewer was the best means of measuring tangential velocity with the use of PIV. Tests with a cross-sectional viewer could not be carried out since the PIV system was only available for a short time.

7.4.3 Swirl Pipe Results Validation

The measurements obtained using the cross-sectional viewer by Tonkin were used for the validation effort since the above attempt was unsuccessful.

Tonkin measured the tangential velocity 250mm ($L/D=5$) downstream of a 400mm long 4-lobed swirling flow pipe using PIV at different axial velocities. The experimental results are shown in comparison with predicted results from CFD in Figure 7.11a - e. An average tangential velocity at a given range of radial co-ordinate was calculated and plotted.

PIV indicated a maximum tangential velocity between $r/R = 0.7$ and 0.9 . CFD predictions indicated a maximum at between 0.8 and 0.9 . The error

between PIV and CFD predicted values of maximum tangential velocity given in Table 7.4 were within 20% except in the case with axial velocity 2m/s (Figure 7.11d). However, the result at axial velocity 2m/s may be disregarded as it is clearly erroneous because the tangential velocity was lower than that measured at lower axial velocities. The lower tangential velocity predicted from CFD in comparison to PIV (except at 2m/s) may be due to the lower inlet axial velocity specified in the CFD simulations.

Overall, least agreement between CFD and PIV in Figure 7.11a - e was at the centre of the pipe and at the pipe wall.

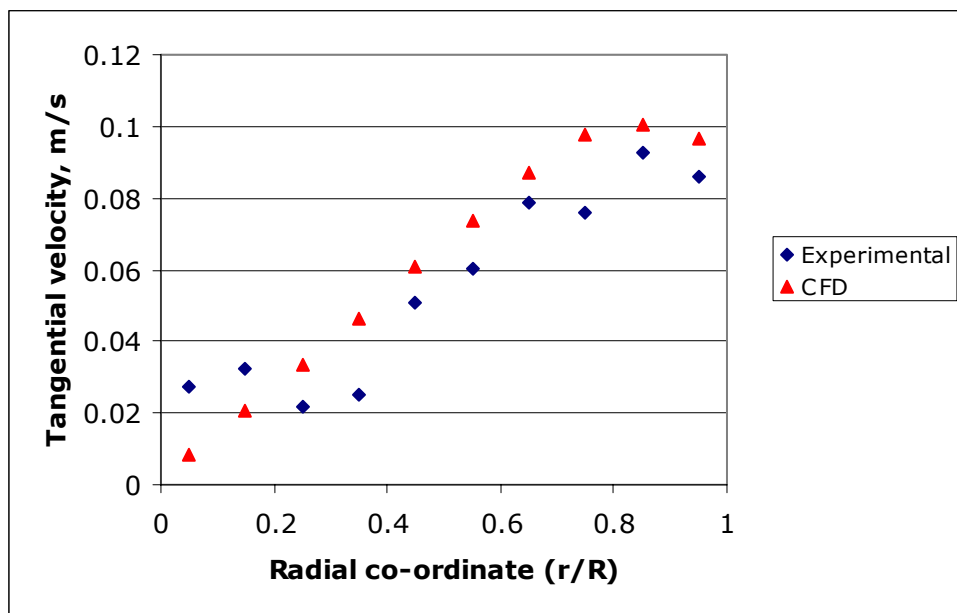


Figure 7.11a: Axial Velocity 0.5m/s

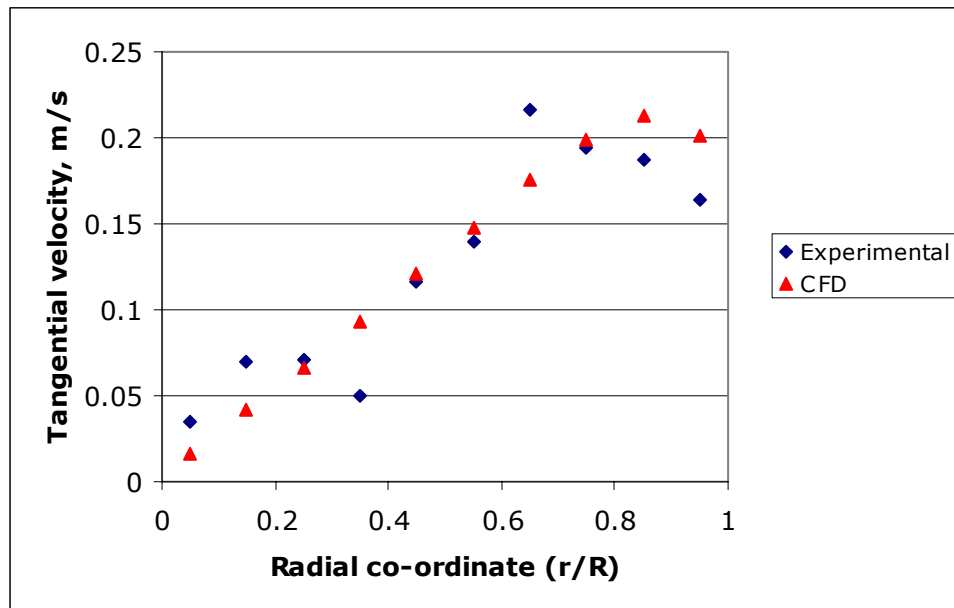


Figure 7.11b: Axial Velocity 1.0m/s

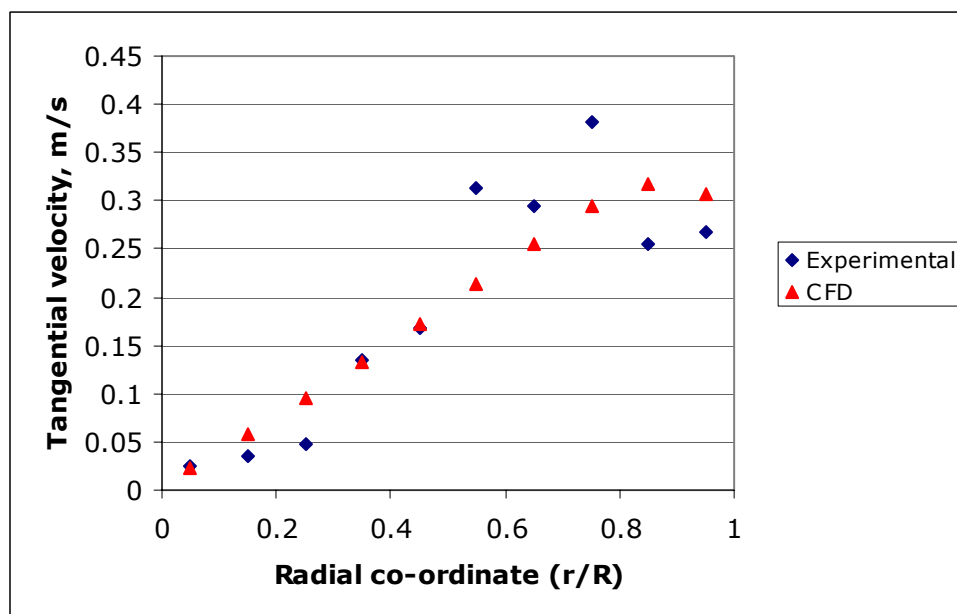


Figure 7.11c: Axial Velocity 1.5 m/s

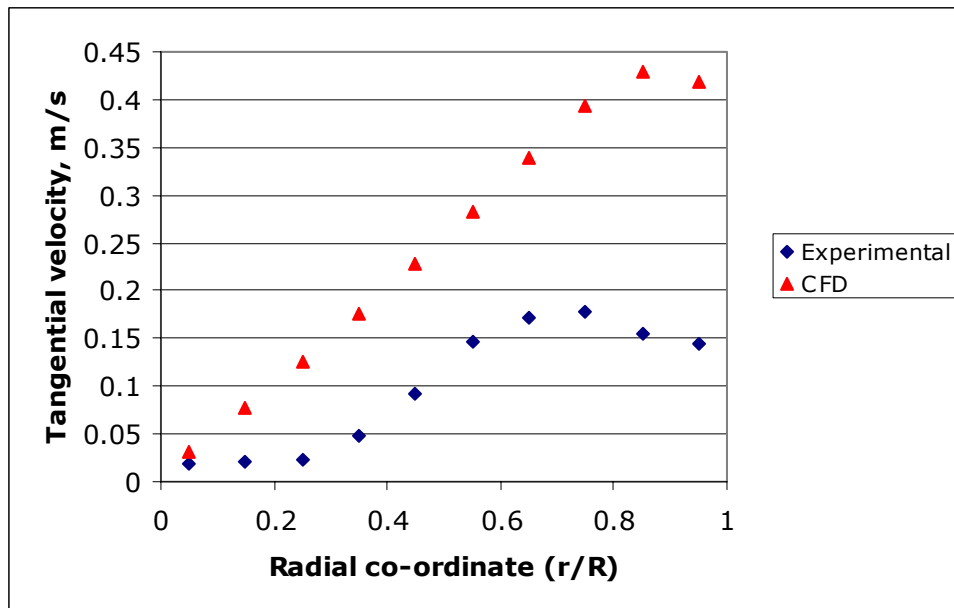


Figure 7.11d: Axial Velocity 2.0 m/s

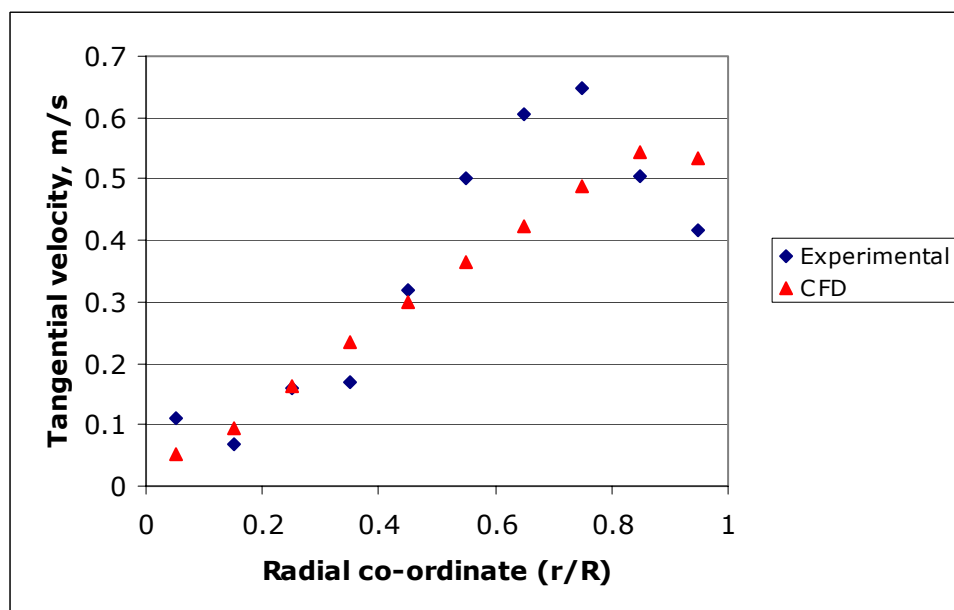


Figure 7.11e: Axial Velocity 2.5 m/s

Figure 7.11a - e: Comparison of Experimentally Measured Tangential Velocity to CFD Prediction at Different Axial Velocities

Table 7.4: Maximum Tangential Velocities

Axial velocity for PIV, m/s	Axial velocity for CFD, m/s	PIV tangential velocity, m/s	CFD tangential velocity, m/s
0.5	0.5	0.1	0.11
1.1	1.0	0.3	0.25
1.7	1.5	0.4	0.38
2.2	2.0	0.2	0.52
2.8	2.5	0.7	0.64

A detailed qualitative discussion of the type of swirl observed in Figure 7.11a – e is given next (Section 7.4.3.1).

7.4.3.1 Qualitative Comparison and Type of Swirl

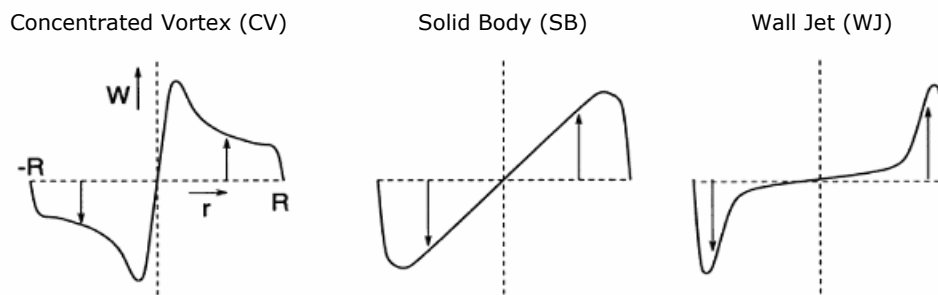


Figure 7.12: Classification of Swirl Types (After Steenbergen and Voskamp, 1998)

Steenbergen and Voskamp defined three different swirl types according to the radial distribution of the tangential velocity field:

1. Concentrated Vortex (CV)- rotation concentrated near the pipe centre
2. Solid Body (SB)- almost uniform rotation
3. Wall Jet (WJ)- angular momentum concentrated near the wall

Ganeshalingam (Ganeshalingam 2002) stated that the radial distribution of the tangential velocities downstream of the *Swirly-Flow* pipe determined by his CFD simulations fitted with the 'Wall Jet' classification of Steenbergen and Voskamp (Steenbergen 1998). His results were at distances of L/D 5 to 25 from the exit of a 3-lobed *Swirly-Flow* pipe for Reynolds numbers of 50,000 and 100,000.

However, during the course of this research it was found from CFD that it was actually a wall jet (WJ) type to begin with inside the swirl pipe itself which rapidly changed into a solid body (SB) type. Raylor's (Raylor 1998) CFD analyses on *Swirly-Flo* pipes all indicated a solid body type rotation at the exit of the pipe in agreement with the current results.

Tonkin's (Tonkin 2004) PIV results conformed more closely to the wall jet type of swirl rather than solid body (Figure 7.11a - e). However, there was a tendency for the high velocity wall region to be wider than expected from the wall jet model.

An investigation was carried out using CFD to further establish the type of swirl. The geometry used consisted of 200mm of cylindrical entry pipe, 400mm of optimised swirling flow pipe and 300mm of cylindrical exit pipe. A Reynolds stress turbulence model was used with 2nd order discretization.

Figure 7.13 shows the results of tangential velocity in several cross-sections within the swirling flow pipe (with $L=0$ being entry to, and $L=0.4$ being exit from, the swirl pipe) and downstream of the swirl pipe. The swirl type inside the swirl pipe itself was closer to the wall jet definition however it gradually developed into a solid body type. At the exit of the swirl pipe the type of swirl was much better fitted to a solid body.

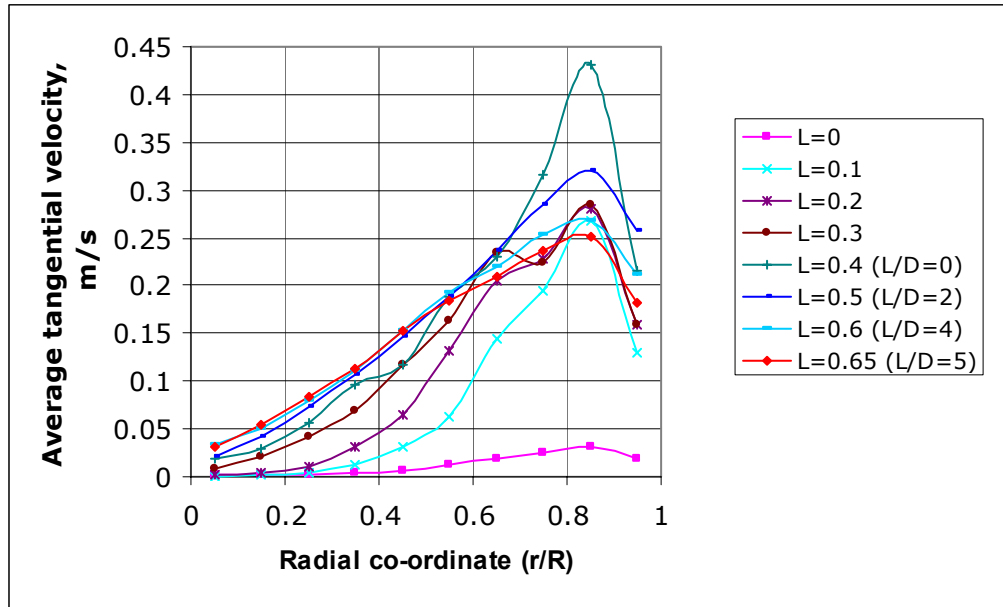


Figure 7.13: Tangential Velocity Development through Length of the Swirl Pipe (L=0 Swirl Pipe Entrance, L=0.4 Swirl Pipe Exit)

7.4.4 Swirl Decay

There are a few experimental and theoretical investigations reported in the literature about decay of swirling flow through pipes (Kreith 1965; Senoo 1972; Ito 1980; Li 1994). However, there seems to be no unanimous agreement on decay rates in swirling pipe flows. The important parameters are Reynolds number, friction factor f and initial swirl intensity S_0 .

A common expression for swirl decay, as quoted by most literature sources is:

$$S = S_0 e^{\beta \frac{x}{D}} \quad (7.6)$$

where:

S = swirl intensity

S_0 = initial swirl intensity

β = swirl decay rate parameter = $\alpha \cdot f'$

x = distance along pipe, m

D = pipe diameter, m

f' = Moody friction factor

α = empirically or numerically determined coefficient

The swirl decay rate parameter β has been estimated both empirically and numerically. Steenbergen and Voskamp (Steenbergen 1998) suggest a value of $\beta = [(1.49 \pm 0.07) \times f']$ for $0 < S < 0.18$ (from experiments with water at $50,000 < Re < 300,000$, $S_0 = 0.18$).

They concluded that the rate of decay appears to decrease with increasing Reynolds number and also seems to be independent of the type of swirl. An overview of the rates of decay, β , found in a large number of experiments in the literature infers it to be between 0.015 and 0.05 approximately for a Reynolds number of 100,000 for a range of smooth and rough pipes.

This shows an uncertainty in the decay rates in the literature of $\pm 50\%$ and Steenbergen and Voskamp suggest that their value of $\beta = [(1.49 \pm 0.07) \times f']$ has reduced the uncertainty to within 5%.

Most literature sources have quoted a value for β between f' and $1.5f'$ for moderate to high initial swirl intensities:

- Youssef (1966), Rapier (1981) and Mottram and Rawat (1986) (as quoted by Halsey (Halsey 1987)) give an exponential decay rate of $\beta = f'$.
- Nystrom and Padmanabhan (1985) (as quoted by Halsey (Halsey 1987)) and Halsey (Halsey 1987) suggest $\beta = 1.5f'$ from experimental results.
- Senoo (Senoo 1972) shows the derivation of the swirl decay equation from the swirl intensity equation and gives $\beta = 0.28f'$. However, this has been shown to be an underestimation (Li 1994).
- Reader-Harris (Reader-Harris 1994) computed an equation of the form of (7.6) above by solving the Navier-Stokes equation and concluded a generalised value of $\beta = 1.07f'$ for smooth and rough pipes. This was found to be in good agreement with experiments in the literature using swirl generated in many different ways.

Figure 7.14 shows the swirl decay that was obtained from CFD with an optimised swirling flow pipe. The parameters used were as follows:

- Geometry: 400mm optimised swirling flow pipe leading into a 1000mm ($d = 50\text{mm}$) cylindrical pipe
- u (inlet axial velocity) = 1.5m/s (Reynolds number = $75,000$)
- Turbulence intensity = 4%
- f' was estimated for flow in perspex piping at 0.02 using the Colebrook-White equation
- Hydraulically smooth pipes assumed
- Gravity was enabled
- Value of 'initial' swirl intensity, S_0 taken at 10mm downstream of the swirl pipe exit
- Swirl intensity calculated and shown as an average at the given cross-section
- Reynolds stress turbulence model (RSM) used

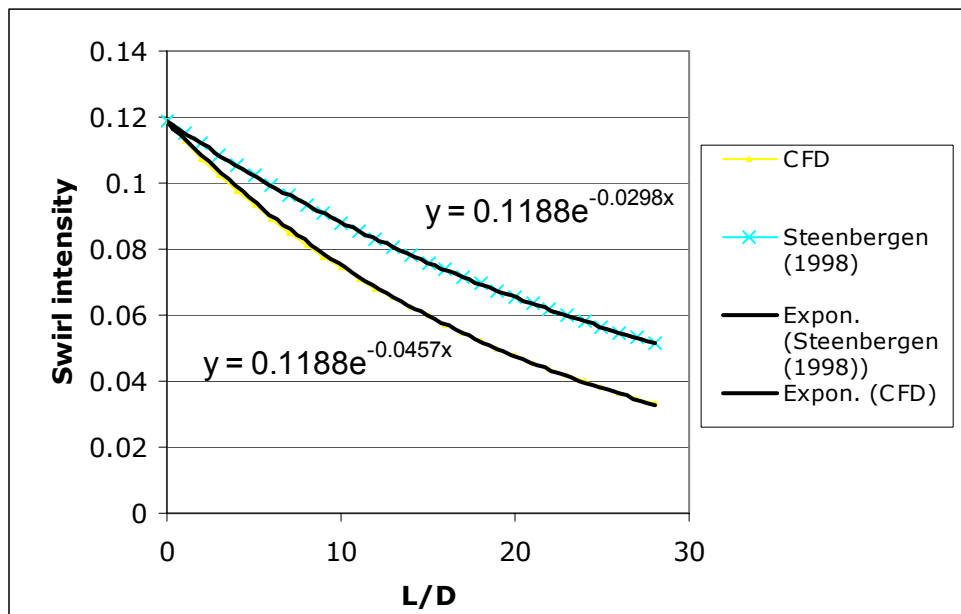


Figure 7.14: Decay of Swirl Intensity with Length (at a Reynolds number of 100,000)

When an exponential decay curve of the form of Equation 7.6 was fitted to the CFD data the value of β was calculated to be $2.27f'$. This was a higher rate of decay than that expected from the suggested value of decay parameter by Steenbergen and Voskamp. However from the scatter of

results that is observed in the literature it was considered reasonable. A logarithmic graph of the swirl decay (Figure 7.15) showed, from the value of R^2 , that it fitted well with the exponential decay formula. The half-life is a more appropriate measurement of decay for non-measurement applications where swirl is a desirable characteristic. The half life in the case of the CFD simulation was approximately 15 diameters.

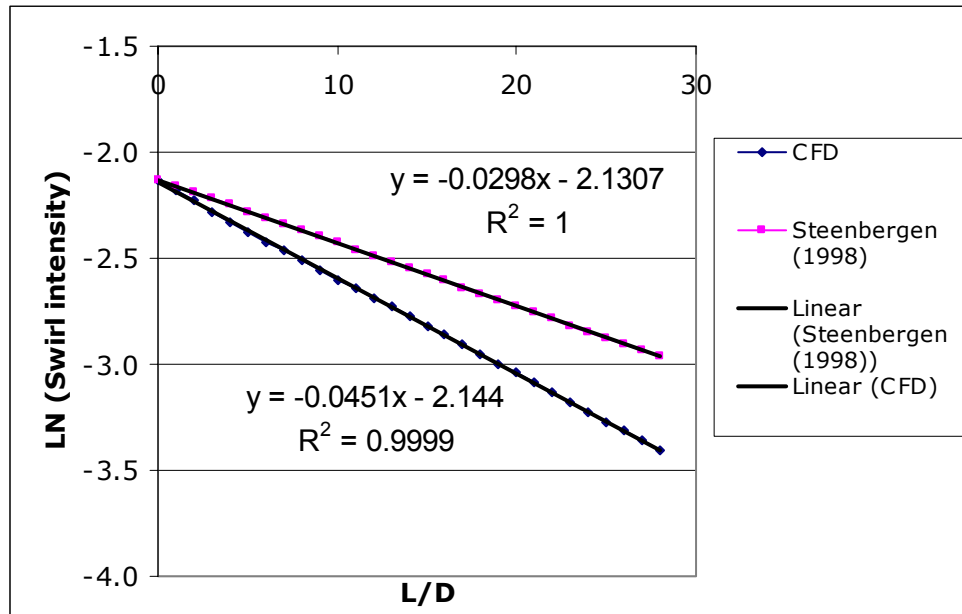


Figure 7.15: Exponential Decay of Swirl Intensity with Length (at a Reynolds number of 100, 000)

Ganeshalingam compared the swirl decay from his CFD simulations with that predicted by the Steenbergen and Voskamp equation (with $\beta = 1.49f'$) and showed much better agreement with the swirl decaying slower (Figure 7.16) with a half-life of 22 diameters.

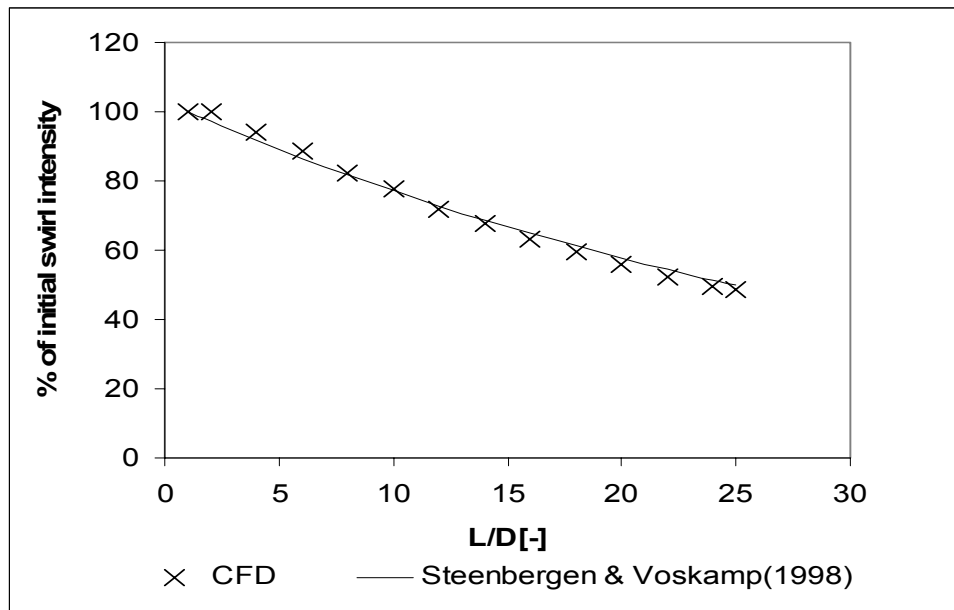


Figure 7.16: Ganeshalingam's (Ganeshalingam 2002) Comparison of CFD Predicted and Calculated (Steenbergen and Voskamp, 1998) Swirl Decay at a Reynolds Number of 100,000

Possible differences in the current simulation from Ganeshalingam's were in:

- turbulence intensity value specified
- pipe roughness value specified
- use of inlet velocity profiles
- use of a 4-lobed pipe instead of 3-lobed
- use of a pipe with larger flow area
- turbulence model used
- calculation of swirl intensity
- mesh
- difference in model parameters

All of the above, except for differences in mesh and model parameters have been investigated and discarded as possible reasons for the discrepancy.

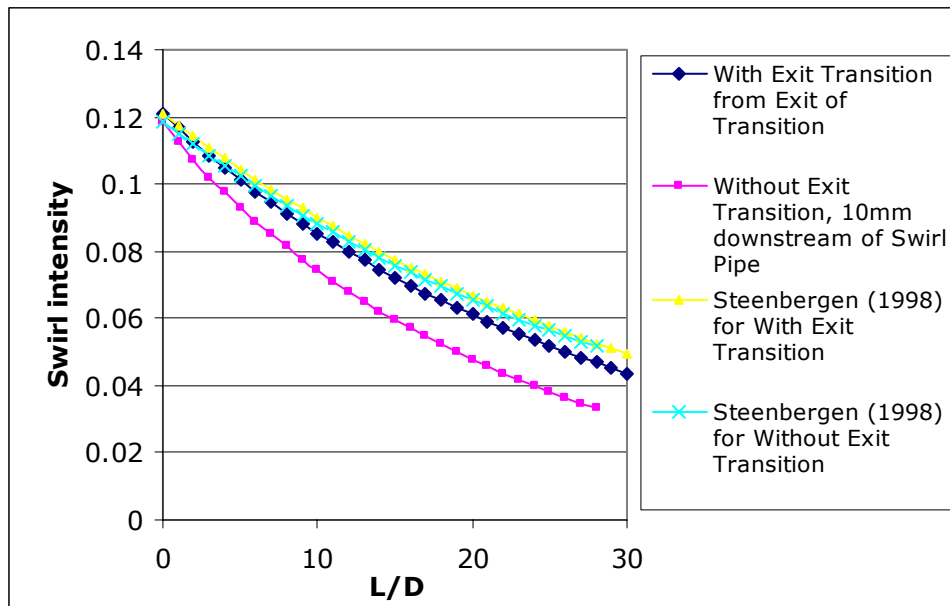


Figure 7.17: Exit Transition Reduces Decay Rate

Figure 7.17 shows that the inclusion of an exit transition pipe reduced the rate of decay of swirl when compared to the simple swirl pipe only. The half life was increased to 20 diameters and the decay trend was much closer to the Steenbergren prediction. However, this showed that the decay of swirl was highly dependent upon exit conditions of the swirl and thus it may not be possible to specify a single value for the decay parameter where different methods of swirl induction have been used.

7.5 Conclusions

- Differences between the physical flow and the numerical solution could be due to one of the following (Shaw 1992):
 1. An inadequate mesh density being used in the regions of high rates of the flow variables, for example in a boundary layer;
 2. Inadequate physical modelling of the flow, especially due to the use of turbulence models which were too simplistic;
 3. Poor specifications of the boundary conditions which have over- or under-constrained the flow, typically at an outlet to the system where the pressure had been fixed as a constant; this may have restricted the flow if it swirled out through the outlet

as the calculated pressure needs to be able to vary across the outlet to provide the necessary centripetal force.

- A combination of grid independence, turbulence model sensitivity studies, examination of near wall modelling approaches and lengthening the pipes beyond the results determination points have ensured that the above stated errors were minimised (Chapter 4).
- The experimental results of pressure and tangential velocity were in reasonable agreement with the CFD predicted results. The maximum error in pressure drop was less than 15% and in tangential velocity was less than 20%.
- The tangential velocity results obtained from CFD indicated that within the swirl pipe, the swirl type was initially wall jet, which developed very quickly into solid-body type swirl.
- The use of exit transition reduced swirl decay rate.
- The swirl decay rate parameter was dependent upon the exit conditions of the swirl inducing mechanism. Therefore it may not be possible to assume a single value for it for all swirling flows.

CHAPTER 8: ADVANTAGE OF TRANSITIONS IN SWIRL INDUCTION ON SETTLING SLURRY

8.1 Introduction

CFD simulations suggested that the use of entry and exit transition pipes with swirl pipes produce greater swirl intensity and reduce pressure cost from swirl induction. However the simulations were limited to single phase flows with no solids. It was necessary to experimentally evaluate whether this advantage holds when transitions are used with settling solids slurry of a range of densities.

The following pipe combinations were used:

1. Optimum swirl pipe incorporated: 'Swirl only'
2. Optimum entry transition and optimum swirl pipe incorporated: 'Swirl + Entry transition'
3. Optimum entry transition, optimum swirl pipe and near-optimum exit transition incorporated: 'Swirl + Entry + Exit transition'

The effect of solids density and concentration on pressure drop and solids settling length were investigated at varying flow velocities.

8.2 Background

Raylor (Raylor 1998) and Ganeshalingam (Ganeshalingam 2002) carried out investigations of swirl induction on settling slurry using *Swirly-Flo* pipe. This is a design of lobed pipe found in marine boilers and it was used due to its immediate availability. The *Swirly-Flo* pipe geometry is described in Chapter 2 (Section 2.3.3).

Raylor observed that the flow pattern downstream of the *Swirly-Flo* pipe was roughly helical. He also showed that when *Swirly-Flo* pipe was used prior to a 90° vertical bend, the particles were well distributed within the bend.

Ganeshalingam carried out an extensive series of tests to determine the advantage of swirl induction in solid-liquid flow pipeline systems. He showed that pressure drop was insensitive to changes in solids concentration when the *Swirly-Flo* pipe was used. This result suggested that much higher solids concentrations can be carried in suspension by swirl inducing pipe without creating any plugging in pipelines.

He also noted that as the flow velocity increased above 1.5m/s the pressure gradient increased for all solids concentrations. Thus the *Swirly-Flo* pipe caused very significant pressure losses at high velocities. The pressure loss across the *Swirly-Flo* pipe was much higher than in cylindrical pipe, approximately 5 times, at higher velocities. However it was not appropriate to compare the two sets of pressure loss data because:

- The *Swirly-Flo* pipe was made of steel whereas the cylindrical pipe was a smooth Perspex pipe. Therefore the friction factor of the *Swirly-Flo* pipe was significantly higher than cylindrical pipe.
- The cross-sectional area of the *Swirly-Flo* pipe was smaller than that of the cylindrical pipe.

Figure 8.1 shows a comparison of the experimental pressure loss (for water only flow) across *Swirly-Flo* pipe, as measured by Ganeshalingam, and the pressure loss across an optimised swirl pipe with and without transitions. This is the same experimental data (manometer readings) which was presented in Chapter 7 for cylindrical and optimised swirling flow pipes with units of Pa/m. The custom-built, optimised swirl pipe eliminates the above concerns of significantly higher surface roughness (though not entirely) and smaller cross-sectional area.

From Figure 8.1, the pressure loss across the *Swirly-Flo* pipe was approximately 5 times the pressure loss across cylindrical pipe. The pressure loss across optimised swirl pipe was approximately 3 times that across cylindrical pipe and when transitions were used, it was just twice that across cylindrical pipe.

The pressure losses used for results in Figure 8.1 were those across just 400mm of optimised swirl pipe and 600 mm of combined swirl and transitions. Therefore it must be kept in mind that, when extrapolating to 1m to obtain units of (Pa/m), the entry and exit losses overestimate the pressure loss in the case of the optimised swirl pipe.

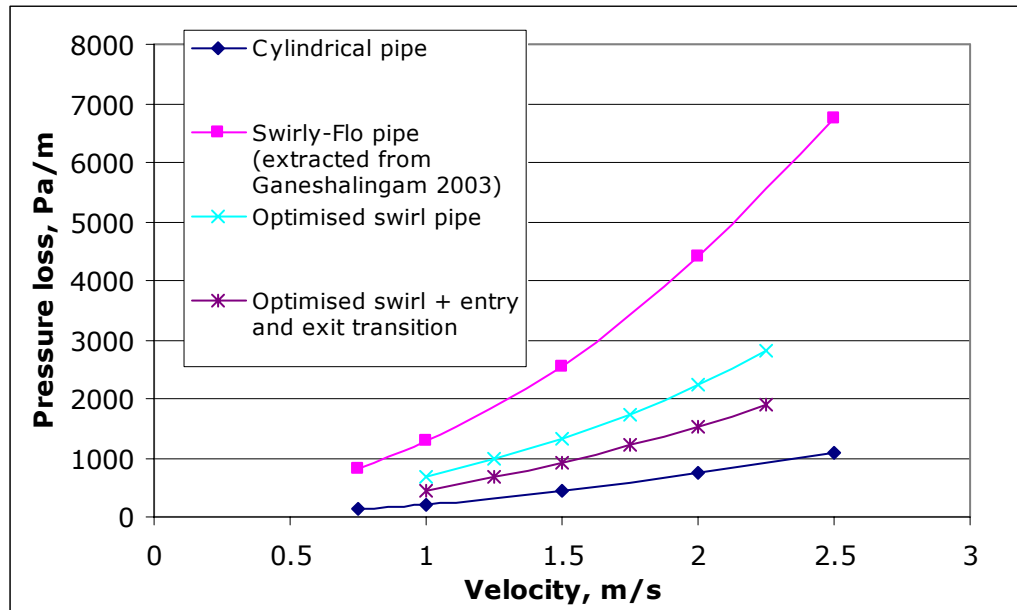


Figure 8.1: Comparison of Pressure Loss across Marine *Swirly-Flo* Pipe and Optimised Swirl Pipe and Transitions

Ganeshalingam (Ganeshalingam 2002) showed through photographic evidence that swirl-inducing pipe promoted flow distribution of solid particles from a moving bed flow to an asymmetric suspension even at very low flow velocities (0.75-2.5m/s). He noticed that the well-distributed particle pattern started to decay after a certain length of pipe and this decay appeared to vary with flow velocity and solids concentration. From the observed swirl decay he suggested that such a pipe every 1.25m would be adequate, for example, at a flow velocity of 1m/s. Further research with optimised swirl pipe was suggested in order that this may be verified.

Tonkin (Tonkin 2004) used a photographic technique to determine tangential velocity in settling slurries subjected to swirl induction with an optimised swirl pipe. She showed that an increase in axial velocity led to an increase in the tangential velocity generated by the swirl pipe, and a decrease in the swirl decay. She also noted a larger rate of decay for denser particle

slurries. Her results confirmed previous findings that swirl was most effective at lower velocities, and indicated that swirl induction holds most advantage for slurries with higher concentrations.

When swirl was induced into sand and coal slurries, at low velocity in horizontal pipe sections, a pressure benefit was measured, i.e. a lower pressure loss with swirl than without, even though a high pressure cost was expected because of the abrupt change in cross-section from cylindrical pipe to swirl pipe and vice versa.

Tonkin also confirmed that, as the solids density increased, the swirl pipe was beneficial at higher velocities because flow regimes where swirl is beneficial, for example, the moving bed flow regime, are extended to higher velocities.

All three researchers encountered problems with concentration measurement in slurry tests and suggested that an online measurement technique needs to be devised for the slurry rigs.

Table 8.1 gives details of solids added and concentrations measured in each of the tests carried out and discussed in later sections. Irregularly-shaped solid particles of the same size and relative densities (RD) of 1.4, 2.7 and 4.5 were used (see Chapter 6).

Table 8.1: Solids Concentration

Test	RD 1.4 solids						RD 2.7 solids		RD 4.5 solids	
	2kg added		4kg added		7.4kg added		2kg added		2kg added	
	C _w	C _v	C _w	C _v	C _w	C _v	C _w	C _v	C _w	C _v
	%	%	%	%	%	%	%	%	%	%
Swirl only	1.64	1.19	4.45	3.32	-	-	2.06	0.78	1.25	0.28
Swirl + Entry transition	1.76	1.28	-	-	-	-	2.13	0.81	1.5	0.34
Swirl + Entry + Exit transition	1.95	1.42	3.75	2.78	5.91	4.49	1.92	0.73	error	error

Concentration measurements were carried out at a single velocity (1.75m/s). A 20l sample of slurry was drawn and analysed in each case.

The results indicated that where the same weight of solids was added for RD 1.4 and 2.7, the tests were comparable. Thus the slurries can be considered as having approximately the same concentration by weight ($\%C_w$). However, tests with the high density solids, RD 4.5, were not comparable as the solids had a tendency to accumulate in the lower horizontal section of the rig, particularly at the lower flow velocities. The resulting low in-situ concentrations and high concentration variation from one test to the next made RD 4.5 data unreliable.

In all results presented, pressure loss was measured using manometers across 3.325m of horizontal pipe. The standard error in the manometer estimation of pressure is indicated by error bars in all figures presenting pressure losses (figures 8.2 to 8.8). Due to the high concentration variations in the rig for tests incorporating solids, a higher standard error in a range of 0.6 to 8% (with one exception where the error was 12.5% for the 'swirl only' case with RD 2.7 solids at 1m/s flow velocity) was calculated compared to water only tests (0.4 to 4%). The percentage standard error generally reduced as flow velocity was increased.

8.3 Pressure Drop

Figures 8.2 to 8.7 show the pressure loss across a total pipe length of 3.325m (including cylindrical, swirl and transition pipes).

8.3.1 Effect of Velocity on Pressure Drop

Figures 8.2 to 8.5 compare the pressure loss measured for different combinations of pipe for 'water only' case (Figure 8.2) and addition of 2kg each of RD 1.4 (Figure 8.3), RD 2.7 (Figure 8.4) and RD 4.5 (Figure 8.5) solids.

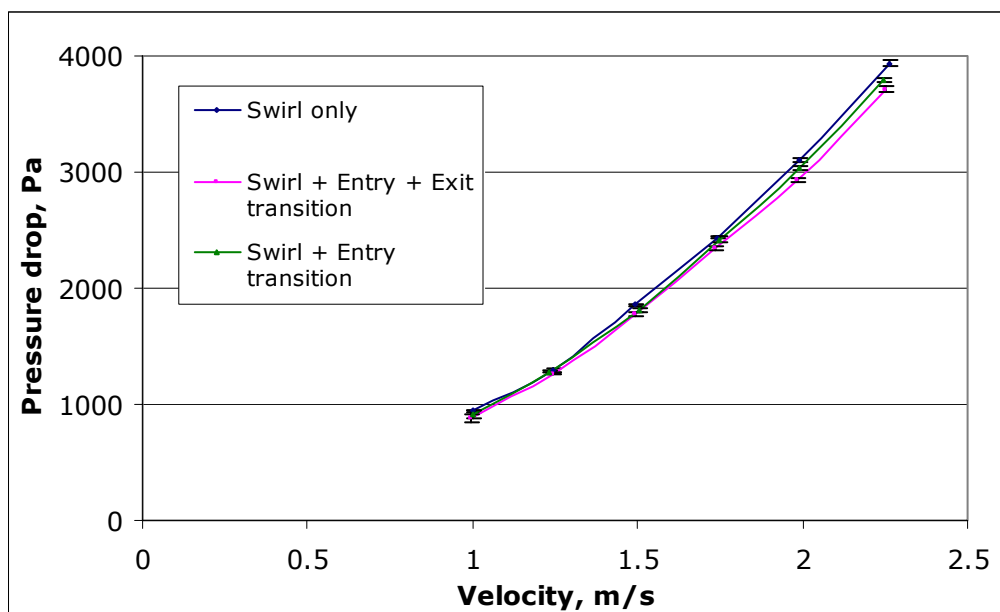


Figure 8.2: Pressure Loss Curve for 'Water only' (error bars indicate standard error in manometer reading)

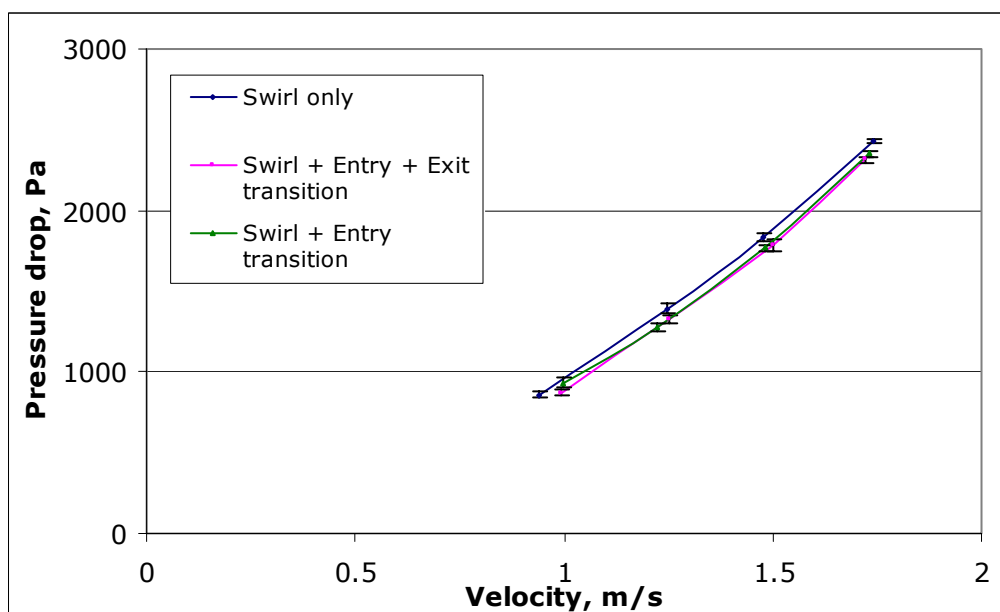


Figure 8.3: Pressure Loss Curve for RD 1.4; 2kg of solids added, 1.8% w/w and 1.35% v/v (error bars indicate standard error in manometer reading)

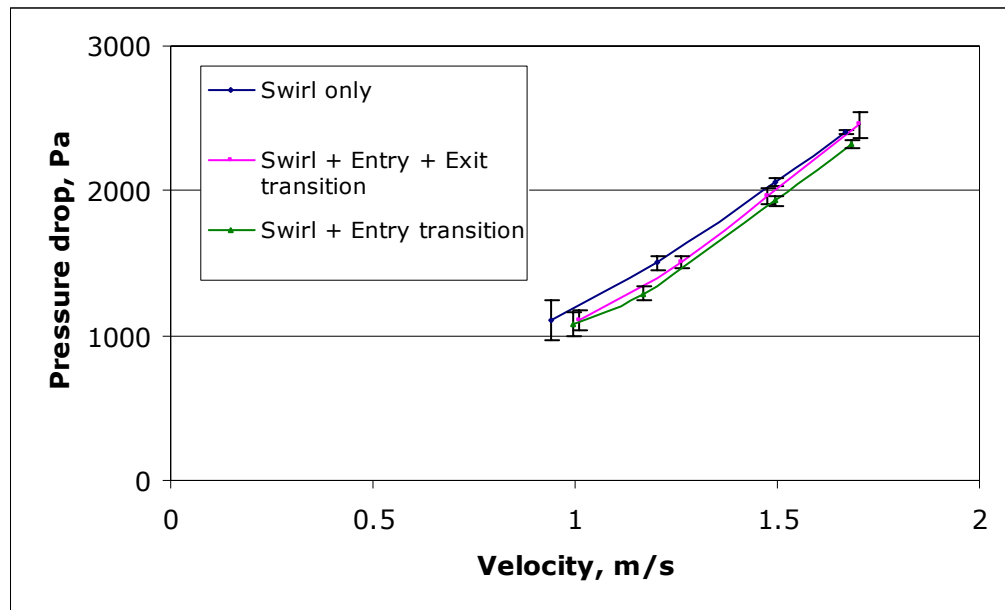


Figure 8.4: Pressure Loss Curve for RD 2.7; 2kg of solids added, 2.0% w/w, 0.77% v/v (error bars indicate standard error in manometer reading)

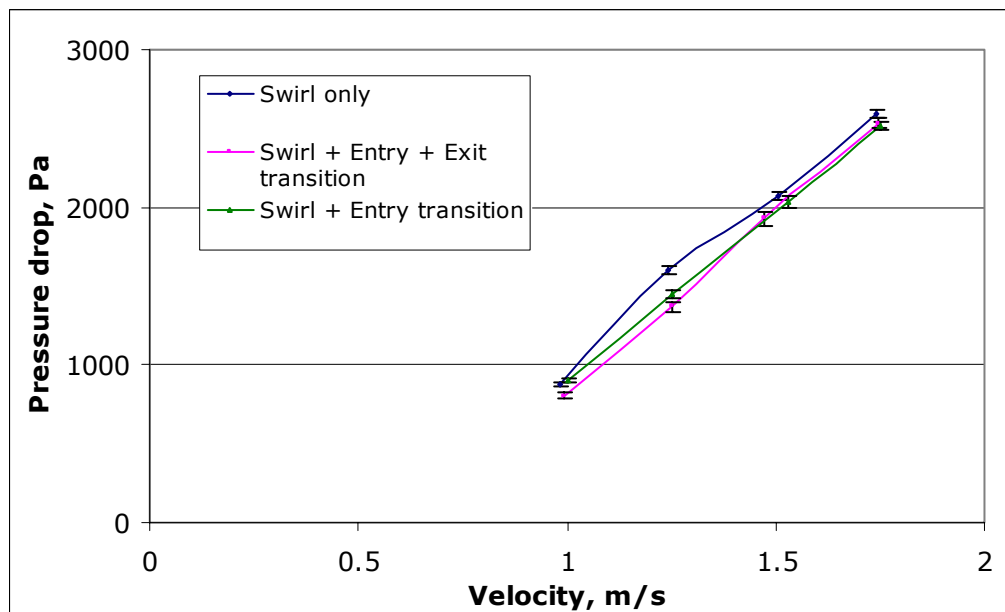


Figure 8.5: Pressure Loss Curve for RD 4.5; 2kg of solids added, 1.38% w/w and 0.31% v/v (error bars indicate standard error in manometer reading)

Pressure drop increased with velocity in all cases, showing an increasing gradient as velocity increased, in agreement with the findings of Ganeshalingam (Ganeshalingam 2002). The water only tests (Figure 8.2) showed that overall pressure loss was lower with the entry transition incorporated and further lower with exit transition incorporated. This may be

attributed to the transitions eliminating exit losses at entry to and exit from the swirl pipe. However, the friction factor of the transition pipes was greater than cylindrical pipe. This will have resulted in higher pressure drop across the transitions themselves.

The optimum swirl pipe used here in conjunction with transitions was optimised for length without inclusion of transitions. With transitions, a shorter length of swirling flow pipe is required to induce the equivalent swirl intensity (Chapter 5), thus pressure loss can be further reduced.

When solids of RD 1.4 were used (Figure 8.3), the pressure saving from the use of transition pipe is slightly more prominent than with water alone. The saving from entry transition was greater with the higher density solids of RD 2.7 (Figure 8.4). However with the inclusion of exit transition pipe a higher pressure loss was recorded when compared to just entry transition. Perhaps the saving gained through avoiding exit losses is not counteracted by the loss due to the roughness of the exit transition pipe surface. With the RD 4.5 solids (Figure 8.5), the pressure loss data were not entirely reliable due to the high variation of in-situ solids concentration. However, a distinct benefit was realised from the use of transitions.

Pressure saving from transitions is further discussed in Section 8.3.4.

8.3.2 Effect of Solids Density on Pressure Drop

Figure 8.6 compares the variation of pressure loss with velocity for the different density solids for the case of 'swirl + entry + exit transition'.

With solids of RD 1.4, the pressure drop did not increase much when compared to pressure drop with water only. This is in agreement with Ganeshalingam's (Ganeshalingam 2002) findings of the relative insensitivity of pressure drop to the presence of solids (he used solids of RD about 1.4). However, with the same concentration by weight of particles of a higher density of RD 2.7 the pressure loss was considerably higher (about 200Pa higher at each velocity). The low pressure drop observed with RD 4.5 solids was due to their accumulation in the lower section of the rig which resulted

in low solids concentration (C_w) in the upper section. As the relative density of solids increased the pressure loss increased.

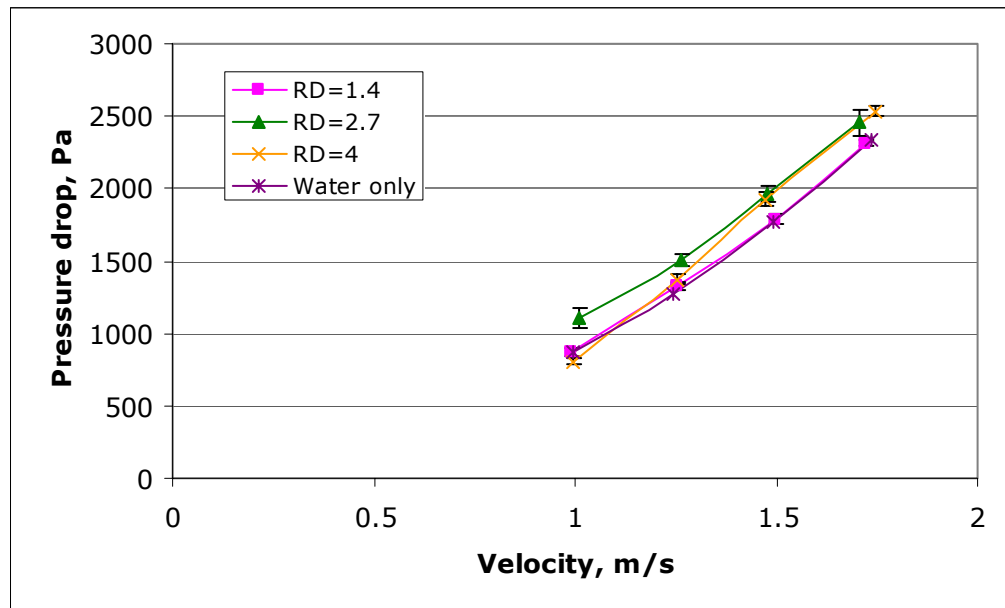


Figure 8.6: Pressure Loss Curve for 'Swirl + Entry + Exit transition' case; 2kg of each density added (RD 1.4 1.9% w/w, RD 2.7 1.9% w/w, RD 4.5 1% w/w) (error bars indicate standard error in manometer reading)

8.3.3 Effect of Solids Concentration on Pressure Drop

Solids concentration could only be determined at the exit to the header tank. From direct observation it was evident that concentration of solids varied throughout the rig. Only one concentration measurement was carried out at the highest flow velocity in each test.

RD 1.4 solids were used in tests to determine the effect of solids concentration on pressure loss. Pressure loss at measured concentrations of approximately 2, 4 and 6% are shown for the case of 'swirl + entry + exit transition' in Figure 8.7.

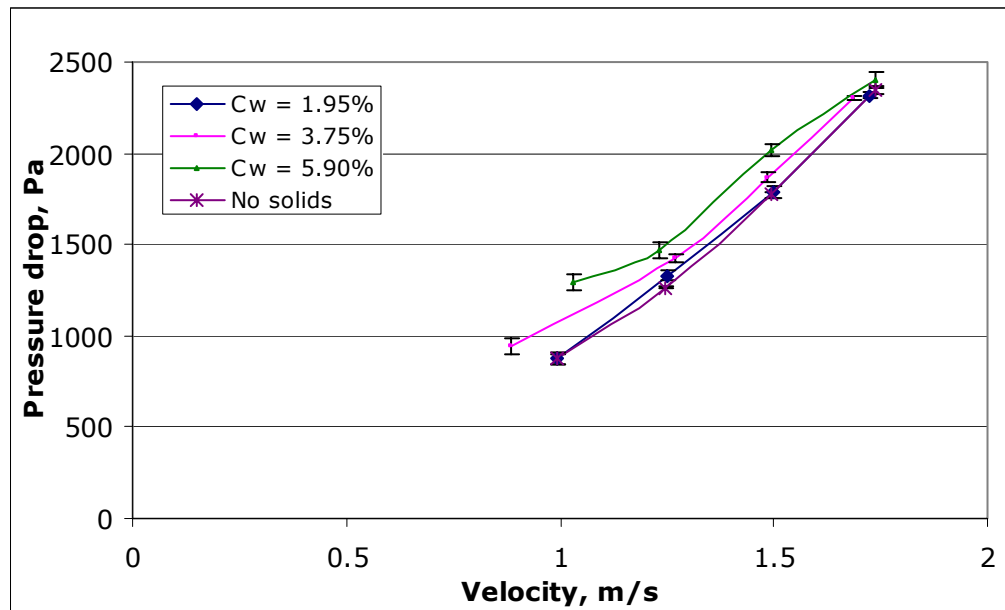


Figure 8.7: Effect of Solids Concentration for 'Swirl +Entry + Exit transition' Case with RD 1.4 Solids (error bars indicate standard error in manometer reading)

In Figure 8.7, the pressure loss where a low concentration of solids was used was not much greater than for water only. However on adding increasing amounts of solids the pressure loss increased. The increased pressure required for higher concentrations was comparatively less as the flow rate increased.

Ganeshalingam (Ganeshalingam 2002) noted that, relative to the increase in pressure loss with increasing solids concentrations in cylindrical pipes, the pressure drop in swirl pipes was insensitive to changes in solids concentration. This finding still holds for the combination of optimised swirl and transition pipes with solids of low relative density. As stated by him, this suggests a clear advantage of swirling pipe flow in that much higher solids loading could be transported without pipeline blockage. However, it may be useful to test this theory on solids of higher relative density since the current results and those of Ganeshalingam were only for solids RD of around 1.4.

8.3.4 Pressure Advantage of Transition

Figure 8.8 shows the advantage in terms of pressure saving from the use of entry and exit transitions in conjunction with swirling flow pipe. The pressure

losses in the cases where entry and exit transitions were included have been subtracted from the pressure loss for swirl pipe only to give the results shown in Figure 8.8. Therefore a positive value indicates the pressure saving from the inclusion of transitions.

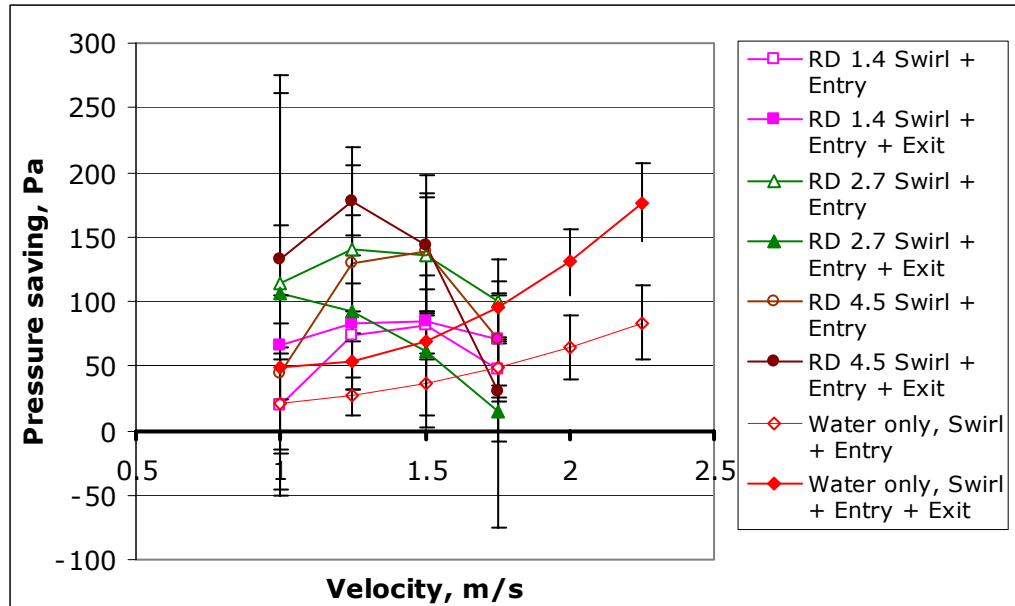


Figure 8.8: Pressure Saving from use of Entry and Exit Transition Pipes (over a total pipe length of approximately 3.325m); 2kg of solids added in each test (error bars indicate standard error)

There was a distinct advantage from the use of entry and exit transition. With water only flow the pressure saving increased with increasing flow velocity. This trend was not observed with the addition of solids. There appeared to be an optimum velocity when the best saving in pressure was gained. This may be the flow velocity at which particles started settling out thereby making it the flow regime when swirl induction was most advantageous. At lower axial flow velocities the pressure saving with settling solids slurry was clearly higher than with water only tests.

Error analysis of manometer readings of pressure was carried out similar to the procedure described in Appendix A7.1 for water only flows. The numerical results are given in Appendix A8.1. The standard error in the reading of the manometers was higher in the cases incorporating solids. This was largely an effect of the high variation in solids concentration in the rig. The errors were also accumulative as the data for pressure loss including transitions was subtracted from that excluding transitions. Since the pressure saving is small in comparison to the pressure loss measured, the

resulting percentage error (based on pressure saving) is high (see Appendix A8.1 for sample calculation). Therefore it is difficult to make a final conclusion regarding the trends observed in Figure 8.8. However, the significantly positive values shown indicate a distinct advantage from the use of transitions.

The high pressure saving that was expected from the water only CFD simulations at higher flow velocities was not achieved with slurry. For the low density (RD 1.4) and high density (RD 4.5) solids, at low to medium velocities, the pressure saving from use of exit transition (in addition to entry transition) was clear. However, for RD 2.7 solids, the run without exit transition showed a higher pressure saving. This may be due to experimental error through varying concentrations in the rig.

As the solids density increased, the pressure saving gained through the use of transitions also increased.

8.4 Settling Length

8.4.1 Effect of Velocity on Settling

From the literature, a graph of settling length versus velocity is expected to have an increasing gradient since swirl decay rate should decrease with increasing velocity (Steenbergen 1998). However, the measurement of settling length was rather crude and taken to the nearest 50mm. Therefore, although the results show overall trends, a more accurate measurement technique (such as tomography or optical absorption) is required.

Where exit transition was used, settling distances were measured from the outlet of the exit transition pipe.

Figures 8.9 to 8.11 show the comparisons of settling length for each combination of pipes studied with solids of RD 1.4 (Figure 8.9), RD 2.7 (Figure 8.10) and RD 4.5 (Figure 8.11).

The results for RD 1.4 solids in Figure 8.9 show no clear advantage of maintaining swirl for longer with the addition of entry and exit transitions.

Ganeshalingam concluded from his experiments with *Swirly-Flo* pipe and plastic beads of RD 1.4 that such a pipe every 1.25m would be sufficient to sustain swirling flow, at say, 1m/s. From Figure 8.9, it is shown that particles began settling approximately 1.25m downstream of the optimised swirl pipe at 1m/s. Thus, an optimised swirl pipe every 1.25m would be sufficient to keep particles in suspension and disallow settling. However, Ganeshalingam used a much longer *Swirly-Flo* pipe than the optimised design used here (1m as opposed to 400mm). Thus the advantage in terms of swirl from the optimisation is evident.

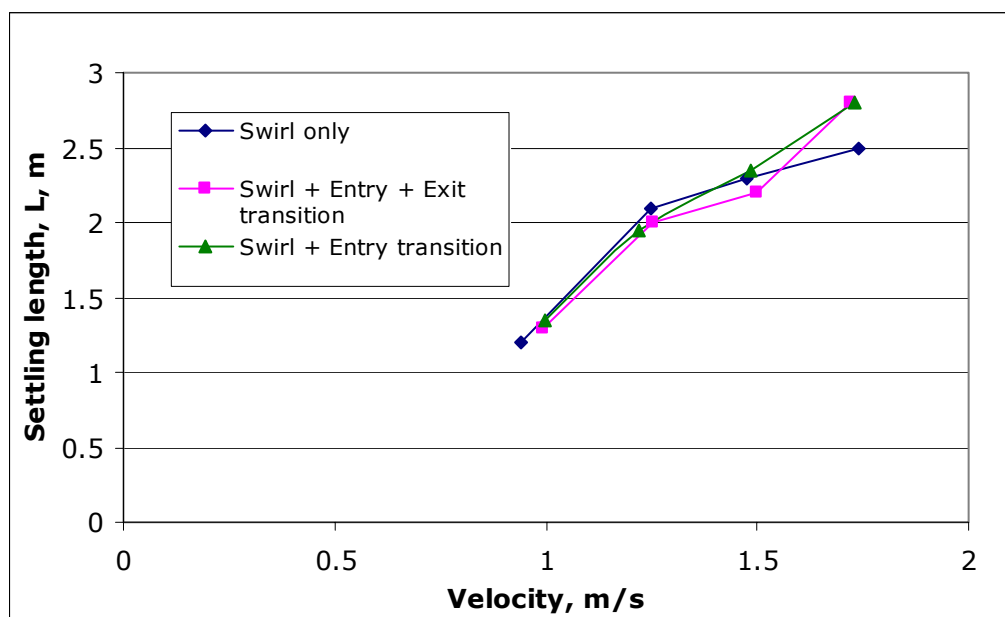


Figure 8.9: Settling Length for RD 1.4 Solids; Length Downstream when Settling Begins; 2kg of solids added in each test

RD 2.7 solids (Figure 8.10) showed a very apparent advantage from combined use of entry and exit transition although there was no discernible advantage from just entry transition.

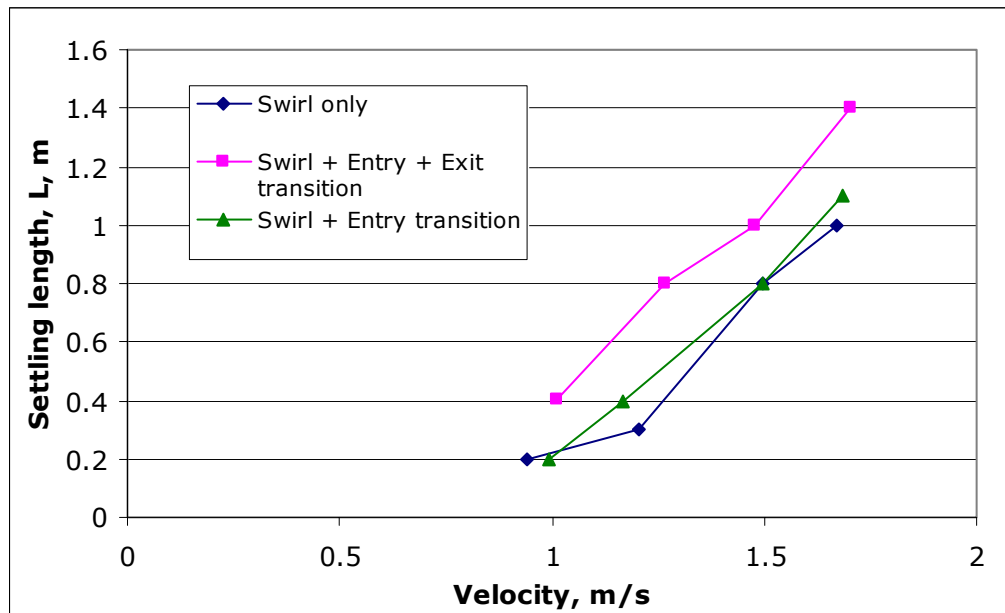


Figure 8.10: Settling Length for RD 2.7 Solids; Length Downstream when Settling Begins; 2kg of solids added in each test

With RD 4.5 solids (Figure 8.11a-b), a second measure of settling length in terms of when settling was clearly visible (rather than the beginning of settling) was used in addition. This showed an advantage from using entry and exit transition together although no advantage was shown from use of entry transition alone.

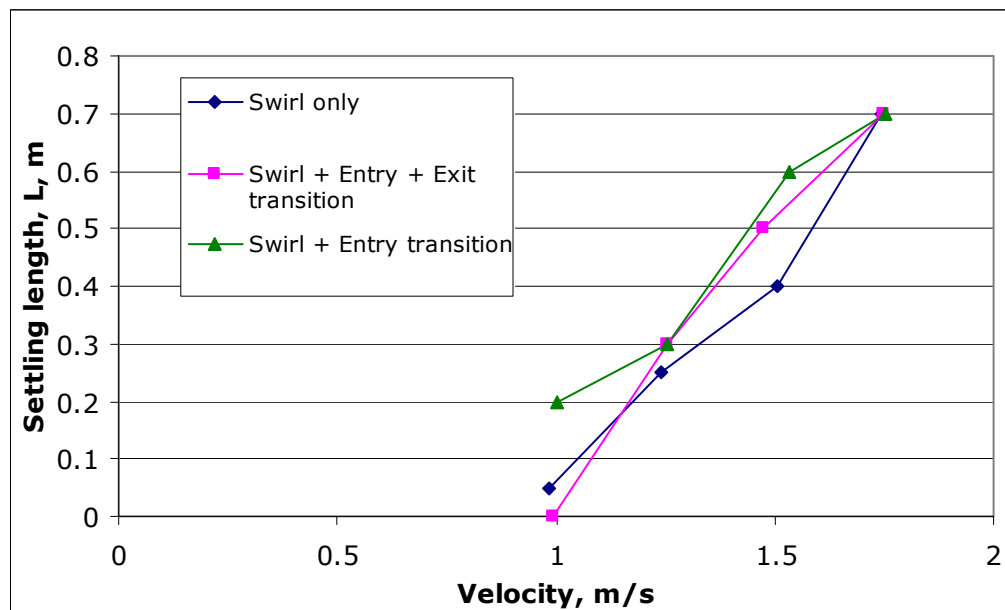


Figure 8.11a: Settling Length for RD 4.5 Solids; Length Downstream when Settling Begins; 2kg of solids added in each test

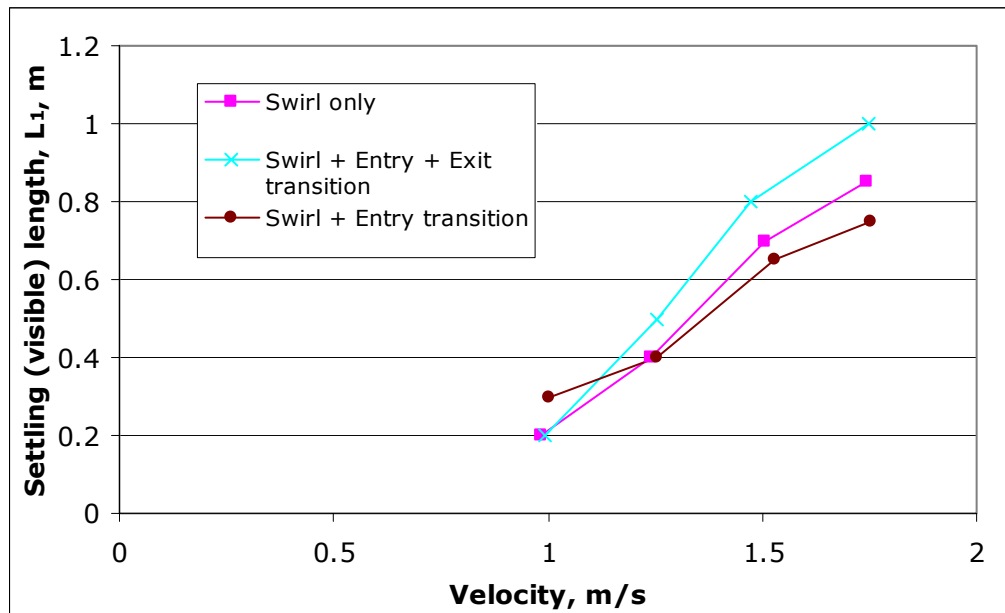


Figure 8.11b: Settling Length for RD 4.5 Solids; Length Downstream when Settling is 'Clearly Visible'; 2kg of solids added in each test

Although an increase in settling length was expected when entry transition was used (since it generates more swirl as predicted by CFD), this was not clear from the crude measurements made in the experiments. The advantage from the use of exit transition however was proven, particularly for the higher density solids. It was difficult to distinguish any particular trends (such as exponential increase in settling distance with increasing flow velocity as suggested by other researchers).

8.4.2 Effect of Solids Density on Settling

The problems of varying in-situ concentration of RD 4.5 solids did not affect the settling length results as drastically as the pressure loss results.

Figure 8.12 shows the variation of settling length with velocity for the different density solids for the case of 'swirl + entry + exit transition'. The higher the density, the greater was the tendency of the particles to settle. Also the lower density particles showed a higher gradient of increasing settling distance with increasing velocity.

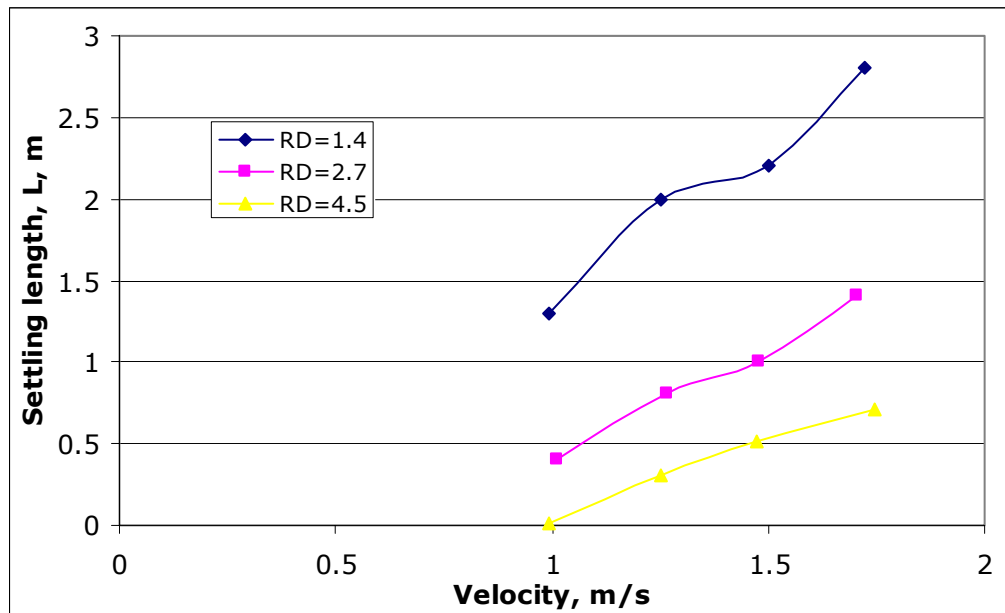


Figure 8.12: Effect of Solids Density on Settling for 'Swirl + Entry + Exit Transition' Case; 2kg of solids added in each test

8.4.3 Effect of Solids Concentration on Settling

Figure 8.13 shows the variation of settling length with velocity at different solids concentrations for the case of 'swirl + entry + exit transition'. The results given are for RD 1.4 solids.

The difference in solids concentration did not affect the settling length at lower concentrations (2-4% w/w). However, on increasing the solids concentration to 6% w/w, settling distance shortened by approximately 20% at the lower velocities. This is in agreement with observations by Ganeshalingam (Ganeshalingam 2002). As velocity increased the detrimental effect of concentration on settling length reduced.

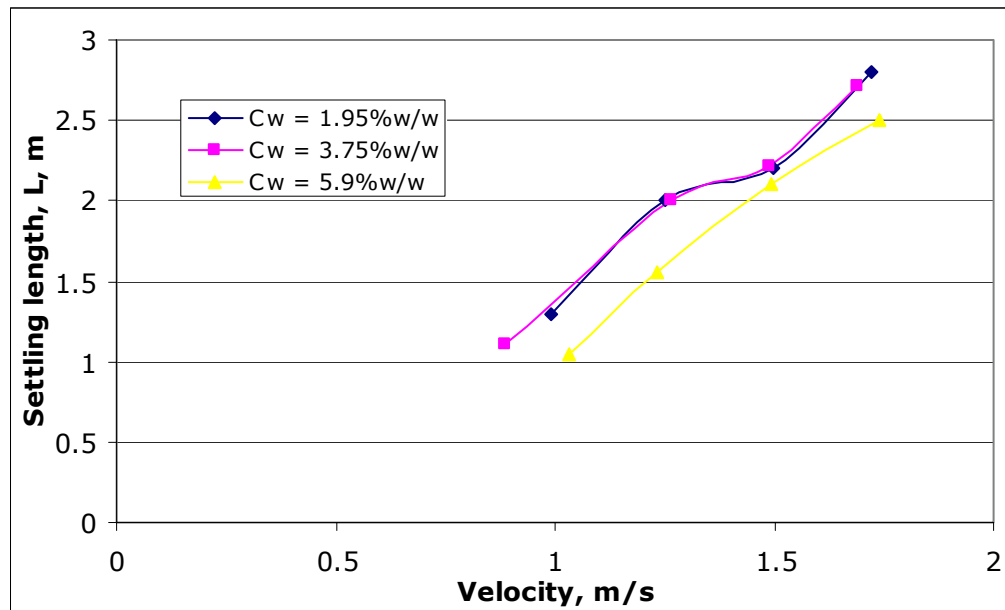


Figure 8.13: Effect of Solids Concentration on Settling for 'Swirl + Entry + Exit Transition' Case; RD 1.4 solids

The effect of concentration on the advantage provided by the transitions was not investigated due to time constraints.

8.4.4 Advantage of Transition in Delaying Settling

There was an overall increase in the length before settling began with the use of transitions. This may be attributed to the greater swirl intensity generated and, in the case of the exit transition, reduced swirl decay (as established from CFD, Chapter 7).

Figure 8.14 shows the advantage in terms of lengthening the distance before settling occurs when transitions are included. The settling length for swirl pipe only was subtracted from settling length measured when including entry and exit transitions to give the additional length for which the particles are kept in suspension due to inclusion of transitions.

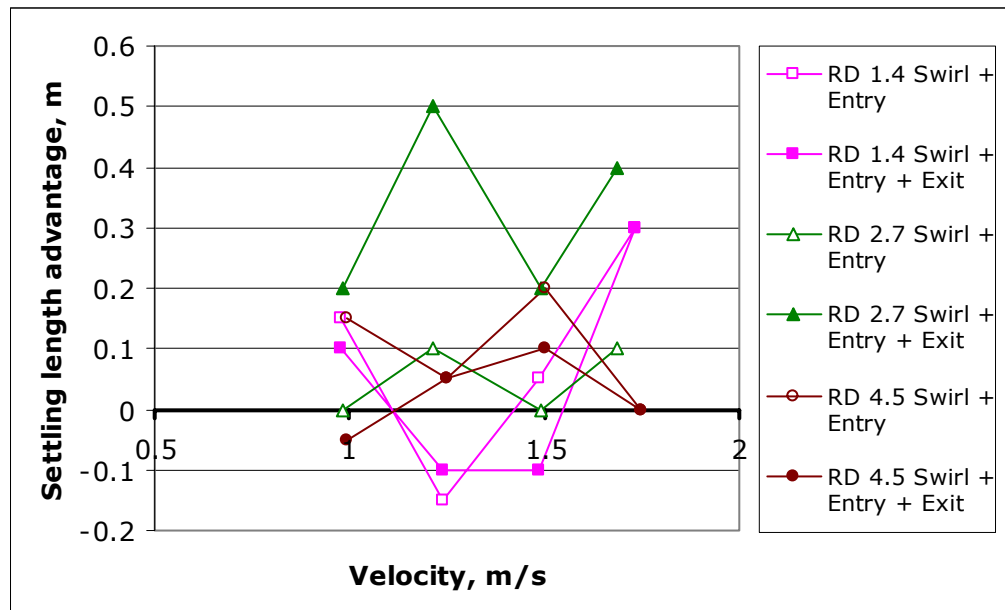


Figure 8.14: Swirl Advantage from use of Entry and Exit Transition Pipes; 2kg of solids added in each test

The results in Figure 8.14 have not been adjusted for the differences in flow velocity in the different runs which may have affected settling distance considerably. Therefore, as with the estimation of pressure saving (Section 8.3.4, Figure 8.8), there are high experimental errors.

However, from the overall positive values in Figure 8.14, it can be inferred that the effect of both entry and exit transition was to increase the length before settling began. The advantage was more prominent for the higher density solids. The best advantage was observed for the RD 2.7 solids. However the variations in concentration made estimating settling length difficult for RD 4.5 solids.

CFD indicated that exit transition did not lower the swirl intensity, rather, it ensured that swirl decayed slower in the pipe (see Chapter 7, Section 7.4.4). Therefore, the settling length was expected to be greater with exit transition in place in addition to entry transition. However, other than for RD 2.7 solids, this advantage is not clearly distinguishable in Figure 8.14. As stated previously, the measurement of settling length was rather crude and a better method of estimating settling length may show the advantage more clearly.

8.5 Flow Patterns

The flow patterns of particles downstream of the swirling flow pipe with and without transitions were photographed. A range of flow patterns were encountered from saltation, sliding bed and asymmetric distribution of particles prior to the swirl pipe, to almost homogeneously distributed particles after the swirl pipe. The particles tended to follow the helical paths defined by the four lobe surfaces of the swirl pipe as illustrated in Figure 8.15. This was particularly visible with low solids concentrations, and in the cylindrical pipe immediately downstream of the swirl pipe exit.

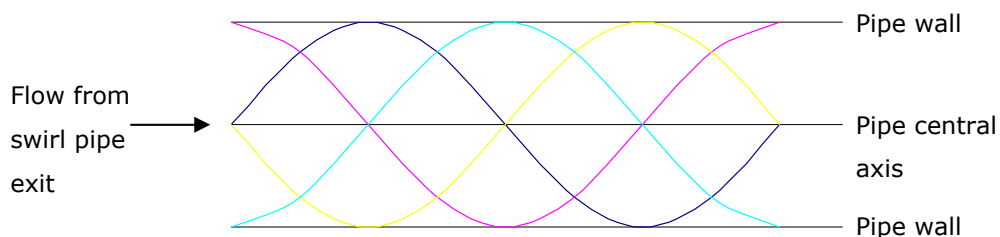
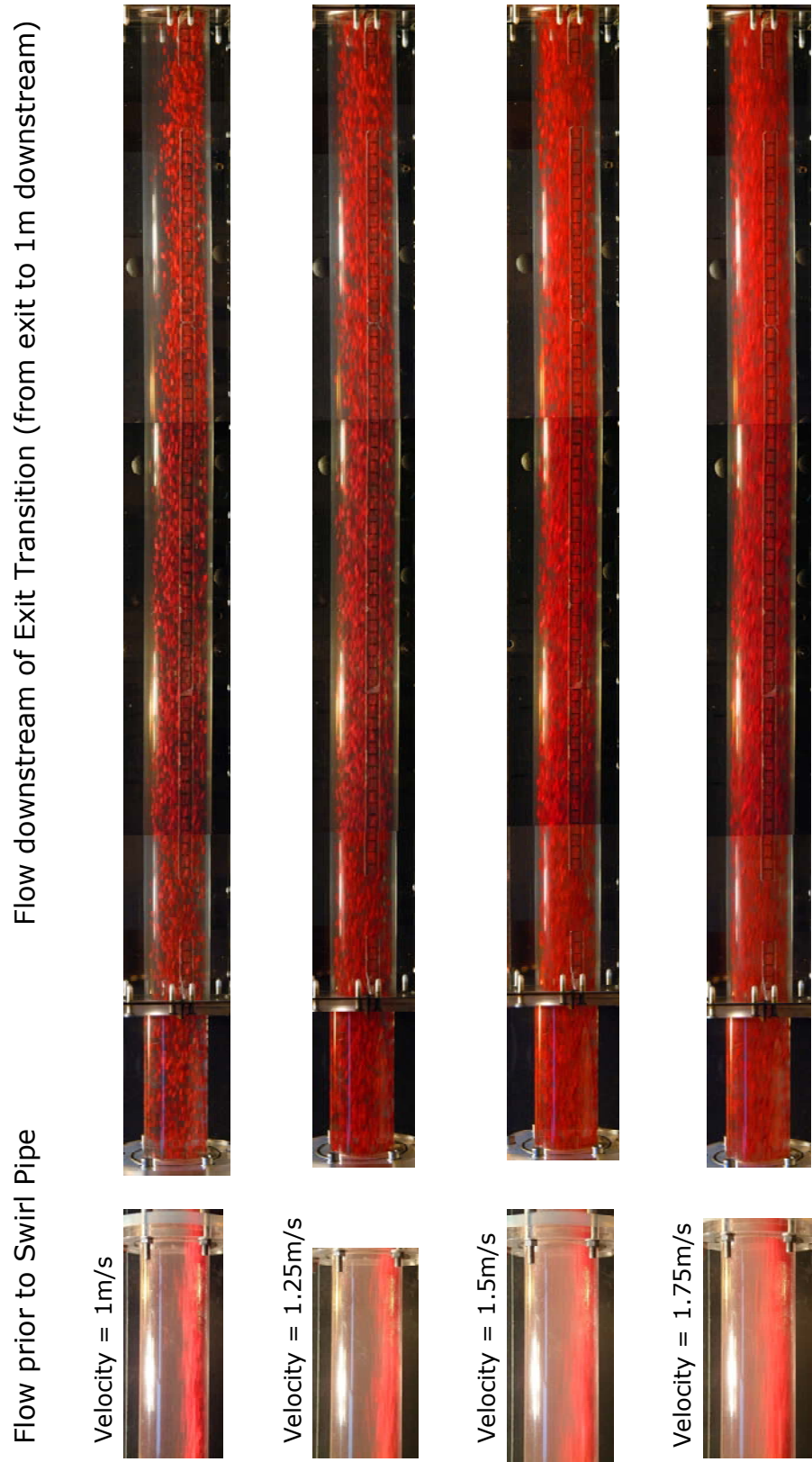


Figure 8.15: Illustration of Particle Tracks in the Cylindrical Pipe following Helical Paths defined by Lobe Surfaces of the Swirl Pipe

Figure 8.16 shows the photographs of flow immediately downstream of the exit transition pipe (in the case with 'swirl + entry + exit transition') for RD 1.4 solids at a concentration of approximately 4% w/w. At all velocities employed, the particles prior to the swirl pipe were asymmetrically distributed travelling principally along the bottom of the pipe. Downstream of the swirl and transition pipes the particles were well distributed. The flow pattern thus changed from heterogeneous suspension to almost homogeneous suspension at exit of swirl pipe, which continued for several diameters downstream of the swirl pipe. In this case the turbulence generated by the swirl and transition pipes was sufficient to counteract the settling tendency of the heterogeneous slurry, resulting in better particle distribution. At all velocities, but for the lowest, the particles remained in suspension and did not settle out within the distance photographed (about 1m).



**Figure 8.16: Photographs of Flow at Velocities 1 to 1.75m/s;
'Swirl + Entry + Exit Transition' Case, RD 1.4 Solids, 4% w/w**

As with the lower density solids, the RD 2.7 solids were asymmetrically distributed and travelling along the bottom of the pipe prior to the swirl and transition pipes (Appendix A8.2). At lower velocities, dune-like motion of particles was observed prior to the swirl pipe as a result of saltation over a moving bed of particles. Downstream of the swirl pipe, the flow pattern changed to a heterogeneous suspension, however with relatively good distribution of particles. At higher velocities, flow changed from heterogeneous suspension to almost homogeneous suspension downstream of the swirl pipe.

The solids started settling out much quicker due to their higher density and except at the highest velocity of 1.75m/s, settling began in the distance photographed at all lower velocities. At the lower velocities in particular (1-1.25m/s), it was clear that the combination of entry, swirl and exit transition sustained swirl for longer than the swirl pipe alone. Breakage of the solids clouded the water in some of the photographs taken therefore they are not very clear.

With RD 4.5 solids saltation flow was observed upto 1.5m/s before the swirl and transition pipes which changed to heterogeneous suspension after the swirl pipe (Appendix A8.3). The particles settled within the photographed distance at all velocities used. Breakage of the solids resulted in clouding the water which made it difficult to clearly distinguish settling lengths, especially at higher velocities.

The observed elimination of the flow dragging along the bottom of the pipe would mean that the working life of the pipes could be increased since wear will be distributed more evenly around the pipe surface. Wear measurements could be taken or predicted using a CFD technique for simple horizontal pipe flow to show this effect (see Chapter 2, Section 2.4.1).

A further rig run was carried out with mixed densities of solids. The weights of solids added to obtain approximately the same volume of each density of solids in the slurry are given in Table 8.2.

Table 8.2: Mixed Density Run

	Blue, RD = 2.7	Red, RD = 1.4	Yellow, RD = 4.5
Weight added, kg	1	0.519	1.667
Volume of solids, m ³	0.00037	0.00037	0.00037

The photographs of the mixed run (Figure 8.17) show the settling tendencies of the different densities at a range of velocities. They show that the RD 4.5 density (yellow) settled fastest downstream of the swirl and transition pipes and travelled along the bottom of the pipe. The RD 2.7 density (blue) settled next forming a layer that roughly travelled along the top of the yellow solids. The RD 1.4 solids did not settle in the distance photographed and showed an even distribution in the pipe above the settled solids. In the photographs taken prior to the swirl and transition pipes, the three densities tended to form 3 layers with the most dense solids travelling along the bottom of the pipe, upon which was the medium density, and the lowest density solids travelled more towards the pipe centre-line.

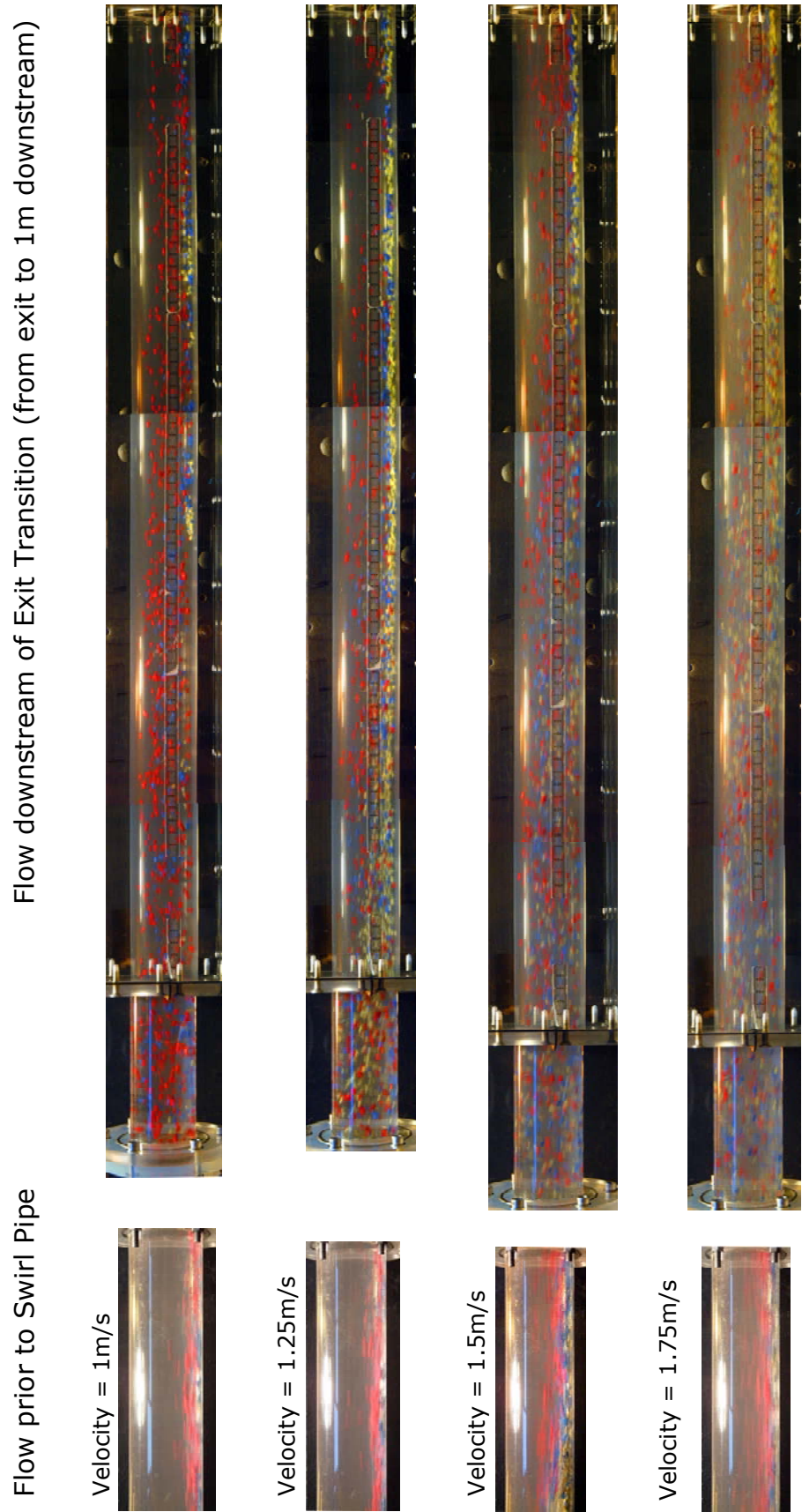


Figure 8.17: Photographs of Flow at Velocities 1 to 1.75m/s; 'Swirl + Entry + Exit Transition' Case, Mixed Densities RD 1.4 (Red), 2.7 (Blue) and 4.5 (Yellow)

8.6 Conclusions

- The high variation in solids concentration in the tests resulted in relatively high experimental errors.
- Steady state may not have been reached during the tests prior to taking results because not enough time was allowed between changing velocity and taking readings. However, this was unavoidable due to the high friability of the solids used.
- An online concentration measurement would be beneficial since carrying out measurements at the exit to the slurry tank was not sufficient.
- Transitions reduced pressure loss across the swirl pipe. As the solids density increased, the pressure saving also increased.
- Overall effect of transitions was to increase the settling distance.
- All experimental results were found to be in general agreement with findings of Raylor, Ganeshalingam and Tonkin, who carried out previous research on similar swirl pipe geometries.
- Tonkin showed that, as the solids density increased, the swirl pipe was beneficial at higher velocities because flow regimes where swirl is beneficial are extended to higher velocities. It was difficult to discern from the current results whether the benefits from transitions are also greater at higher velocities as solids density increased. A better method of estimating settling length would have to be devised and problems with solids concentration changes must be eliminated before this is possible.
- The theory that higher solids loading can be carried at low pressure cost in swirl pipe should be tested for solids of higher density than RD 1.4.

- Image processing of the photographs of flow patterns should be carried out to evaluate concentration and size distribution of the particles, in particular for the mixed density run. This would give further insight into the particle distribution achieved through optimised swirl and transition pipes.

CHAPTER 9: OPTIMISING SWIRL PIPE FOR NON-NEWTONIAN FLUIDS

9.1 Introduction and Background

The use of a helically shaped swirl-inducing pipe can improve particle distribution and reduce critical velocity for transport of settling slurries with Newtonian fluids (Raylor 1998; Ganeshalingam 2002). Recent efforts by Tonkin (Tonkin 2004) have been aimed towards investigating the effect of swirling flow on non-Newtonian transporting media.

Preliminary experimental results by Tonkin using Particle Image Velocimetry (PIV) showed that the optimum swirl pipe (4-lobed, pitch-to-diameter (P:D) ratio 8, see Chapter 2) designed with water as the transporting medium does not sufficiently induce swirl when Carboxymethyl cellulose (CMC) solutions were used as the transporting medium. The tangential velocity downstream of an optimised swirl pipe measured at different axial velocities lay within ± 0.2 m/s with no discernible swirl pattern. This is because more swirl intensity is required to overcome the higher shear stress in CMC solutions. It was therefore concluded that for CMC, a smaller P:D ratio was required in order to achieve the same effectiveness of swirling the flow as for water. This chapter details CFD optimisation of the 4-lobed swirl pipe based on P:D ratio for non-Newtonian fluids taking CMC as an example.

The optimum swirling flow pipe P:D ratio of 8 found from previous investigations with water (Raylor 1998; Ganeshalingam 2002) was not entirely in agreement with previous researchers who used other forms of swirl-inducing pipes consisting of helical ribs and rifling. However, many have stated that an optimum between about 5 and 11 exists.

- In 1967 S.E. Wolfe (Wolfe 1967) carried out investigations on a helically ribbed pipe. He concluded a pipe with P:D ratio of π ($\pi = 3.14$) appeared to be optimum in causing slurry rotation at minimum energy expenditure.

- Chu (Chu 1969) concluded that a P:D ratio of about 5 was optimum.
- Charles (Charles 1971) in 1971 carried out optimisation of a spirally ribbed pipe, and found that a P:D ratio of 5 gave the best efficiency. However, he only tested a range of P:D ratios from 1 to 5.
- Shriek (Schriek 1974) found in 1974, that a P:D ratio of approximately 8 was optimum.

The disagreement, particularly in the case of Wolfe, may be due to different viscosities of the fluids used.

9.2 Non-Newtonian Fluids

Viscosity can be defined by taking the physical example of a fluid between two parallel planes (Figure 9.1) (Schlichting 1979). If the bottom plane is stationary and the upper is moving and no slip between fluid and surfaces is assumed, a velocity gradient will be produced in the fluid. This velocity gradient, dv/dx or γ , is called the shear rate. The shear stress, τ , is applied to produce this shear rate. The viscosity of a fluid is then the proportionality constant that relates shear stress and shear rate.

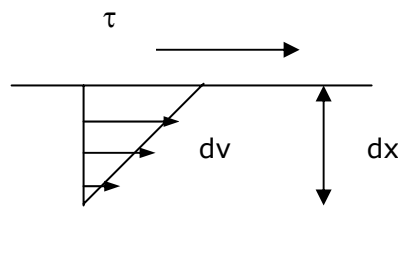


Figure 9.1: Velocity Distribution of Fluid between Two Planes

The viscosity of a Newtonian fluid is a constant value and shows no variation with applied shear rate. In contrast, the viscosity of non-Newtonian fluids varies with the applied shear (Hanks 1986; Nesbitt 2000). For a more thorough description of viscosity and the different forms of non-Newtonian fluids, refer to Tonkin (Tonkin 2004).

CMC is a pseudoplastic or shear-thinning fluid, so that its viscosity decreases with increasing rate of shear. The viscosity of pseudoplastic fluids can be related by the power law model. This model contains two constants to be estimated through viscometry (Heywood 1999):

$$\tau = k \times \gamma^n \quad (9.1)$$

k = consistency coefficient

n = flow behaviour index or power law index

τ = shear stress

γ = shear rate

k is a measure of the average viscosity of the fluid and n is a measure of the deviation of the fluid from Newtonian behaviour:

$n = 1$: Newtonian

$n < 1$: Shear-thinning

$n > 1$: Shear thickening

9.3 CFD Methodology

9.3.1 Defining a Non-Newtonian Fluid in Fluent CFD Software

The power law in Fluent was considered appropriate to model the non-Newtonian viscosity of CMC. It is defined as follows:

$$\eta = k \times \gamma^{n-1} \times e^{\frac{T_0}{T}} \quad (9.2)$$

η = non-Newtonian viscosity, kg/ms

T = temperature, K

T_0 = reference temperature, K

The viscosity was assumed to be temperature independent for the present case. In addition Fluent allows the user to define a minimum and maximum viscosity to give upper and lower limits of the power law (Figure 9.2). If the viscosity computed from the power law is less than η_{\min} , the value of η_{\min} will be used. Similarly, if the computed viscosity is greater than η_{\max} , the value of η_{\max} will be used. Values of η_{\min} of 0.001 kg/ms (viscosity of water) and η_{\max} of 1 kg/ms were used.

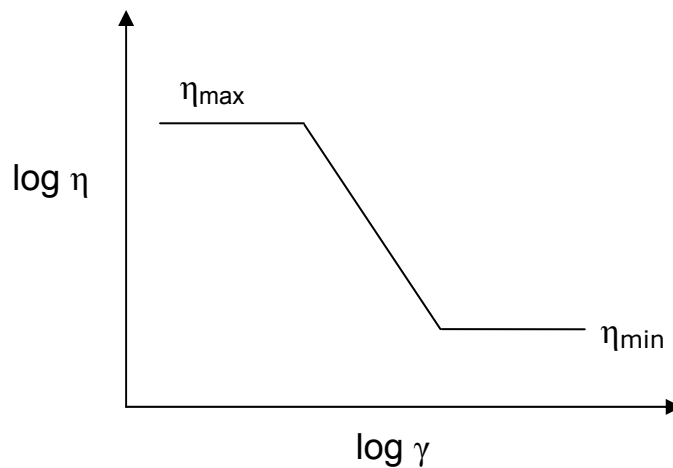


Figure 9.2: Variation of Viscosity with Shear Rate according to the Non-Newtonian Power Law (Fluent Inc. Lebanon 2001)

Tonkin measured viscosity of the CMC used in her experimental work using a rheometer and plotted the results as shown in Figure 9.3. She then used a best-fit curve of the form of Equation 9.1 to extract the values of k and n . With regards to the variation in the results, the following two conditions were selected for use as an input to two different sets of CFD simulations:

1. $n = 0.6, k = 0.6$
2. $n = 0.6, k = 1.2$

The second set will have a higher viscosity than the previous by definition of the consistency coefficient.

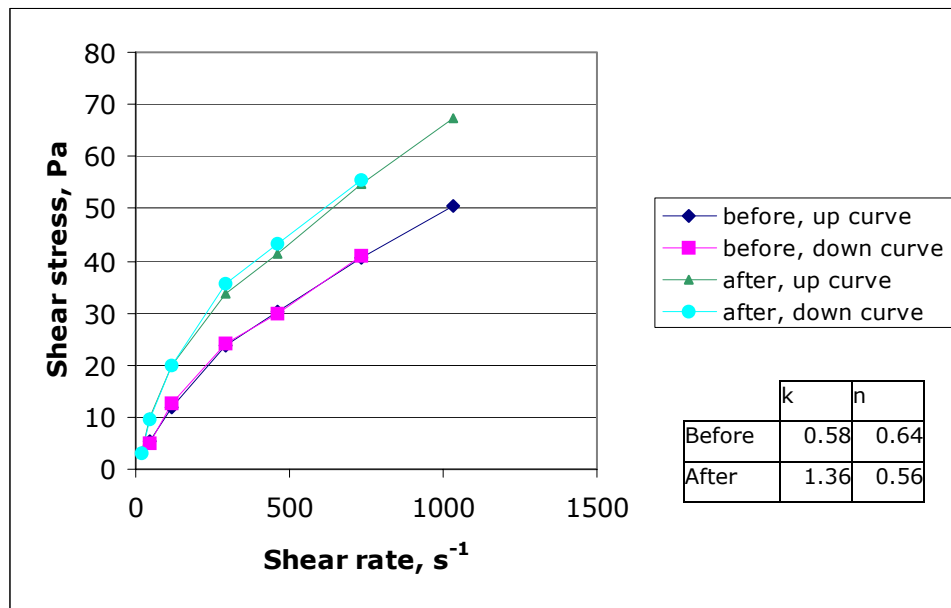


Figure 9.3: Rheograms and Rheological Parameters (Pseudoplastic Model) of the CMC Before and After Testing, (up and down curves shown, each is mean of 3 trials, after Tonkin (Tonkin 2004)).

9.3.2 Swirl Pipe Geometry

Swirl pipe geometries were created with different P:D ratios as illustrated in Figure 9.4. The geometry creation was carried out in Gambit software (Chapter 3). An unstructured tetrahedral mesh was applied (Chapter 4).

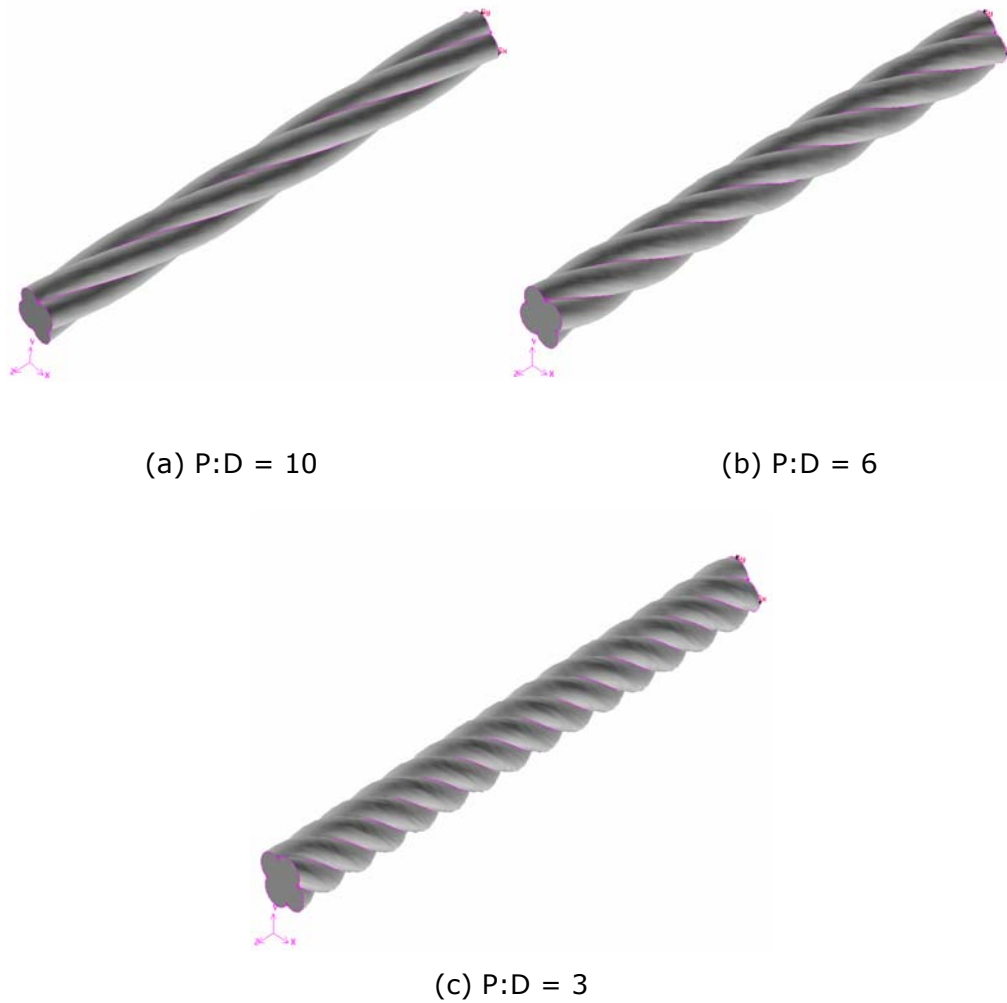


Figure 9.4: Swirl Pipes of Different P:D Ratios

The pipe with the smallest P:D ratio will have the tightest twist, thereby generating the highest swirl intensity. However, this will also result in the greatest pressure loss across the pipe. The optimisation process therefore consisted of determining the best P:D ratio that gives the greatest swirl intensity with relatively little pressure loss, i.e. greatest swirl effectiveness (see Chapter 2).

9.3.3 Parameters used in the Solver

The parameters used were as described in Chapter 4, except that the fluid used had the properties of CMC instead of water. The main assumptions were as follows:

- Uniform axial velocity at the inlet of 1.5m/s was assumed unless explicitly stated otherwise
- Laminar flow was assumed
- Simulations were carried out with single-phase flow (CMC only)

The flow parameters which were assumed for the simulations are given in Table 9.1.

Table 9.1: Flow Parameters for the CFD Simulations

Length of pipe	0.55 m
Axial velocity (u) at inlet*	1.5ms ⁻¹
Radial velocity (v) at inlet*	0 ms ⁻¹
Tangential velocity (w) at inlet*	0 ms ⁻¹
Pressure at outlet	0 Pa
Density of CMC	1002.8kgm ⁻³
Consistency index for CMC viscosity, k	0.6 / 1.2
Power law index for CMC viscosity, n	0.6

*Except where a velocity profile was loaded for the inlet

9.3.4 Grid Independence Tests

Grid independence tests were carried out to ensure that the results were independent of the number of cells in the mesh. The number of elements in the original grid was doubled until the difference in results at the outlet of tangential velocity and pressure loss was less than 5% and the trends were closely in agreement.

The results are presented in Appendix A9.1 for the pipes of P:D ratios 10 and 4.

9.4 Optimisation Results

9.4.1 Optimisation Results for $k = 0.6$

The variation of viscosity through the swirl pipe for a pipe of P:D ratio 4 is shown in Figures 9.5 and 9.6. An inlet circular velocity profile was used in this particular case only to ensure that the viscosity profile was established in the regions considered.

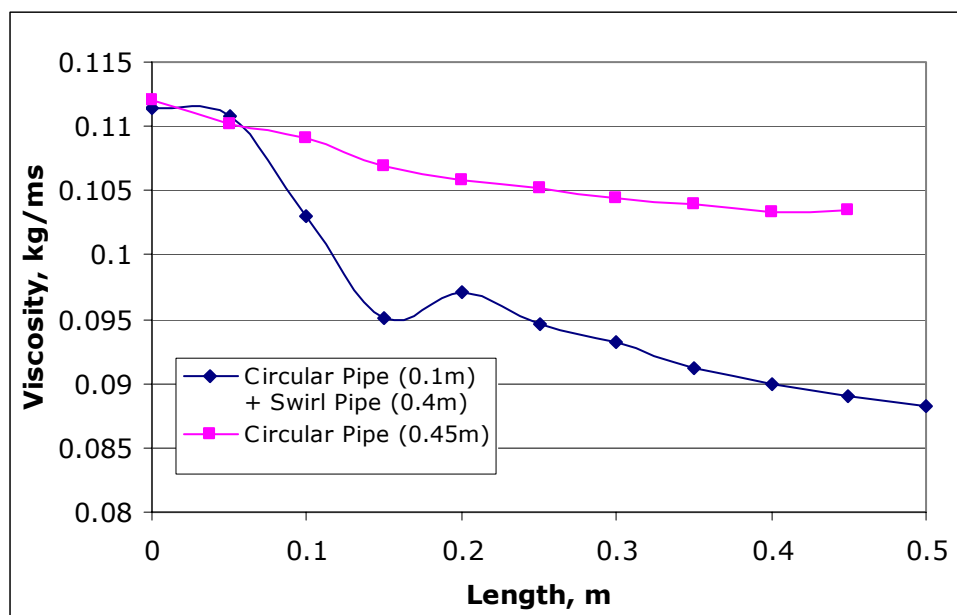


Figure 9.5: Viscosity Variation through the Pipe

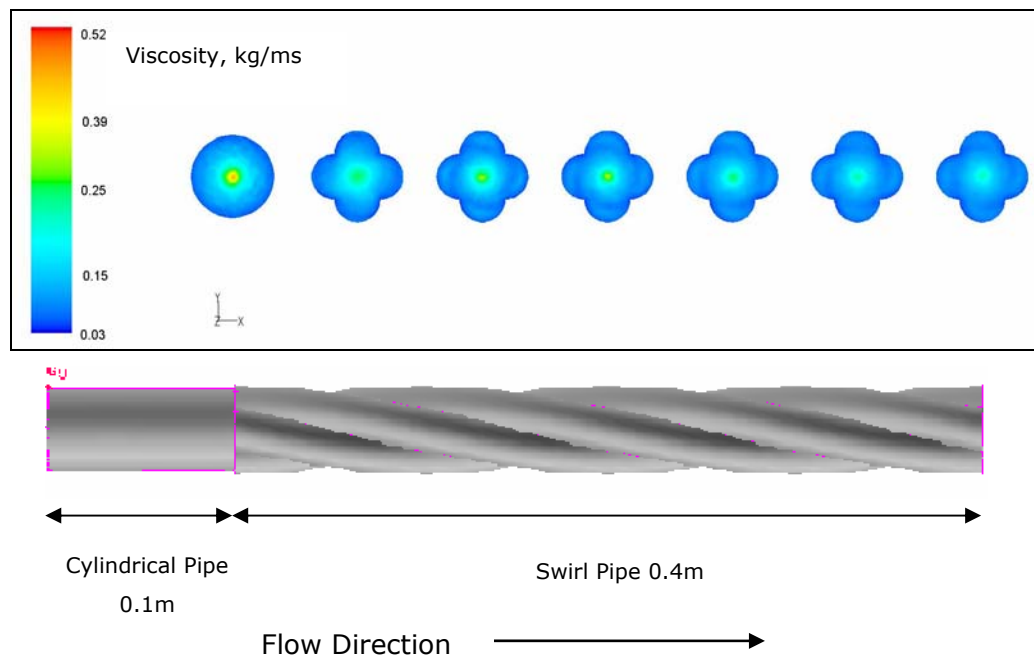


Figure 9.6: Viscosity Patterns in Pipe Cross-sections (P:D = 4) and Simulated Geometry

The variation of viscosity through the pipe, throughout length and in each cross-section, was interesting. Consider the principle behind the Hagen-Poiseuille equations. The fluid in the centre of the pipe is driven by upstream pressure, whereas at the pipe wall, the no slip assumption dictates zero velocity. This creates a velocity gradient across the pipe (Schlichting 1979). By definition the viscosity of a non-Newtonian fluid changes with shear rate (velocity gradient). If a non-Newtonian fluid is pumped through a swirl pipe it will be subject to velocity gradients in three directions, axial, tangential and radial. This could lead to complex viscosity patterns in the non-Newtonian fluid. This will also mean that a more uniform viscosity profile will be obtained in the swirl pipe as opposed to circular pipe due to the greater degree of mixing achieved.

In agreement with the above, CFD results indicated the existence of a high viscosity core in fully developed circular pipe flow (Figure 9.6 far left). This core can be broken down with the use of swirl pipes giving a more uniform viscosity profile (Figure 9.6, far right).

Figures 9.7 and 9.8 present the results of optimisation simulations carried out. The simulation geometries were as shown in Figure 9.4 with no inlet cylindrical pipe sections. The difference from using CMC as the transporting medium in place of water in the same pipe geometry is highlighted. Due to its lower viscosity, water resulted in much lower pressure loss, and a greater amount of tangential momentum was achievable with a pipe of the same P:D ratio.

It was also evident that the smaller the P:D ratio, and thereby the tighter the twist, the greater was the tangential velocity imparted upon the flow. However this also resulted in an increased pressure drop.

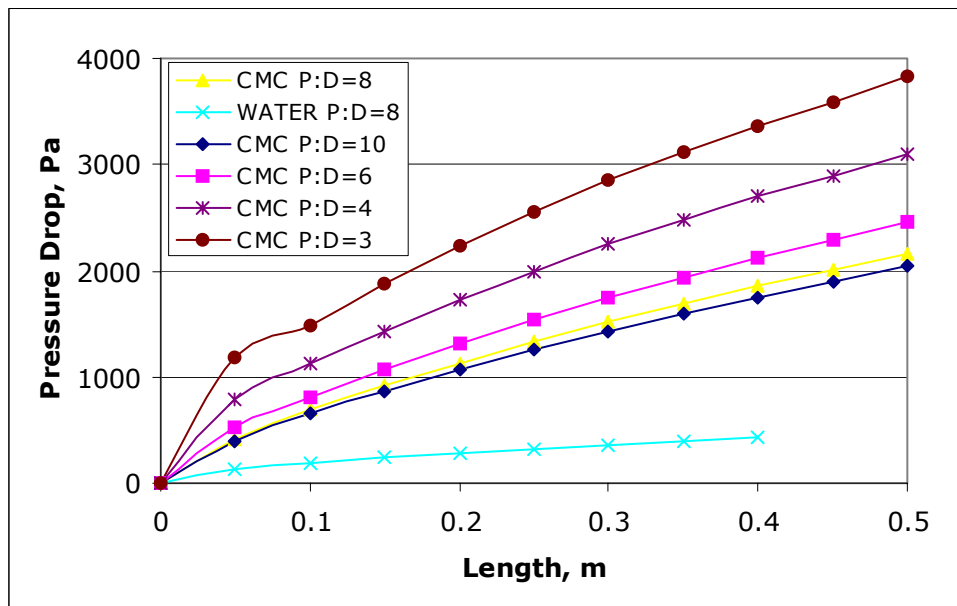


Figure 9.7: Pressure Drop versus Length Characteristic for Pipes of Different P:D with CMC (Result for Water is shown for comparison)

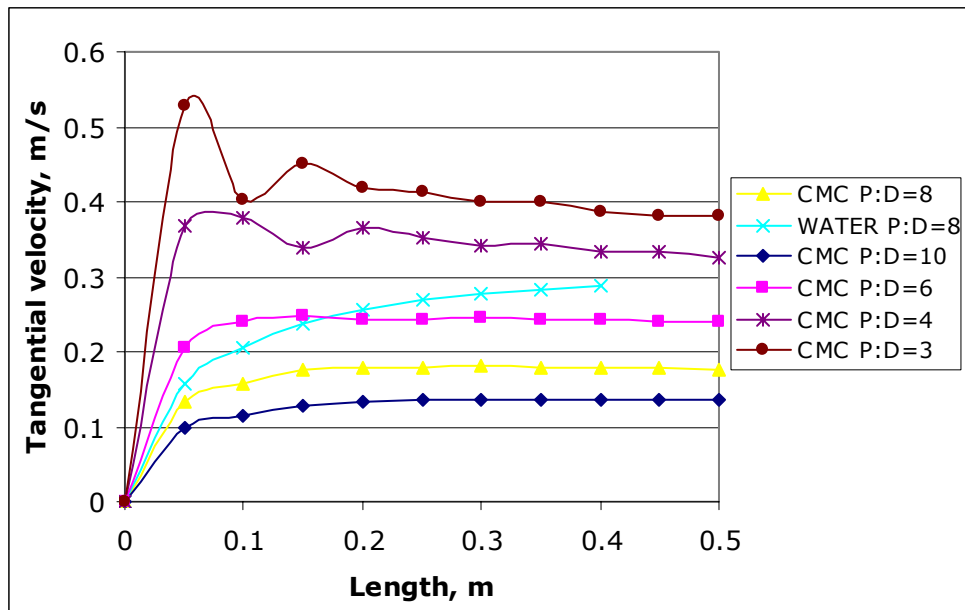


Figure 9.8: Tangential Velocity versus Length Characteristic for Pipes of Different P:D with CMC (Result for water is shown for comparison)

From the plot of swirl effectiveness for the different pipes (Figure 9.9; evaluated at a length of 0.5m), the pipe with P:D ratio 6 showed the maximum value. A P:D ratio between 4 and 6 gave superior swirl effectiveness depending on the length of the swirl pipe at which the parameter was evaluated. A pipe of P:D ratio of around 5 was therefore the optimum geometry for swirl induction to CMC solutions with viscosity defined by a consistency coefficient of 0.6.

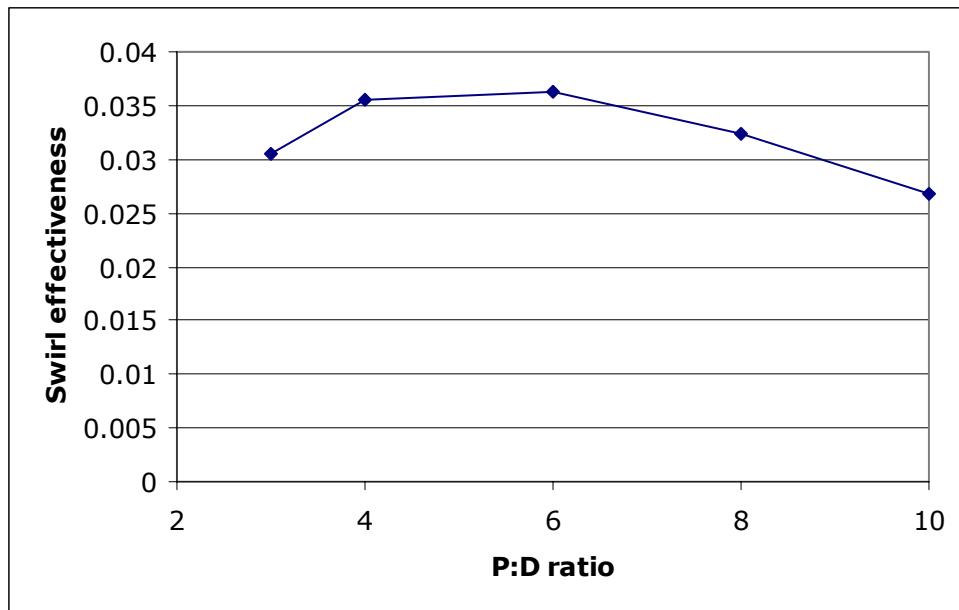


Figure 9.9: Optimising Swirl Pipe for P:D Ratio with respect to Swirl Effectiveness Parameter (evaluated at a length of 0.5m)

9.4.2 Optimisation Results for $k = 1.2$

The same procedure of optimisation was repeated for CMC with a higher consistency coefficient, and thereby a higher overall viscosity. The optimum was found to be at around P:D ratio of 4. The higher viscosity fluid showed a lower optimum P:D ratio (Figure 9.10) as compared to the lower viscosity fluid. It is also interesting to note the severe reduction in swirl effectiveness for the higher viscosity fluid (maximum swirl effectiveness was 0.02 (Figure 9.10) compared to 0.036 (Figure 9.9) for lower viscosity fluid).

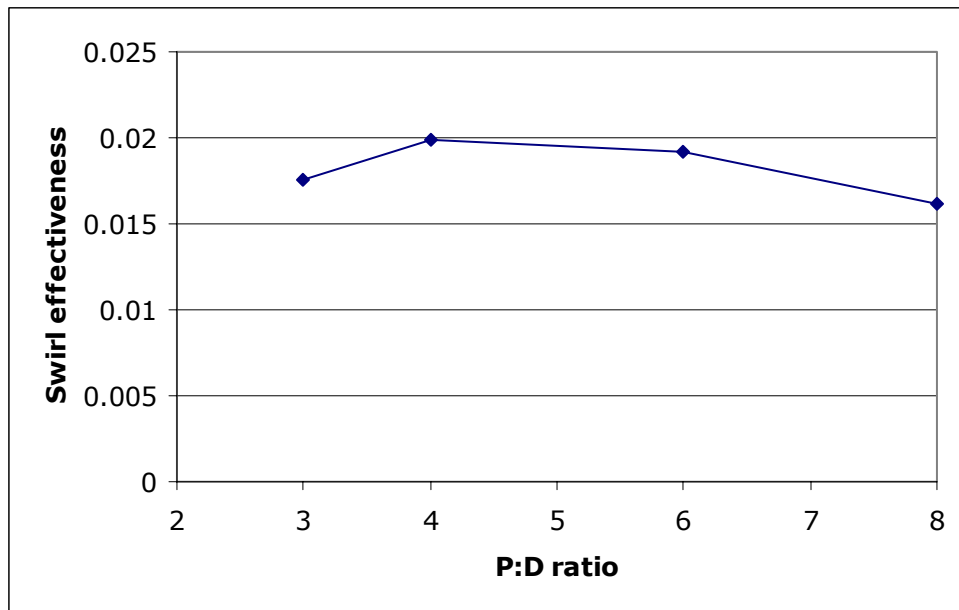
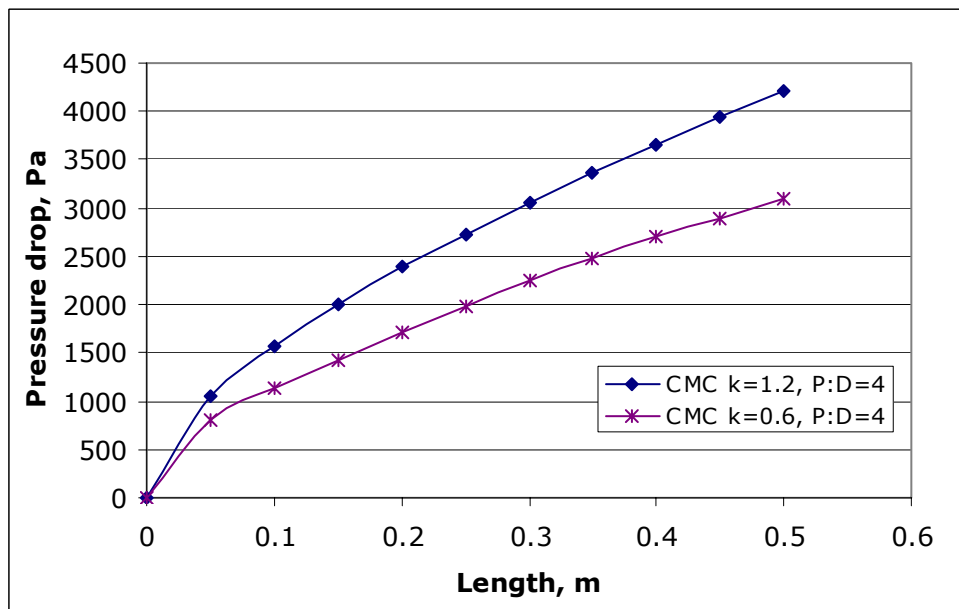
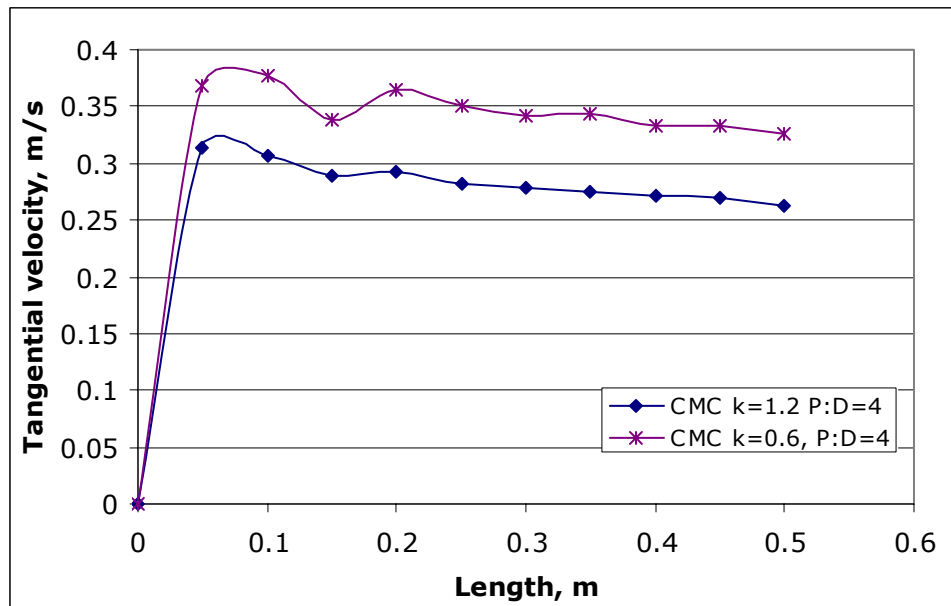


Figure 9.10: Optimising Swirl Pipe for P:D Ratio with respect to Swirl Effectiveness Parameter (evaluated at a length of 0.5m)

Figure 9.11 shows that, for the same pipe geometry, the higher viscosity CMC resulted in a much higher pressure loss across the pipe with a lower imparted tangential velocity.



(a) Pressure Loss



(b) Tangential Velocity

Figure 9.11: Comparison of High ($k=1.2$) and Low ($k=0.6$) Viscosity CMC Solutions

9.5 Conclusions

- Swirl pipe geometry for non-Newtonian fluids was optimised on the basis of swirl effectiveness.
- Key CFD results were in agreement with experimental results obtained for CMC on a pipe flow rig by Tonkin. Further validation of CFD simulation of non-Newtonian fluids is for future work.
- The optimum P:D ratio for CMC/water mixtures was shown to be close to 5. This contrasts with the figure for water of nearly 8 and estimates in the literature between 3 and 11 for slurries.
- Swirl intensity for the CMC/water mixtures was significantly reduced on those from water trials. Swirl intensity for the higher viscosity mixture was much reduced on the mixture with lower viscosity, and the optimum P:D ratio also reduced. P:D ratio was approximately 4 for the higher viscosity and approximately 5 for the lower viscosity.
- The findings from the CFD trials backed up PIV results by Tonkin (Tonkin 2004) showing low transmission of tangential velocities with CMC as the carrier fluid.
- Swirling motion, which creates circumferential shear, appeared to break down the higher viscosity core present in circular cross-

sections. This higher viscosity core flow is to be expected with a shear-thinning liquid. The lowering of viscosity at the core could be shown to occur over the length of the swirl-generating pipe in CFD trials.

- Other non-Newtonian fluids can be simulated in a similar way, including simulating the presence of solids by using Einstein's equation for laminar suspensions of spheres as was carried out by Ganeshalingam (Chapter 2, Equation 2.18).

CHAPTER 10: CONCLUSIONS AND FUTURE WORK

10.1 Conclusions

10.1.1 CFD Optimisation and Validation for Single Phase Flow

- The 4-lobed transition pipe was found to be superior to the 3-lobed in agreement with swirl pipe optimisation results. A transition design based on lobe area growth to core area growth, and with a greater lobe development at the start of the pipe, was found to be optimum for use as an entry transition. The same geometry was the optimum when used as an exit transition. No advantage was gained from the use of the variable helix studied over the geodesic helix for entry transition.
- Entry transition pipes were more effective at swirl induction, inducing more tangential velocity at a lower pressure cost, than the optimised swirl pipe geometry. However, the tangential velocities generated by the transitions were not as high as the swirl pipe, therefore their benefits accrue from use in conjunction with swirl pipe.
- Use of entry and exit transition for swirling flow pipe in place of cylindrical pipe showed a clear advantage in reducing pressure losses at the entrance to the swirl pipe and at the exit from the swirl pipe.
- Where entry transition was used in conjunction with swirl pipe a higher tangential velocity was generated which appeared to be constrained by the geodesic swirl pipe geometry. A shorter length of swirl pipe will therefore be required to generate an equivalent amount of swirl. The use of exit transition reduced the swirl decay rate thereby sustaining the induced swirl for longer.
- All CFD predicted pressure losses for circular, swirl and transition pipes for single phase water flow were in agreement to within 15%

with the experimentally measured results. The maximum tangential velocity predicted by CFD was in agreement with PIV results to within 20%.

- CFD indicated a wall jet type of swirl within the swirl pipe which rapidly develops into a solid body type. The swirl decay observed from CFD was in good agreement with the exponential trend that is established for many swirling flows. The swirl decay rate parameter is dependent upon the exit conditions of the initial swirl and therefore it is not possible to assign a single value for swirling pipe flows.
- CFD simulations showed that as the viscosity of the transporting medium increased, a smaller pitch (thereby a smaller P:D ratio) was required in the swirl pipe to generate swirl. A swirl pipe with P:D ratio of about 5 was found to be the optimum geometry for a non-Newtonian fluid with the characteristics of CMC as opposed to a pipe with P:D ratio of 8 for water.
- The current CFD model may be modified to simulate more complex mixtures of slurry flow incorporating non-Newtonian fluids and solids.
- The pressure saving indicated by CFD from the use of entry and exit transitions in single phase flow has been proven experimentally.

10.1.2 Swirling Flow and Transitions in Settling Slurry

- A much shorter length of the optimised swirling flow pipe kept particles in suspension for an equivalent length as the original *Swirly-Flo* pipe used by previous researchers. This shows first-hand the effect of the optimisation carried out.
- There is a distinct pressure saving from the use of transitions in slurry flow.
- Although the pressure saving from transitions increased with increasing velocity in single phase flows, this trend was not observed

in slurry tests. There appeared to be an optimum velocity when the best advantage is gained from the use of transitions.

- As the solids density increased, the pressure saving from transitions also increased.
- Settling length of solids increased when exit transition was used helping to sustain the swirl for longer in settling slurry flows.
- Swirl and transition pipes aid in particle distribution and prevent particles from dragging along the bottom of the pipe. A clear change in flow regime was observed downstream of swirling flow and transition pipes.

10.1.3 Contributions to Knowledge

- A thorough literature review of slurry transport and swirling flow was carried out with emphasis on modelling and definition of terms and equations used by previous researchers.
- CFD techniques for modelling swirling flow in pipes have been analysed and experimentally validated.
- An optimised transition geometry has been identified which reduces pressure losses and increases swirl generation in swirling flow pipe.
- The effect of different density solids on swirling pipe flow was investigated.
- It was shown that as the viscosity of the carrier fluid increases, a smaller pitch is required in the swirling flow pipe to generate swirl.

10.2 Future Work

10.2.1 CFD Modelling

- With improvements in commercial CFD code the possibilities for multiphase modelling of slurry flow should be investigated. In particular, Discrete Phase Modelling in CFD software may be used with some modifications and the inclusion of additional forces. The effect of particle density and shape on the flow paths taken by the particles in the swirling flow pipe could be determined. Erosive wear of the pipe wall can also be calculated in such a model.
- It was shown that in most cases, CFD over-predicted the pressure loss across the pipes. Future improvements in meshing and wall boundary conditions should give better agreement.

10.2.2 Changes to Swirl Pipe Geometry

- With the inclusion of transitions, a shorter length of swirling flow pipe than previously determined is optimum. A CFD investigation should be carried out to optimise the transitions and swirling flow pipe geometry as a whole.
- The use of a variable helix in swirling flow pipe and transitions should be investigated in more detail. The apparent ineffectiveness of the variable helix is puzzling. Accelerating the tangential flow through the swirl pipe should be beneficial and the simplest way to express this is as a constant angular acceleration (as expressed by the formula used for variable helix in this thesis). It is surprising that the geodesic proves to be better than the variable helix designs when, as shown from the entry transition inclusion with swirl pipe in particular (see Section 5.6), it is constraining the swirl. It may however, be that our criterion for optimisation, swirl effectiveness, is accentuating pressure loss. So although the variable helix gives 'optimum swirl' it is not the 'minimal cost' design. In addition, the practise of averaging the swirl

over a cross-section may be hiding the dynamic effects of the swirl. The use of a variable helix with non-Newtonian fluids may also yield interesting results.

- The effect of swirl bends has not yet been investigated although bends of different radii have been manufactured. Slurry tests and CFD simulations on the swirl bend geometries would be an immediate avenue for future research. Additionally the use of transition within a bend should be investigated.
- The design of the 3-lobed swirl pipe was inspired by the E.F. Spanner patent of the early 1940s (Spanner 1940). Spanner's lobes were asymmetrical to give slightly greater useful swirl (Spanner 1945). The cusps in the cross-section act as vanes sweeping the fluid into a swirling motion. In the direction of swirl, the first cusp to meet the fluid will give it swirl while the trailing edge of the lobe will merely be creating the next cusp. The other side of the cusp will be accelerating another bite of fluid. The lobes were simplified by making the cusps symmetrical by Ganeshalingam and Raylor (Raylor 1998; Ganeshalingam 2002). However, further optimisation in the circumferential sense is still possible as per Spanner's 1945 patent (Jones 2004).

10.2.3 Experimental Methodology

- As detailed in Chapter 2, there are many experimental techniques to measure swirl velocity components (Section 2.2.5) other than PIV. PIV or an alternative technique should be considered for swirl velocity and decay measurement downstream of the swirl pipe. Experimental results for the dissipation of swirl may also be obtained by injecting some dye downstream of the swirl pipes. With the use of a video camera the decay could be measured as the dye emerges. The measurement of settling length in slurry tests was rather crude and a better method should be identified for its estimation. This will show the advantage of transitions more clearly.

- Image analysis of the photographs of flow patterns (Chapter 8) should be carried out to evaluate concentration and size distribution of the particles, in particular for the mixed density run. This would give further insight into the particle distribution achieved through optimised swirl pipes (Chapter 8). Tools such as Matlab can be used for the analysis.

BIBLIOGRAPHY

Alderman, N. J., Heywood, N.I. (2004). "Making accurate slurry flow curve measurements." Chem. Engng. Progress **100** (5).

Aude, T. C., Cowper, N. T., Thompson, T.L., Wasp, E. J. (1971). "Slurry piping systems: trends, design methods and guidelines." Chem. Engng. Progress June 28.

Bain, A. G., Bonnington, S.T. (1970). The Hydraulic Transport of Solids by Pipeline, Pergammon, Oxford.

Baker, P. J., Jacobs, B.E.A., (1979). A Guide to Slurry Pipeline Systems, Cranfield: BHRA Fluid Engineering.

Bali, T., Ayhan, T. (1999). "Experimental investigation of propellor type swirl generator for a circular pipe flow." Int. Comm. Heat Mass Transfer **26** (1) 13-22.

Bhaskaran, R. (2003). Introduction to CFD Basics. <http://instruct1.cit.cornell.edu/courses/fluent/cfd/intro.pdf>. Last accessed June 2005.

Binder, J. L., Hanratty, T.J (1993). "Use of Lagrangian Statistics to Describe Slurry Transport." AIChE Journal **39** (10).

Bitter, J. G. A. (1963). "A Study of Erosion Phenomena, Part I." Wear **6** 5-21.

Bitter, J. G. A. (1963a). "A Study of Erosion Phenomena, Part II." Wear **6** 169-190.

Blanchard, D. J., Griffith, P., Rabonowicz, E. (1984). "Erosion of a Pipe Bend by Solid Particles Entrained in Water." Transactions of the ASME, J. of Engng. Ind. **106** August.

Blazek, J. (2001). Computational fluid dynamics: principles and applications, Elsevier.

Bolton (2003). "Validate CFD results using Process Tomography." Chemical Engineering November.

Charles, M. E., Cheh, C. H-S, Chu, L. H-L. (1971). "Flow of Settling Slurries in Horizontal Pipes with Internal Spiral Ribs." The Can. J. Chem. Engng. **49** December.

Chase, D. P. (1992). "A Model for the Effect of Velocity on Erosion of N80 Steel Tubing due to the Normal Impingement of Solid Particles." Transactions of the ASME, J. Engng. Res. Tech. **114** March.

Chen, H. C. (1988). "Near Wall turbulence models for complex flows including separation." AIAA Journal **26** (6).

Chien, S.-F. (1994). "Critical Velocity of Sand-Fluid Mixtures in a Horizontal Pipe, Liquid-Solid Flows." ASME FED **189** 231-246.

Chu, L. H.-L. (1969). Solid-Liquid Flow within Pipes with Internal Spiral Ribs. MSc Thesis, University of Toronto.

Clark, H. M. (2002). "Particle Velocity and Size Effects in Laboratory Slurry Erosion Measurements OR... do you know what your particles are doing?" Tribology International **35** 617-624.

Deen, N. G., Hjertager, B. H., Solberg, T. (2000). Comparison of PIV and LDA measurement methods applied to a gas-liquid flow in a bubble column. 10th Int. Symp. on Appl. of Laser Techniques to Fluid Mech.

Doron, P. (1995). "Pressure Drop and Limit Deposit Velocity for Solid-Liquid Flow in Pipes." Chem. Engng. Sci. **50** (10) 1595-1604.

Doron, P., Barnea, D. (1996). "Flow pattern maps for solid-liquid flow in pipes." Int. J. Multiphase Flow **22** (2) 273-283.

Doron, P., Simkhis, M., Barnea, D. (1997). "Flow of solid-liquid mixtures in inclined pipes." Int. J. Multiphase Flow **23** (2) 313-323.

Duchanoy, C. (2003). "Efficient simulation of liquid-solid flows with high solids fraction in complex geometries." Computers and Fluids **32** 1453-1471.

Einstein (1906). "Laminar flow of a dilute suspension of small spheres." Annals of Physics **29** (371).

Elkholly, A. (1983). "Prediction of abrasion wear for slurry pump materials." Wear **84** 39-49.

Fan, J., Yao, J., Zhang, X., Cen, K. (2001). "Experimental and numerical investigation of a new method for protecting bends from erosion in gas-particle flows." Wear **251** 853-860.

Finnie, I. (1958). The Mechanism of Erosion of Ductile Metals,. 3rd U.S. National Congress of Applied Mechanics.

FlowMap Installation and User's Guide, Dantec Dynamics, Denmark.

Fluent Inc. Lebanon, NH, USA (2000). Gambit User's Guide.

Fluent Inc. Lebanon, NH, USA (2001). Fluent 6.0 Documentation, User's Guide.

Fluent Inc. Lebanon, NH, USA (2005). "Fluent 6.2 User's Guide."

Fokeer, S., Kingman, S., Lowndes, I., Reynolds, A. (2004). "Characterisation of the cross section particle concentration distribution in horizontal dilute flow conveying- a review." Chem. Engng and Processing **43**.

Fokeer, S. (2004a). Personal communication.

Ganeshalingam, J. (2002). Swirl Induction for Improved Solid-Liquid Flow in Pipes. PhD Thesis, University of Nottingham.

Geldard, R. J. J., Jones, T.F. (2002). Selection of a suitable non-newtonian fluid for swirling pipe flow tests. 15th International Symposium on Hydrotransport, Banff, Canada.

Gomez-Diaz, D., Navaza, J. M. (2002). "Rheological characterization of aqueous solutions of the food additive carboxymethyl cellulose." Electronic Journal of Environmental, Agricultural and Food Chemistry **1**.

Gordon, H. (1899). Conduit or Pipe. US Patent 630,605.

Grace, J. R., Taghipour, F. (2004). "Verification and Validation of CFD models and dynamic similarity for fluidised beds." Powder Tech. **139** 99-110.

Graham, G., Steffan, D. (2002). Inside Pro/Engineer 2001, Onword Press.

Grant, I. (1997). "Particle Image Velocimetry: A Review." Proc Instn Mech Engrs **211** 55 - 76.

Grossel, S. S. (1998). "Improved Design Practises for Slurry Piping Systems." Chem. Engng. Progress April.

Gupta, A. K. (1984). Swirl Flows, Abacus Press.

Gupta, R., Singh, S. N., Sehadri, V. (1995). "Prediction of uneven wear in a slurry pipeline on the basis of measurements in a pot tester." Wear **184** 169-178.

Gupta, R., Singh, S. N., Sehadri, V. (1997). "Migration of Solid Particles in the Heterogeneous Slurry Flow through a 90 degree Bend." Indian Journal of Engineering and Materials Sciences **4** February: 10-20.

Halsey, D. M. (1987). "Flowmeters in Swirling Flows." J. Phys. E: Sci Instrum. **20**.

Hanks, R. W. (1986). Encyclopedia of Fluid Mechanics, Houston: Gulf Publishing Co.

Harrison, P. (2003). Rapid Prototyping User Guide, Faculty of Computing Sciences and Engineering, DeMontfort University.

http://www.imeche.org.uk/manufacturing/pdf/rp_userguide2003.pdf. Last accessed November 2005

Heywood, N. I. (1999). "Stop Your Slurries Stirring up Trouble." Chem. Engng. Progress September.

Heywood, N. I., Alderman, N.J. (2003). "Developments in Slurry Pipeline Technologies." Chem. Engng. Progress April: 36-43.

Heywood, N. I., Alderman, N.J. (2004). "Improving slurry viscosity and flow curve measurements." Chem. Engng. Progress **100** (4).

Hou, R. (1999). "Acoustic monitoring of pipeline flows: particulate slurries." Powder Technology **106**.

Howard, G. W. (1938). "Transportation of Sand and Gravel in a Four-Inch Pipe." Trans. ASCE **106** 1334-1380.

Howard, G. W. (1939). "Effects of Rifling on Four-Inch Pipe Transporting Solids." Am. Soc. Civ. Eng., Transactions, Paper no. 2101.

Hughmark, G. A. (1961). "Aqueous Transport of Settling Slurries." Ind. Engng. Chem **53** (5) May.

Hutchings, I. M. (1987). "Wear by Particulates." Chem. Engng. Sci. **42** (4) 869-878.

Ito, S., Ogawa, K., Kuroda, C. (1980). "Turbulent Swirling Flow in a Circular Pipe." J. Chem. Engng. Japan **13** (1).

Jacobs, P. F. (1992). Rapid prototyping and manufacturing: fundamentals of stereolithography. New York, McGraw-Hill.

Jacobs, P. F. (1996). Stereolithography and other RP&M technologies: from rapid prototyping to rapid tooling.

James, J. G., Broad, B.A. (1983). Wear in slurry pipelines: experiments with 38mm diameter specimens in a closed loop test rig, TRRL Supp. Rep. 773.

Jones, T. F. Improved slurry presentation for measurement, control and optimisation: In-situ diagnostic methods. ECSC Coal RTD Programme.

Jones, T. F., Miles, N. (1999). Pipe Design for Improved Particle Distribution and Reduced Wear. ECSC Research Project TCR/EUR 17975

Jones, T. F. (2004). Personal communication.

Jones, T. F., Ariyaratne, C. (2004a). An efficient swirl-pipe transition geometry. 16th Int. Conf. on Hydrotransport, Santiago, Chile.

Jones, T. F., Ganeshalingam, J. (2002). Towards optimal swirl inducing pipe. 15th International Symposium on Hydrotransport, Banff, Canada.

Jones, T. F., Tonkin, R.J.J. (2004b). Velocity distributions in swirling pipe flows. 16th Int. Conf. on Hydrotransport, Santiago, Chile.

Karabelas, A. J. (1978). An experimental study of pipe erosion by turbulent slurry flow. 5th Int. Conf. on Hydrotransport, BHRA, Cranfield, UK.

Karabelas, A. J. (1978a). An experimental study of pipe erosion by turbulent slurry flow. 5th Int. Conf. on Hydrotransport.

Keating, A., Nesic, S. (2001). "Numerical Prediction of Erosion-Corrosion in Bends, Corrosion." Corrosion **57** (7).

Kitoh, O. (1987). "Swirling Flow through a Bend." J. Fluid Mech. **175** 429-446.

Kitoh, O. (1991). "Experimental study of turbulent swirling flow in a straight pipe." J. Fluid Mech. **225** 445-479.

Kreith, F., Sonju, O. K. (1965). "The decay of a turbulent swirl in a pipe." J. Fluid Mech. **22** 257-271.

Launder, B. E., Spalding, D. B. (1974). "The numerical computation of turbulent flows." Comp. Methods in Appl. Mech. And Engng. **3** 269-289.

Li, H., Tomita, Y. (1994). "Characteristics of Swirling Flow in a Circular Pipe." Transactions of the ASME, J. Fluids Engng. **116** June.

Li, H., Tomita, Y. (2000). "Particle velocity and concentration characteristics in a horizontal dilute swirling flow pneumatic conveying." Powder Tech. **107** 144-152.

Liptak, B. G. (1967). "Instruments to measure and control slurries and viscous materials." Chem. Engng. Progress February 13th.

Marumaya, T., Ando, J., Mizushima, T. (1980). "Flow of Settling Slurries in Horizontal Pipes." J. Chem. Engng. of Japan **13** (4).

Marumaya, T., Kojima, K., Mizushima, T. (1979). "The Flow Structure of Slurries in Horizontal Pipes." J. Chem. Engng. of Japan **12** (3).

Masden, B. W. (1985). A study of parameters using a new constant-wear-rate slurry test, in Wear of Materials. Int. Conf. On Wear of Materials, New York, NY:ASM.

Massey, B. S. (1998). Mechanics of fluids, London: Chapman and Hall.

Mathiesen, V., et al (2003). "Predictions of gas/particle flow with an Eulerian model including a realistic particle size distribution." Powder Tech. **112** 34-45.

Mattiussi, C. (1997). "An analysis of finite volume, finite element and finite difference methods using some concepts from algebraic topology." J. Comput. Phys. **133** 289-309.

Mishra, R., Singh, S.N., Seshadri, V. (1998). "Study of wear characteristics and solid distribution in constant area and erosion resistant long-radius pipe bends for the flow of multisized particulate slurries." Wear **217** 297-306.

Mukhtar, A. (1991). Investigation of the Flow of multisized slurries in straight pipe and pipe bends. PhD Thesis, IIT, Delhi.

Neilson, J. H., Gilchrist, A., (1968). "Erosion by a stream of solid particles." Wear **11** 111-121.

Nesbitt, B. (editor) (2000). Guide to European Pumps and Pumping, Professional engineering publishing.

Oberkampf, W., Blottner, F. (1998). "Issues in Computational Fluid Dynamics Code Verification and Validation." AIAA Journal **36** (5) May.

Oberkampf, W. L., Trucano, G. T. (2002). "Verification and Validation in Computational Fluid Dynamics." Progress in Aerospace Sciences **38** 209-272.

Oka, Y., Matsumara, M. (1983). "Erosive Wear Testing Apparatus-simulation of erosion caused by slurry of low impingement velocity." Wear of Materials, ASME, New York 360-366.

Padmanabhan, M. (1994). "Characteristics of swirling flows in a circular pipe- Discussion of Li and Tomita (June 1994)." J. of Fluids Engng.

Portela, L. M., Cota, P., Oliemans R. V. A. (2002). "Numerical study of the near-wall behaviour of particles in turbulent pipe flows." Powder Technology **125** 149-157.

Postlethwaite, J., Nesic, S. (1993). "Erosion in Disturbed Liquid/Particle Pipe Flow; Effect of Flow Geometry and Particle Surface Roughness." Corrosion **49** (10) October.

Rabinowicz, E. (1965). Friction and wear materials, Wiley.

Raffel, M., Willert, C. E., Kompenhans, J. (1962). Particle image velocimetry: a practical guide. Berlin, Springer.

Rajat, G. (1994). Erosion wear in pipelines. IIT, Delhi.

Raylor, B. (1998). Pipe Design for Improved Distribution and Improved Wear. PhD Thesis, University of Nottingham.

Raylor, B. (1999). Helically formed pipes improve the efficient transportation of particle-laden liquids,. 14th Int. Conf. on Hydrotransport, Maastricht, The Netherlands.

Raylor, B. (2003). Personal communication.

Reader-Harris, M. J. (1994). "The decay of swirl in a pipe." Int. J. Heat and Fluid Flow **15** (3) 212-217.

Rivoalen, E., Huberson, S., Bratec, H. (2004). "Particle simulation of swirling flows." Flow, Turbulence and Combustion **72** 69-90.

Roache, P. J. (1994). "Perspective: A method for uniform grid reporting of grid refinement studies." J. of Fluids Engng. **116** September.

Roache, P. J. (1998). "Verification of codes and calculations." AIAA Journal **36** (5) May.

Robinson, A. W. (1921). Delivery pipe for hydraulic dredging machine. US Patent 504,809.

Rocklage-Marliani, G., Schmidts, M., Vasantharam, V. I. (2003). "3D Laser Doppler Velocimeter measurements in swirling turbulent pipe flow." Flow Turbulence and Combustion **70** 43-67.

Roco, M. C. (1987). "Erosion wear in slurry pumps and pipes." Powder Tech. **50** (1) March: 35-46.

Sauermann, H. B. (1978). Hydraulic transportation in a segmented pipe. 5th Int. Conf. on the Hydraulic Transport of Solids in Pipes, Hanover.

Schlichting, H. (1979). Boundary-Layer Theory, McGraw-Hill Inc.

Schriek, W., Smith, L. G., Haas, D. B., Husband, W. H. W (1974). "The Potential of Helically Ribbed Pipes for Solids Transport." CIM Bull. Oct.: 84-91.

Senoo, Y., Nagata, T. (1972). "Swirl Flow in Long Pipes with Different Roughness." Bull. Of the JSME **15** (90).

Shaw, C. T. (1992). Using Computational Fluid Dynamics, New York: Prentice Hall.

Shook, C. A., Mckibben, M., Small, M. (1990). "Experimental investigation of some hydrodynamic factors affecting slurry pipeline wall erosion." The Can. J. of Chem. Engng. **68** Feb.

Singh, V. P. (1976). "The flow of sand/water slurries in horizontal pipes with internal spiral ribs - Effect of rib height." The Can. J. Chem. Engng. **54** August.

Smits, A. J., Lim, T. T. (2000). Flow visualisation: techniques and examples, Imperial College Press.

Song, X. Q., Lin, J. Z., Zhao, J. F., Shen, T. Y. (1996). "Research on reducing erosion by adding ribs on the wall in particulate two-phase flows." Wear **193** 1-7.

Spanner, E. F. (1940). Improvements in tubular heat exchanger apparatus. GB Patent GB521548.

Spanner, E. F. (1945). Improvements in tubes for heat exchanger apparatus. GB Patent GB569000.

Steenbergen, W., Voskamp, J. (1998). "The rate of decay of swirl in turbulent pipe flow." Flow measurement and instrumentation **9** 67-78.

Stern, F., Wilson, R. V., Coleman, H. W., Paterson, E. G. (2001). "Comprehensive approach to verification and validation of CFD simulations- Part 1: Methodology and Procedures." Journal of Fluids Engineering **123**.

Talbot, L. (1954). "Laminar swirling pipe flow." Journal of Applied Mechanics March.

Taylor, R.J. (1997). An introduction to error analysis: the study of uncertainties in physical measurements, 2nd ed., Sausalito, Calif. University Science Books.

Thomas, D. (1961). "Transport characteristics of suspensions: Minimum transport velocity." A.I.Ch.E. Journal **7** (3) September.

Toda, M., Komori, N., Saito, S., Maeda, S. (1972). "Hydraulic conveying of solids through pipe bend." J. Chem. Engng. Japan **5**.

Toivakka, M., Eklund, D., Bousfield, D. W. (1995). "Prediction of suspension viscoelasticity through particle motion modelling." J. Non-Newtonian Fluid Mech. **56** 49-64.

Tonkin, R. J. J. (2004). Swirling pipeflow of non-Newtonian and particle-laden fluids. PhD Thesis, University of Nottingham.

Triesch, O., Bohnet, M. (2001). "Measurement and CFD prediction of velocity and concentration profiles in a decelerated gas-solids flow." Powder Tech. **115** 101-113.

Tripath, A., Chhabra, R. P. (1995). "Drag on spheroidal particles in dilatant fluids." AIChE Journal **41** (3).

Truscott, G. F. (1975). A literature survey on wear on pipelines, BHRA Fluid Engineering, Cranfield Publ., Cranfield, UK.

van Wachem, B. G. M., Almstedt, A. E. (2003). "Methods for multiphase computational fluid dynamics." Chemical Engineering Journal **96** 81-98.

Versteeg, H. K. (1995). An introduction to computational fluid dynamics: the finite volume method, Harlow; Longman Scientific & Technical.

Vyas, B., Preece, C. M. (editor) (1979). "Erosion-Corrosion." Treatise on Mat. Sci. and Techn. **16** 357-394.

Wang, J., Andrews, J.R.G. (1995). "Numerical simulation of flow in helical ducts." AICHE Journal **41** (5) May.

Wang, M., Jones, T. F., Williams, R. A. (2003). "Visualisation of asymmetric solids distribution in horizontal swirling flows using electrical resistance tomography." Trans IChemE **81** September.

Wang, R. C., Seman, J. J. (1973). Solid-liquid flow in non-circular pipes. U.S. Dept. of Interior Bureau of Mines, Report of Investigations 7725.

Wasp, E. J., Kenny, J.P., Ghandi, R.L. (1977). Solid-Liquid Flow Slurry Pipeline Transportation, Rockport: Trans Tech, 1977.

Wilson, K. C., Addie, G. R. (1997). "Coarse-particle pipeline transport: effect of particle degradation on friction." Powder Technology **94** Dec. 15: 235-238.

Wolfe, S. E. (1967). Method and apparatus for transporting slurries. US Patent 3313577.

Wolfe, S. E. (1967a). "The Transport of Solids in Helically-Ribbed Pipes." C.I.M Bull. **60** 221-223.

Wolfe, S. E. (1967b). Method and apparatus for transporting slurries. U.S. Patent 3,313,577.

Wolfe, S. E. (1969). Method and apparatus for transporting slurries. GB Patent 1139889.

Wood, R. J. K. (1999). The erosion performance of candidate internal coatings for slurry handling and pipeline transport. 14th Int. Conf. on Hydrotransport, Maastricht, The Netherlands, BHR Group.

Wood, R. J. K. (2001). "Upstream swirl-induction for reduction of erosion damage from slurries in pipeline bends." Wear **250** 770-778.

Wood, R. J. K., Jones, T. F., Ganeshalingam, J., Miles, N. J. (2004). "Comparison of predicted and experimental erosion estimates in slurry ducts." Wear **256** 937-947.

Yao, J., Fan, J., Cen, K. (2000). "An experimental investigation of a new method for protecting bends from erosion in gas-particle flows." Wear **240** 215-222.

Yao, J., Zhang, B., Fan, J., (2002). "Numerical investigation of a new method for reducing bends erosion from particles impacts." Chinese J. Chem. Engng. **10** (1) 93-101.

Yin, M. J., Beddow, J. K., Vetter, A. F. (1983). "Effects of particle shape on solid-liquid transportation in pipes." 25-39.

Yuille, N. (1927). Dredger Pipeline. US Patent 162,035.

Zu, J. B. (1990). Wear of metals by slurry erosion. PhD Thesis, University of Cambridge.

Appendix A3.1: Calculations for Defining Swirl and Transition Pipe Geometry

Swirl Pipe Cross-sectional Area Calculation:

3-Lobed Pipe

Cross-sectional area of swirl pipe = Area of triangle EBD + Area of 3 Lobes

$$= \sqrt{3}r_f \times r_f + \left(\frac{\pi r_f^2}{2} \right) \times 3$$

$$= r_f^2 \left(\frac{3\pi}{2} + \sqrt{3} \right)$$

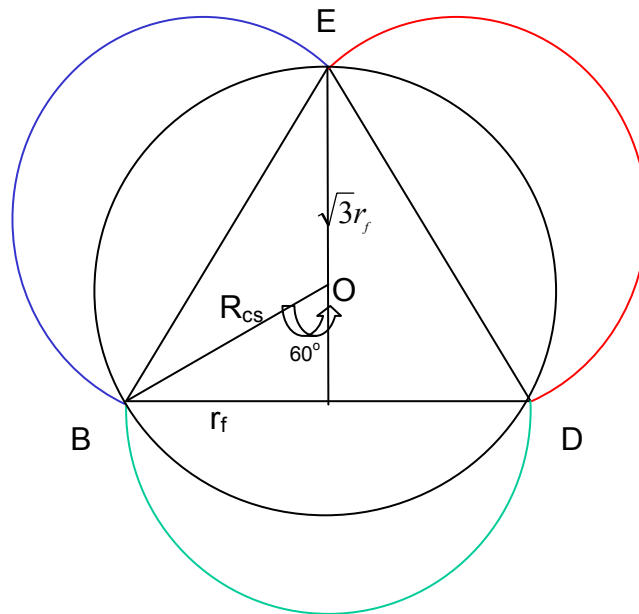


Figure A3.1: Fully Developed Swirl Pipe

Swirl Pipe Calculations in Spreadsheet:

3-Lobed Pipe

From calculation equating lobed pipe cross-sectional area to circular pipe cross-sectional area;

$$r_f^2 \left(\frac{3\pi}{2} + \sqrt{3} \right) = \pi R_1^2$$

$$r_f = \frac{R_1}{\sqrt{\frac{1.5\pi + \sqrt{3}}{\pi}}} \quad (A1)$$

where,

- r_f (see Figure A3.1) = Lobe radius of swirl pipe equivalent to circular pipe (with equal area)
- R_1 = Radius of circular pipe

Thereby for a given circular pipe radius, the required lobe radius r_f for a swirl pipe with equal cross-sectional area can be calculated.

The x and y offsets for each lobe (1, 2 or 3) are calculated using the following formulae:

For Lobe n,

$$x_{offset} = z \times \cos \left[\left(\theta_n + Twist\ Angle \right) \times \frac{\pi}{180} \right] \quad (A2)$$

$$y_{offset} = z \times \sin \left[\left(\theta_n + Twist\ Angle \right) \times \frac{\pi}{180} \right] \quad (A3)$$

Where,

- z = distance of lobe centre from origin O (see Figure A3.2)
- Twist Angle = 0° (increases from 0 to -360° for a full revolution; negative sign for a clockwise rotation)
- n = lobe number
- $\theta_n = 30, 150, 270^\circ$ for lobes 1, 2, 3 respectively

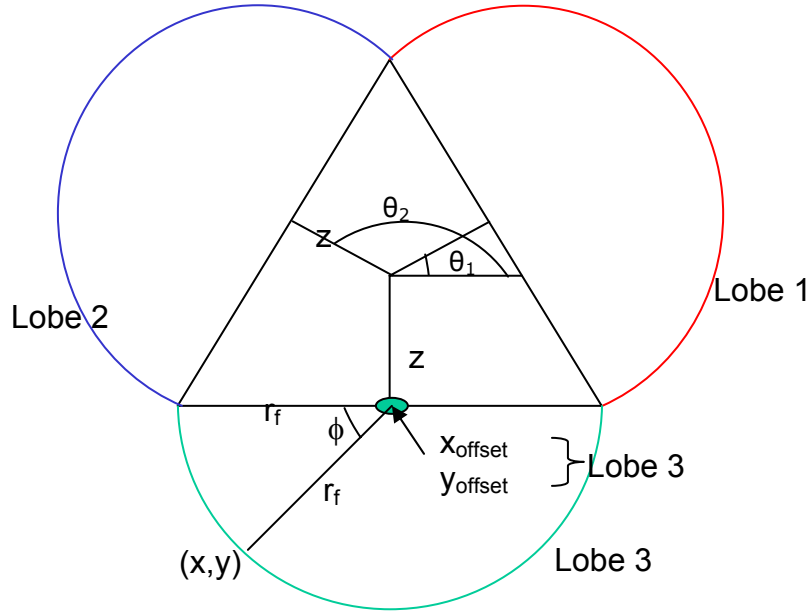


Figure A3.2: Illustration of Calculation of x_{offset} and y_{offset}

Calculate x , y data for Lobe n :

Lobe Radius, r_f

$\phi_{\text{start}} = -60, +60, +180$ for lobes 1, 2, 3 respectively

x_{offset} for Lobe $n = x_{\text{offset}}$ calculated from Equation A2

y_{offset} for Lobe $n = y_{\text{offset}}$ calculated from Equation A3

x and y co-ordinates:

$$x = x_{\text{offset}} + [r_f \times \cos(\phi + \phi_{\text{start}} + \text{Twist Angle})]$$

$$y = y_{\text{offset}} + [r_f \times \sin(\phi + \phi_{\text{start}} + \text{Twist Angle})]$$

This calculation is repeated for $\phi = 0$ to $\phi = 180$ to obtain placement of all points on lobe.

		Lobe 1		Lobe 2		Lobe 3	
ϕ deg	ϕ rad	x mm	y mm	x mm	y mm	x mm	y mm
0							
1							
--							
180							

Transition Pipe Calculations in Spreadsheet:

3-Lobed Transition

- r = Lobe radius at intermediate stage of transition
- r_f = Lobe radius for fully developed swirl pipe, calculated using Equation A1

$$Twist (\text{deg}/m) = \frac{360^\circ}{(P:D \text{ Ratio}) \times d_e}$$

- d_e = Equivalent diameter of pipe (= 50mm)
- P:D Ratio = pitch-to-diameter ratio of pipe (= 6)

$$Twist = \frac{360}{6 \times 0.05} = 1200 \text{ deg}/m$$

- L = length of transition based on one lobe twisted 120°

$$L = \frac{1000mm}{1200^\circ} \times 120^\circ = 100mm$$

- Twist direction = -1 (-ve for anticlockwise helix)
- R = circular core radius for intermediate stage of transition pipe
- R_{cs} = Minimum circular core radius for fully developed lobes

$$R_{cs} = \frac{r_f}{\sin 60} = \frac{2}{\sqrt{3}} r_f \text{ (see Figure A3.1)}$$

- R_1 = Radius of circular pipe of equivalent area (pipe radius before lobes start to develop, stage 1)

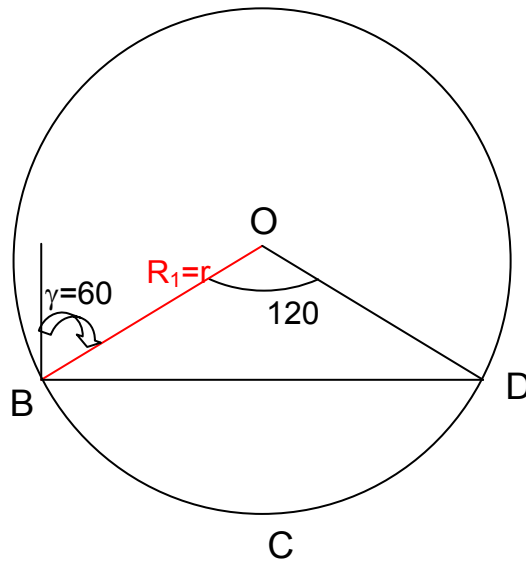


Figure A3.3: Transition Pipe at Stage 1 (No Lobes)

Define γ :

- γ = Angle between perpendicular to lobe origin (point B) and lobe radius r ,

$\gamma = 60 \rightarrow 90^\circ$, from no lobes (stage 1) to fully developed lobes in given no. of incremental steps ($N_{inc}=10$)

For intermediate value of γ , we have y , r , R (see Figure A3.4)

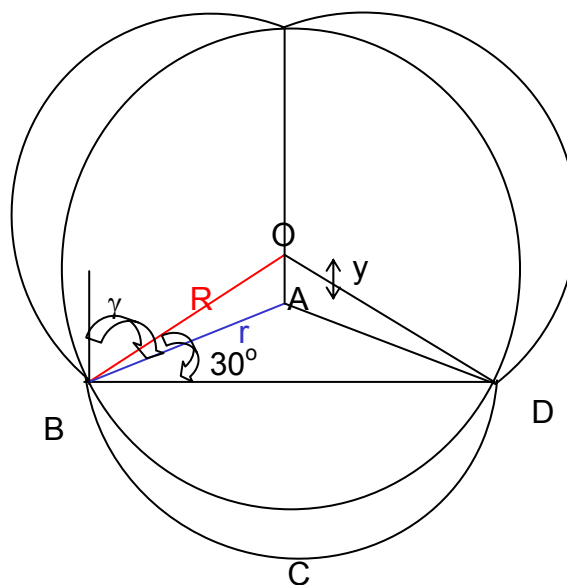


Figure A3.4: Transition Pipe at Intermediate Stage (Lobes Developing)

Area of segment BCD = Area of sector ABCD – Area of triangle ABD

$$\text{Area of sector ABCD} = \frac{1}{2} r^2 \theta = \frac{1}{2} r^2 \times (2\gamma) = r^2 \gamma$$

$$\text{Area of triangle ABD} = r \sin \gamma \times r \cos \gamma = r^2 \sin \gamma \cos \gamma = r^2 \times \frac{1}{2} \sin 2\gamma$$

$$\text{Area of segment BCD} = r^2 \gamma - \frac{1}{2} r^2 \sin 2\gamma = r^2 \left(\gamma - \frac{1}{2} \sin 2\gamma \right)$$

Introduce variable f;

$$f = \left(\gamma - \frac{1}{2} \sin 2\gamma \right) \quad (\text{A4})$$

Therefore,

$$\text{Area of segment BCD} = f r^2 \quad (\text{A5})$$

Where the segment area increases as lobes form

Introduce variable y;

where,

- y = distance of lobe centre from origin O (see Figure A3.4):

Applying Sine Rule,

$$\frac{R}{\sin(180 - \gamma)} = \frac{y}{\sin(\gamma - 60)}$$

$$\frac{R}{\sin \gamma} = \frac{y}{\sin \gamma \cos 60 - \cos \gamma \sin 60}$$

Dividing by Cos 60 and multiplying by sin 60,

$$y = \frac{\sqrt{3}}{2} R \left[\frac{\sin \gamma - \cos \gamma \tan 60}{\sin \gamma \tan 60} \right] = R \left[\frac{\tan \gamma - \sqrt{3}}{2 \tan \gamma} \right]$$

Introduce another variable f_1 :

$$f_1 = \left[\frac{\tan \gamma - \sqrt{3}}{2 \tan \gamma} \right] \quad (A6)$$

Therefore,

$$y = f_1 \times R \quad (A7)$$

Therefore variable f facilitates the calculation of segmental area and f_1 facilitates the calculation of y .

Calculating R for intermediate stage with equal cross-sectional area at all stages:

πR_1^2 = Area of pipe with no lobes (stage 1), i.e. circular pipe

Pipe area at intermediate stage = πR_1^2 = Area of 3 segmental lobes (BCD, DGE, EFB) + Area of triangle EBD

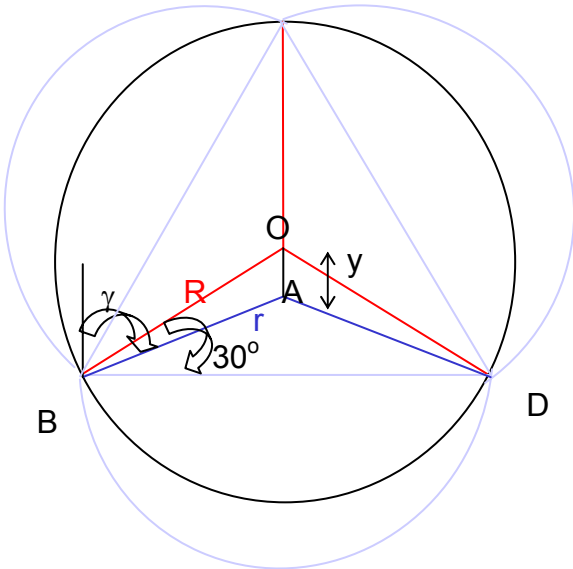


Figure A3.5: Transition Pipe at Intermediate Stage; Calculating R

Area of 3 segmental lobes (from Equation A5) = $3 \times fr^2$

Substituting for r using Cosine Rule,

$$r^2 = R^2 + y^2 - 2Ry \cos 60 = R^2 + y^2 - R \times y \quad (\text{A8})$$

Therefore,

$$\text{Area of 3 segmental Lobes} = 3 \times f(R^2 + y^2 - Ry)$$

Substituting for y from Equation A7,

$$\text{Area of 3 segmental Lobes} = 3 \times f(R^2 + f_1^2 R^2 - R^2 f_1)$$

$$\text{Area of triangle EBD} = R \sin 60 \times (R \cos 60 + R) = \frac{3\sqrt{3}}{4} R^2 \quad (\text{A9})$$

Adding area of triangle and segmental lobes,

$$\text{Pipe Area at intermediate stage} = 3f(R^2 + f_1^2 R^2 - R^2 f_1) + \frac{3\sqrt{3}}{4} R^2$$

Equating Area of circular pipe,

$$\pi R_1^2 = 3f \left(R^2 + f_1^2 R^2 - R^2 f_1 \right) + \frac{3\sqrt{3}}{4} R^2$$

$$R^2 = R_1^2 \left[\frac{\pi}{3 \frac{\sqrt{3}}{4} + 3f + 3f_1^2 f - 3f_1 f} \right]$$

$$R = R_1 \sqrt{\frac{\pi}{3 \frac{\sqrt{3}}{4} + 3f + 3f_1^2 f - 3f_1 f}} \quad (A10)$$

So calculate y from Equation A7 and calculate r from Equation A8

Calculating Lobe Area as a function of length,

$$\text{Total area of 3 segmental lobes (BCD, DGE, EFB)} = 3fr^2$$

Total area of INNER segments = Area of circle – Area of triangle EBD

$$\text{Area of circle} = \pi R^2$$

$$\text{Area of triangle EBD (from Equation A9)} = 3 \frac{\sqrt{3}}{4} R^2$$

$$\text{Total area of INNER segments} = \pi R^2 - 3 \frac{\sqrt{3}}{4} R^2$$

$$\text{Total Lobe Area at intermediate stage (LA}_i\text{)} = 3fr^2 - \left(\pi R^2 - 3 \frac{\sqrt{3}}{4} R^2 \right) \quad (A11)$$

LA_i is therefore the sum of the total area of pipe minus the area of the circular core at any given stage of transition.

Introducing a function alpha;

$$\alpha = \frac{LA_i}{LA_{FD}} \quad (A12)$$

where,

- LA_i = intermediate lobe area from A11
- LA_{FD} = lobe area of fully developed swirl pipe

LA_{FD} = (Swirl pipe area – Area of circle only for R_{cs})

$$= r_f^2 \left(\frac{3\pi}{2} + \sqrt{3} \right) - \pi \times R_{cs}^2$$

To ensure that the discontinuity obtained in the case of linear relationship is avoided, vary lobe area along length as a cosine relationship.

Define,

$$\frac{x}{L} = \frac{\cos^{-1}(1 - 2\alpha)}{\pi} \quad (A13)$$

Where,

- x = intermediate length
- L = total length

The above function can be varied to give different types of transition development based on lobe area growth.

Intermediate twist is calculated using:

$$Twist[0,120] = \frac{x}{L} \times 120 \times Twist \ Direction \quad (A14)$$

Overall geometry generation:

γ increases from 60 to 90 in the given number of increments (N_{inc}) as lobes develop. For each increment of γ , functions f and f_1 are calculated using Equations A4 and A6 respectively. These in turn are used to calculate R (from Equation A10), y (Equation A7) and r (Equation A8) at each incremental stage. Lobe area can then be calculated as a function of r , R and f using Equation A11, hence α (Equation A12) and x/L (Equation A13) and the respective Twist (Equation A14). Thereby, generating a table as shown below:

γ rad	f_1	f	R mm	y mm	r mm	LA mm^2	α	x/L	Twist rad
-----------------	-------	-----	-----------	-----------	-----------	----------------	----------	-------	--------------

Next, the values of γ above are used for cross-section geometry calculation at each stage of x/L .

Generating lobe co-ordinates:

At each value of γ (therefore at each intermediate stage) along the length of the pipe, 100 increments are taken.

- $\gamma_o \rightarrow -\gamma_o$ in 100 increments (see Figure A3.6).

For Lobe 1:

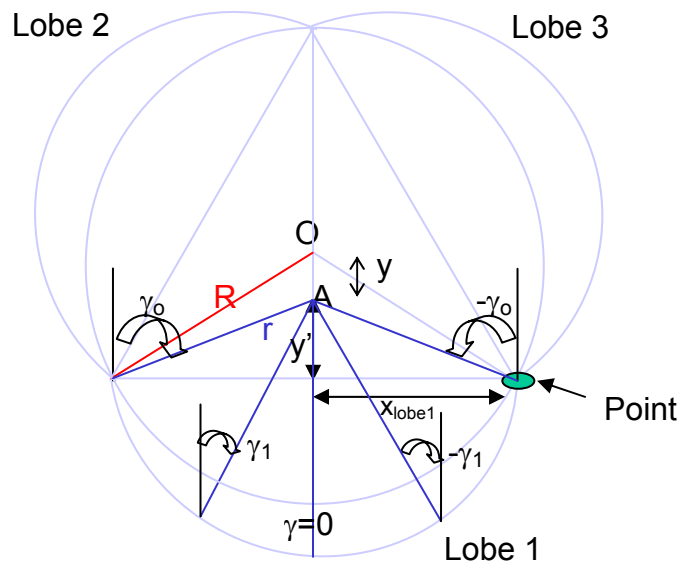


Figure A3.6: Calculation of Lobe Co-ordinates at Intermediate Stage

$$x_{lobe1} = r \sin \gamma$$

$$y' = r \cos \gamma$$

Therefore,

$$y_{lobe1} = -(y' + y) = -(y + r \cos \gamma)$$

Lobe co-ordinates:

$$x_{1twisted} = x_{lobe1} \cos(Twist) - y_{lobe1} \sin(Twist) \quad (A15)$$

$$y_{1twisted} = y_{lobe1} \cos(Twist) + x_{lobe1} \sin(Twist) \quad (A16)$$

Continue calculation of x, y twisted data for lobes 2 and 3 where for lobe 2,

$$x_{lobe2} = y_{lobe1} \sin\left(\frac{2\pi}{3}\right) + x_{lobe1} \cos\left(\frac{2\pi}{3}\right) \quad (A17)$$

$$y_{lobe2} = y_{lobe1} \cos\left(\frac{2\pi}{3}\right) + x_{lobe1} \sin\left(\frac{2\pi}{3}\right) \quad (A18)$$

For lobe 3, replace $(2\pi/3)$ with $(4\pi/3)$.

Hence the twisted lobe values ($x_{2twisted}$, $y_{2twisted}$, etc.) are calculated for lobes 2 and 3 as well using Equations A15 and A16.

γ	x	y	x_1	y_1	x	y	x_2	y_2	x	y	x_3	y_3
rad	lobe1	lobe1	twisted	twisted	lobe2	lobe2	twisted	twisted	lobe3	lobe3	twisted	twisted

Appendix A3.2 presents tabulated data for overall geometry calculation, and lobe co-ordinate data for stage 1. The transition development from this data is illustrated in A3.3.

Swirl Pipe Cross-sectional Area Calculation:

4-Lobed Pipe

Cross-sectional area of swirl pipe = Area of square (BDEF) + Area of 4 Lobes

$$= 2r_f \times 2r_f + \left(\frac{\pi r_f^2}{2} \right) \times 4$$

$$= 4r_f^2 + 2\pi r_f^2 = r_f^2(2\pi + 4)$$

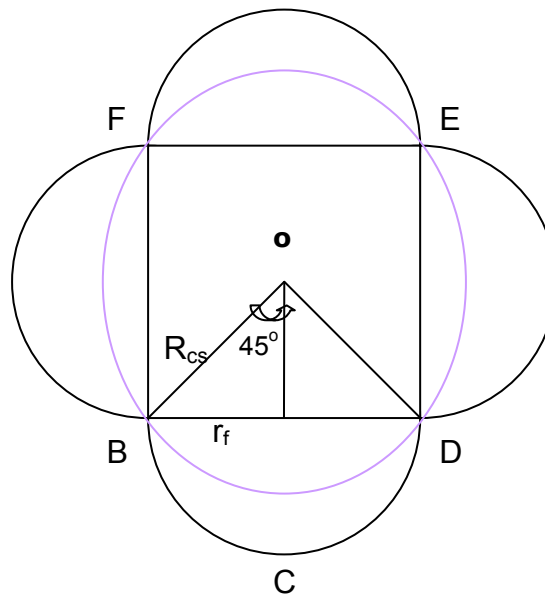


Figure A3.7: Fully Developed Swirl Pipe

Swirl Pipe Calculations in Spreadsheet:

4-Lobed Pipe

As with the 3-lobed pipe, equating lobed pipe cross-sectional area to circular pipe,

$$r_f = \sqrt{\frac{R^2}{2 + \frac{4}{\pi}}} \quad (A19)$$

x_{offset} , y_{offset} are calculated for each lobe ($n = 1, 2, 3$ and 4) (see Figure A3.8) using Equations A2 and A3 as with 3-lobed pipe:

$$x_{offset} = z \times \cos \left[(\theta_n + Twist\ Angle) \times \frac{\pi}{180} \right] \quad (A2)$$

$$y_{offset} = z \times \sin \left[(\theta_n + Twist\ Angle) \times \frac{\pi}{180} \right] \quad (A3)$$

- Twist Angle = -90 (-ve for clockwise)
- $\theta_n = 0, 90, 180, 270^\circ$ for lobes 1, 2, 3, 4 respectively
- Twist Angle = 0° (increases from 0 to 360° for a full revolution; negative for clockwise rotation)

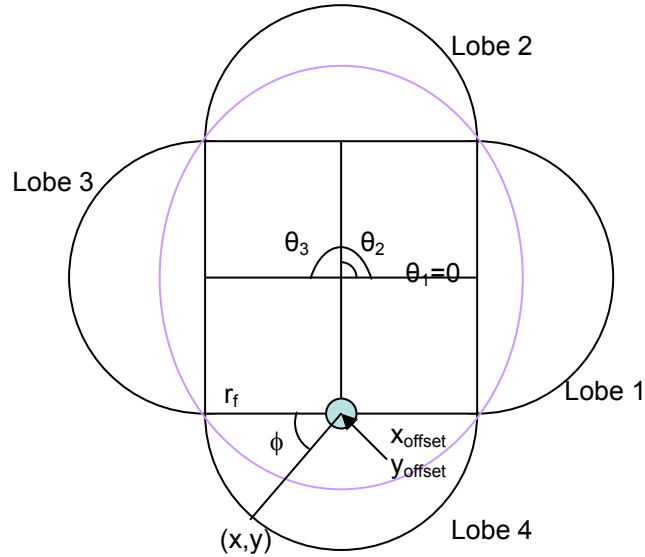


Figure A3.8: Illustration of Calculation of x_{offset} and y_{offset}

Calculate x, y data for Lobe n:

Lobe Radius, r_f

$\phi_{\text{start}} = -90, 0, 90, 180$ for lobes 1, 2, 3, 4 respectively

x_{offset} for Lobe n = x_{offset} calculated from Equation A2

y_{offset} for Lobe n = y_{offset} calculated from Equation A3

x and y co-ordinates (as with 3-lobed):

$$x = x_{\text{offset}} + [r_f \times \cos(\phi + \phi_{\text{start}} + \text{Twist Angle})]$$

$$y = y_{\text{offset}} + [r_f \times \sin(\phi + \phi_{\text{start}} + \text{Twist Angle})]$$

This calculation is repeated for $\phi = 0$ to $\phi = 180$ to obtain placement of all points on lobe.

Transition Pipe Calculations in Spreadsheet:

4-Lobed Transition

Calculations are similar to the 3-lobed design and the same procedure is employed, except that P:D ratio used is 8 for 4-lobed. The terminology is as given for the 3-lobed design.

The equations that are altered are listed:

$$Twist = \frac{360}{8 \times 0.05} = 900 \text{ deg/} m$$

Based on a P:D Ratio of 8 and diameter of 50mm

Length of transition based on one lobe twisted 90° :

$$L = \frac{1000mm}{900^\circ} \times 90^\circ = 100mm$$

$$R_{cs} = \frac{r_f}{\sin 45} = \frac{1}{\sqrt{2}} r_f \text{ (see Figure A3.7)}$$

Define γ :

- γ = Angle between perpendicular to lobe origin (point B) and lobe radius r ,

γ /deg = $45 \rightarrow 90^\circ$, from no lobes (stage 1) to fully developed lobes in given no. of incremental steps ($N_{inc}=10$)

For intermediate value of γ , we have y , r , R (see Figure A3.9)

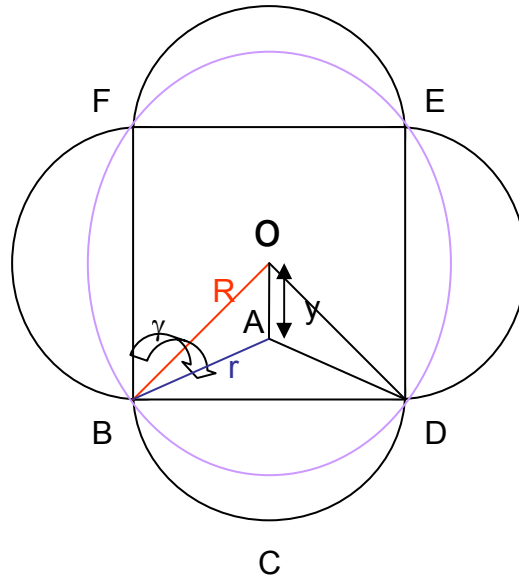


Figure A3.9: Transition Pipe at Intermediate Stage (Lobes Developing)

Area of segment BCD = Area of sector ABCD – Area of triangle ABD

$$\text{Area of sector ABCD} = \frac{1}{2} r^2 \theta = \frac{1}{2} r^2 \times (2\gamma) = r^2 \gamma$$

$$\text{Area of triangle ABD} = r \sin \gamma \times r \cos \gamma = r^2 \sin \gamma \cos \gamma = r^2 \times \frac{1}{2} \sin 2\gamma$$

$$\text{Area of segment BCD} = r^2 \gamma - \frac{1}{2} r^2 \sin 2\gamma = r^2 \left(\gamma - \frac{1}{2} \sin 2\gamma \right)$$

Introduce variable f (as with 3-lobed);

$$\left(\gamma - \frac{1}{2} \sin 2\gamma \right) = f \quad (\text{A4})$$

Therefore,

$$\text{Area of segment BCD} = f r^2 \quad (\text{A5})$$

Where the segment area increases as lobes form

Introduce variable y :

where,

- y = distance of lobe centre from origin O (see Figure 3):

Applying Sine Rule,

$$\frac{R}{\sin(180 - \gamma)} = \frac{y}{\sin(\gamma - 45)}$$

$$\frac{R}{\sin \gamma} = \frac{y}{\sin \gamma \cos 45 - \cos \gamma \sin 45}$$

Dividing by Cos 60 and multiplying by sin 60,

$$y = \frac{1}{\sqrt{2}} R \left[\frac{\sin \gamma - \cos \gamma}{\sin \gamma} \right] = \frac{1}{\sqrt{2}} R \left[1 - \frac{1}{\tan \gamma} \right]$$

Introduce another variable f_1 :

$$f_1 = \frac{1}{\sqrt{2}} \left[1 - \frac{1}{\tan \gamma} \right] \quad (\text{A20})$$

Therefore (as with 3-lobed),

$$y = f_1 \times R \quad (\text{A7})$$

Calculating R for intermediate stage with equal cross-sectional area at all stages:

πR_1^2 = Area of pipe with no lobes (stage 1), i.e. circular pipe

Pipe area at intermediate stage = πR_1^2 = Area of 4 segmental lobes (BCD x 3) + Area of square BDEF

$$\text{Area of 4 segmental lobes (from Equation A5)} = 4 \times f r^2$$

Substituting for r using Cosine Rule,

$$r^2 = R^2 + y^2 - 2R \cdot y \cos 45 = R^2 + y^2 - \sqrt{2}R \cdot y \quad (\text{A21})$$

Therefore,

$$\text{Area of 4 segmental Lobes} = 4 \times f (R^2 + y^2 - \sqrt{2}R \cdot y)$$

Substituting for y from Equation A7,

$$\text{Area of 4 segmental Lobes} = 4 \times f (R^2 + f_1^2 R^2 - \sqrt{2}R^2 f_1)$$

$$\text{Area of square BDEF} = (2R \cos 45)^2 = \left(2R \times \frac{1}{\sqrt{2}}\right)^2 = 2R^2 \quad (\text{A22})$$

Adding area of square and segmental lobes,

$$\text{Pipe Area at intermediate stage} = 4fR^2(1 + f_1^2 - \sqrt{2}f_1) + 2R^2$$

Equating Area of circular pipe,

$$\pi R_1^2 = R^2 (4f + 4f_1^2 - 4\sqrt{2}f_1 + 2)$$

$$R^2 = R_1^2 \left[\frac{\pi}{4f + 4f_1^2 - 4\sqrt{2}f_1 + 2} \right]$$

$$R = R_1 \times \sqrt{\frac{\pi}{4f + 4f_1^2 - 4\sqrt{2}f_1 + 2}} \quad (\text{A23})$$

So calculate y from Equation A7 and calculate r from Equation A21

Calculating Lobe Area as a function of length,

$$\text{Total area of 3 segmental lobes (BCD, DGE, EFB)} = 4fr^2$$

Total area of INNER segments = Area of circle – Area of square BDEF

$$\text{Area of circle} = \pi R^2$$

$$\text{Area of square BDEF (from Equation A27)} = 2R^2$$

$$\text{Total area of INNER segments} = \pi R^2 - 2R^2$$

$$\text{Total Lobe Area at intermediate stage (LA}_i\text{)} = 4fr^2 - R^2(\pi - 2) \text{ (A24)}$$

Introducing a function alpha;

Function Alpha and Twist are defined as for 3-lobed pipe (Equations A12, A13 and A14).

Lobe Area for fully developed lobes (LA_{FD}) = (Swirl pipe area – Area of circle only for R_{cs})

$$= r_f^2(2\pi + 4) - \pi \times R_{cs}^2$$

Overall geometry generation:

γ increases from 45 to 90 in the given number of increments (N_{inc}) as lobes develop. For each increment of γ , functions f and f_1 are calculated using Equations A4 and A20 respectively. These in turn are used to calculate R (from Equation A23), y (Equation A7) and r (Equation A21) at each incremental stage. Lobe area is calculated using Equation A24, hence α (Equation A12) and x/L (Equation A13) and the respective Twist (Equation A14). Thereby, generating a table as before:

γ rad	f_1	f	R mm	y mm	r mm	LA mm ²	α	x/L	Twist rad
-----------------	-------	-----	-----------	-----------	-----------	-----------------------	----------	-------	--------------

Next, the values of γ above are used for cross-section geometry calculation at each stage of x/L .

Generating lobe co-ordinates

At each value of γ (therefore at each intermediate stage) along the length of the pipe, 100 increments are taken.

- $\gamma_0 \rightarrow -\gamma_0$ in 100 increments

As with 3-lobed pipe, for Lobe 1:

$$x_{lobe1} = r \sin \gamma$$

$$y' = r \cos \gamma$$

Therefore,

$$y_{lobe1} = -(y' + y) = -(y + r \cos \gamma)$$

Lobe Co-ordinates:

$$x_{1twisted} = x_{lobe1} \cos(Twist) - y_{lobe1} \sin(Twist) \quad (A15)$$

$$y_{1twisted} = y_{lobe1} \cos(Twist) - x_{lobe1} \sin(Twist) \quad (A16)$$

Continue calculation of x , y twisted data for lobes 2, 3 and 4 where for lobe 2,

$$x_{lobe2} = y_{lobe1} \sin\left(\frac{\pi}{2}\right) + x_{lobe1} \cos\left(\frac{\pi}{2}\right) \quad (A25)$$

$$y_{lobe2} = y_{lobe1} \cos\left(\frac{\pi}{2}\right) + x_{lobe1} \sin\left(\frac{\pi}{2}\right) \quad (A26)$$

For lobe 3, replace $(\pi/2)$ with (π) , and for lobe 4, with $(3\pi/2)$.

Hence the twisted lobe values ($x_{2\text{twisted}}$, $y_{2\text{twisted}}$, etc.) are calculated for lobes 2, 3 and 4 as well using Equations A15 and A16.

Appendix A3.2: Spreadsheet for 3-lobed Transition Pipe

Overall Geometry

3-lobe Transition Calculations - Geodesic Helix

INPUTS

ENTRY LINE

R= 25

Original pipe radius

Ninc= 10

rf= 17.4551

Lobe radius (Swirly Flo Design)

Rcs= 20.1554

Minimum core radius (Swirly Flo Design)

GEODESIC DATA

Pitch: Diameter

6 1

twist degrees p.m. = 1200 degrees of twist per metre

twist direction = -1 (-1 =anticlockwise)

LA(Total)= 687.253

Lobe area for fully-developed Swirly Flo design

L= 100

Length of transition based on one lobe twisted 120 degrees

γ/deg	γ/rad	f_1	f	R/mm	y/mm	r/mm	lobe area /mm ²	a	$x/L(cos)$	twist /deg
60	1.05	0.00	0.61	25.00	0.00	25.00	0.00	0.00	0.00	0.00
63	1.10	0.06	0.70	24.51	1.44	23.82	76.47	0.11	0.22	-25.98
66	1.15	0.11	0.78	24.02	2.75	22.77	150.75	0.22	0.31	-37.24
69	1.20	0.17	0.87	23.54	3.94	21.83	223.06	0.32	0.39	-46.31
72	1.26	0.22	0.96	23.06	5.04	20.99	293.58	0.43	0.45	-54.42
75	1.31	0.27	1.06	22.57	6.05	20.24	362.47	0.53	0.52	-62.10
78	1.36	0.32	1.16	22.09	6.98	19.56	429.89	0.63	0.58	-69.69
81	1.41	0.36	1.26	21.61	7.84	18.95	495.97	0.72	0.65	-77.54
84	1.47	0.41	1.36	21.13	8.64	18.40	560.82	0.82	0.72	-86.13
87	1.52	0.45	1.47	20.64	9.39	17.90	624.55	0.91	0.80	-96.56
90	1.57	0.50	1.57	20.16	10.08	17.46	687.25	1.00	1.00	-120.00

Lobe Co-ordinates: Stage 1

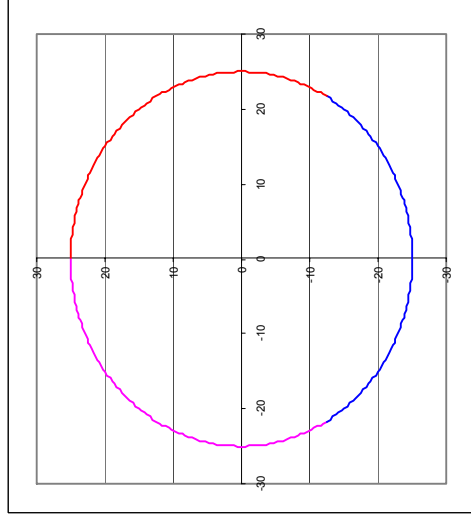
γ/deg	γ/rad	$f1$	f	R/mm	y/mm	r/mm	LA/mm^2	u	$x/L(\cos)$	twist/deg	twist/rad	twist/dim	N_{inc}
60.00	1.05	0.00	0.61	25.00	0.00	25.00	0.00	0.00	0.00	0.00	0.00	-1.00	100.00
γ/deg	γ/rad	$x(\text{lobe}1)$	$y(\text{lobe}1)$	$x1$	$y1$	$x(\text{lobe}2)$	$y(\text{lobe}2)$	$x2$	$y2$	$x(\text{lobe}3)$	$y(\text{lobe}3)$	$x3$	$y3$
60.00	1.05	21.65	-12.50	21.65	-12.50	-21.65	-12.50	-21.65	-12.50	0.00	0.00	25.00	0.00
58.80	1.03	21.38	-12.95	21.38	-12.95	-21.91	-12.04	-21.91	-12.04	0.52	24.99	0.52	24.99
57.60	1.01	21.11	-13.40	21.11	-13.40	-22.16	-11.58	-22.16	-11.58	1.05	24.98	1.05	24.98
56.40	0.98	20.82	-13.83	20.82	-13.83	-22.39	-11.12	-22.39	-11.12	1.57	24.95	1.57	24.95
55.20	0.96	20.53	-14.27	20.53	-14.27	-22.62	-10.64	-22.62	-10.64	2.09	24.91	2.09	24.91
54.00	0.94	20.23	-14.69	20.23	-14.69	-22.84	-10.17	-22.84	-10.17	2.61	24.86	2.61	24.86
52.80	0.92	19.91	-15.11	19.91	-15.11	-23.05	-9.69	-23.05	-9.69	3.13	24.80	3.13	24.80
51.60	0.90	19.59	-15.53	19.59	-15.53	-23.24	-9.20	-23.24	-9.20	3.65	24.73	3.65	24.73
50.40	0.88	19.26	-15.94	19.26	-15.94	-23.43	-8.71	-23.43	-8.71	4.17	24.65	4.17	24.65
49.20	0.86	18.92	-16.34	18.92	-16.34	-23.61	-8.22	-23.61	-8.22	4.68	24.56	4.68	24.56
48.00	0.84	18.58	-16.73	18.58	-16.73	-23.78	-7.73	-23.78	-7.73	5.20	24.45	5.20	24.45
46.80	0.82	18.22	-17.11	18.22	-17.11	-23.93	-7.23	-23.93	-7.23	5.71	24.34	5.71	24.34
45.60	0.80	17.86	-17.49	17.86	-17.49	-24.08	-6.72	-24.08	-6.72	6.22	24.21	6.22	24.21
44.40	0.77	17.49	-17.86	17.49	-17.86	-24.21	-6.22	-24.21	-6.22	6.72	24.08	6.72	24.08
43.20	0.75	17.11	-18.22	17.11	-18.22	-24.34	-5.71	-24.34	-5.71	7.23	23.93	7.23	23.93
42.00	0.73	16.73	-18.58	16.73	-18.58	-24.45	-5.20	-24.45	-5.20	7.73	23.78	7.73	23.78
40.80	0.71	16.34	-18.92	16.34	-18.92	-24.56	-4.68	-24.56	-4.68	8.22	23.61	8.22	23.61
39.60	0.69	15.94	-19.26	15.94	-19.26	-24.65	-4.17	-24.65	-4.17	8.71	23.43	8.71	23.43
38.40	0.67	15.53	-19.59	15.53	-19.59	-24.73	-3.65	-24.73	-3.65	9.20	23.24	9.20	23.24
37.20	0.65	15.11	-19.91	15.11	-19.91	-24.80	-3.13	-24.80	-3.13	9.69	23.05	9.69	23.05
36.00	0.63	14.69	-20.23	14.69	-20.23	-24.86	-2.61	-24.86	-2.61	10.17	22.84	10.17	22.84
34.80	0.61	14.27	-20.53	14.27	-20.53	-24.91	-2.09	-24.91	-2.09	10.64	22.62	10.64	22.62
33.60	0.59	13.83	-20.82	13.83	-20.82	-24.95	-1.57	-24.95	-1.57	11.12	22.39	11.12	22.39
32.40	0.57	13.40	-21.11	13.40	-21.11	-24.98	-1.05	-24.98	-1.05	11.58	22.16	11.58	22.16
31.20	0.54	12.95	-21.38	12.95	-21.38	-24.99	-0.52	-24.99	-0.52	12.04	21.91	12.04	21.91
30.00	0.52	12.50	-21.65	12.50	-21.65	-25.00	0.00	-25.00	0.00	12.50	21.65	12.50	21.65
28.80	0.50	12.04	-21.91	12.04	-21.91	-24.99	0.52	-24.99	0.52	12.95	21.38	12.95	21.38
27.60	0.48	11.58	-22.16	11.58	-22.16	-24.98	1.05	-24.98	1.05	13.40	21.11	13.40	21.11
26.40	0.46	11.12	-22.39	11.12	-22.39	-24.95	1.57	-24.95	1.57	13.83	20.82	13.83	20.82
25.20	0.44	10.64	-22.62	10.64	-22.62	-24.91	2.09	-24.91	2.09	14.27	20.53	14.27	20.53
24.00	0.42	10.17	-22.84	10.17	-22.84	-24.86	2.61	-24.86	2.61	14.69	20.23	14.69	20.23
22.80	0.40	9.69	-23.05	9.69	-23.05	-24.80	3.13	-24.80	3.13	15.11	19.91	15.11	19.91
21.60	0.38	9.20	-23.24	9.20	-23.24	-24.73	3.65	-24.73	3.65	15.53	19.59	15.53	19.59
20.40	0.36	8.71	-23.43	8.71	-23.43	-24.65	4.17	-24.65	4.17	15.94	19.26	15.94	19.26
19.20	0.34	8.22	-23.61	8.22	-23.61	-24.56	4.68	-24.56	4.68	16.34	18.92	16.34	18.92
18.00	0.31	7.73	-23.78	7.73	-23.78	-24.45	5.20	-24.45	5.20	16.73	18.58	16.73	18.58
16.80	0.29	7.23	-23.93	7.23	-23.93	-24.34	5.71	-24.34	5.71	17.11	18.22	17.11	18.22
15.60	0.27	6.72	-24.08	6.72	-24.08	-24.21	6.22	-24.21	6.22	17.49	17.86	17.49	17.86
14.40	0.25	6.22	-24.21	6.22	-24.21	-24.08	6.72	-24.08	6.72	17.86	17.49	17.86	17.49
13.20	0.23	5.71	-24.34	5.71	-24.34	-23.93	7.23	-23.93	7.23	18.22	17.11	18.22	17.11
12.00	0.21	5.20	-24.45	5.20	-24.45	-23.78	7.73	-23.78	7.73	18.58	16.73	18.58	16.73
10.80	0.19	4.68	-24.56	4.68	-24.56	-23.61	8.22	-23.61	8.22	18.92	16.34	18.92	16.34
9.60	0.17	4.17	-24.65	4.17	-24.65	-23.43	8.71	-23.43	8.71	19.26	15.94	19.26	15.94
8.40	0.15	3.65	-24.73	3.65	-24.73	-23.24	9.20	-23.24	9.20	19.59	15.53	19.59	15.53
7.20	0.13	3.13	-24.80	3.13	-24.80	-23.05	9.69	-23.05	9.69	19.91	15.11	19.91	15.11
6.00	0.10	2.61	-24.86	2.61	-24.86	-22.84	10.17	-22.84	10.17	20.23	14.69	20.23	14.69
4.80	0.08	2.09	-24.91	2.09	-24.91	-22.62	10.64	-22.62	10.64	20.53	14.27	20.53	14.27
3.60	0.06	1.57	-24.95	1.57	-24.95	-22.39	11.12	-22.39	11.12	20.82	13.83	20.82	13.83
2.40	0.04	1.05	-24.98	1.05	-24.98	-22.16	11.58	-22.16	11.58	21.11	13.40	21.11	13.40
1.20	0.02	0.52	-24.99	0.52	-24.99	-21.91	12.04	-21.91	12.04	21.38	12.95	21.38	12.95

Lobe Co-ordinates contd...

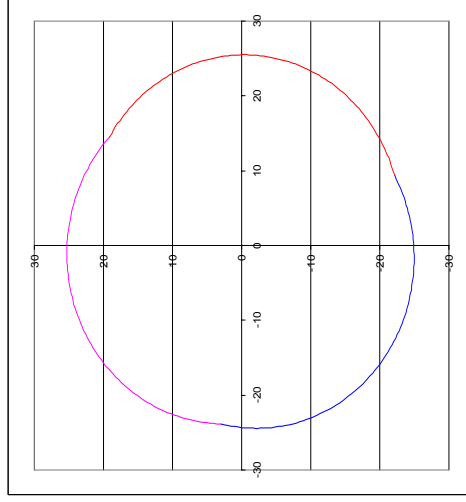
θ / deg	r / rad	$x(lobe1)$	$y(lobe1)$	$x1$	$y1$	$x1$ twisted	$y1$ twisted	$x(lobe2)$	$y(lobe2)$	$x2$ twisted	$y2$ twisted	$x(lobe3)$	$y(lobe3)$	$x3$ twisted	$y3$ twisted
0.00	0.00	0.00	-25.00	-25.00	0.00	-25.00	-21.65	12.50	-21.65	12.50	-21.65	12.50	-21.65	12.50	-21.65
-1.20	-0.02	-0.52	-24.99	-24.99	-0.52	-24.99	-21.38	12.95	-21.38	12.95	-21.38	12.95	-21.38	12.95	-21.38
-2.40	-0.04	-1.05	-24.98	-24.98	-1.05	-24.98	-21.11	13.40	-21.11	13.40	-21.11	13.40	-21.11	13.40	-21.11
-3.60	-0.06	-1.57	-24.95	-24.95	-1.57	-24.95	-20.82	13.83	-20.82	13.83	-20.82	13.83	-20.82	13.83	-20.82
-4.80	-0.08	-2.09	-24.91	-24.91	-2.09	-24.91	-20.53	14.27	-20.53	14.27	-20.53	14.27	-20.53	14.27	-20.53
-6.00	-0.10	-2.61	-24.86	-24.86	-2.61	-24.86	-20.23	14.69	-20.23	14.69	-20.23	14.69	-20.23	14.69	-20.23
-7.20	-0.13	-3.13	-24.80	-24.80	-3.13	-24.80	-19.91	15.11	-19.91	15.11	-19.91	15.11	-19.91	15.11	-19.91
-8.40	-0.15	-3.65	-24.73	-24.73	-3.65	-24.73	-19.59	15.53	-19.59	15.53	-19.59	15.53	-19.59	15.53	-19.59
-9.60	-0.17	-4.17	-24.65	-24.65	-4.17	-24.65	-19.26	15.94	-19.26	15.94	-19.26	15.94	-19.26	15.94	-19.26
-10.80	-0.19	-4.68	-24.56	-24.56	-4.68	-24.56	-18.92	16.34	-18.92	16.34	-18.92	16.34	-18.92	16.34	-18.92
-12.00	-0.21	-5.20	-24.45	-24.45	-5.20	-24.45	-18.58	16.73	-18.58	16.73	-18.58	16.73	-18.58	16.73	-18.58
-13.20	-0.23	-5.71	-24.34	-24.34	-5.71	-24.34	-18.22	17.11	-18.22	17.11	-18.22	17.11	-18.22	17.11	-18.22
-14.40	-0.25	-6.22	-24.21	-24.21	-6.22	-24.21	-17.86	17.49	-17.86	17.49	-17.86	17.49	-17.86	17.49	-17.86
-15.60	-0.27	-6.72	-24.08	-24.08	-6.72	-24.08	-17.49	17.86	-17.49	17.86	-17.49	17.86	-17.49	17.86	-17.49
-16.80	-0.29	-7.23	-23.93	-23.93	-7.23	-23.93	-17.11	18.22	-17.11	18.22	-17.11	18.22	-17.11	18.22	-17.11
-18.00	-0.31	-7.73	-23.78	-23.78	-7.73	-23.78	-16.73	18.58	-16.73	18.58	-16.73	18.58	-16.73	18.58	-16.73
-19.20	-0.34	-8.22	-23.61	-23.61	-8.22	-23.61	-16.34	18.92	-16.34	18.92	-16.34	18.92	-16.34	18.92	-16.34
-20.40	-0.36	-8.71	-23.43	-23.43	-8.71	-23.43	-15.94	19.26	-15.94	19.26	-15.94	19.26	-15.94	19.26	-15.94
-21.60	-0.38	-9.20	-23.24	-23.24	-9.20	-23.24	-15.53	19.59	-15.53	19.59	-15.53	19.59	-15.53	19.59	-15.53
-22.80	-0.40	-9.69	-23.05	-23.05	-9.69	-23.05	-15.11	19.91	-15.11	19.91	-15.11	19.91	-15.11	19.91	-15.11
-24.00	-0.42	-10.17	-22.84	-22.84	-10.17	-22.84	-14.69	20.23	-14.69	20.23	-14.69	20.23	-14.69	20.23	-14.69
-25.20	-0.44	-10.64	-22.62	-22.62	-10.64	-22.62	-14.27	20.53	-14.27	20.53	-14.27	20.53	-14.27	20.53	-14.27
-26.40	-0.46	-11.12	-22.39	-22.39	-11.12	-22.39	-13.83	20.82	-13.83	20.82	-13.83	20.82	-13.83	20.82	-13.83
-27.60	-0.48	-11.58	-22.16	-22.16	-11.58	-22.16	-13.40	21.11	-13.40	21.11	-13.40	21.11	-13.40	21.11	-13.40
-28.80	-0.50	-12.04	-21.91	-21.91	-12.04	-21.91	-12.95	21.38	-12.95	21.38	-12.95	21.38	-12.95	21.38	-12.95
-30.00	-0.52	-12.50	-21.65	-21.65	-12.50	-21.65	-12.50	21.65	-12.50	21.65	-12.50	21.65	-12.50	21.65	-12.50
-31.20	-0.54	-12.95	-21.38	-21.38	-12.95	-21.38	-12.04	21.91	-12.04	21.91	-12.04	21.91	-12.04	21.91	-12.04
-32.40	-0.57	-13.40	-21.11	-21.11	-13.40	-21.11	-11.58	22.16	-11.58	22.16	-11.58	22.16	-11.58	22.16	-11.58
-33.60	-0.59	-13.83	-20.82	-20.82	-13.83	-20.82	-11.12	22.39	-11.12	22.39	-11.12	22.39	-11.12	22.39	-11.12
-34.80	-0.61	-14.27	-20.53	-20.53	-14.27	-20.53	-10.64	22.62	-10.64	22.62	-10.64	22.62	-10.64	22.62	-10.64
-36.00	-0.63	-14.69	-20.23	-20.23	-14.69	-20.23	-10.17	22.84	-10.17	22.84	-10.17	22.84	-10.17	22.84	-10.17
-37.20	-0.65	-15.11	-19.91	-19.91	-15.11	-19.91	-9.69	23.05	-9.69	23.05	-9.69	23.05	-9.69	23.05	-9.69
-38.40	-0.67	-15.53	-19.59	-19.59	-15.53	-19.59	-9.20	23.24	-9.20	23.24	-9.20	23.24	-9.20	23.24	-9.20
-39.60	-0.69	-15.94	-19.26	-19.26	-15.94	-19.26	-8.71	23.43	-8.71	23.43	-8.71	23.43	-8.71	23.43	-8.71
-40.80	-0.71	-16.34	-18.92	-18.92	-16.34	-18.92	-8.22	23.61	-8.22	23.61	-8.22	23.61	-8.22	23.61	-8.22
-42.00	-0.73	-16.73	-18.58	-18.58	-16.73	-18.58	-7.73	23.78	-7.73	23.78	-7.73	23.78	-7.73	23.78	-7.73
-43.20	-0.75	-17.11	-18.22	-18.22	-17.11	-18.22	-7.23	23.93	-7.23	23.93	-7.23	23.93	-7.23	23.93	-7.23
-44.40	-0.77	-17.49	-17.86	-17.86	-17.49	-17.86	-6.72	24.08	-6.72	24.08	-6.72	24.08	-6.72	24.08	-6.72
-45.60	-0.80	-17.86	-17.49	-17.49	-17.86	-17.49	-6.22	24.21	-6.22	24.21	-6.22	24.21	-6.22	24.21	-6.22
-46.80	-0.82	-18.22	-17.11	-17.11	-18.22	-17.11	-5.71	24.34	-5.71	24.34	-5.71	24.34	-5.71	24.34	-5.71
-48.00	-0.84	-18.58	-16.73	-16.73	-18.58	-16.73	-5.20	24.45	-5.20	24.45	-5.20	24.45	-5.20	24.45	-5.20
-49.20	-0.86	-18.92	-16.34	-16.34	-18.92	-16.34	-4.68	24.56	-4.68	24.56	-4.68	24.56	-4.68	24.56	-4.68
-50.40	-0.88	-19.26	-15.94	-15.94	-19.26	-15.94	-4.17	24.65	-4.17	24.65	-4.17	24.65	-4.17	24.65	-4.17
-51.60	-0.90	-19.59	-15.53	-15.53	-19.59	-15.53	-3.65	24.73	-3.65	24.73	-3.65	24.73	-3.65	24.73	-3.65
-52.80	-0.92	-19.91	-15.11	-15.11	-19.91	-15.11	-3.13	24.80	-3.13	24.80	-3.13	24.80	-3.13	24.80	-3.13
-54.00	-0.94	-20.23	-14.69	-14.69	-20.23	-14.69	-2.61	24.86	-2.61	24.86	-2.61	24.86	-2.61	24.86	-2.61
-55.20	-0.96	-20.53	-14.27	-14.27	-20.53	-14.27	-2.09	24.91	-2.09	24.91	-2.09	24.91	-2.09	24.91	-2.09
-56.40	-0.98	-20.82	-13.83	-13.83	-20.82	-13.83	-1.57	24.95	-1.57	24.95	-1.57	24.95	-1.57	24.95	-1.57
-57.60	-1.01	-21.11	-13.40	-13.40	-21.11	-13.40	-1.05	24.98	-1.05	24.98	-1.05	24.98	-1.05	24.98	-1.05
-58.80	-1.03	-21.38	-12.95	-12.95	-21.38	-12.95	-0.52	24.99	-0.52	24.99	-0.52	24.99	-0.52	24.99	-0.52
-60.00	-1.05	-21.65	-12.50	-12.50	-21.65	-12.50	0.00	25.00	0.00	25.00	0.00	25.00	0.00	25.00	0.00

Appendix A3.3: 3-Lobed Transition Development

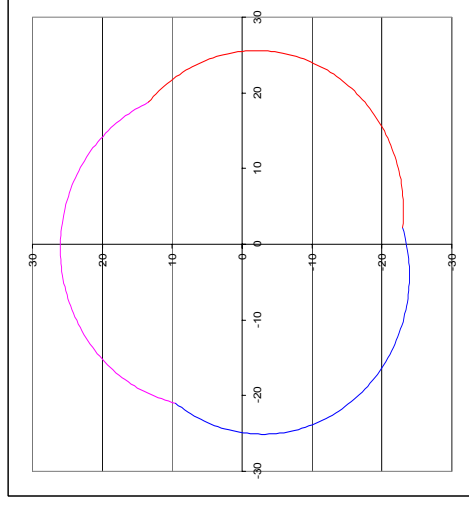
Stage 1, $\gamma=60$



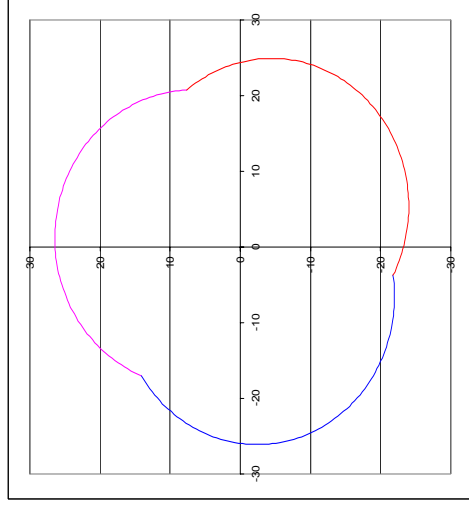
Stage 3, $\gamma=66$



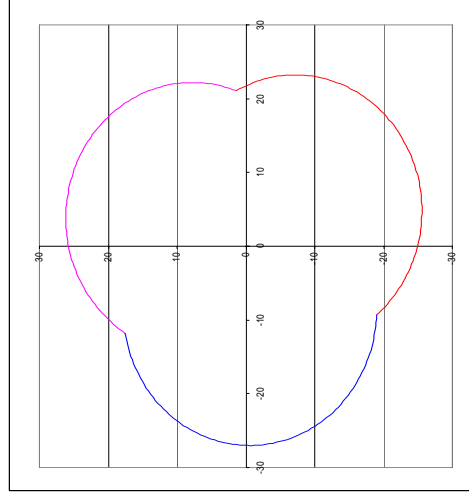
Stage 5, $\gamma=72$



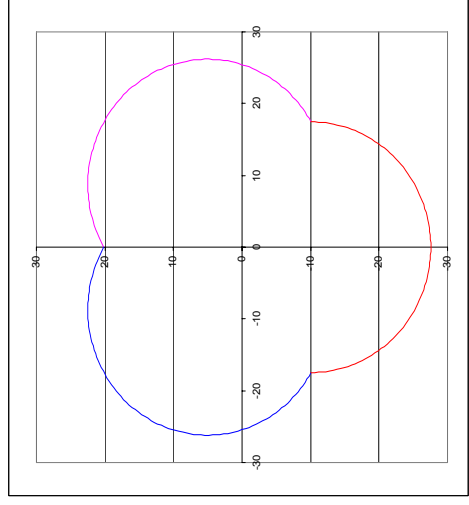
Stage 7, $\gamma=78$



Stage 9, $\gamma=83$

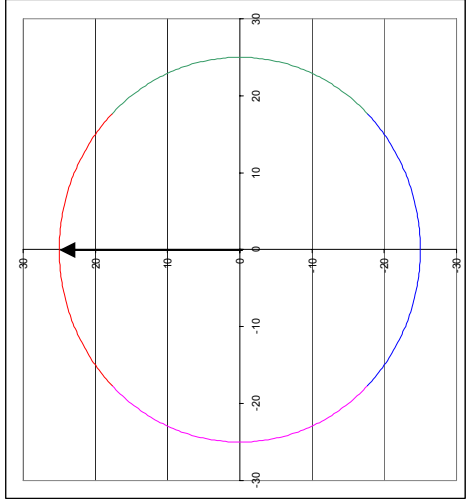


Stage 11 (final), $\gamma=90$

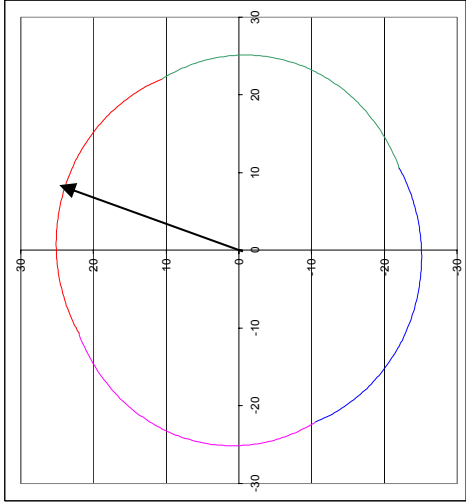


Appendix A3.4: 4-Lobed Transition Development

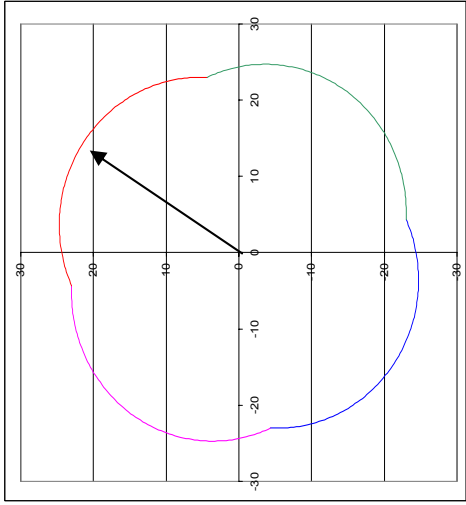
Stage 1, $\gamma=45$



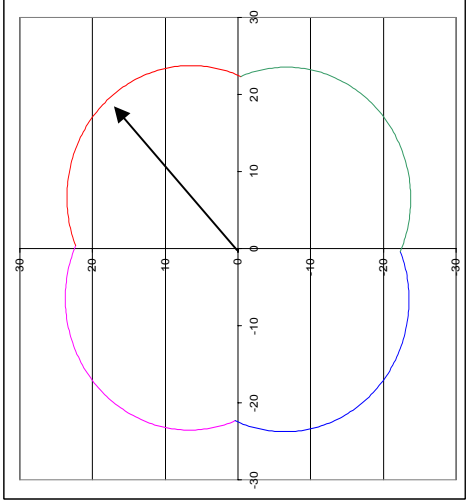
Stage 3, $\gamma=49.5$



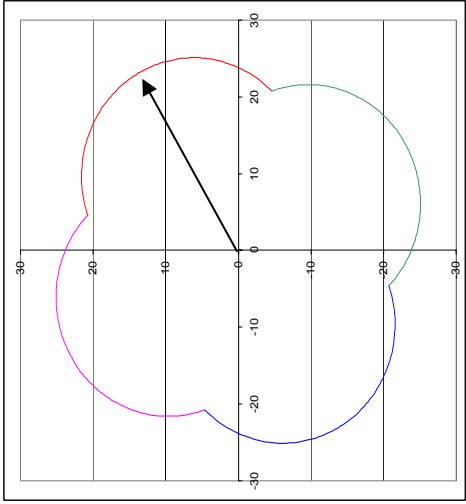
Stage 5, $\gamma=58.5$



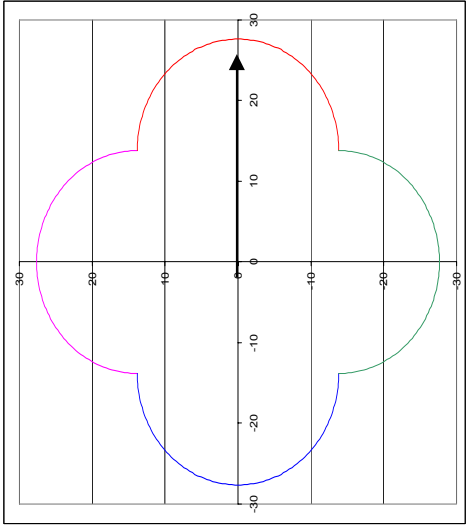
Stage 7, $\gamma=67.5$



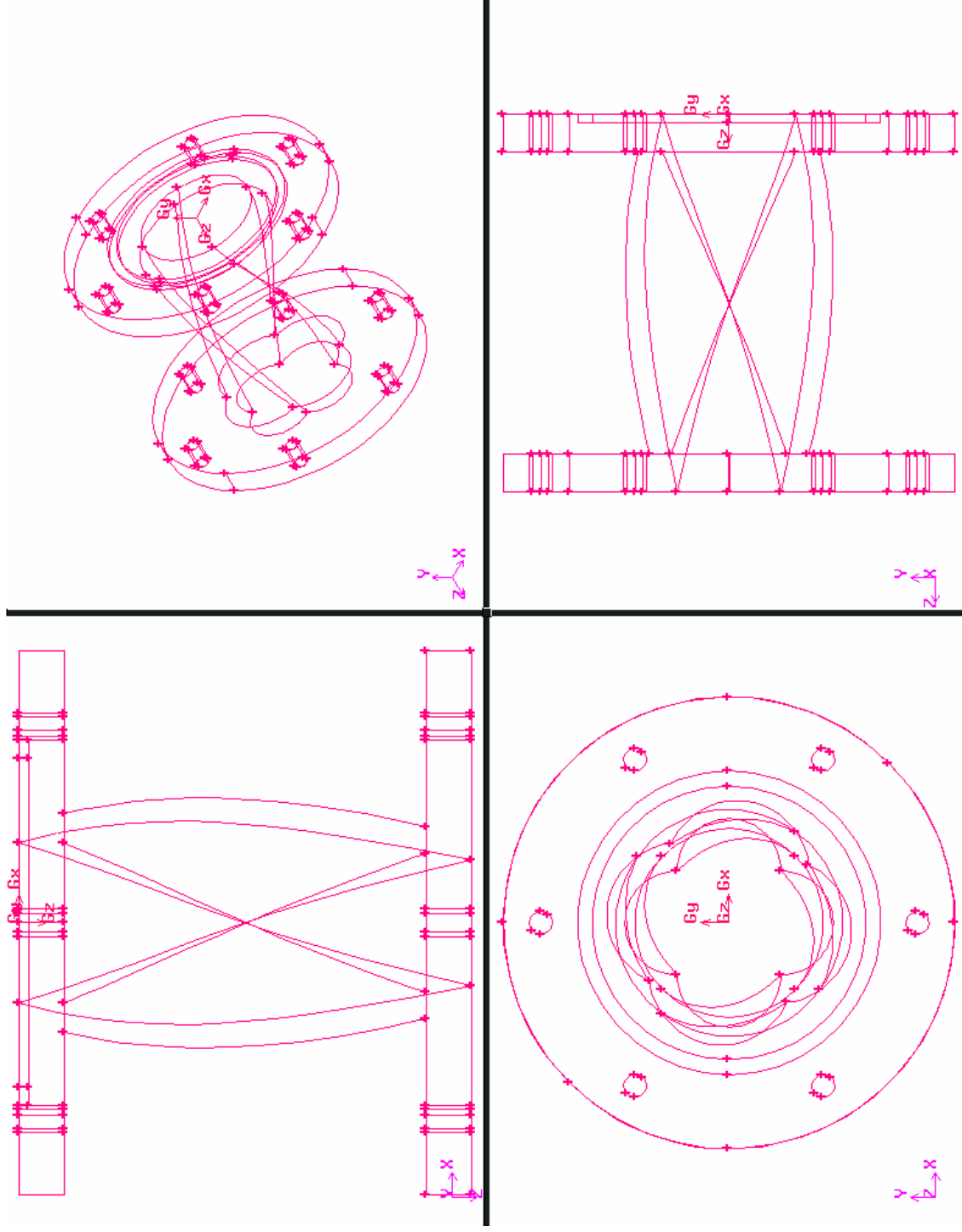
Stage 9, $\gamma=76.5$



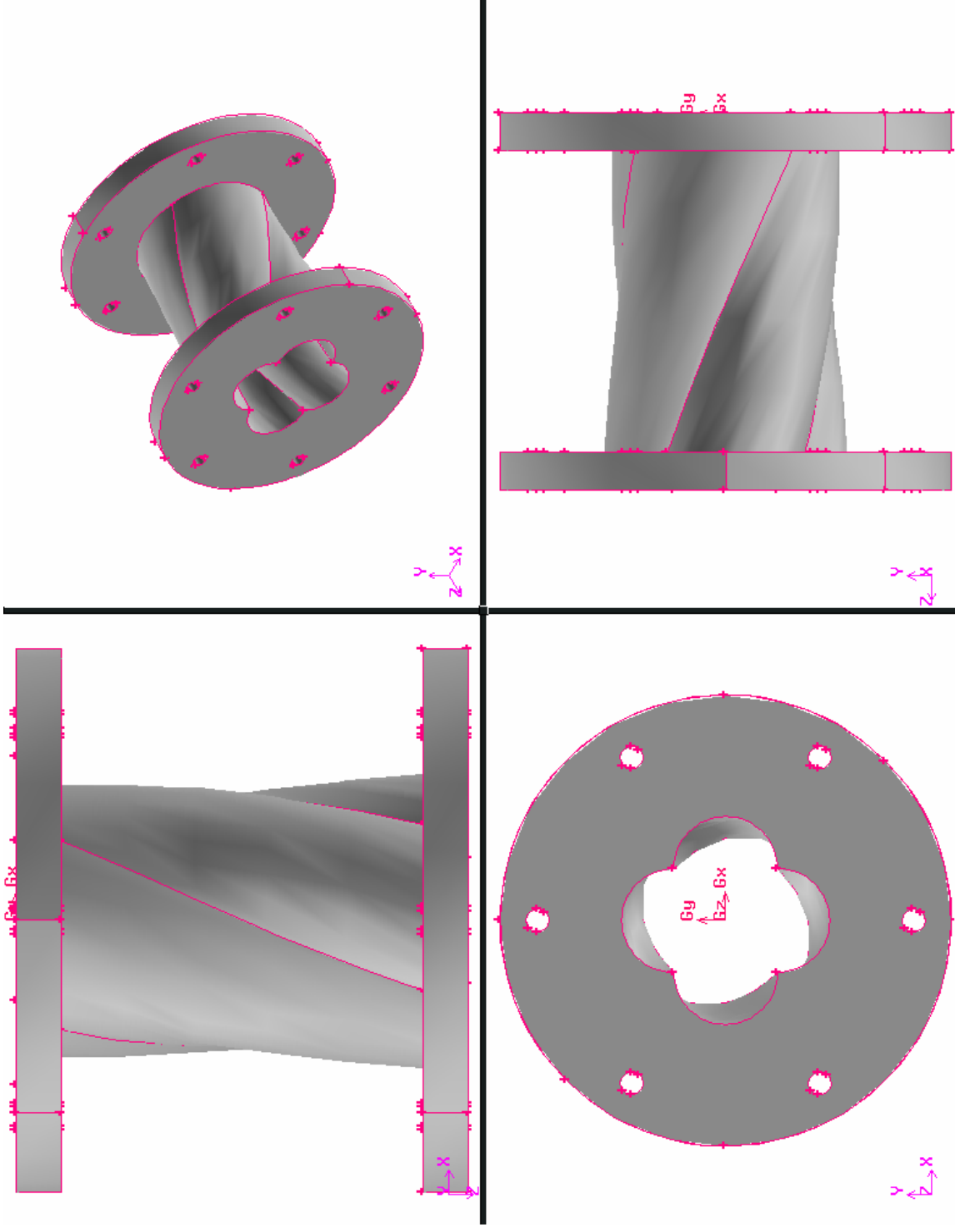
Stage 11 (final), $\gamma=90$



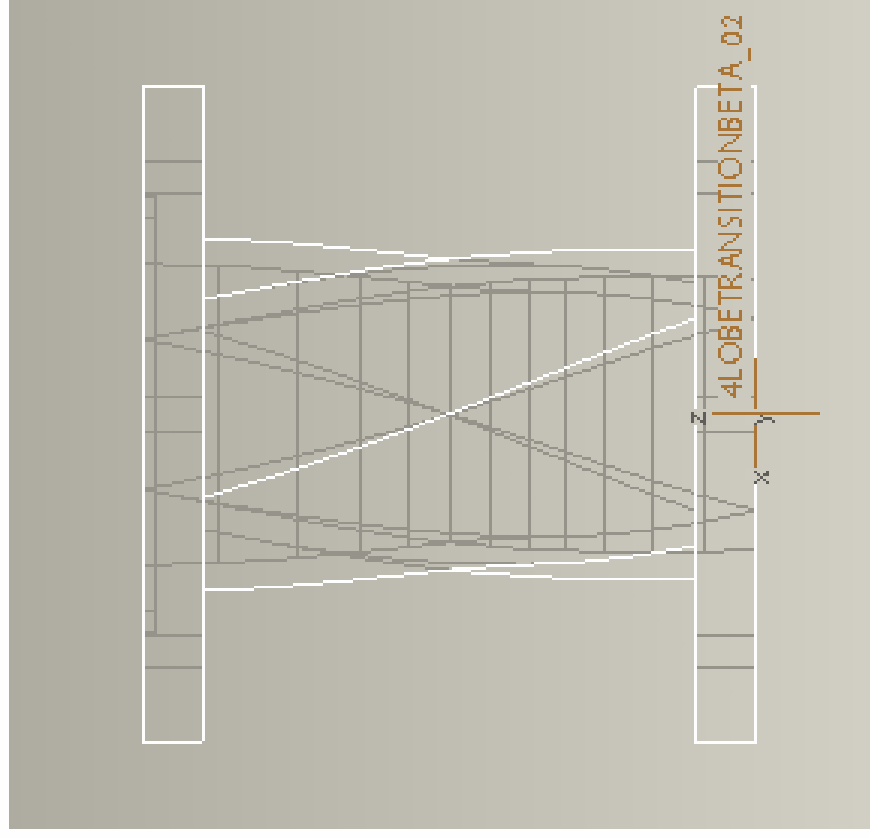
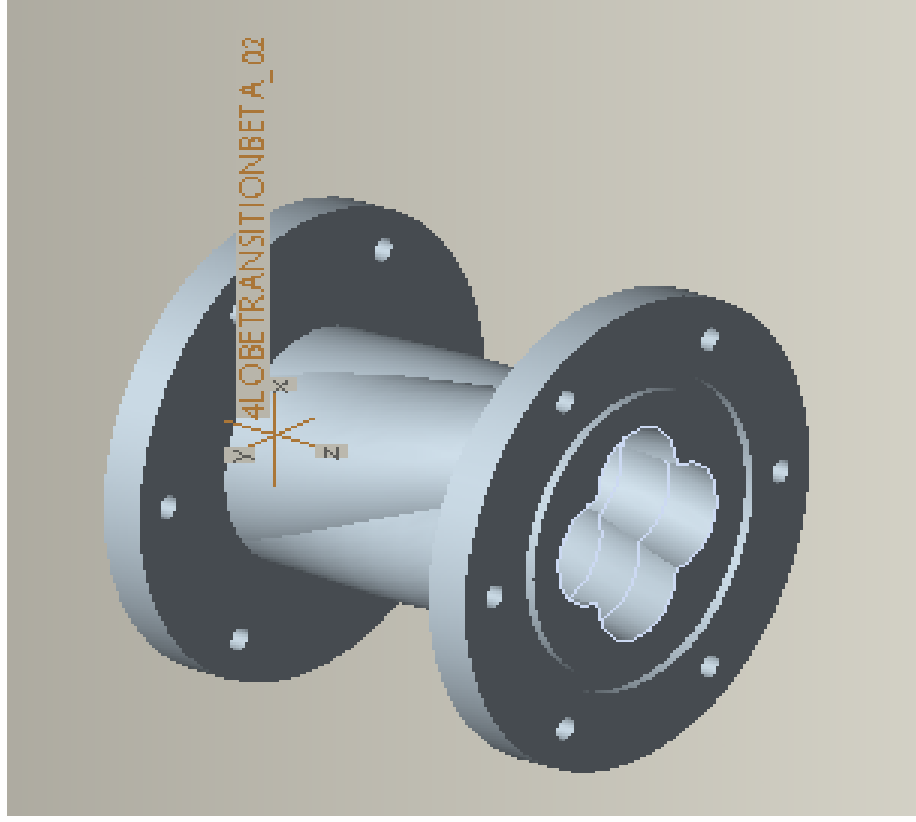
Appendix A3.5: 4-Lobed Transition Pipe (Beta, $n=1$)



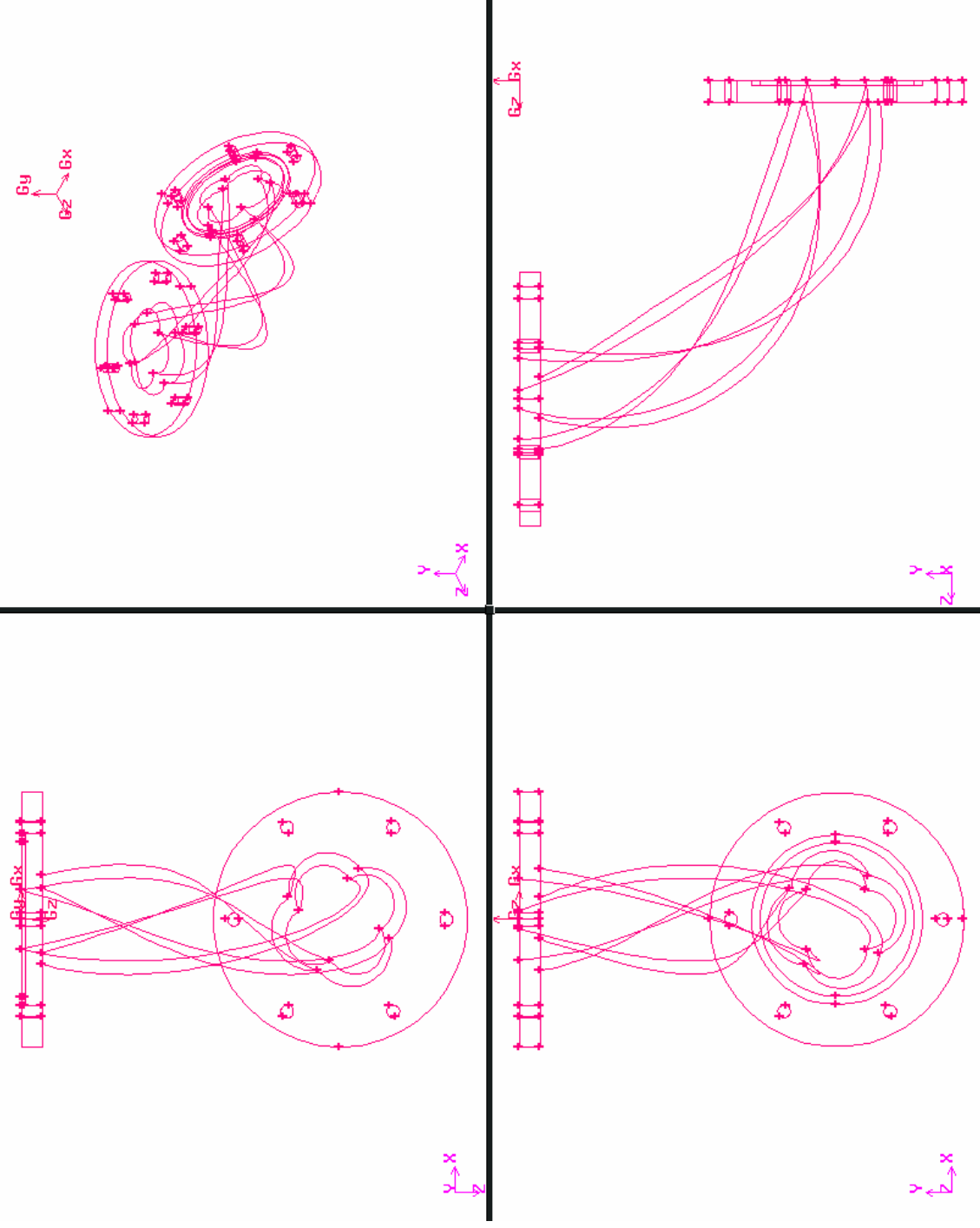
Appendix A3.5: 4-Lobed Transition Pipe (Beta, $n=1$)



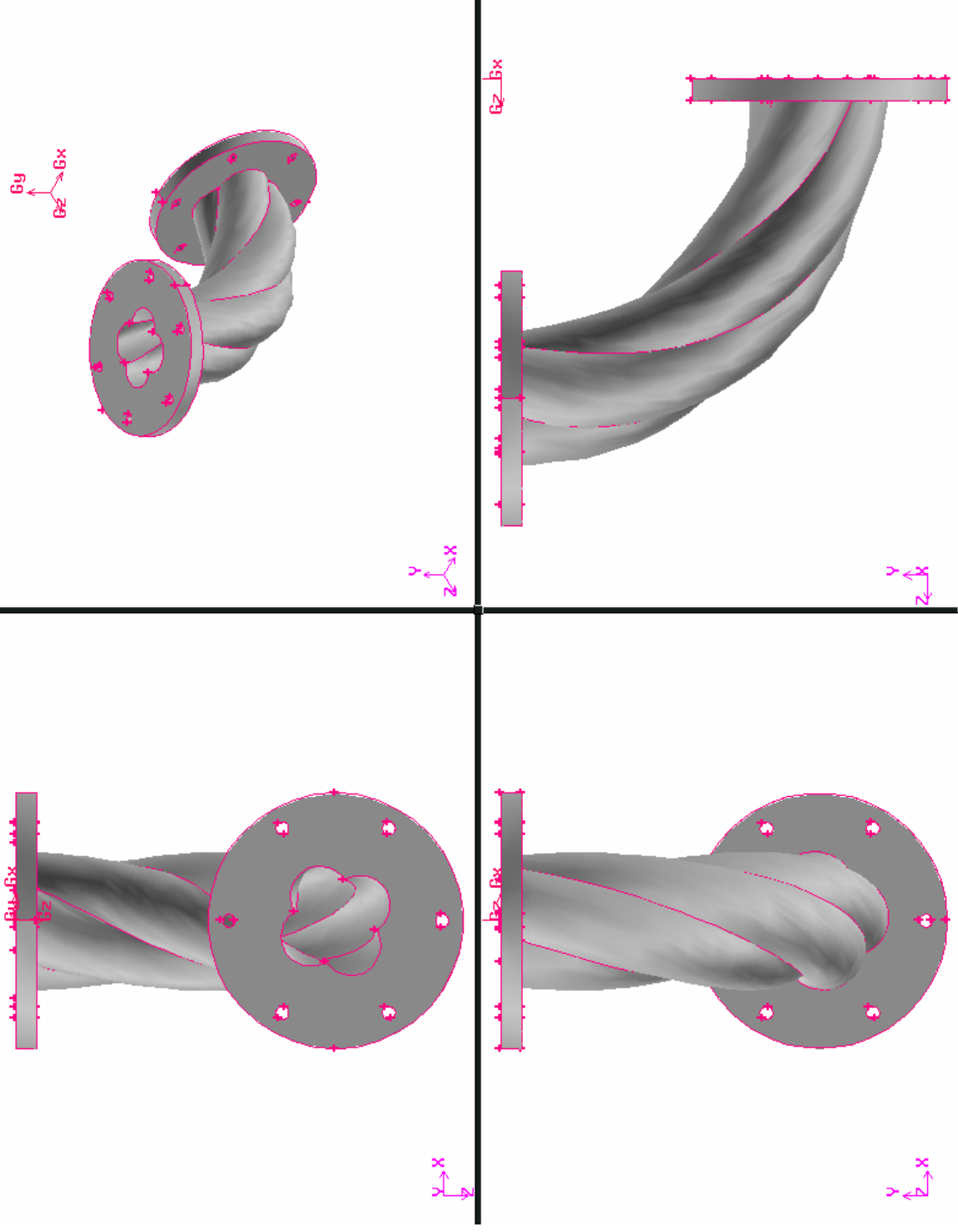
Appendix A3.5: Transition Pipe (Beta, $n=1$)



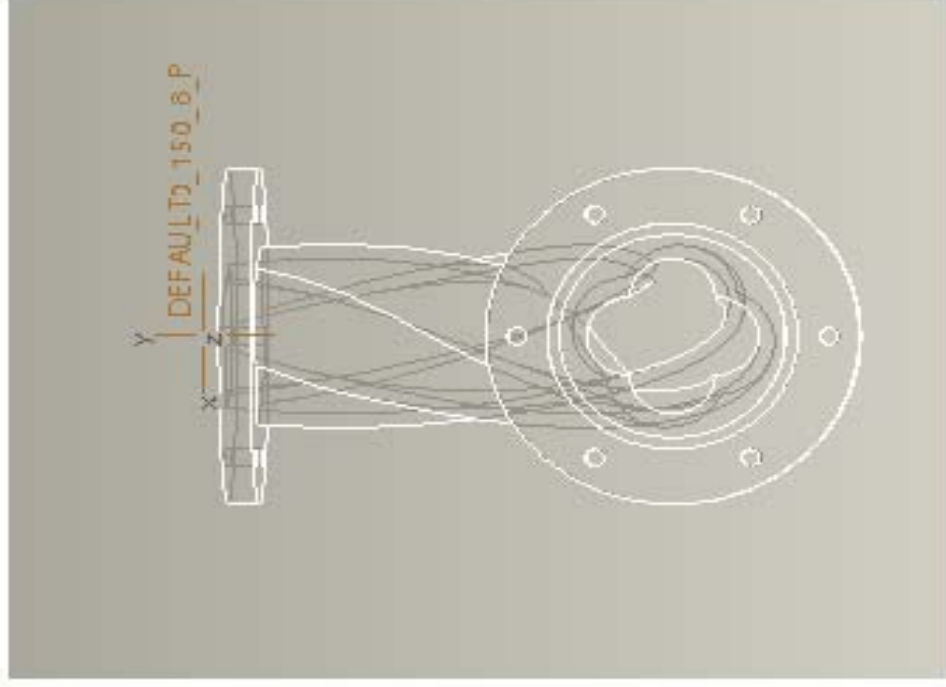
Appendix A3.5: 4-Lobed Swirl Bend ($R_c/D = 1.5$)



Appendix A3.5: 4-Lobed Swirl Bend ($R_c/D = 1.5$)



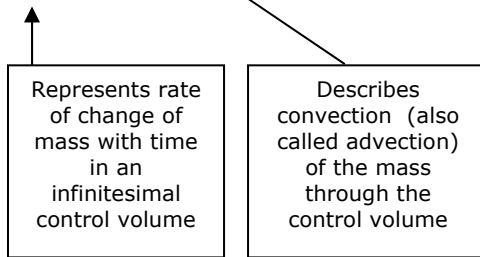
Appendix A3.5: 4-Lobed Swirl Bend ($R_c/D = 1.5$)



Appendix A4.1: Navier-Stokes Equations

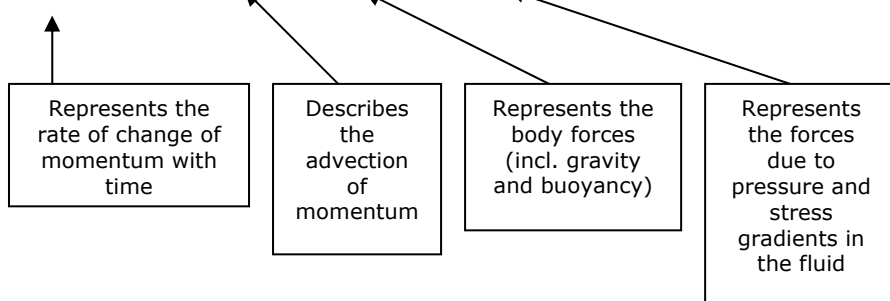
Continuity Equation:

$$\frac{\partial \rho}{\partial t} + \nabla \cdot (\rho V) = 0 \quad (\text{A4.1})$$



Viscous Momentum Equation:

$$\frac{\partial(\rho V)}{\partial t} + \nabla \cdot (\rho V V) = \rho f + (-p\delta_{ij} + \tau_{ij}) \quad (\text{A4.2})$$



δ_{ij} is the Kronecker delta and τ_{ij} is the viscous stress tensor:

$$\tau_{ij} = \mu \left[\left(\frac{\partial u_i}{\partial x_j} + \frac{\partial u_j}{\partial x_i} \right) - \frac{2}{3} \delta_{ij} \mu \frac{\partial u_k}{\partial x_k} \right] \quad (\text{A4.3})$$

u_i, u_j, u_k = general velocity term

Energy Equation:

The diagram illustrates the Energy Equation (A4.4) with arrows pointing from descriptive boxes to specific terms in the equation:

- Represents the rate of energy with time** points to $\frac{\partial E_t}{\partial t}$.
- Represents the rate of heat loss by conduction** points to $-\nabla q$.
- Represents the advection of energy** points to $\nabla \cdot (E_t V)$.
- Represents the rate of heat generation (Q) by external sources** points to $\frac{\partial Q}{\partial t}$.
- Represents the power associated with the body forces and the pressure and stress gradients respectively.** points to the bracketed term $\rho f \cdot V + \nabla \cdot [(-p\delta_{ij} + \tau_{ij}) \cdot \nabla]$.

$$\frac{\partial E_t}{\partial t} + \nabla \cdot (E_t V) = \frac{\partial Q}{\partial t} - \nabla q + \rho f \cdot V + \nabla \cdot [(-p\delta_{ij} + \tau_{ij}) \cdot \nabla] \quad (\text{A4.4})$$

E_t = total Energy

Appendix A4.2: Comparison of Non-Equilibrium Wall Functions to Standard Wall Functions

Pipe: 4-lobed swirl pipe 400mm length + 4-lobed exit beta transition pipe
n=1 100mm length

Model parameters: Water only simulation, uniform axial velocity inlet of
1.5m/s

Length	Standard Wall Functions			Non-Equilibrium Wall Functions		
	P, Pa	w, m/s	ΔP , Pa	P, Pa	w, m/s	ΔP , Pa
0	494.39	0.000	0	480.06	0.000	0
0.05	373.88	0.161	120.51	360.82	0.161	119.24
0.1	318.54	0.205	175.85	306.77	0.204	173.29
0.15	271.37	0.229	223.02	260.96	0.228	219.1
0.2	227.59	0.245	266.8	218.58	0.244	261.48
0.25	185.86	0.255	308.53	178.22	0.255	301.84
0.3	145.46	0.262	348.93	139.19	0.262	340.87
0.35	105.3	0.267	389.09	100.29	0.267	379.77
0.4	64.81	0.270	429.58	61.08	0.270	418.98
0.41	58.64	0.271	435.75	55.11	0.271	424.95
0.42	52.47	0.268	441.92	49.29	0.269	430.77
0.43	46.08	0.266	448.31	43.26	0.266	436.8
0.44	41.41	0.261	452.98	38.88	0.262	441.18
0.45	32.74	0.255	461.65	30.37	0.256	449.69
0.46	34.35	0.249	460.04	32.51	0.250	447.55
0.47	31.7	0.243	462.69	30.27	0.243	449.79
0.48	28.03	0.237	466.36	26.93	0.238	453.13
0.49	24.07	0.233	470.32	23.27	0.233	456.79
0.5	19.28	0.228	475.11	18.85	0.229	461.21

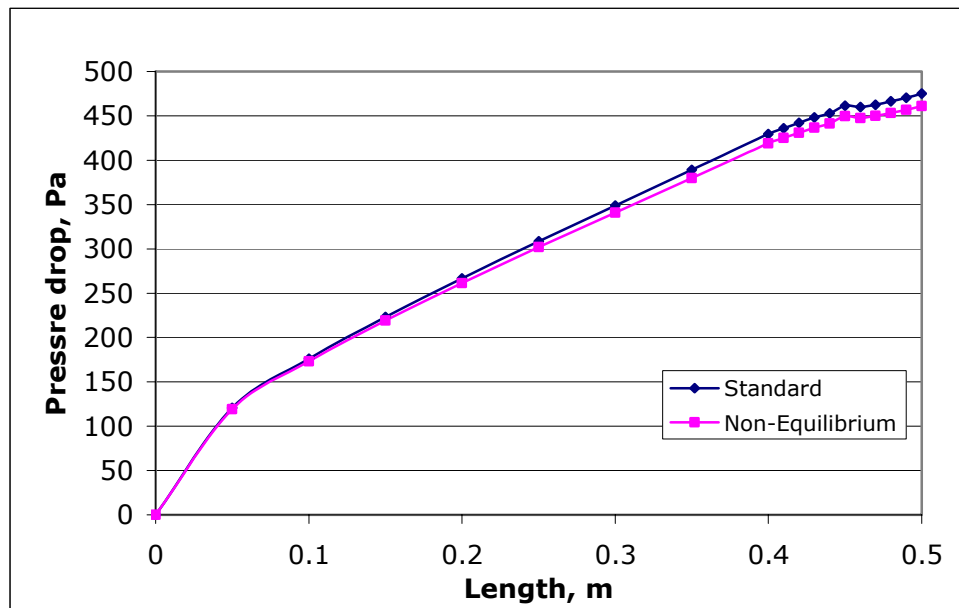


Figure A4.1: Comparison of Wall Functions for Pressure drop

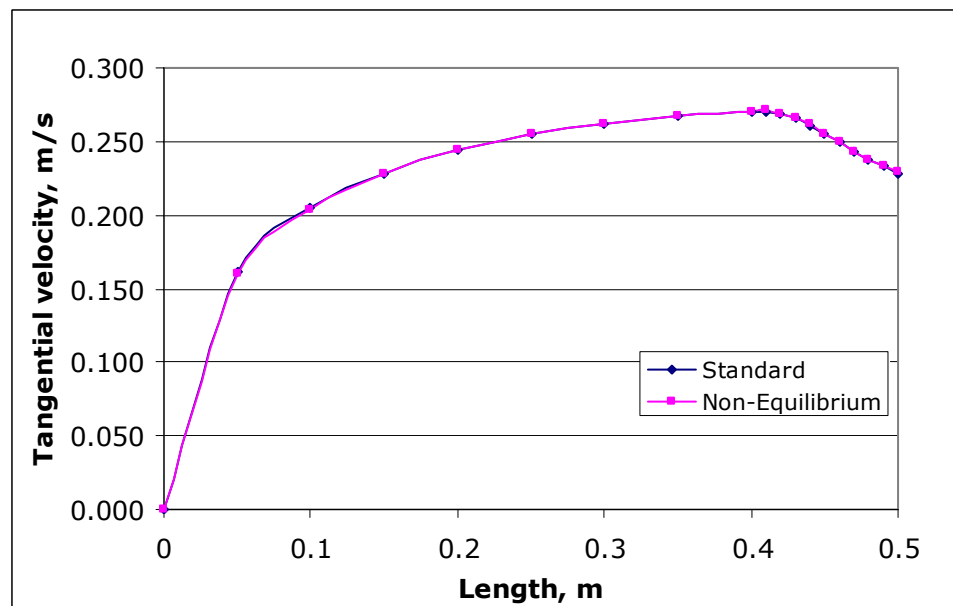


Figure A4.2: Comparison of Wall Functions for Tangential Velocity

Appendix A4.3: Comparison of Difference in Turbulence Intensity

Ganeshalingam and Raylor used 10% (Raylor 1998; Ganeshalingam 2002). A turbulence intensity of 4% as calculated from equation provided in Fluent manual (Fluent Inc. Lebanon 2001) was used for all simulations in this thesis. The difference in the final results is highlighted below.

Pipe: 4-lobed beta entry transition pipe, $n=1$, 100mm length

Model parameters: Water only simulation, uniform axial velocity inlet of 1.5m/s

Turbulence Intensity, I	10%	4%
ΔP , Pa	137.27	119.81
w, m/s	0.084	0.077
k , m^2/s^2	0.0288	0.0137
ε , m^2/s^3	0.83	0.49
I at end of simulation (volumetric average)	13.75	9.26

Appendix A4.4: Comparison of Structured Hexahedral Mesh to Unstructured Tetrahedral Mesh

Exit Transition

Pipe: 4-lobed beta exit transition, $n = 0.5$, 100mm length

Model Parameters: Water only simulation, uniform axial velocity inlet of 1.5m/s

Length, m	Structured Hexahedral Mesh			Unstructured Tetrahedral Mesh		
	P, Pa	w, m/s	ΔP , Pa	P, Pa	w, m/s	ΔP , Pa
0	149.19	0	0	147.02	0	0
0.01	90.57	0.06742	58.62	81.81	0.07224	65.21
0.02	67.33	0.0895	81.86	58.02	0.09786	89
0.03	52.15	0.10402	97.04	43.29	0.11422	103.73
0.04	38.38	0.11569	110.81	31.57	0.12448	115.45
0.05	28.86	0.12153	120.33	22.98	0.13079	124.04
0.06	21.48	0.12365	127.71	15.54	0.1327	131.48
0.07	15.44	0.1231	133.75	9.82	0.13194	137.2
0.08	10.5	0.12178	138.69	5.55	0.12985	141.47
0.09	5.39	0.11919	143.8	2	0.12674	145.02
0.099	-0.34	0.11858	149.53	-1.13	0.12432	148.15

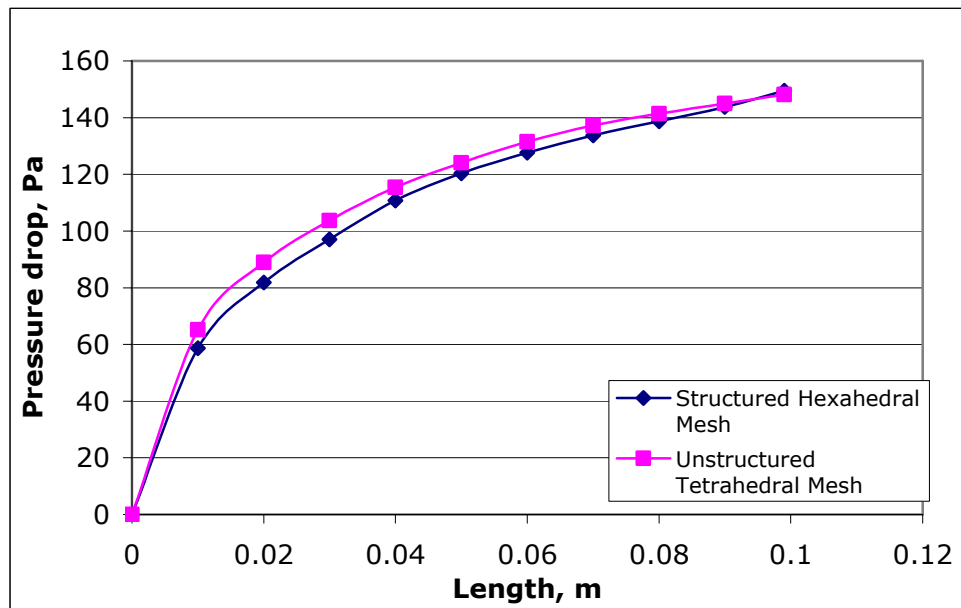


Figure A4.6: Comparison of Structured and Unstructured Mesh for Pressure Drop

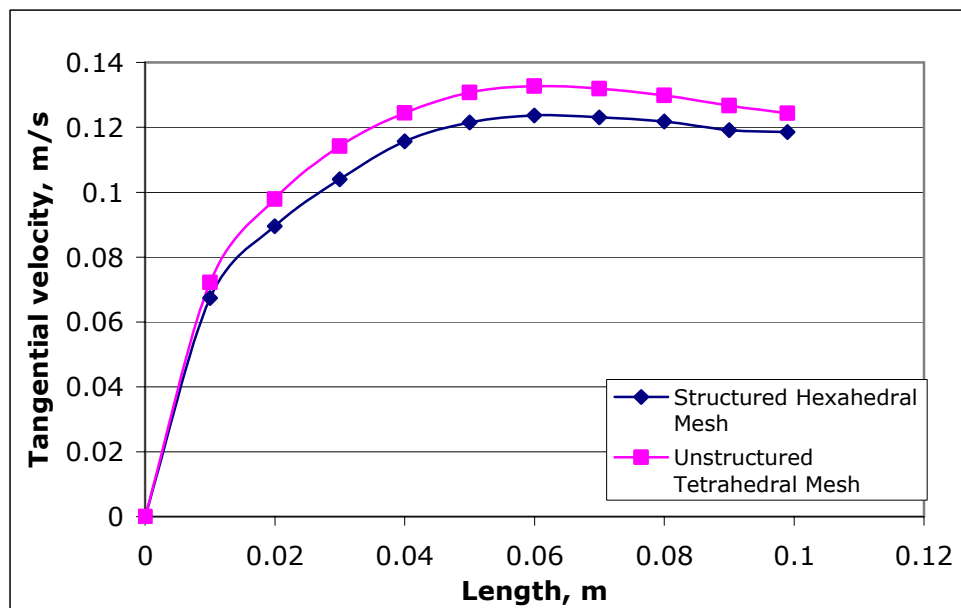


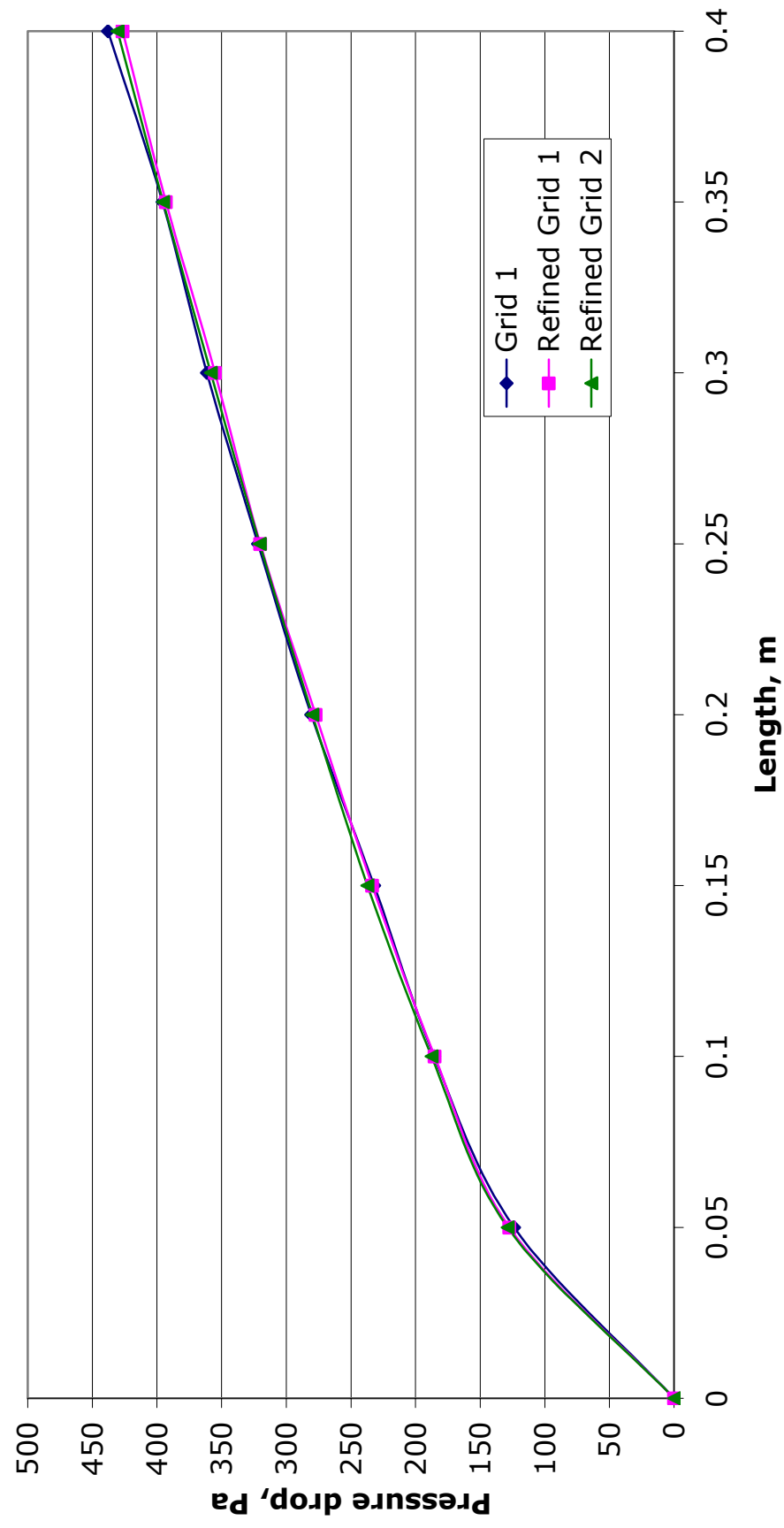
Figure A4.7: Comparison of Structured and Unstructured Mesh for Tangential Velocity

Appendix A4.5: Grid Independence Data

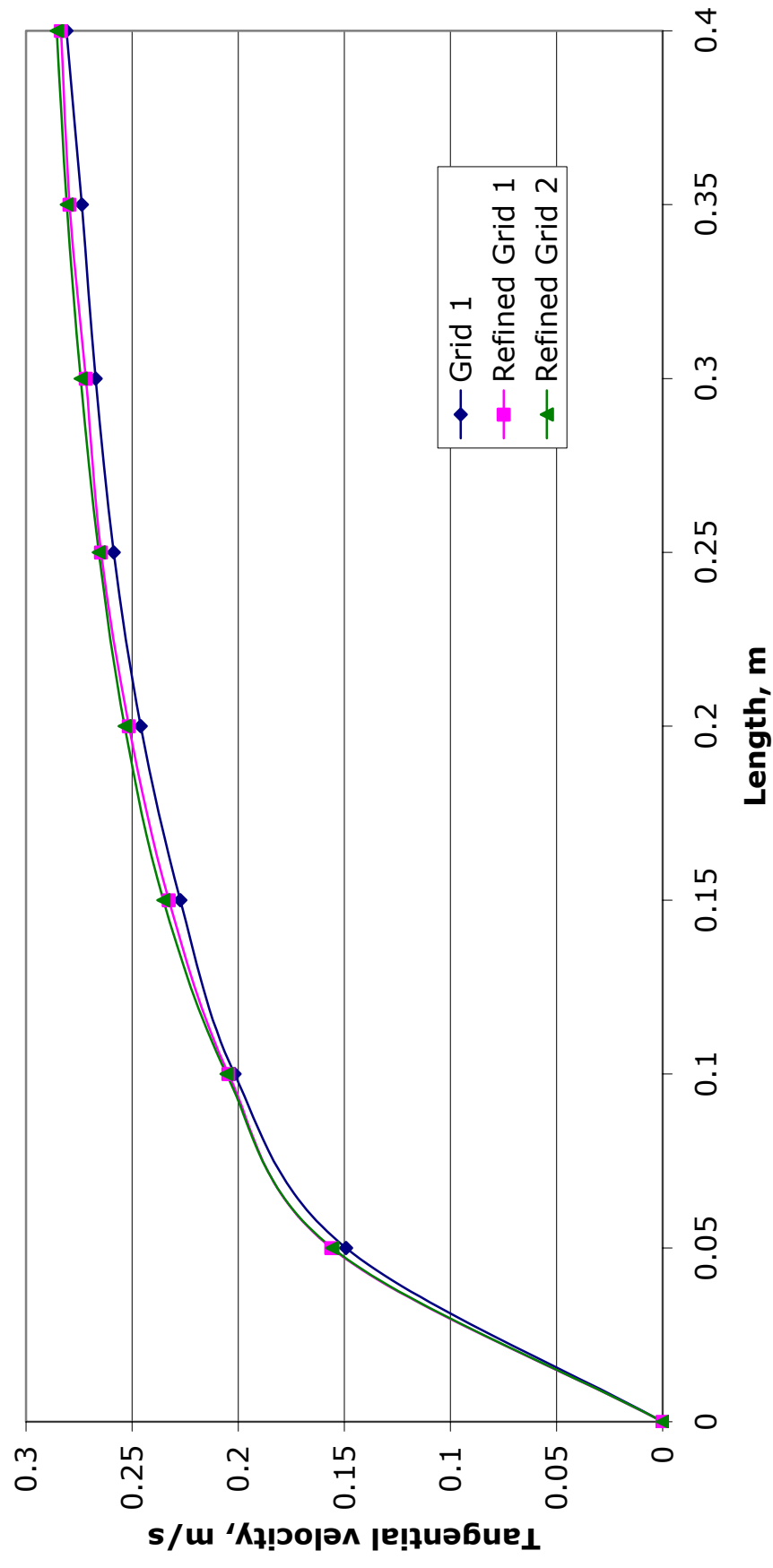
Swirl Pipe Grid Independence Data

Length 400mm, extended by 50mm												
Length, m	is = 5				is = 4				is = 3			
	number of cells = 56079				number of cells = 98914				number of cells = 205412			
	P, Pa	w, m/s	ΔP , Pa	P, Pa	w, m/s	ΔP , Pa	P, Pa	w, m/s	ΔP , Pa	P, Pa	w, m/s	ΔP , Pa
0	463.65	0	0	454.52	0	0	457.41	0	0	0	0	0
0.05	340.01	0.14923	123.64	327.1	0.15611	127.42	328.65	0.15566	128.76	0.15566	128.76	128.76
0.1	278.02	0.2017	185.63	269.43	0.20453	185.09	269.88	0.20549	187.53	0.20549	187.53	187.53
0.15	231.77	0.22724	231.88	220.95	0.23266	233.57	220.27	0.23522	237.14	0.23522	237.14	237.14
0.2	182.97	0.2459	280.68	177.25	0.25142	277.27	177.66	0.25357	279.75	0.25357	279.75	279.75
0.25	141.78	0.25863	321.87	134.54	0.26458	319.98	136.8	0.26565	320.61	0.26565	320.61	320.61
0.3	102.34	0.26715	361.31	99.42	0.27177	355.1	99.02	0.27415	358.39	0.27415	358.39	358.39
0.35	67.94	0.27362	395.71	61.39	0.2795	393.13	62.07	0.28082	395.34	0.28082	395.34	395.34
0.4	25.79	0.2809	437.86	28	0.28353	426.52	27.04	0.28549	430.37	0.28549	430.37	430.37
Swirl Intensity		0.14338			0.14776			0.15013		0.15013		
Swirl Effectiveness		0.36773			0.38903			0.39174		0.39174		

Swirl Pipe: Pressure Drop versus Length



Swirl Pipe: Tangential Velocity versus Length



Entry Transition Grid Independence Data

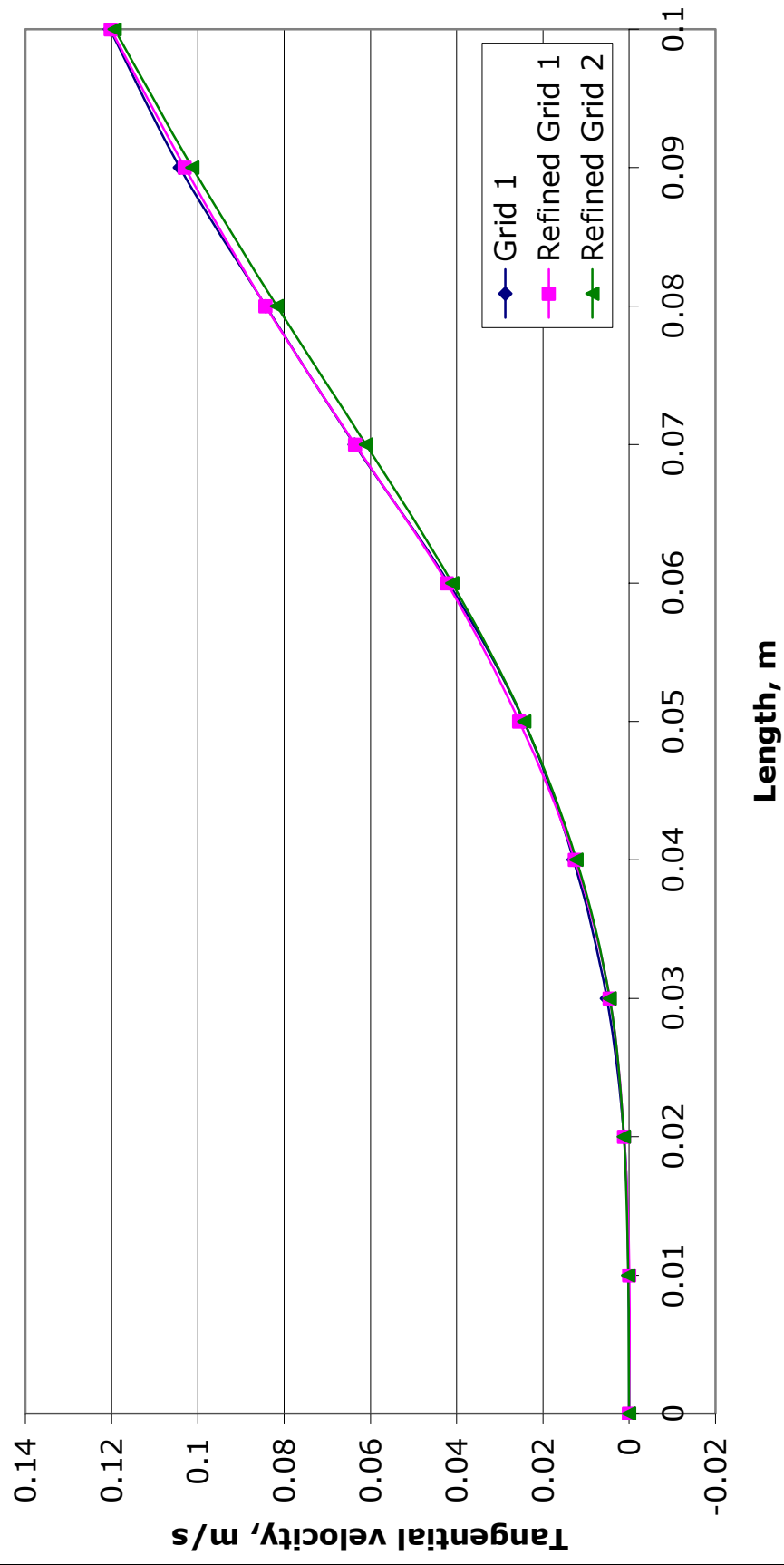
Length 100mm, extended by 50mm, Beta n=1 type

Length, m	is = 4				is = 3.3				is = 2.6			
	number of cells = 27434				number of cells = 52360				number of cells = 122831			
	P, Pa	w, m/s	ΔP , Pa	P, Pa	w, m/s	ΔP , Pa	P, Pa	w, m/s	ΔP , Pa	P, Pa	w, m/s	ΔP , Pa
0	191.74	0	0	191.55	0	0	190.95	0	0	190.95	0	0
0.01	184.45	0.00019	7.29	183.67	-0.000053	7.88	183.39	0.00021	7.56	183.39	0.00021	7.56
0.02	178.18	0.00117	13.56	178.17	0.00116	13.38	177.27	0.00126	13.68	177.27	0.00126	13.68
0.03	169.53	0.00522	22.21	169.99	0.00452	21.56	168.89	0.00451	22.06	168.89	0.00451	22.06
0.04	160.28	0.0129	31.46	159.93	0.01256	31.62	159.36	0.01227	31.59	159.36	0.01227	31.59
0.05	142.69	0.02445	49.05	143.09	0.0255	48.46	143.37	0.02433	47.58	143.37	0.02433	47.58
0.06	133	0.04184	58.74	133.62	0.04221	57.93	133.55	0.04103	57.4	133.55	0.04103	57.4
0.07	115.83	0.06369	75.91	116.26	0.06356	75.29	118.27	0.06106	72.68	118.27	0.06106	72.68
0.08	98.16	0.08425	93.58	99.37	0.08427	92.18	101.06	0.08166	89.89	101.06	0.08166	89.89
0.09	77.43	0.10421	114.31	83.47	0.10305	108.08	84.61	0.10129	106.34	84.61	0.10129	106.34
0.1	58.94	0.12037	132.8	66.5	0.1202	125.05	65.34	0.11933	125.61	65.34	0.11933	125.61
Swirl Intensity		0.07198			0.07238			0.0723			0.0723	
Swirl Effectiveness		0.60867			0.64999			0.64637			0.64637	

Entry Transition Pipe: Pressure Drop versus Length



Entry Transition Pipe: Tangential Velocity versus Length



Exit Transition Grid Independence Data

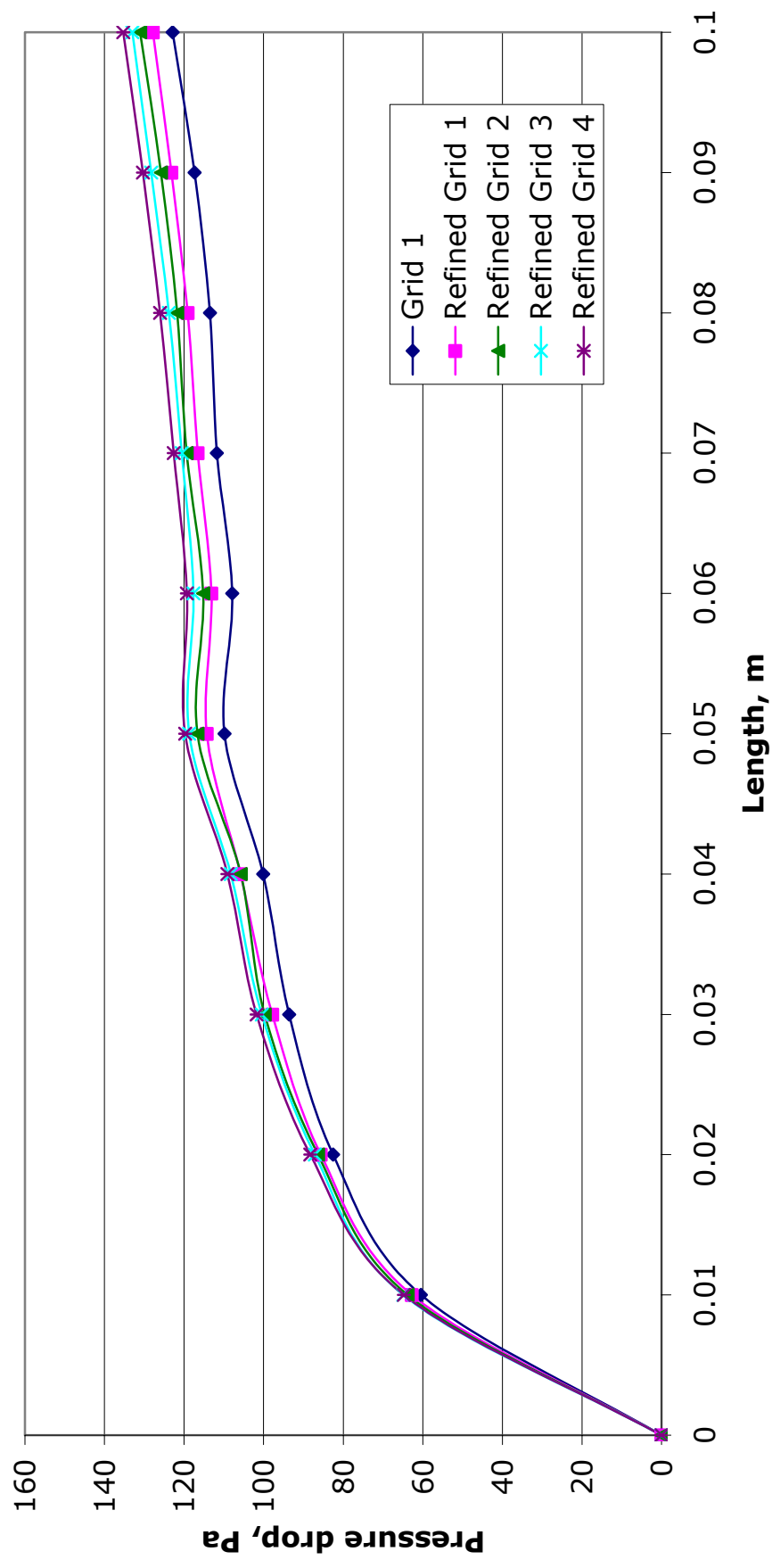
Length 100mm, extended by 50mm, Beta n=1 type
Uniform axial velocity at inlet of 1.5m/s
 y^+ (30-60) adaption after 1st order solution, before 2nd order solution

is = 3.3						is = 2.6						is = 2.2					
			number of cells = 57672			number of cells = 109963			number of cells = 202157								
Length, m	P, Pa	w, m/s	ΔP , Pa	P, Pa	P, Pa	w, m/s	ΔP , Pa	P, Pa	w, m/s	ΔP , Pa	P, Pa	w, m/s	ΔP , Pa	P, Pa	w, m/s	ΔP , Pa	P, Pa
0	143.34	0	0	150.1	153.9	0	0	153.9	0	0	153.9	0	0	153.9	0	0	153.9
0.01	82.88	0.07264	60.46	87.3	90.07	0.07162	62.8	90.07	0.07145	63.83	90.07	0.07145	63.83	90.07	0.07145	63.83	90.07
0.02	60.79	0.09377	82.55	64.5	67.57	0.09342	85.6	67.57	0.09361	86.33	67.57	0.09361	86.33	67.57	0.09361	86.33	67.57
0.03	49.77	0.10481	93.57	52.32	54.19	0.10599	97.78	54.19	0.10527	99.71	54.19	0.10527	99.71	54.19	0.10527	99.71	54.19
0.04	43.24	0.10803	100.1	44.25	48.13	0.11074	105.85	48.13	0.1103	105.77	48.13	0.1103	105.77	48.13	0.1103	105.77	48.13
0.05	33.51	0.10718	109.83	35.83	37.25	0.10962	114.27	37.25	0.11021	116.65	37.25	0.11021	116.65	37.25	0.11021	116.65	37.25
0.06	35.4	0.10399	107.94	36.95	38.66	0.10668	113.15	38.66	0.10741	115.24	38.66	0.10741	115.24	38.66	0.10741	115.24	38.66
0.07	31.57	0.10046	111.77	33.54	34.55	0.10314	116.56	34.55	0.10386	119.35	34.55	0.10386	119.35	34.55	0.10386	119.35	34.55
0.08	29.83	0.09789	113.51	31.03	32.18	0.10037	119.07	32.18	0.10124	121.72	32.18	0.10124	121.72	32.18	0.10124	121.72	32.18
0.09	25.99	0.09624	117.35	26.9	28.05	0.09872	123.2	28.05	0.0996	125.85	28.05	0.0996	125.85	28.05	0.0996	125.85	28.05
0.1	20.47	0.09557	122.87	22.29	22.82	0.09835	127.81	22.82	0.09876	131.08	22.82	0.09876	131.08	22.82	0.09876	131.08	22.82

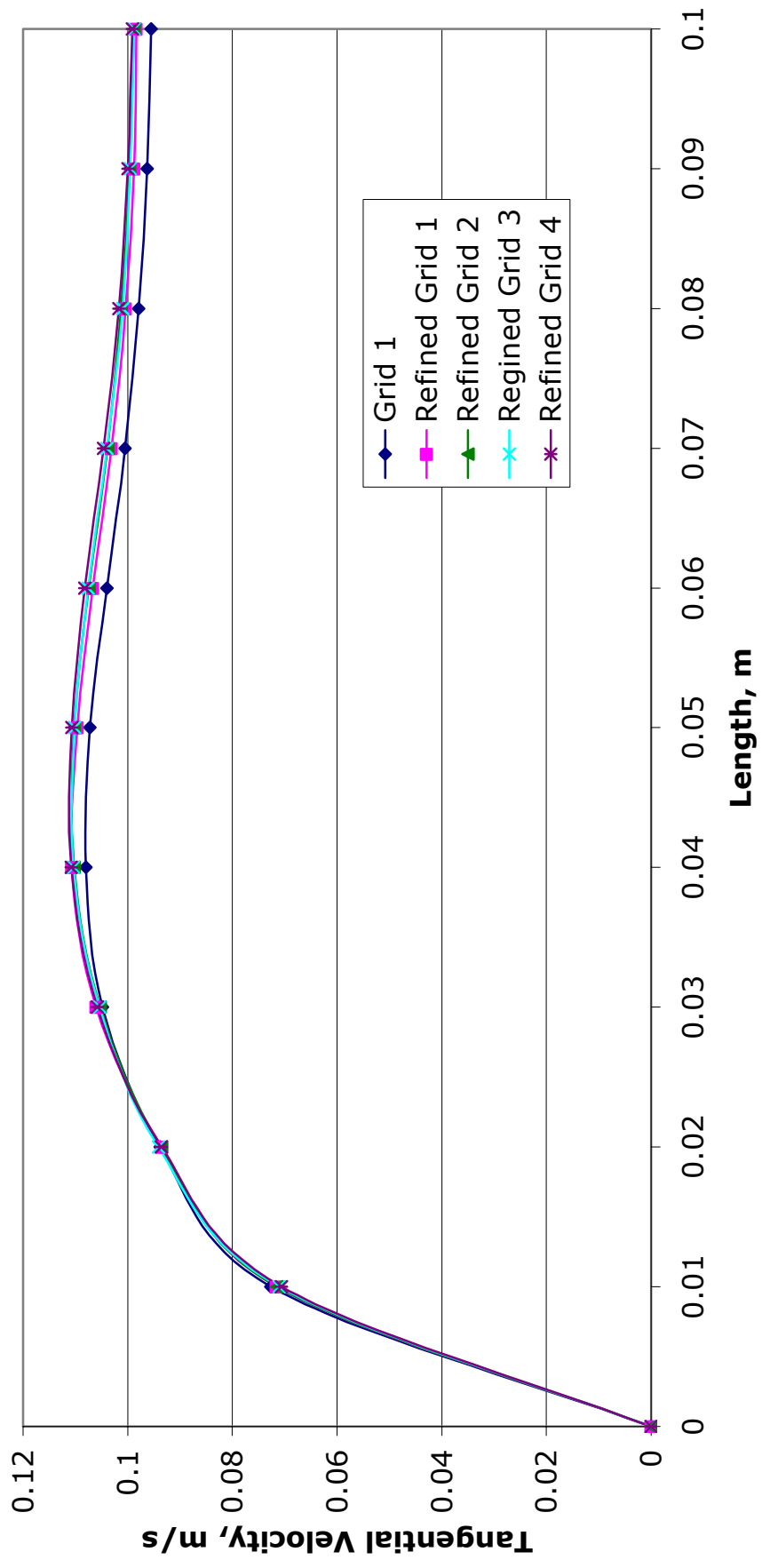
Exit Transition Grid Independence Data continued..

is = 1.9					is = 1.7				
no. of cells=312300					no. of cells=404500				
Length, m	P, Pa	w, m/s	ΔP , Pa	P, Pa	w, m/s	ΔP , Pa	P, Pa	w, m/s	ΔP , Pa
0	156.96	0	0	159.91	0	0			0
0.01	92.02	0.0711	64.94	95.17	0.07058	64.74			64.74
0.02	69.83	0.09415	87.13	71.62	0.09359	88.29			88.29
0.03	56.53	0.1054	100.43	58.19	0.10582	101.72			101.72
0.04	48.7	0.11038	108.26	50.8	0.11079	109.11			109.11
0.05	38.21	0.11018	118.75	40.18	0.11068	119.73			119.73
0.06	39.3	0.10751	117.66	40.64	0.1082	119.27			119.27
0.07	36.37	0.10397	120.59	37.29	0.10464	122.62			122.62
0.08	33.13	0.10099	123.83	33.88	0.10166	126.03			126.03
0.09	28.7	0.0995	128.26	29.59	0.09993	130.32			130.32
0.1	23.97	0.09873	132.99	24.6	0.09907	135.31			135.31

Exit Transition Pipe: Pressure Drop versus Length



Exit Transition Pipe: Tangential Velocity vs. Length



Circular Pipe Grid Independence Data

Length 100mm, extended by 50mm
y⁺ (30-60) adaption after 1st order solution, before 2nd order solution
Tetrahedral cells used

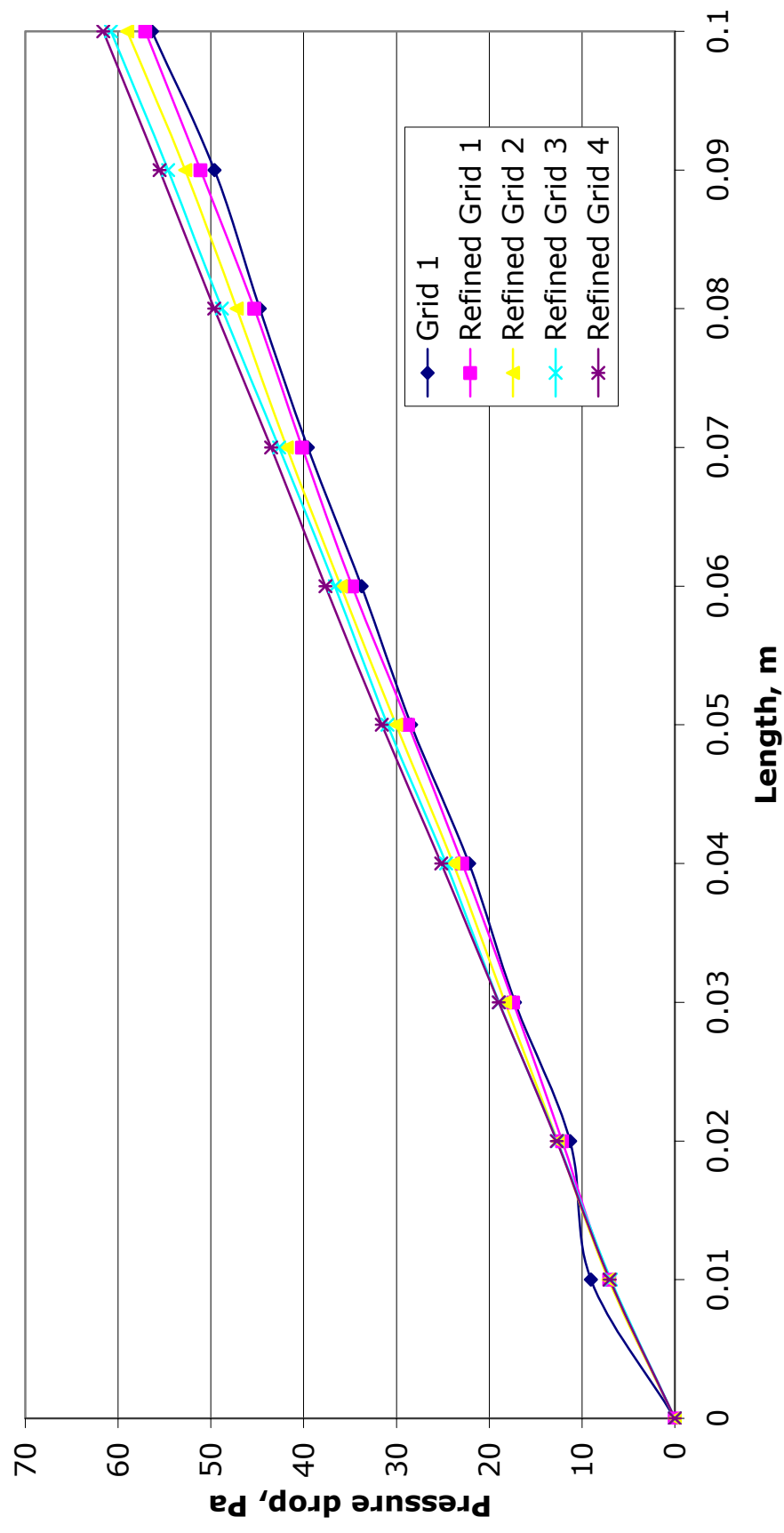
is = 4				is = 3				is = 2.4			
		no. of cells=54660		no. of cells=85616		no. of cells=163407					
Length, m	P, Pa	w, m/s	ΔP, Pa	P, Pa	w, m/s	ΔP, Pa	P, Pa	w, m/s	ΔP, Pa	w, m/s	ΔP, Pa
0	82.79	-	0	81.29	-	0	84.08	-	0	-	0
0.01	73.73	-	9.06	74.23	-	7.06	76.93	-	7.15	-	7.15
0.02	71.51	-	11.28	69.15	-	12.14	71.44	-	12.64	-	12.64
0.03	65.56	-	17.23	63.86	-	17.43	65.78	-	18.3	-	18.3
0.04	60.61	-	22.18	58.38	-	22.91	60.19	-	23.89	-	23.89
0.05	54.36	-	28.43	52.57	-	28.72	54.03	-	30.05	-	30.05
0.06	49.04	-	33.75	46.53	-	34.76	48.09	-	35.99	-	35.99
0.07	43.23	-	39.56	41.12	-	40.17	42.27	-	41.81	-	41.81
0.08	38.07	-	44.72	35.96	-	45.33	36.85	-	47.23	-	47.23
0.09	33.17	-	49.62	30.17	-	51.12	31.32	-	52.76	-	52.76
0.1	26.42	-	56.37	24.22	-	57.07	25.06	-	59.02	-	59.02

Circular Pipe Grid Independence Data continued...

is = 2.1							is = 1.9		
number of cells = 216894							number of cells = 329192		
Length, m	P, Pa	w, m/s	ΔP , Pa	P, Pa	w, m/s	ΔP , Pa	P, Pa	w, m/s	ΔP , Pa
0	86.54	-	0	88.29	-	0	88.29	-	0
0.01	79.65	-	6.89	81.26	-	7.03	81.26	-	7.03
0.02	73.88	-	12.66	75.58	-	12.71	75.58	-	12.71
0.03	67.59	-	18.95	69.3	-	18.99	69.3	-	18.99
0.04	61.9	-	24.64	63.13	-	25.16	63.13	-	25.16
0.05	55.57	-	30.97	56.72	-	31.57	56.72	-	31.57
0.06	49.91	-	36.63	50.64	-	37.65	50.64	-	37.65
0.07	43.89	-	42.65	44.78	-	43.51	44.78	-	43.51
0.08	37.73	-	48.81	38.64	-	49.65	38.64	-	49.65
0.09	31.93	-	54.61	32.75	-	55.54	32.75	-	55.54
0.1	25.77	-	60.77	26.69	-	61.6	26.69	-	61.6

With an interval size of 2.1 some cells were too fine (for y^+ requirement > 30)

Circular Pipe: Pressure Drop versus Length



Appendix A5.1: Comparison of Alpha and Beta Transitions (n=1 Type) and Optimised Swirl Pipe

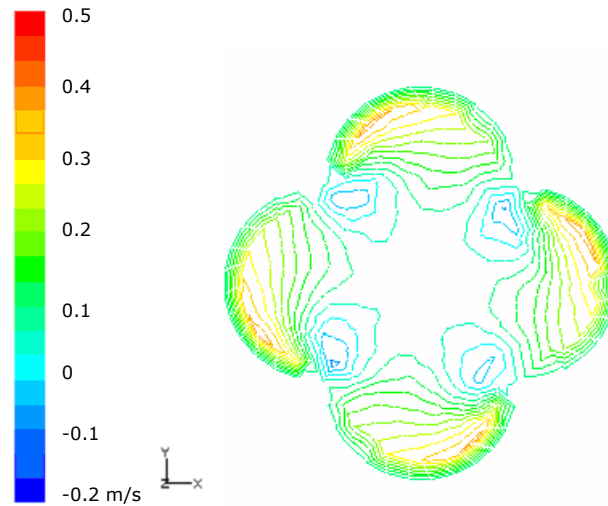


Figure A5.1a Alpha Transition

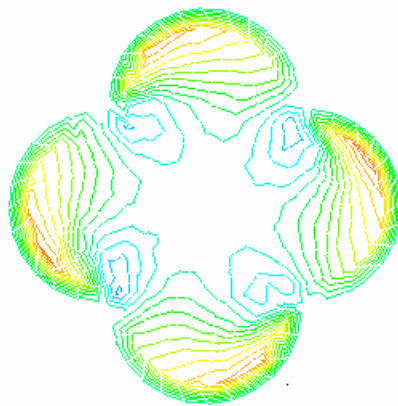


Figure A5.1b Beta Transition

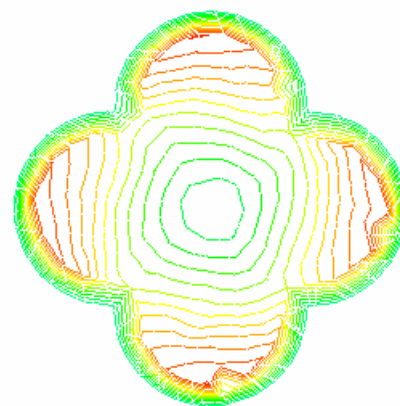


Figure A5.1c Swirl Pipe

Figure A5.1: Contours of Tangential Velocity at the Exit; Transition Length 0.1m, Swirl Pipe Length 0.4m

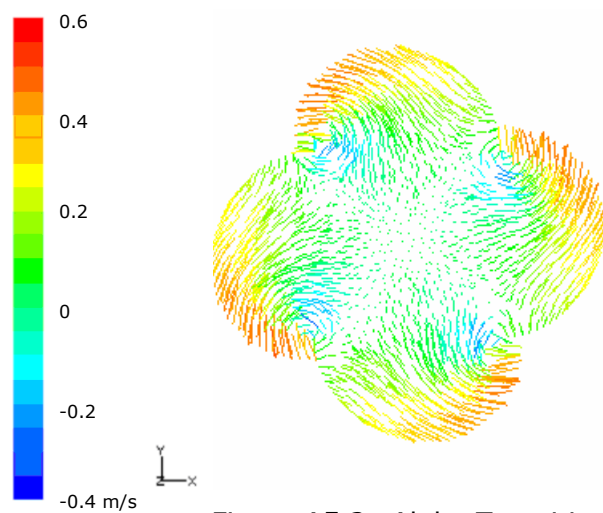


Figure A5.2a Alpha Transition

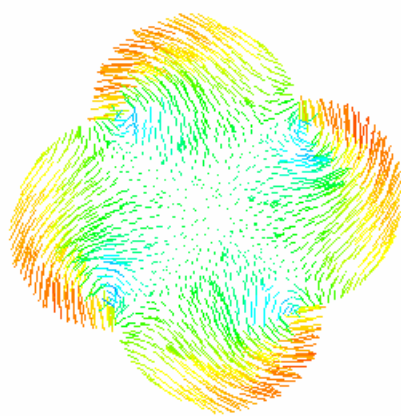


Figure A5.2b Beta Transition

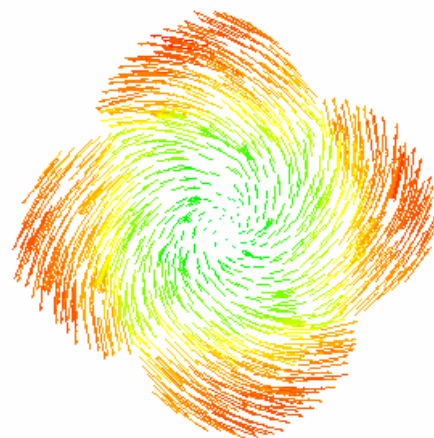


Figure A5.2c Swirl Pipe

Figure A5.2: Tangential Velocity Vector Plots; Transition Length 0.1m, Swirl Pipe Length 0.4m

Appendix A6.1: Flow meter Calibration

Computer scale for calculating flow rate from raw measured data:

$$y = m_1x + c_1 \quad (\text{A6.1})$$

where x = raw value

y = computer value for flow rate

Equation calculated from experimentation for corrected value of flow rate,
 y_{actual} :

$$y_{\text{actual}} = m_2y + c_2 \quad (\text{A6.2})$$

where y_{actual} = actual flow rate as measured by collecting water with timer

Therefore,

$$y_{\text{actual}} = m_2 (m_1x + c_1) + c_2$$

$$y_{\text{actual}} = (m_2m_1) x + (m_2c_1 + c_2) \quad (\text{A6.3})$$

Change computer value of gradient and intercept accordingly:

$$m_{1\text{modified}} = (m_2m_1)$$

$$c_{1\text{modified}} = (m_2c_1 + c_2)$$

Original computer values of gradient and intercept:

$$m_1 = 0.3068$$

$$m_2 = -1.2272$$

From Figure A6.1,

$$m_2 = 1.1834$$

$$c_2 = -0.3357$$

$$m_{1\text{modified}} = 0.3631$$

$$c_{1\text{modified}} = -1.7883$$

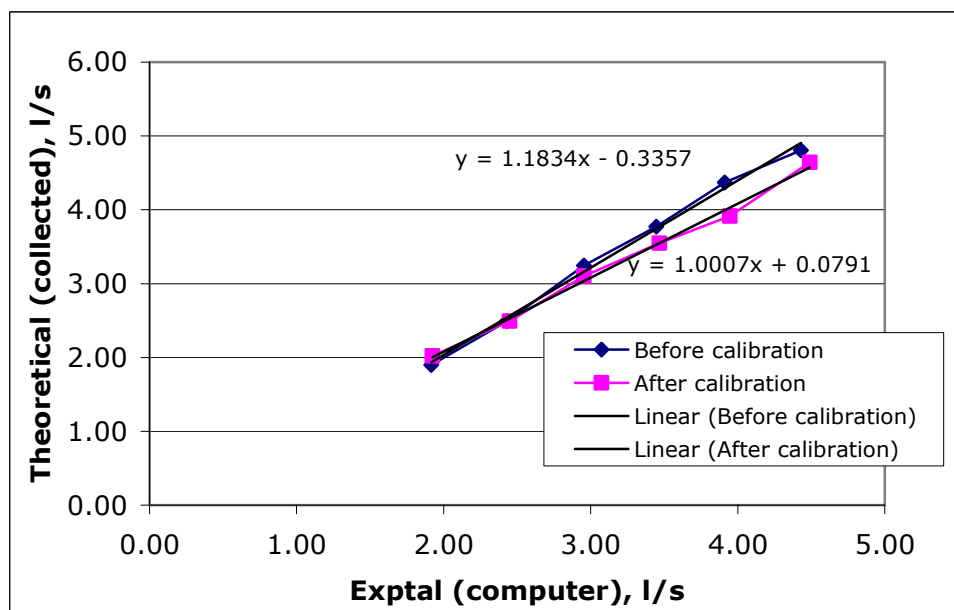


Figure A6.1: Flow meter Calibration

Appendix A6.2: Float and Sink Density Tests on Plastic Beads (Basis for Elimination)

Float and sink tests were carried out first on new (unused) beads, and next on the beads used by Ganeshalingam in slurry tests. Sodium Polytungstate (SPT) solution was used with distilled water to make the necessary densities of solution. 1kg each of new and used beads were tested. The beads were scattered onto the surface of the solution a little at a time in a beaker. A stirrer was used to gently disperse the floating beads at the surface and to further disperse any surface tension effects.

The new beads had static forces and surface tension and a tendency to lump together. Therefore a small amount of dispersant (Brij 35) was used. It was unnecessary to use dispersant with the used beads.

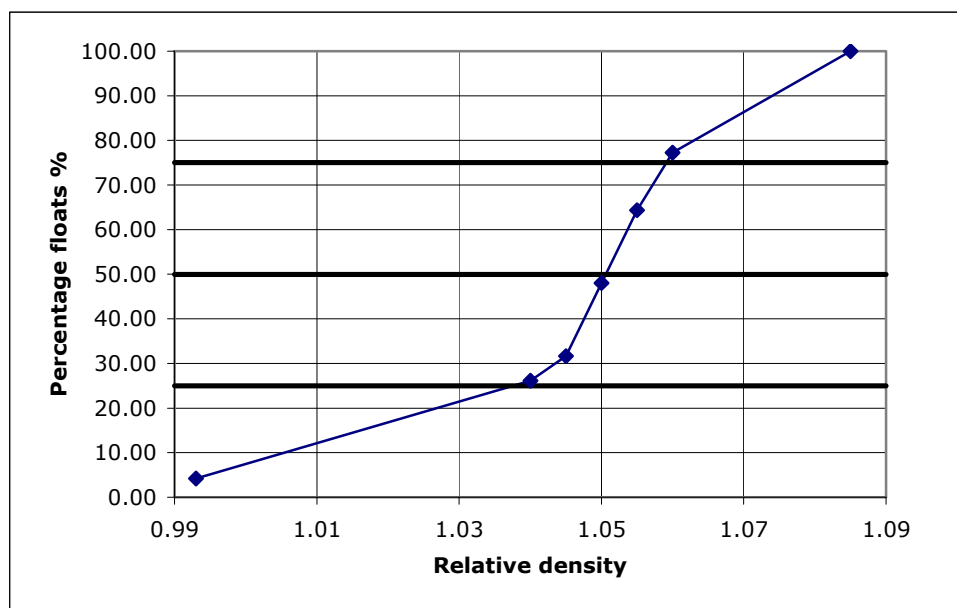
The floating beads were sieved off of the surface and the sunken beads collected at the end of the test. Both sets of beads were washed in water to remove any remaining SPT or dispersant and placed in an oven (79°C for a few hours). Once dried, the beads were weighed.

Table A6.1: Density of New (Unused) Beads

Relative Density	Mass (g) Floats	Cumulative Floats (g)	Mass % Floats	Cumulative % Floats
Floats at 0.993	42.55	42.55	4.26	4.26
1.04	218.69	261.24	21.87	26.13
1.045	54.90	316.14	5.49	31.62
1.05	163.94	480.08	16.40	48.02
1.055	163.17	643.25	16.32	64.34
1.06	128.77	772.02	12.88	77.22
Sinks at 1.065	227.79	999.81	22.78	100.00
Total	999.81		100.00	

Table A6.2: Density of Used Beads

Relative Density	Mass (g) Floats Actual	Cumulative Floats (g)	Mass % Floats	Cumulative % Floats
0.993	0	0	0	0
1.28	204.42	204.42	20.49	20.49
1.300	226.73	431.15	22.73	43.22
1.31	110.98	542.13	11.12	54.34
1.32	114.94	657.07	11.52	65.87
1.33	81.73	738.80	8.19	74.06
1.36	139.69	878.49	14.00	88.06
S at 1.36	119.10	997.59	11.94	100.00
Total	997.59		100.00	

**Figure A6.2: Float and Sink Data for New Beads**

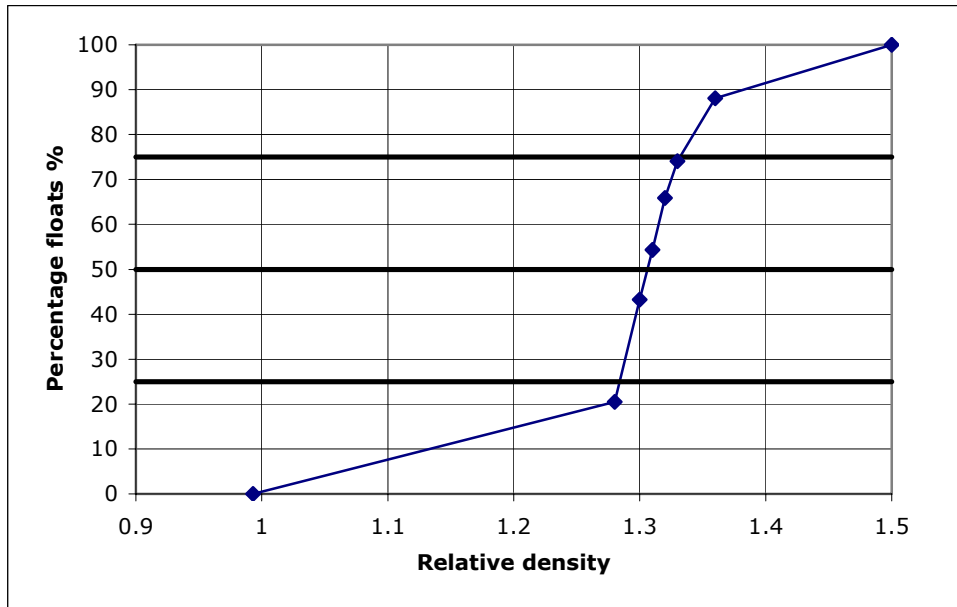


Figure A6.3: Float and Sink Data for Used Beads

The value of d_{50} for new beads was 1.05. Pycnometry estimated d_{50} at 1.061. For Used beads d_{50} was 1.305 and value from pycnometry was 1.351. This was a surprising result since Raylor (Raylor 1998) carried out float and sink analysis on the beads and concluded a value of d_{50} of around 1.45. Long-term storage may have affected the density of the beads.

During this analysis, several discrepancies were noted with a trend of increase in density as the test proceeded (on repeating the analysis on the same set of beads). It may be that atmospheric conditions and the wetting process and drying in oven affect the bead density. It is thus expected that in running the rig the beads will continue to increase in density and the flattening process by the rig will further affect the bead density as well as particle shape and size.

Appendix A6.3: Size Analysis of Density Tracers

Table A6.3: Size Analysis of Blue Tracers (RD 2.7)

Sieve size, mm		Mass (g)	Mass %	Cumulative mass % passing
less than 850 -				
850	0.85	0.30	0.03	0.03
850 - 1	1.00	0.00	0.00	0.03
1 - 1.18	1.18	0.00	0.00	0.03
1.18 - 1.7	1.70	0.90	0.09	0.12
1.7 - 2.0	2.00	52.10	5.21	5.33
2.0 - 2.36	2.36	216.00	21.62	26.95
2.36 - 2.8	2.80	304.00	30.43	57.38
2.8 - 3.15	3.15	425.20	42.56	99.94
3.15 - 3.35	3.35	0.40	0.04	99.98
greater than 3.35	3.50	0.20	0.02	100.00
TOTAL		999.10	100.00	
Median =	2.6			
Mean =	2.8			

Table A6.4: Size Analysis of Red Tracers (RD 1.4)

Sieve size, mm		Mass (g)	Mass %	Cumulative mass % passing
less than 850 -				
850	0.85	0.3	0.06	0.06
850 - 1	1	0	0	0.06
1 - 1.18	1.18	0	0	0.06
1.18 - 1.7	1.7	2.3	0.46	0.52
1.7 - 2.0	2	38.1	7.62	8.14
2.0 - 2.36	2.36	122.8	24.56	32.7
2.36 - 2.8	2.8	164.7	32.94	65.64
2.8 - 3.15	3.15	171.4	34.28	99.92
3.15 - 3.35	3.35	0.3	0.06	99.98
greater than 3.35	3.5	0.1	0.02	100
TOTAL		500	100	
Median =	2.6			
Mean =	2.75			

Table A6.5: Size Analysis of Yellow Tracers (RD 4.5)

Sieve size, mm		Mass (g)	Mass %	Cumulative mass % passing
less than 850 -				
850	0.85	4.30	0.43	0.43
850 - 1	1.00	0.00	0.00	0.43
1 - 1.18	1.18	0.00	0.00	0.43
1.18 - 1.7	1.70	0.70	0.07	0.50
1.7 - 2.36	2.36	217.50	21.76	22.26
2.36 - 2.8	2.80	335.00	33.52	55.78
2.8 - 3.15	3.15	441.10	44.14	99.92
3.15 - 3.35	3.35	0.70	0.07	99.99
greater than 3.35	3.50	0.10	0.01	100.00
TOTAL		999.40	100.00	
Median =	2.7			
Mean =	2.85			

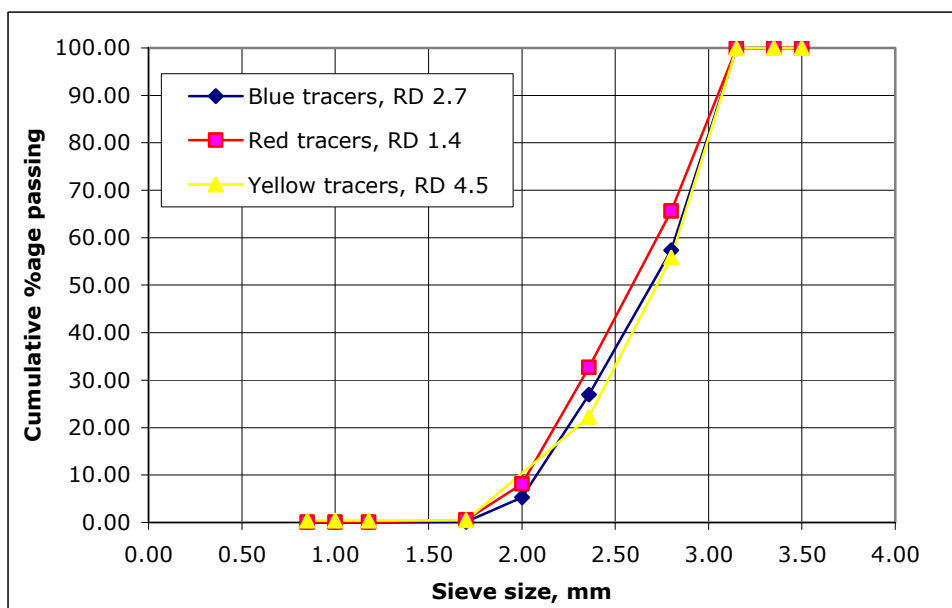
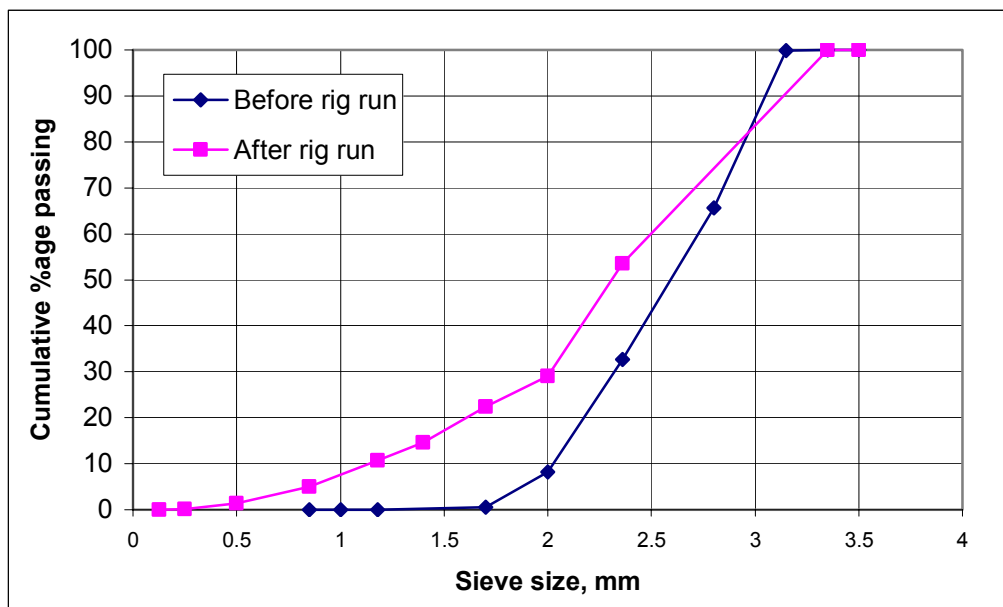


Figure A6.4 Size Comparison of Tracers

Table A6.6: Size Analysis of Red Tracers after Rig Run of 1 hour at Velocity 1 to 1.75m/s

Sieve size, mm		Mass (g)	Mass %	Cumulative mass % passing
less than 125 -				
125	0.13	0.63	0.03	0.03
125 - 250	0.25	2.67	0.14	0.17
250 - 500	0.50	23.47	1.21	1.38
500 - 850	0.85	70.95	3.67	5.05
850 - 1.18	1.18	108.48	5.61	10.66
1.18 - 1.4	1.40	75.30	3.89	14.56
1.4 -1.7	1.70	152.42	7.88	22.44
1.7 - 2.0	2.00	129.18	6.68	29.12
2.0 - 2.36	2.36	473.42	24.48	53.60
2.36 - 3.35	3.35	897.02	46.39	99.99
greater than 3.35	3.50	0.22	0.01	100.00
TOTAL		1933.76	100.00	
Median =	2.30			
Mean =	2.56			

**Figure A6.5 Particle Breakage from Pump (after 1 hour's run at 1-1.75m/s, red tracers shown)**

Appendix A7.1: Error Analysis on Manometer Measurement of Pressure Loss

Definition of Equations and Terms

S = standard deviation

E = standard error

$E(x)$ = standard error in x

$E_T(x)$ = total standard error taking propagated cumulative errors into account

N = number of readings

h_1 = manometer 1 reading, cm

h_2 = manometer 2 reading, cm

ΔP_{total} = total pressure loss measured across swirling flow pipes and circular pipes, Pa

ΔP_{circ} = pressure loss from circular pipe only, Pa

$\Delta P_{\text{circ}}'$ = pressure loss from circular pipe only per metre of pipe, Pa/m

ΔP_{swirl} = pressure loss from swirl pipe only, Pa

$\Delta P_{\text{trans+swirl}}$ = pressure loss from transition and swirl pipe only, Pa

ΔH = [mean (h_1) – mean (h_2)], cm

$$E = \frac{S}{\sqrt{N}} \quad (\text{A7.1})$$

$$E(\Delta H) = \sqrt{E(h_1)^2 + E(h_2)^2} \quad (\text{A7.2})$$

$$\Delta P = \Delta H \times \rho_w \times g \quad (\text{A7.3})$$

$$\Delta P_{\text{swirl}} = \Delta P_{\text{total}} - \Delta P_{\text{circ}} \quad (\text{A7.4})$$

Sample Calculation for Swirl Pipe Data

Table A7.4, $v = 2.266\text{m/s}$

$$\text{Mean } h_1 = 82.85\text{cm}$$

$$\text{Mean } h_2 = 42.71\text{cm}$$

$$\Delta H = 82.85 - 42.71 = 40.14\text{cm}$$

$$S(h_1) = 0.639$$

$$S(h_2) = 0.300$$

From equation A7.1:

$$E(h_1) = \frac{0.639}{\sqrt{12}} = 0.184$$

$$E(h_2) = \frac{0.3}{\sqrt{10}} = 0.087$$

From equation A7.2:

$$E(\Delta H) = \sqrt{0.184^2 + 0.087^2} = 0.204$$

$$E(\Delta H) \% = (0.204/40.14) * 100 = 0.508\%$$

From equation A7.3:

$$\Delta P_{\text{total}} = (40.14/100) * 1000 * 9.81 = 3937.90\text{Pa}$$

$$E(\Delta P_{\text{total}}) = 0.508\% * 3937.90 = 19.99\text{Pa}$$

Calculated data tabulated in Table A7.5

Pressure loss at 2.25m/s for comparison to CFD data from quadratic fit in Figure A7.2:

$$\Delta P_{\text{total}} = 683.96 * (2.25)^2 + 149.45 * (2.25) + 90.724 = 3889.53\text{Pa}$$

Calculated data tabulated in Table A7.6

Swirl pipe only pressure loss:

$$\Delta P_{\text{swirl}} = 3889.53 - [\Delta P'_{\text{circ}} (\text{from Table A7.3}) * \text{length of cylindrical pipe}]$$

$$\Delta P_{\text{swirl}} = 3889.53 - (946.02 * 2.925) = 1122.42\text{Pa}$$

$$E(\Delta P_{\text{swirl}}) = 0.508\% * 1122.42\text{Pa} = 5.70\text{Pa}$$

$$E(\Delta P_{\text{circ}}) = 0.90\% * (946.02 * 2.925) = 24.83\text{Pa}$$

$$E_T(\Delta P_{\text{swirl}}) = \sqrt{5.70^2 + 24.83^2} = 25.48\text{Pa}$$

$$E_T(\Delta P_{\text{swirl}}) \% = (25.48/1122.42)*100 = 2.27\%$$

Calculated data tabulated in Table A7.7

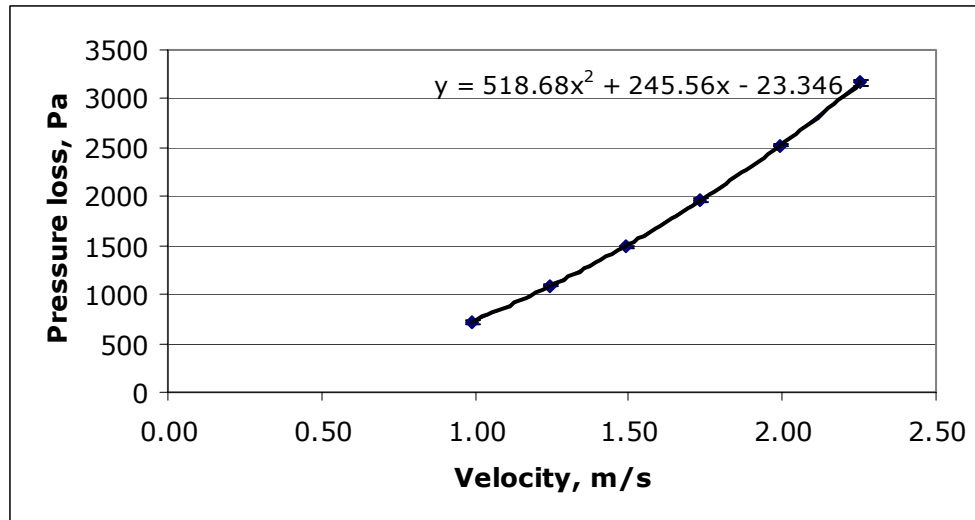
Cylindrical pipe head loss data

Table A7.1: Head loss measured across 3.335m cylindrical pipe

Velocity, m/s	2.254		1.992		1.732		1.493		1.246		0.987	
	h_1 , cm	h_2 , cm	h_1 , cm	h_2 , cm	h_1 , cm	h_2 , cm	h_1 , cm	h_2 , cm	h_1 , cm	h_2 , cm	h_1 , cm	h_2 , cm
Reading												
1	49.20	17.80	41.00	15.00	52.20	32.10	44.40	29.00	37.90	26.90	32.10	26.00
2	49.70	17.30	40.80	15.50	52.00	32.50	44.10	29.00	38.20	26.80	33.10	25.40
3	50.60	17.20	41.10	15.60	51.80	32.30	44.20	29.40	37.70	26.90	33.20	25.10
4	51.60	17.00	41.50	15.20	52.30	31.90	44.60	28.60	38.20	27.00	33.10	25.40
5	49.70	18.20	41.20	15.20	52.50	32.30	43.70	29.20	37.90	26.90	31.70	24.30
6	49.40	17.10	40.50	15.10	52.50	32.20	44.00	28.90	38.20	26.70	33.10	25.70
7	49.50	17.00	41.30	15.70	52.40	32.20	44.40	28.80	38.00	26.60	32.70	25.60
8	49.60	17.30	41.20	15.50	52.00	32.00	44.00	28.60	37.80	26.80	33.20	25.50
9	49.30	18.20	41.10	15.20	51.80	32.10	44.10	29.10	37.90	26.80	32.60	25.40
10	49.20	18.20	40.90	15.20	52.60	32.20	43.90	29.10	37.80	26.80	33.30	25.90
Mean	49.78	17.53	41.06	15.32	52.21	32.18	44.14	28.97	37.96	26.82	32.81	25.43
ΔH , cm		32.25		25.74		20.03		15.17		11.14		7.38
S	0.757	0.514	0.280	0.235	0.296	0.169	0.267	0.254	0.184	0.114	0.536	0.476
$E(h_1), E(h_2)$	0.239	0.163	0.088	0.074	0.094	0.053	0.085	0.080	0.058	0.036	0.170	0.151
$E(\Delta H)$		0.289		0.115		0.108		0.117		0.068		0.227
$E(\Delta H)$ %		0.897		0.449		0.538		0.769		0.613		3.073

Table A7.2: Cylindrical pipe pressure loss

v , m/s	ΔP_{circ} , Pa	$E(\Delta P_{\text{circ}})$, Pa	$E(\Delta P_{\text{circ}})$, %
0.987	723.98	22.25	3.07
1.246	1092.83	6.70	0.61
1.493	1488.18	11.44	0.77
1.732	1964.94	10.57	0.54
1.992	2525.09	11.33	0.45
2.254	3163.73	28.39	0.90

**Figure A7.1: Pressure loss versus flow velocity and quadratic fit for cylindrical pipe****Table A7.3: Pressure loss from quadratic fit to data for cylindrical pipe**

v , m/s	ΔP_{circ} , Pa	$\Delta P'_{\text{circ}}$, Pa/m	$E(\Delta P'_{\text{circ}})$, Pa/m
1	740.89	222.16	6.83
1.25	1094.04	328.05	2.01
1.5	1512.02	453.38	3.49
1.75	1994.84	598.15	3.22
2	2542.49	762.37	3.42
2.25	3154.98	946.02	8.49

A quadratic fit to the data was performed so that the pressure loss at exactly 1.0, 1.25, 1.5, 1.75m/s could be obtained for comparison to CFD simulations and for use in calculations of pressure loss across swirling flow pipes. Therefore the errors in Table A7.3 have been estimated from the nearest data point.

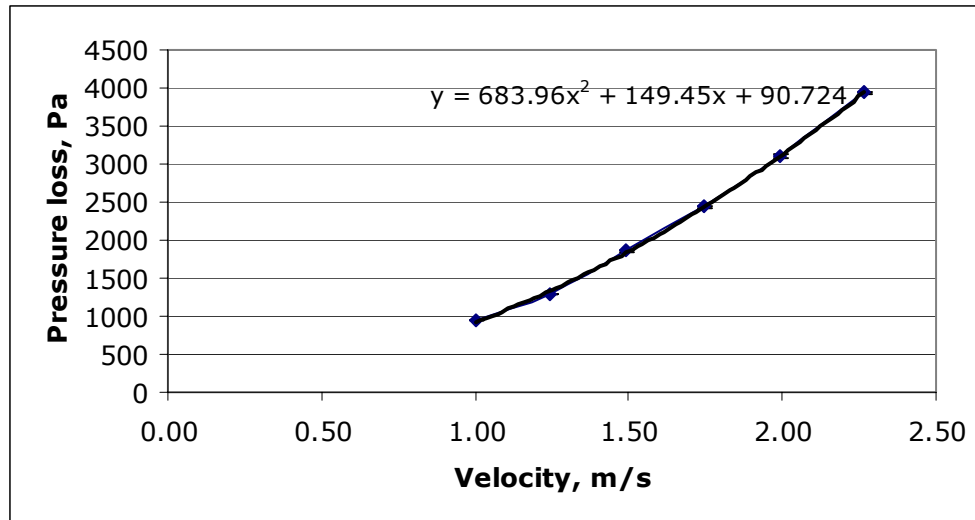
Swirl pipe data

Table A7.4: Head loss measured across swirling flow pipe (0.4m) + 2.925m cylindrical pipe

Velocity, m/s		2.266		1.993		1.742		1.493		1.243		1.001	
Reading	h_1 , cm	h_2 , cm	h_1 , cm	h_2 , cm	h_1 , cm	h_2 , cm	h_1 , cm	h_2 , cm	h_1 , cm	h_2 , cm	h_1 , cm	h_2 , cm	
1	83.3	42.4	69.9	37.4	58.4	33.5	48.9	29.8	39.8	26.9	34.7	25.1	
2	82.1	42.2	68.9	37.2	58.6	33.4	49.1	29.9	39.7	27	34.6	25	
3	83.6	42.8	68.4	37.3	57.9	33.5	48.4	29.5	40.1	26.7	34.9	25.2	
4	83.2	42.9	68.9	37.3	58.4	33.2	48.2	29.8	39.8	27.4	34.3	24.8	
5	81.8	42.8	69.1	37.1	58.3	33.5	48.9	29.8	39.9	26.8	34.5	25.2	
6	82.8	43	68.5	38.2	58.3	33.2	48.8	30	39.8	26.8	34.4	25.1	
7	83.7	42.7	69.4	37.3	58.2	33.4	48.7	30	39.9	26.3	34.7	25	
8	82.4	42.5	69.3	37.1	58.2	33.5	49	29.7	40.3	26.5	34.6	24.6	
9	83.6	43.2	69.5	37.8	58.4	33.5	48.9	29.8	40.1	26.9	34.7	25.1	
10	82.2	42.3	68.9	37.4	58.2	33.8	48.6	29.9	39.9	26.4	34.7	24.7	
11	82.7	42.8	68.6	37.5									
12	82.8	42.9	68.9	37.1									
Mean	82.85	42.71	69.03	37.39	58.29	33.45	48.75	29.82	39.93	26.77	34.61	24.98	
ΔH , cm		40.14		31.63		24.84		18.93		13.16		9.63	
S	0.639	0.300	0.439	0.323	0.185	0.172	0.280	0.148	0.183	0.320	0.173	0.210	
$E(h_1), E(h_2)$	0.184	0.087	0.127	0.093	0.059	0.054	0.089	0.047	0.058	0.101	0.055	0.066	
$E(\Delta H)$		0.204		0.157		0.080		0.100		0.117		0.086	
$E(\Delta H)$ %		0.508		0.498		0.322		0.529		0.885		0.893	

Table A7.5: Swirl and cylindrical pipe pressure loss

v , m/s	ΔP_{total} , Pa	$E(\Delta P_{\text{total}})$, Pa	$E(\Delta P_{\text{total}})$, %
1.001	944.70	8.43	0.89
1.243	1291.00	11.43	0.89
1.493	1857.03	9.82	0.53
1.742	2436.80	7.83	0.32
1.993	3103.23	15.44	0.50
2.266	3937.90	19.99	0.51

**Figure A7.2: Pressure loss versus flow velocity and quadratic fit for swirling flow and cylindrical pipe****Table A7.6: Pressure loss from quadratic fit to data for swirling flow and cylindrical pipe**

v , m/s	ΔP_{total} , Pa
1	924.13
1.25	1346.22
1.5	1853.81
1.75	2446.89
2	3125.46
2.25	3889.53

Table A7.7: Swirl pipe only pressure loss

v , m/s	ΔP_{swirl} , Pa	$E(\Delta P_{\text{swirl}})$, Pa	$E(\Delta P_{\text{circ}})$, Pa	$E_T(\Delta P_{\text{swirl}})$, Pa	$E_T(\Delta P_{\text{swirl}})$, %
1	274.32	2.45	19.97	20.12	7.33
1.25	386.68	3.42	5.88	6.81	1.76
1.5	527.67	2.79	10.20	10.57	2.00
1.75	697.29	2.24	9.41	9.68	1.39
2	895.54	4.46	10.00	10.95	1.22
2.25	1122.42	5.70	24.83	25.48	2.27

Entry transition and swirl pipe data

Table A7.8: Pressure loss measured across entry transition (0.1m) + swirling flow pipe (0.4m) + 2.83m cylindrical pipe														
Velocity, m/s		2.246		1.993		1.748		1.502		1.233		1.002		
Reading	$h_{1,}$ cm	$h_{2,}$ cm	$h_{1,}$ cm	$h_{2,}$ cm	$h_{1,}$ cm	$h_{2,}$ cm	$h_{1,}$ cm	$h_{2,}$ cm	$h_{1,}$ cm	$h_{2,}$ cm	$h_{1,}$ cm	$h_{2,}$ cm	$h_{1,}$ cm	$h_{2,}$ cm
1	57.2	18.5	46.8	16.3	57.4	32.8	46.8	29.2	39.6	26.6	32.9	26.2	32.9	26.2
2	57.8	19	46.3	16.6	58.2	32.1	47	29.1	39.8	26.2	34.9	24.3	34.9	24.3
3	57	17.7	48.1	16.2	56.8	32.2	47.7	29.3	39.6	26.7	34.5	24.2	34.5	24.2
4	56.2	17.6	47.5	16.7	56.8	33	46.7	29	40	26.5	35.2	25.4	35.2	25.4
5	57.4	18.9	48.4	16.6	56.4	32.3	47	29.4	39.6	26.6	33.6	23.7	33.6	23.7
6	57.2	18.7	47.1	16.7	57.7	32.8	46.5	29.1	39.7	26.5	34.7	25.9	34.7	25.9
7	56.8	18.7	47.4	16.2	58	32.1	48.3	28.1	39.4	26.7	34.6	23.9	34.6	23.9
8	56.8	18.9	47	16.4	56.7	32.5	47.7	28.8	39.5	26.7	32.8	24.1	32.8	24.1
9	57.5	18.6	47.7	16.4	57.1	32.9	47.6	28.1	39.7	26.7	34.1	24.2	34.1	24.2
10	57.5	18.6	47.5	16.2	57.1	33	47.5	29	39.1	26.7	32.7	25.5	32.7	25.5
11			47.8				47	28.1			34.2	23.7	34.2	23.7
12											32.6	23.6	32.6	23.6
Mean	57.14	18.52	47.42	16.43	57.22	32.57	47.25	28.84	39.60	26.59	33.90	24.56	33.90	24.56
$\Delta H,$ cm		38.62		30.99		24.65		18.42		13.01		9.34		9.34
S	0.460	0.485	0.598	0.206	0.592	0.371	0.543	0.499	0.240	0.160	0.941	0.927	0.941	0.927
$E(h_1),$														
$E(h_2)$	0.145	0.153	0.180	0.065	0.187	0.117	0.164	0.150	0.076	0.050	0.272	0.268	0.272	0.268
$E(\Delta H)$		0.211		0.192		0.221		0.222		0.091		0.381		0.381
$E(\Delta H)$ %		0.547		0.619		0.897		1.207		0.701		4.081		4.081

Table A7.9: Entry transition, swirling flow and cylindrical pipe pressure loss

v , m/s	ΔP_{total} , Pa	$E(\Delta P_{\text{total}})$, Pa	$E(\Delta P_{\text{total}})$, %
1.002	916.42	37.40	4.08
1.233	1276.28	8.95	0.70
1.502	1806.82	21.80	1.21
1.748	2418.17	21.68	0.90
1.993	3039.94	18.80	0.62
2.246	3788.62	20.73	0.55

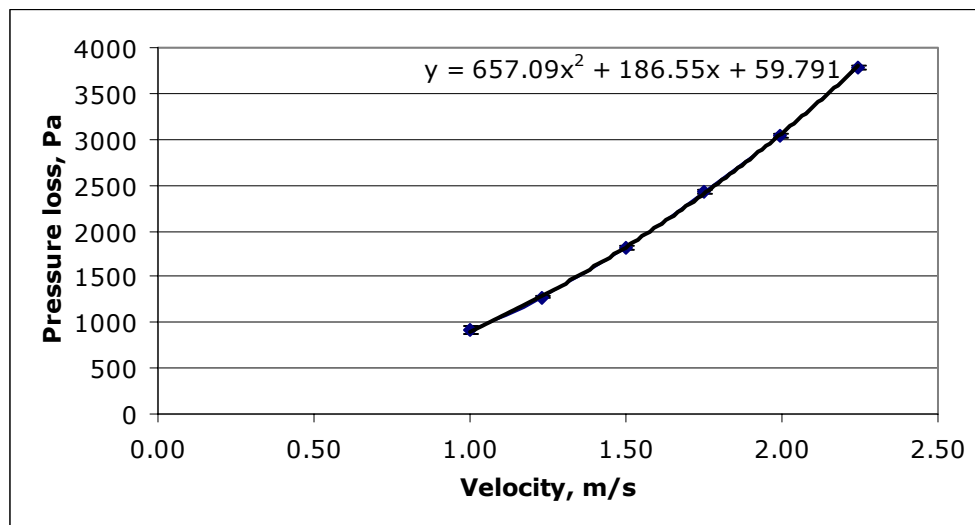


Figure A7.3: Pressure loss versus flow velocity and quadratic fit for transition, swirling flow and cylindrical pipe

Table A7.10: Pressure loss from quadratic fit to data for transition, swirl and cylindrical pipe

v , m/s	ΔP_{total} , Pa
1	903.43
1.25	1319.68
1.5	1818.07
1.75	2398.59
2	3061.25
2.25	3806.05

Table A7.11: Entry transition and swirl pipe only pressure loss

$v, \text{ m/s}$	$\Delta P_{\text{trans+swirl}},$ Pa	$E\Delta P_{(\text{trans+swirl})},$ Pa	$E (\Delta P_{\text{circ}}),$ Pa	$E_T(\Delta P_{\text{trans+swirl}}),$ Pa	$E_T(\Delta P_{\text{trans+swirl}}),$ %
1	274.73	11.21	19.32	22.34	8.13
1.25	391.30	2.74	5.69	6.32	1.62
1.5	535.00	6.46	9.87	11.79	2.20
1.75	705.82	6.33	9.11	11.09	1.57
2	903.75	5.59	9.68	11.18	1.24
2.25	1128.81	6.18	24.02	24.80	2.20

Appendix A8.1: Additional Results for Settling Slurry Tests

Numerical Results of Errors for Figure 8.8, Chapter 8

Sample Calculation for RD 1.4, 1m/s

$S(x)$ = Standard error in x

Swirl only

$$\Delta P = 956.9 \text{ Pa}$$

$$S(\Delta P \text{ 'swirl only'}) = 18.76 \text{ Pa}$$

Swirl + Entry + Exit transition

$$\Delta P = 891.42 \text{ Pa}$$

$$S(\Delta P \text{ 'swirl + entry + exit'}) = 23.88 \text{ Pa}$$

$$\text{Advantage 'swirl + entry + exit'} = 956.9 - 891.42 = 65.49 \text{ Pa}$$

$$S(\text{advantage}) = \sqrt{18.76^2 + 23.88^2} = 30.37 \text{ Pa}$$

Water only

Velocity, m/s	Swirl + Entry		Swirl + Entry + Exit	
	Advantage, Pa	Standard Error, Pa	Advantage, Pa	Standard Error, Pa
1.00	20.70	38.39	48.89	34.57
1.25	26.54	14.52	53.96	14.81
1.50	35.74	23.91	69.26	22.21
1.75	48.30	23.06	94.78	21.09
2.00	64.21	24.33	130.53	25.18
2.25	83.49	28.80	176.50	30.06

RD 1.4 solids

Velocity, m/s	Swirl + Entry		Swirl + Entry + Exit	
	Advantage, Pa	Standard Error, Pa	Advantage, Pa	Standard Error, Pa
1.00	20.13	34.91	65.49	30.37
1.25	73.01	41.37	82.56	44.18
1.50	81.82	27.34	84.27	39.35
1.75	46.56	23.45	70.60	23.48

RD 2.7 solids

Velocity, m/s	Swirl + Entry		Swirl + Entry + Exit	
	Advantage, Pa	Standard Error, Pa	Advantage, Pa	Standard Error, Pa
1.00	114.20	160.61	106.00	155.63
1.25	140.83	64.95	91.59	59.67
1.50	136.10	44.11	61.33	58.37
1.75	100.00	33.08	15.23	90.04

RD 4.5 solids

Velocity, m/s	Swirl + Entry		Swirl + Entry + Exit	
	Advantage, Pa	Standard Error, Pa	Advantage, Pa	Standard Error, Pa
1.00	44.21	19.62	131.85	27.45
1.25	129.73	37.00	177.48	42.57
1.50	138.54	45.76	143.56	54.45
1.75	70.64	35.99	30.11	39.39

Effect of Solids Density on Pressure Loss

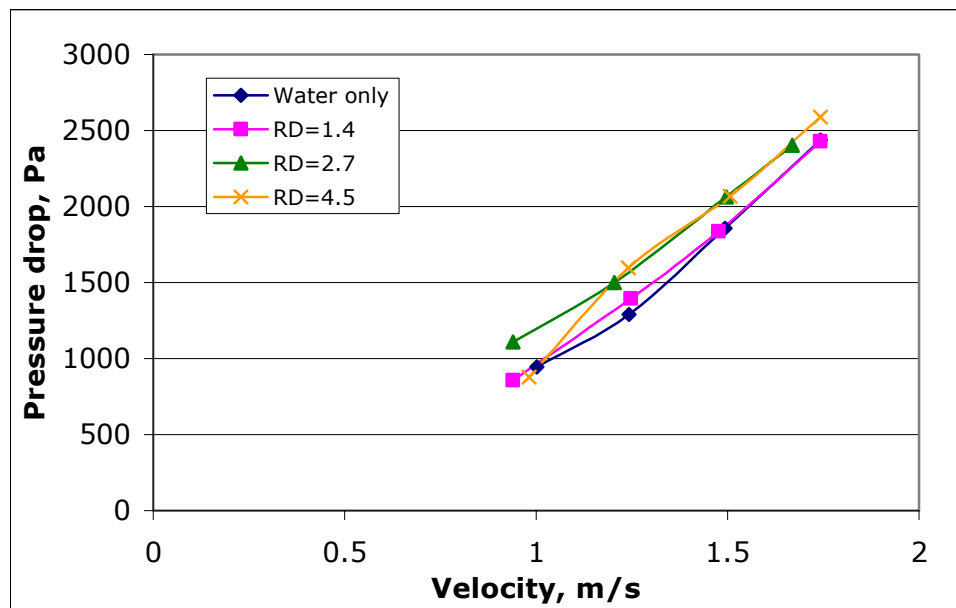


Figure A8.1: Pressure Loss Curve for 'Swirl Only' Case; 2kg of solids added (R.D. 1.4 1.6% w/w, R.D. 2.7 2% w/w, R.D. 4.5 1.25% w/w)

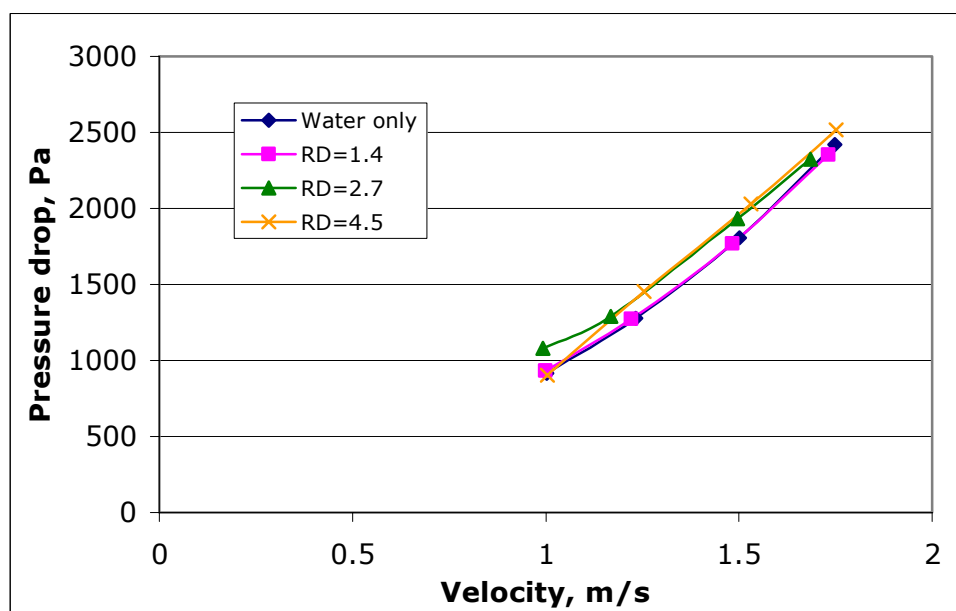


Figure A8.2: Pressure Loss Curve for 'Swirl + Entry Transition' Case; 2kg of solids added (R.D. 1.4 1.8% w/w, R.D. 2.7 2.1% w/w, R.D. 4.5 1.5% w/w)

Effect of Solids Density on Settling

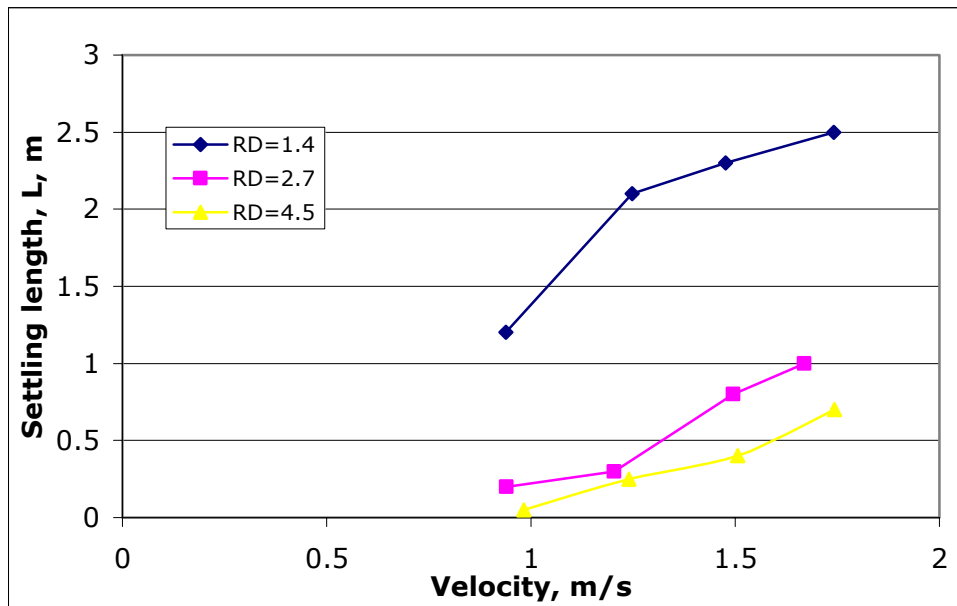


Figure A8.3: Effect of Solids Density on Settling for 'Swirl Only' Case; 2kg of solids added in each test

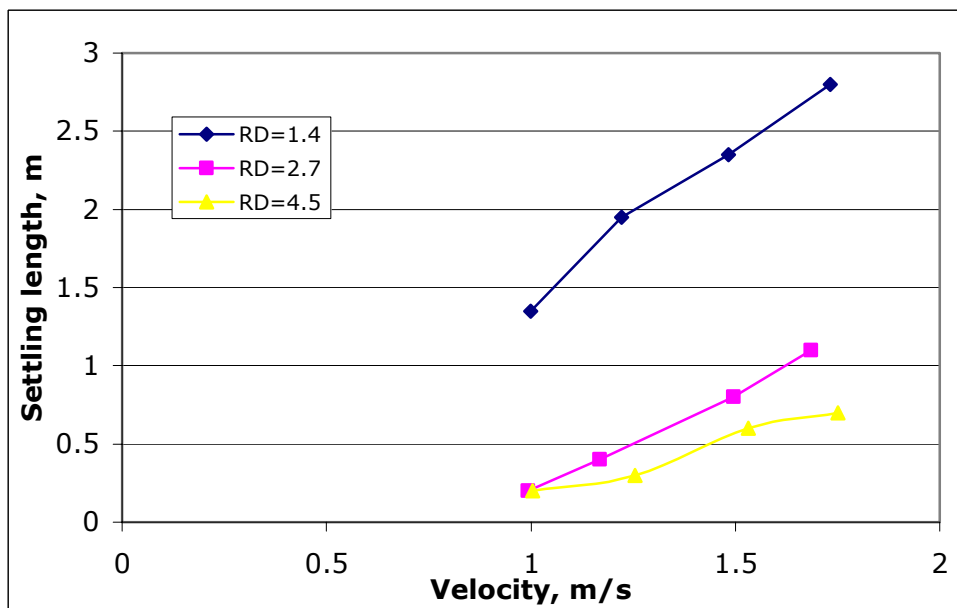


Figure A8.4: Effect of Solids Density on Settling for 'Swirl + Entry Transition' Case; 2kg of solids added in each test

Effect of Solids Concentration on Settling

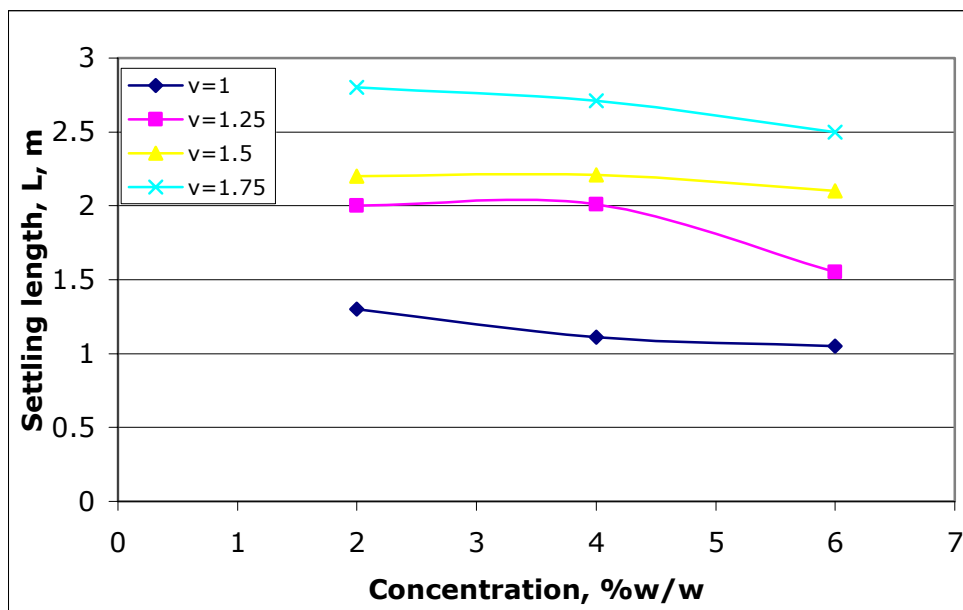


Figure A8.5: Effect of Solids Concentration on Settling Length for 'Swirl + Entry + Exit Transition' Case; R.D. 1.4 solids

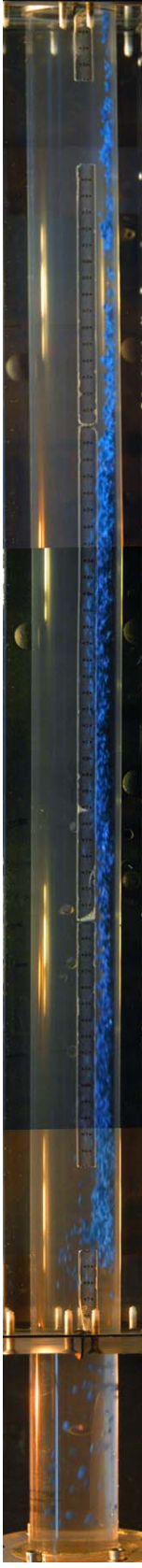
Appendix A8.2

Velocity = 1m/s, Solids RD 2.7, 2% w/w

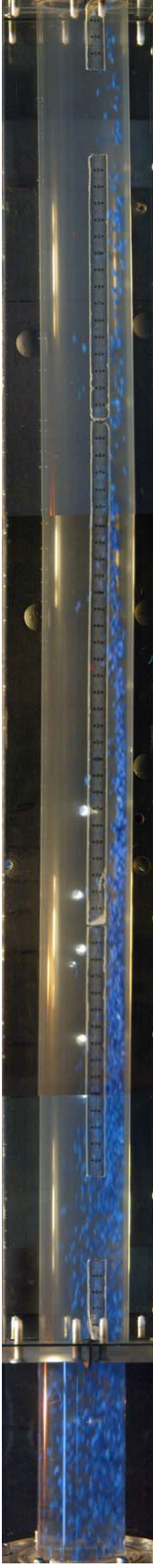
Flow prior to Swirl Pipe



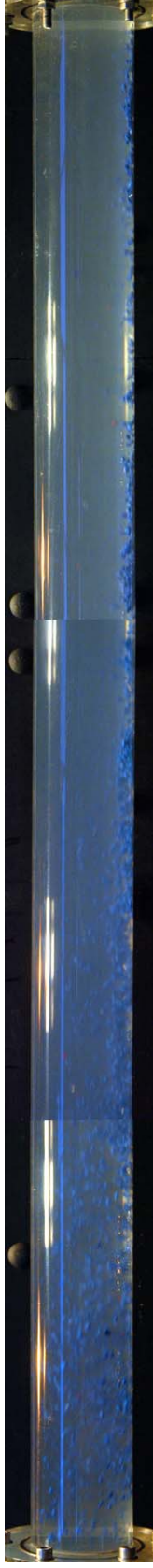
'Swirl Pipe only' Case: Flow downstream of Swirl Pipe (from exit to 1m downstream)



'Swirl + Entry Transition' Case: Flow downstream of Swirl Pipe (from exit to 1m downstream)



'Swirl + Entry + Exit Transition' Case: Flow downstream of Exit Transition (from exit to 1m downstream)

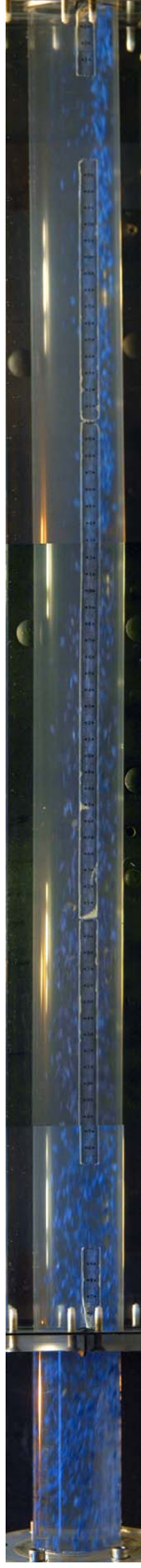


Velocity = 1.25m/s, Solids RD 2.7, 2% w/w

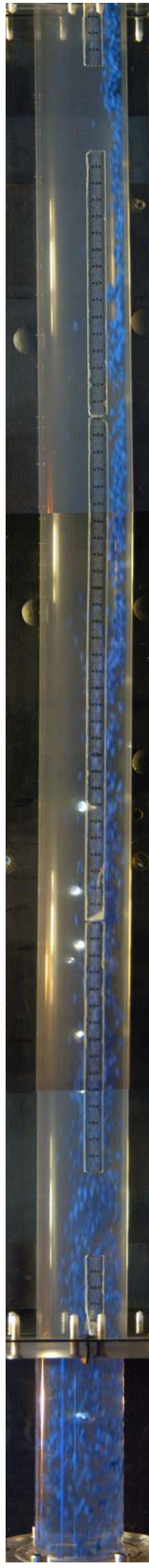
Flow prior to Swirl Pipe



'Swirl Pipe only' Case: Flow downstream of Swirl Pipe (from exit to 1m downstream)



'Swirl + Entry Transition' Case: Flow downstream of Swirl Pipe (from exit to 1m downstream)



'Swirl + Entry + Exit Transition' Case: Flow downstream of Exit Transition (from exit to 1m downstream)

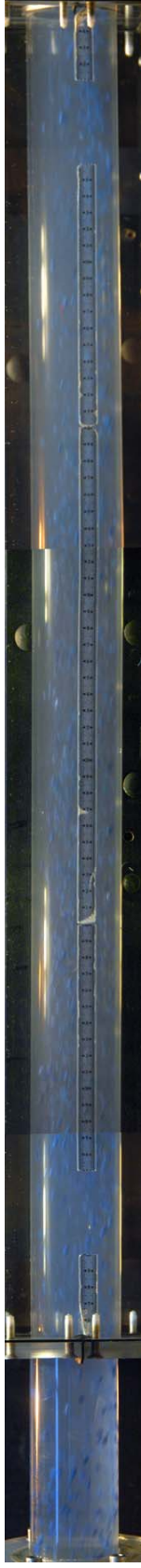


Velocity = 1.5m/s, Solids RD 2.7, 2% w/w

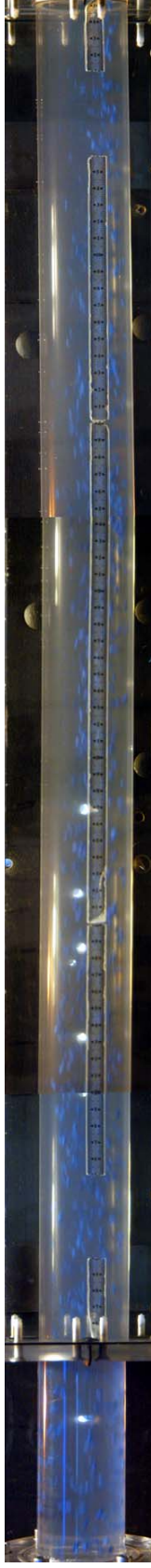
Flow prior to Swirl Pipe



'Swirl Pipe only' Case: Flow downstream of Swirl Pipe (from exit to 1m downstream)



'Swirl + Entry Transition' Case: Flow downstream of Swirl Pipe (from exit to 1m downstream)

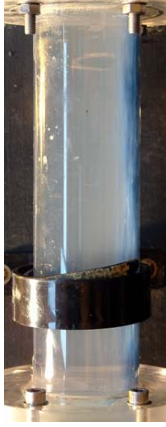


'Swirl + Entry + Exit Transition' Case: Flow downstream of Exit Transition (from exit to 1m downstream)

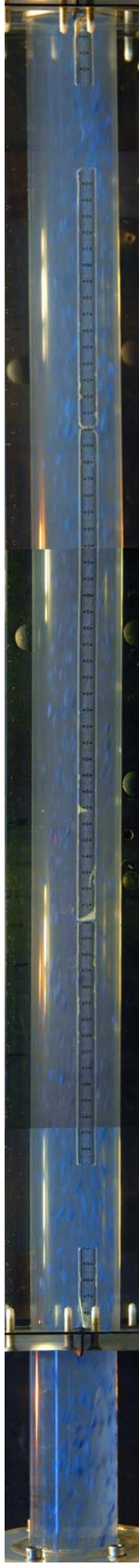


Velocity = 1.75m/s, Solids RD 2.7, 2% w/w

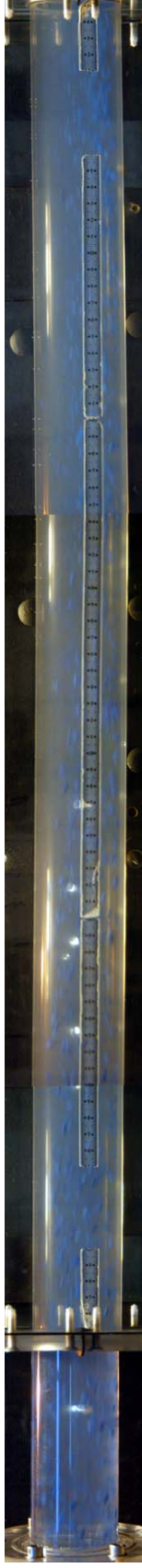
Flow prior to Swirl Pipe



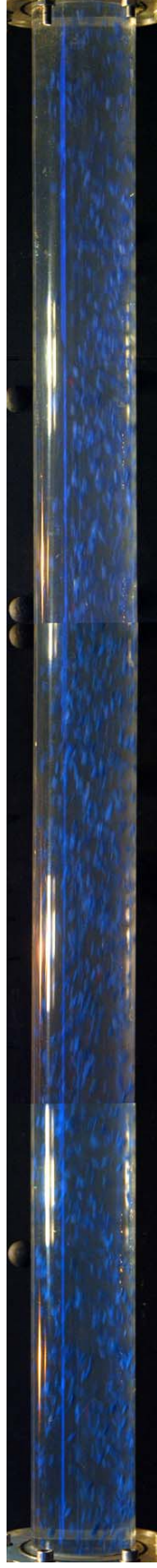
'Swirl Pipe only' Case: Flow downstream of Swirl Pipe (from exit to 1m downstream)



'Swirl + Entry Transition' Case: Flow downstream of Swirl Pipe (from exit to 1m downstream)



'Swirl + Entry + Exit Transition' Case: Flow downstream of Exit Transition (from exit to 1m downstream)



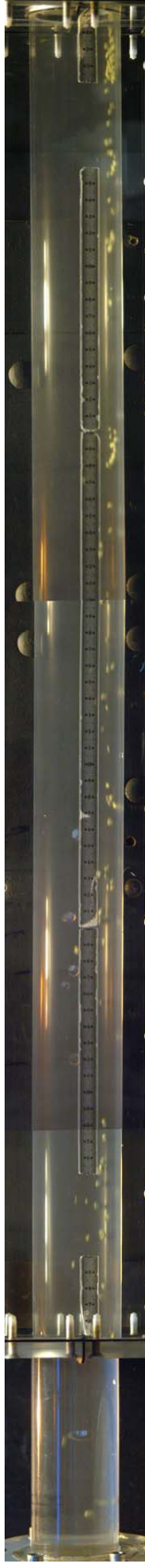
Appendix A8.3

Velocity = 1m/s, Solids RD 4.5, 2kg of solids added

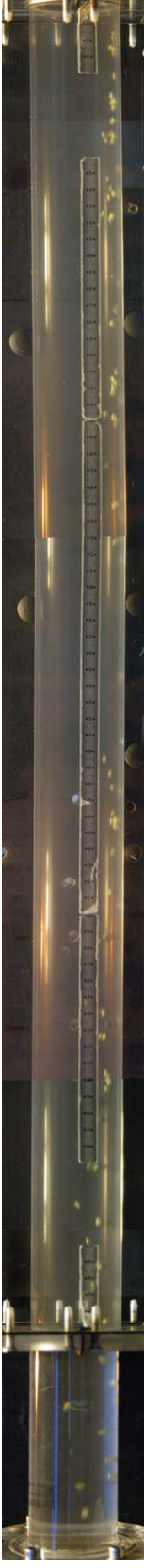
Flow prior to Swirl Pipe



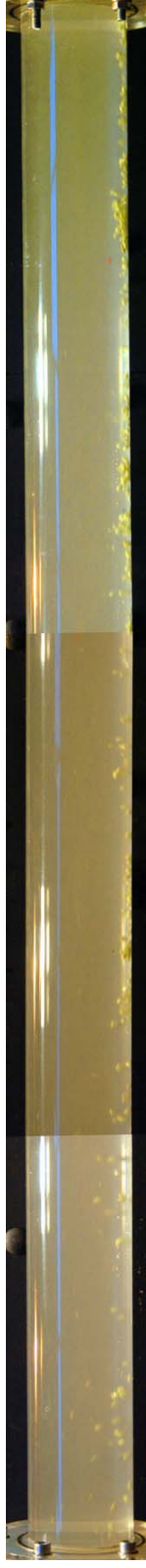
'Swirl Pipe only' Case: Flow downstream of Swirl Pipe (from exit to 1m downstream)



'Swirl + Entry Transition' Case: Flow downstream of Swirl Pipe (from exit to 1m downstream)



'Swirl + Entry + Exit Transition' Case: Flow downstream of Exit Transition (from exit to 1m downstream)

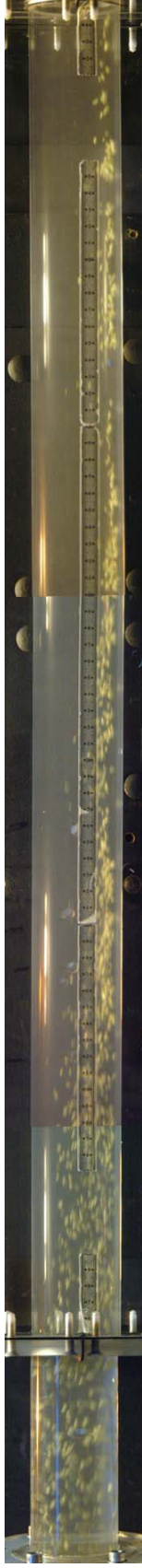


Velocity = 1.25m/s, Solids RD 4.5, 2kg of solids added

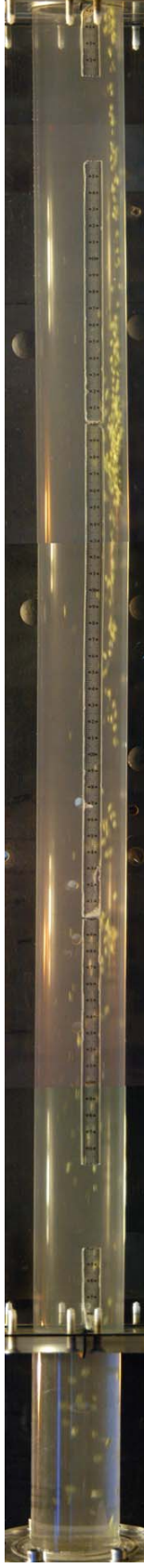
Flow prior to Swirl Pipe



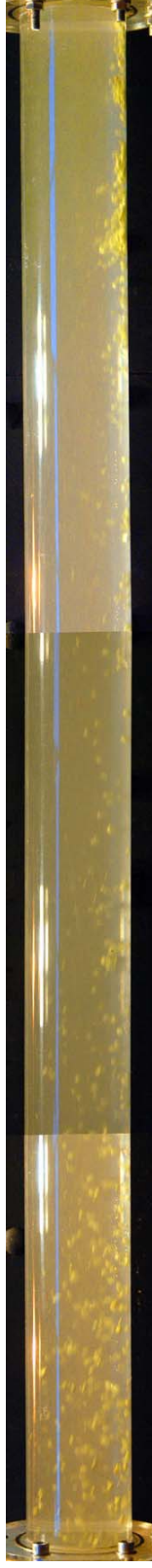
'Swirl Pipe only' Case: Flow downstream of Swirl Pipe (from exit to 1m downstream)



'Swirl + Entry Transition' Case: Flow downstream of Swirl Pipe (from exit to 1m downstream)



'Swirl + Entry + Exit Transition' Case: Flow downstream of Exit Transition (from exit to 1m downstream)

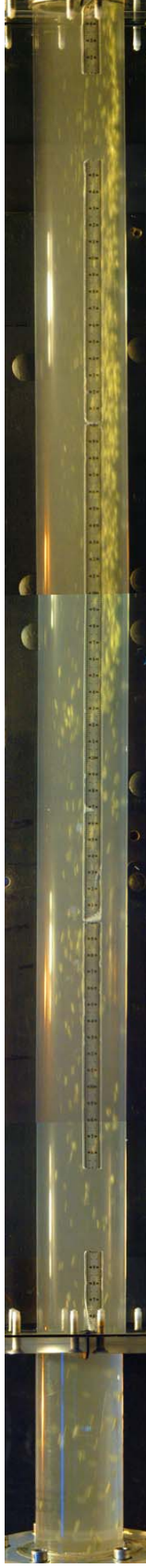


Velocity = 1.5m/s, Solids RD 4.5, 2kg of solids added

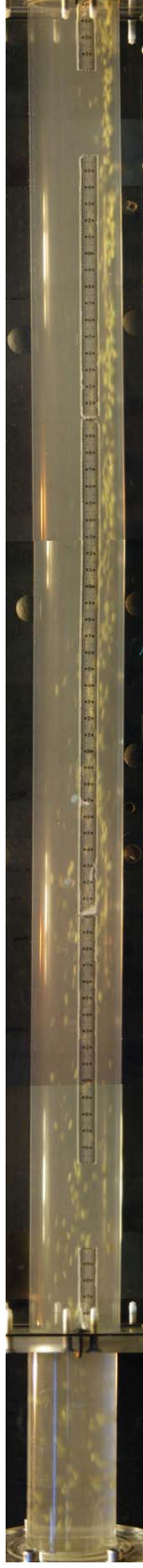
Flow prior to Swirl Pipe



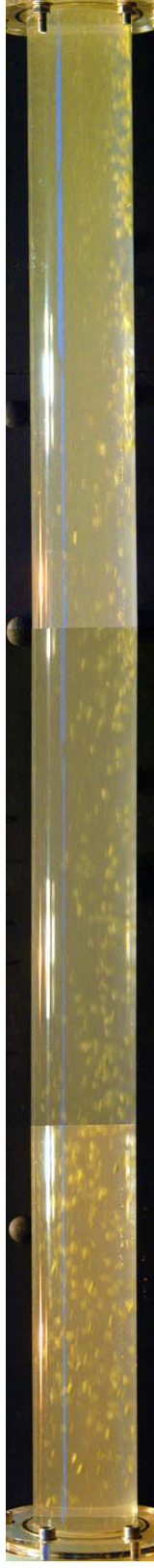
'Swirl Pipe only' Case: Flow downstream of Swirl Pipe (from exit to 1m downstream)



'Swirl + Entry Transition' Case: Flow downstream of Swirl Pipe (from exit to 1m downstream)



'Swirl + Entry + Exit Transition' Case: Flow downstream of Exit Transition (from exit to 1m downstream)

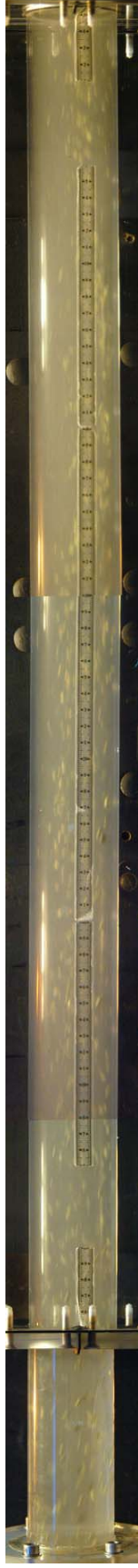


Velocity = 1.75m/s, Solids RD 4.5, 2kg of solids added

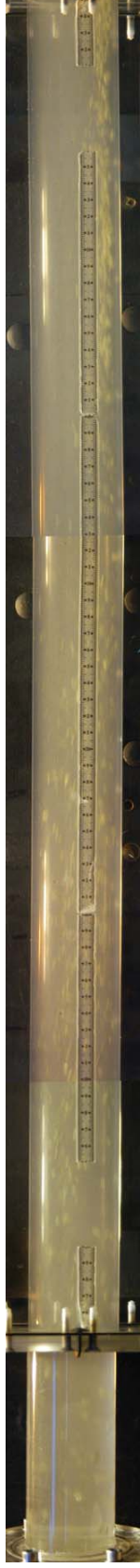
Flow prior to Swirl Pipe



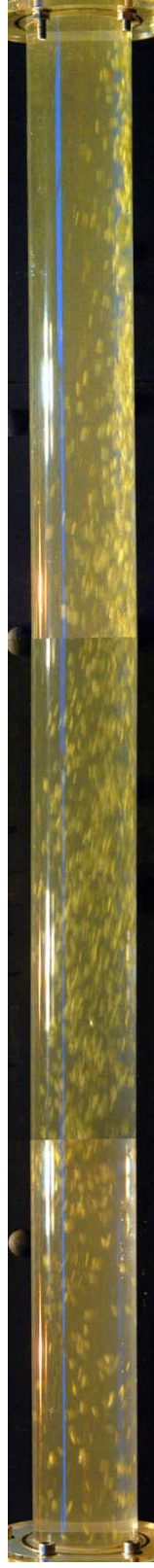
'Swirl Pipe only' Case: Flow downstream of Swirl Pipe (from exit to 1m downstream)



'Swirl + Entry Transition' Case: Flow downstream of Swirl Pipe (from exit to 1m downstream)



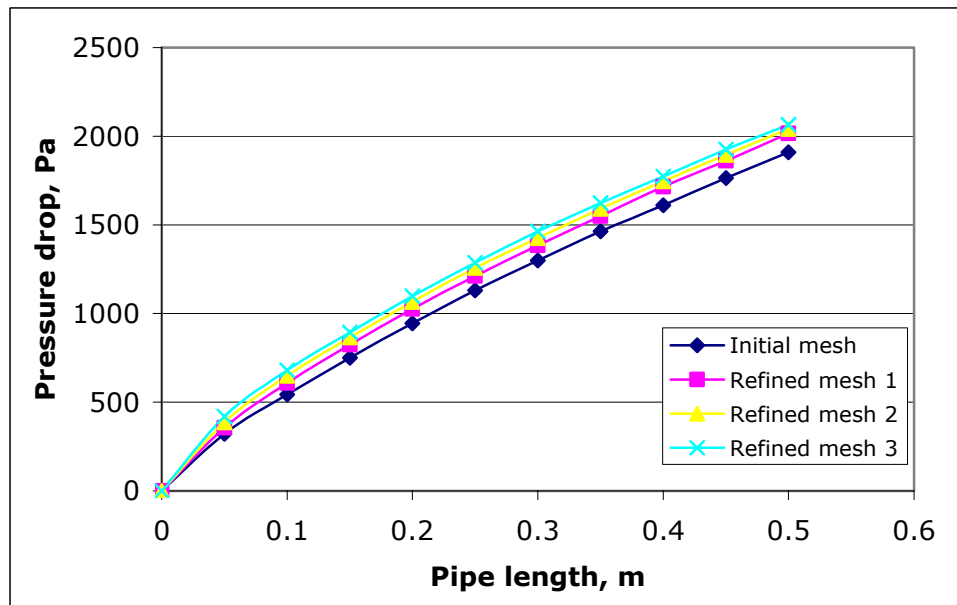
'Swirl + Entry + Exit Transition' Case: Flow downstream of Exit Transition (from exit to 1m downstream)



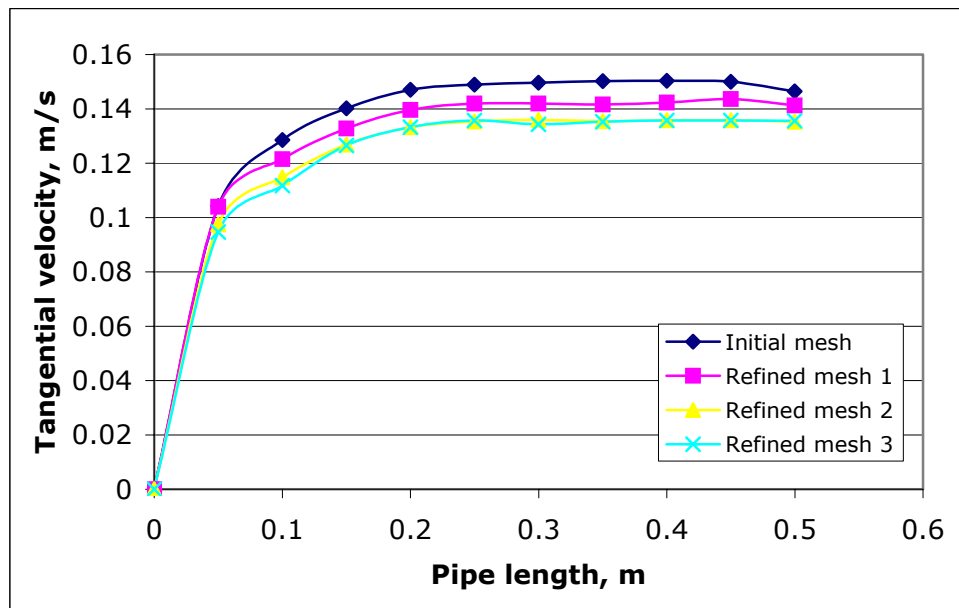
Appendix A9.1

Table A9.1: Grid Independence Test for P:D=10 pipe

Number of cells	Tangential velocity at exit, m/s	Pressure drop, Pa	Swirl effectiveness
129930	0.14649	1909.47	0.044
265360	0.14127	2015.78	0.04
576160	0.1353	2041.88	0.038
1109430	0.1356	2064.26	0.037



(a) Pressure drop for different sized meshes



(b) Tangential velocity for different sized meshes

Figure A9.1: Grid independence for pipe of P:D = 10

Table A9.2: Grid independence test for P:D=4 pipe

Number of cells	Tangential velocity at exit, m/s	Pressure drop, Pa	Swirl Effectiveness
479430	0.32665	3099.03	0.059
931400	0.31279	3140.42	0.056

A grid of approximately 500,000 cells (refined mesh 2) was considered sufficient in both cases since the difference in results from the case with a further refined mesh was small and trends were closely followed.